DOCTORAL THESIS

Topology Optimization for Improved Magnetic Core Utilization and Torque Density in Additively Manufactured Electrical Machines

Shahid Hussain

TALLINNA TEHNIKAÜLIKOOL
TALLINN UNIVERSITY OF TECHNOLOGY
TALLINN 2026

TALLINN UNIVERSITY OF TECHNOLOGY
DOCTORAL THESIS
80/2026

Topology Optimization for Improved Magnetic Core Utilization and Torque Density in Additively Manufactured Electrical Machines

SHAHID HUSSAIN

TAL TECH PRESS

TALLINN UNIVERSITY OF TECHNOLOGY
School of Engineering
Department of Electrical Power Engineering and Mechatronics
This dissertation was accepted for the defence of the degree: 05/11/2026

Supervisor:
Prof. Ants Kallaste
School of Engineering
Tallinn University of Technology
Tallinn, Estonia

Opponents:
Prof. Nick Simpson
Faculty of Electrical, Electronic and Mechanical Engineering
University of Bristol
Bristol, United Kingdom

Prof. Roman Pechánek
Faculty of Electrical Engineering
University of West Bohemia
Pilsen, Czech Republic

Defence of the thesis: 11/12/2026, Tallinn

Declaration:
Hereby I declare that this doctoral thesis, my original investigation and achievement, submitted for the doctoral degree at Tallinn University of Technology has not been submitted for doctoral or equivalent academic degree.

Shahid Hussain

Signature

European Union
European Regional Development Fund

Investing in your future

Copyright: Shahid Hussain, 2026
ISSN 2585-6898 (paperback)
ISBN 978-9916-80-598-5 (paperback)
ISSN 2585-6901 (PDF)
ISBN 978-9916-80-597-8 (PDF)
https://doi.org/10.23658/taltech.80/2026
Printed by Koopia Niini & Rauam

Hussain, S. (2026). Topology Optimization for Improved Magnetic Core Utilization and Torque Density in Additively Manufactured Electrical Machines [TalTech Press]. https://doi.org/10.23658/taltech.80/2026

TALLINNA TEHNIKAÜLIKOOL
DOKTORITÖÖ
80/2026

Kihtlisandus meetodil valmistatud elektrimasinate topoloogia optimeerimine pöördemomendi tiheduse ja magnetsüdamike tõhususe suurendamiseks

SHAHID HUSSAIN

TAL TECH
KIRJASTUS

Contents

List of Publications 8
Author's Contribution to the Publications 9
Introduction 10
1.1 Problem Definition 10
1.2 Hypotheses 11
1.3 Research Objectives 12
1.4 Contributions of the Thesis 12
1.4.1 Scientific Novelties 12
1.4.2 Practical Novelties 13
1.5 Thesis Outline 13
Abbreviations 14
Symbols 15
2 State of the Art in Topology Optimization and Additive Manufacturing 19
2.1 Electrical Machine Optimization Techniques 19
2.1.1 Parametric Optimization 19
2.1.2 Shape Optimization 20
2.1.3 Topology Optimization 21
2.2 Topology Optimization Methods for Electrical Machines 22
2.2.1 ON/OFF Method 22
2.2.2 Level-Set Method 22
2.2.3 Density Based Method 23
2.2.4 Machine learning assisted TO 24
2.3 Applications of Topology Optimization in Electrical Machines 24
2.3.1 TO for PM Machines 25
2.3.2 Reluctance Machines 25
2.4 Additive Manufacturing of Electrical Machine Magnetic Components 27
2.4.1 Integration of Topology Optimization and Additive Manufacturing 27
2.4.2 Additively Manufactured Rotor and Stator Cores 27
2.5 Summary 29
3 From Numerical Search to Physics Guided Design: Topology Optimization of a Permanent Magnet Machine 30
3.1 Motivation for Rotor Back Iron Topology Optimization 30
3.2 Commercial E-Scooter Motor 31
3.2.1 FE Model 32
3.3 Physical Basis for Rotor Back Iron Optimization 33
3.3.1 Quasi-Static Rotor Field 33
3.3.2 Optimization Problem 33
3.4 NGNet Based TO 34
3.4.1 Material Representation Using NGNet 34
3.4.2 Genetic Algorithm Search 35
3.4.3 NGNet Performance 35
3.5 Density Based TO 36
3.5.1 SIMP Material Interpolation 37
3.5.2 2D Magnetostatic Formulation 37
3.5.3 Objective Function Evaluation 38

3.5.4 Adjoint Sensitivity Analysis 39
3.5.5 Electromagnetic Performance Evaluation 39
3.5.6 Density Method Performance 40
3.6 Physics Guided Analytical TO 43
3.6.1 Magnetic Flux Model 43
3.6.2 Minimum Back Iron Width 44
3.6.3 Analytical TO Result 45
3.7 Comparison of the Three Back Iron Material Reduction Techniques 46
3.7.1 Manufacturing Oriented Design Modifications 48
3.8 Rotor Back Iron Fabrication Through AM 49
3.9 Experimental Testing and Validation 50
3.10 Summary 52
4 Design and TO of an AFDR-SRM 53
4.1 Benchmark AFDR-SRM Design and Numerical Validation 53
4.1.1 Machine Configuration and Operating Principle 53
4.1.2 Analytical Sizing Formulation 54
4.1.3 3D Benchmark FEM Validation 58
4.1.4 Magnetic Flux Density Validation 58
4.1.5 Flux Linkage and Inductance Characteristics 59
4.1.6 Static Flux Linkage and Torque Characteristics 60
4.1.7 Dynamic Performance Under Single Pulse and Current Chopping Control 61
4.1.8 Torque–Speed, Loss, and Efficiency Characteristics 62
4.2 Equivalent 2D Linearized Model 65
4.2.1 Basis of the Rotary to Linear Transformation 65
4.2.2 Mean Radius Geometric Mapping 65
4.2.3 Conversion from Rotational Speed to Linear Velocity 66
4.2.4 FEM Simulation of Linear Flux SRM 66
4.3 NGNet-Based Topology Optimization 67
4.3.1 Design Domain and Material Representation 67
4.3.2 Optimization Objective and Symmetry Reduction 69
4.3.3 Optimized Linear Topology and Thrust Performance 69
4.4 Analytical TO of Back Iron of AFDR-SRM 71
4.4.1 2D Equivalent Rotor Model 71
4.4.2 Minimum Rotor Back Iron Width 72
4.4.3 Analytically Reduced Rotor Geometry 73
4.5 Additive Manufacturing of the AFDR-SRM 74
4.5.1 Manufacturing Oriented Core Design 74
4.5.2 LPBF Printing Process 76
4.5.3 Heat Treatment and Component Preparation 77
4.6 Experimental Setup and Test Results 78
4.6.1 Dynamic Operation Under Load 78
4.7 Summary 79
5 Conclusions and Future Work 80
5.1 Conclusion of the Thesis 80
5.2 Future Work 80
List of Figures 82
List of Tables 84

References 85
Acknowledgements 91
Abstract 92
Lühikokkuvõte 94
Curriculum Vitae 173
Elulookirjeldus 174

List of Publications

The list of author's publications, on the basis of which the thesis has been prepared:

I S. Hussain, A. Kallaste, and T. Vaimann, "Recent Trends in Additive Manufacturing and Topology Optimization of Reluctance Machines," *Energies*, vol. 16, no. 9, p. 3840, 2023, doi: 10.3390/en16093840.

II S. Hussain, A. Kallaste, M. U. Naseer, Z. Ahmad, and T. Vaimann, "Topology Optimization of Outer Rotor BLDC Motor for Electric Scooter Application," in *2026 IEEE International Magnetic Conference—Short Papers (INTERMAG Short Papers)*, Manchester, United Kingdom, 2026, pp. 1–2, doi: 10.1109/INTERMAGShortPapers 68882.2026.11596512.

III S. Hussain, A. Kallaste, M. U. Naseer, Z. Ahmad, H. Tiismus, T. Plopeanu, M. Ibrahim, and T. Vaimann, "Topology Optimization of Additively Manufactured Outer Rotor Permanent Magnet Motor," *IEEE Transactions on Magnetics*, 2026, doi: 10.1109/TMAG.2026.3701312.

IV S. Hussain, A. Kallaste, P. Gangl, N. Krenn, T. Cherrière, M. U. Naseer, Z. Ahmad, and T. Vaimann, "Electromagnetic Topology Optimization of Brushless DC Motor Based on Density Method," *2026 International Conference on Electrical Machines (ICEM)*, Funchal (Madeira), Portugal, 2026, pp. 1-7, doi: 10.1109/ICEM68283.2026. 11757987.

V S. Hussain, A. Kallaste, M. U. Naseer, M. Sarap, H. Tiismus, and T. Vaimann, "Preliminary Design Analysis of an Axial Flux Yokeless Stator Switched Reluctance Machine," in *2023 IEEE 64th International Scientific Conference on Power and Electrical Engineering of Riga Technical University (RTUCON)*, Riga, Latvia, 2023, pp. 1–6, doi: 10.1109/RTUCON60080.2023.10413130.

VI S. Hussain, A. Kallaste, M. U. Naseer, H. Tiismus, and T. Vaimann, "Development of an Axial Flux SRM Through Additive Manufacturing," in *2024 International Conference on Electrical Machines (ICEM)*, Torino, Italy, 2024, pp. 1–6, doi: 10.1109/ICEM60801.2024.10700569.

VII S. Hussain, A. Kallaste, M. U. Naseer, H. Tiismus, M. Sarap, B. Asad, and T. Vaimann, "Design and Prototyping of Additively Manufactured Axial Flux Switched Reluctance Machine," *IEEE Transactions on Industry Applications*, vol. 62, no. 2, pp. 2587–2597, March–April 2026, doi: 10.1109/TIA.2025.3604357.

Author's Contribution to the Publications

Contribution to the papers in this thesis are:

I S. Hussain is the primary author of this review article. He conducted the literature review on additive manufacturing and topology optimization of reluctance machines, analysed and organized the reviewed studies, and prepared the initial manuscript.

II S. Hussain is the primary author. He implemented the NGNet based TO of the outer-rotor BLDC motor, formulated the optimization problem, performed the FEA simulations, evaluated the optimized rotor back iron design, and prepared the conference paper.

III S. Hussain is the primary author. He developed the physics guided analytical TO method for the rotor back iron, adapted the optimized geometry for additive manufacturing, performed the numerical analysis, contributed to prototype fabrication and experimental testing, analyzed the results, and prepared the initial manuscript.

IV S. Hussain is the primary author. He developed and implemented the density based TO framework using SIMP interpolation and adjoint sensitivity analysis, performed the nonlinear FE simulations, evaluated the electromagnetic performance of the optimized design, and prepared the conference paper.

V S. Hussain is the primary author. He developed the analytical design and 3D FEM of the 6/4 axial-flux yokeless stator switched reluctance machine, evaluated its electromagnetic performance, and prepared the conference paper.

VI S. Hussain is the primary author. He developed the manufacturing-oriented design of the axial-flux switched reluctance machine, performed the electromagnetic simulations, contributed to the fabrication and assembly of the magnetic components, and prepared the conference paper.

VII S. Hussain is the primary author. He developed the complete design and prototyping methodology for the AFDR-SRM, performed the analytical and numerical analysis, coordinated the manufacturing and assembly of the prototype, conducted the experimental testing, analyzed the measured results, and prepared the initial manuscript.

Introduction

Electrical machines are the cornerstone of modern industry, transportation, and energy generation, consuming approximately 53% of the world's electricity [1] . The accelerating demand for higher power density, greater efficiency, and application specific customization driven particularly by electric vehicles, drones, and aerospace propulsion systems places stringent new requirements on machine design that are increasingly difficult to meet with conventional manufacturing methods [2], [3].

Additive Manufacturing (AM) and in particular Laser Powder Bed Fusion (LPBF) has emerged as a transformative technology capable of overcoming many of these limitations [4], [5] . By building parts layer by layer directly from a 3D digital model, AM permits almost unlimited geometric freedom without the need for tooling. Complex internal channels, lattice structures, functionally graded materials, and topologically optimized shapes become manufacturable in a single process. For electrical machines, this means that the designer is no longer forced to conceive the magnetic circuit as a mere extrusion of a 2D section, but can instead think in 3D, integrating electromagnetic, thermal, and mechanical functions [6], [7] .

However, unlocking the full potential of AM requires more than the ability to print a given shape, it demands a systematic methodology for determining which shape to print. This is precisely the role of Topology Optimization (TO). TO is a computational design method that distributes material optimally within a prescribed design domain in order to maximize a chosen performance metric such as torque, flux linkage, or stiffness while respecting constraints on volume, stress, or magnetic saturation. When coupled with AM, TO can generate non-intuitive geometries that achieve significantly better performance than conventional heuristic designs, and that can be directly fabricated without manual simplification.

Despite the synergy between AM and TO, their integrated application to electrical machines remains fragmented. Reviews of electromagnetic TO indicate that most published studies have focused on Permanent Magnet (PM) machines, whereas switched and Synchronous Reluctance Machines (SynRM) have received comparatively less attention [8], [9] . Moreover, axial flux topologies, which offer inherent advantages in torque density and form factor for in-wheel and propulsion applications, are rarely subjected to TO because their 3D flux paths make full 3D TO computationally expensive [10]. A further gap exists in experimental validation, the overwhelming majority of TO studies for electrical machines end with a numerical simulation. Very few have proceeded to AM of the optimized geometry, and fewer still to experimental testing under realistic operating conditions.

The work presented in this thesis is to close these gaps. It systematically investigates the design, TO, and AM of two distinct machine types, an outer rotor PM BLDC motor for electric scooter applications, and an Axial Flux Dual Rotor Switched Reluctance Motor (AFDR-SRM) intended for high-speed propulsion. Across these platforms, the thesis develops and validates new optimization methods, demonstrates the fabrication of optimized geometries via LPBF, and experimentally confirms that the AM built machines perform as predicted by simulation.

1.1 Problem Definition

Conventional magnetic cores of electrical machines are generally designed using predefined 2D cross-sections, and established manufacturing rules. Although these

approaches simplify design and production, they restrict the efficient distribution of magnetic material. Consequently, material may be removed in regions that make only a limited contribution to the useful magnetic flux path. TO offers a systematic means of identifying these regions and redistributing the material according to its electromagnetic function.

The current state of the art in electromagnetic TO is dominated by 2D models. This is largely due to the limitations imposed by conventional laminated core manufacturing, which is generally restricted to planar geometries along the axial direction. AM removes many of these geometric restrictions and enables the production of non-uniform magnetic structures with complex 3D flux paths [11]. This expanded design freedom creates opportunities for improved magnetic material utilization, weight reduction, and increased torque density.

Although 2D numerical TO is less computationally demanding than its 3D counterpart, it still requires repeated FEA, sensitivity calculations, filtering procedures, or population-based searches. Their computational burden increases considerably when nonlinear magnetic materials, multiple rotor positions, and different operating conditions are considered. AM further expands the available design space by enabling complex 3D geometries. However, exploiting this freedom requires 3D electromagnetic models, particularly for axial flux machines with inherently 3D flux paths [12]. Consequently, direct 3D TO becomes computationally intensive when repeated FEA simulations are required throughout the iterative optimization process [13].

Despite the potential of TO and AM, the following two research problems limit their broader integration into the design and production of electrical machine magnetic components.

1. **TO based weight reduction of quasi-static back iron regions:** Most electromagnetic TO studies focus on airgap facing geometries to improve performance parameters such as torque and torque ripple, while back iron reduction is commonly limited to parametric optimization of a uniform thickness. The application of TO, to identify and remove weakly utilized material from rotor or stator back iron regions, while preserving the required electromagnetic performance, remains underexplored.

2. **Computationally efficient TO of 3D flux machines:** TO is inherently computationally intensive, and its application to machines with 3D magnetic flux paths remains underexplored because of simulation complexity and the limitations imposed by conventional manufacturing techniques. Additionally, AM enables the fabrication of complex 3D magnetic structures, computationally efficient analytical and equivalent model approaches are required to reduce the number of FE evaluations needed for their optimization.

1.2 Hypotheses

Based on the above research problems, the following hypotheses are proposed.

1. TO of the quasi-static rotor back iron can substantially reduce rotor mass without compromising the electromagnetic performance of PM machine.
2. AM-enabled TO can exploit the geometrical freedom available in machines with 3D magnetic flux paths to improve electromagnetic performance.
3. For PM machines, a physics guided analytical TO method can minimize the required back iron material and significantly reducing the computational effort compared with iterative numerical TO methods.

4. The physics guided analytical TO method developed for PM machine back iron reduction can be adapted to field excited machines with 3D magnetic flux paths to reduce rotor mass while preserving the performance.

1.3 Research Objectives

To support the hypotheses proposed in this thesis, a set of specific research objectives were established. These objectives are directed toward the development and experimental validation of design, TO, and AM methodologies for electrical machines, aiming primarily at torque density enhancement and mass reduction. The detailed research objectives are as follows.

1. Identification of research gaps through a review of the state of the art in TO methods for electrical machines.
2. Weight reduction of PM machine for the improved torque density using the established numerical TO methods.
3. Improvement of computational efficiency in TO through the development of a new non-iterative physics guided analytical TO method.
4. Performance improvement of axial flux machine through a computationally efficient 3D TO methodology.
5. Weight reduction of the rotor back iron by adapting the physics guided TO method to field excited axial flux machine.
6. Validation of the optimized design of both machines, manufactured from Fe–3.7%Si powder using LPBF, through experimental testing of the assembled prototypes.

1.4 Contributions of the Thesis

This thesis makes several original contributions to the field of design and optimization of AM electrical machines, spanning both PM and reluctance machine topologies, and combining novel analytical method with experimental verification.

1.4.1 Scientific Novelties

1. Application of established Normalized Gaussian Network (NGNet) and density based TO methods to the rotor back iron of an outer rotor PM BLDC motor, enabling nonuniform material distribution for reduced rotor mass and increased torque density without degrading airgap flux density, back EMF, and torque.
2. Development of a non-iterative, physics guided analytical TO method for directly determining the minimum required rotor back iron distribution, providing a substantial reduction in computational time compared with conventional iterative TO methods.
3. Development of an analytical design methodology for a segmented, yokeless 6/4 AFDR-SRM, establishing a direct relationship between the geometric parameters and the electromagnetic output capability of the machine.
4. Development of a 2D linearized equivalent model of the AFDR-SRM, enabling computationally efficient NGNet based TO of the rotor pole shoe geometry while retaining the electromagnetic characteristics of the original 3D machine.
5. Extension of the physics guided material reduction method from a PM magnetic structure to the electrically excited rotor back iron of the AFDR-SRM,

establishing its applicability to different excitation sources and electrical machine configurations.

1.4.2 Practical Novelties

This thesis presents the following practical novelties, representing tangible engineering achievements that bridge theoretical design, AM, and experimental validation.

1. Physical realization of a TO outer rotor PM BLDC back iron from Fe-3.7 wt% Si powder using LPBF, including manufacturability adaptation, heat treatment, and integration into a complete motor assembly.
2. LPBF manufacture of the complete AFDR-SRM magnetic structure, comprising six segmented stator units and two four pole rotors, followed by their assembly into a functional machine prototype.
3. Implementation of parallel laminated sections in the AM AFDR-SRM stator teeth and rotor poles to restrict eddy current paths.
4. Experimental validation of the LPBF BLDC motor and AFDR-SRM prototypes under different operating conditions, demonstrating close agreement between measured performance and 3D FEA predictions.

1.5 Thesis Outline

The remainder of this thesis is organized as follows.

Chapter 2 reviews parametric, shape, and topology-optimization methods used in electrical machine design. Particular attention is given to ON/OFF, level-set, density based, and machine learning assisted TO methods. The chapter also reviews the application of AM to PM and reluctance machines and identifies the limited number of studies that combine TO, LPBF fabrication, and experimental validation.

Chapter 3 investigates TO of the rotor back iron of an outer rotor PM BLDC motor. Three approaches are applied and compared, ON/OFF NGNet with a genetic algorithm, density-based Solid Isotropic Material Penalization (SIMP) with adjoint sensitivity analysis, and a newly developed physics guided analytical method. The optimized geometry is adapted for LPBF manufacturing, fabricated from Fe-Si material, integrated into a complete motor, and experimentally evaluated against FE predictions.

Chapter 4 presents the analytical design and nonlinear 3D FEA validation of a 6/4 AFDR-SRM. The axial flux machine is transformed into an equivalent 2D linearized model to enable NGNet-based TO of the rotor pole shoe geometry. The physics guided back iron reduction method developed in Chapter 3 is subsequently expanded to the electrically excited AFDR-SRM rotor. The chapter also describes the LPBF manufacturing strategy, laminated and segmented stator construction, prototype assembly, and experimental validation of the optimized machine.

Chapter 5 summarizes the key findings of the thesis, evaluates them in relation to the proposed hypotheses and research objectives, and presents recommendations for future research.

Abbreviations

AM	Additive Manufacturing
AFDR	Axial Flux Dual Rotor
AFDR-SRM	Axial Flux Dual Rotor-Switched Reluctance Motor
AFM	Axial Flux Machine
AFSRM	Axial Flux Switched Reluctance Motor
BLDC	Brushless DC Motor
CAD	Computer-Aided-Design
CCC	Current Chopping Control
CNN	Convolutional Neural Network
CPU	Central Processing Unit
EDM	Electrical Discharge Machining
EDX	Energy-Dispersive X-ray Spectroscopy
EMF	Electromotive Force
FE	Finite Element
FEA	Finite Element Analysis
FDM	Fused Deposition Modelling
FEM	Finite Element Method
GA	Genetic Algorithm
GCMMA	Globally Convergent Method of Moving Asymptotes
IPM	Interior Permanent Magnet
IPMSM	Interior Permanent Magnet Synchronous Motor
LBM	Laser Beam Melting
LPBF	Laser Powder Bed Fusion
LSRM	Linear Switched Reluctance Motor
MMA	Method of Moving Asymptotes
MMF	Magnetomotive Force
NGNet	Normalized Gaussian Network
PCB	Printed Circuit Board
PDE	Partial Differential Equation
PM	Permanent Magnet
PMSM	Permanent Magnet Synchronous Motor
RMS	Root Mean Square
SIMP	Solid Isotropic Material Penalization
SLM	Selective Laser Melting
SMPM	Surface Mounted Permanent Magnet
SPC	Single Pulse Control
SRM	Switched Reluctance Motor
SynRM	Synchronous Reluctance Machine
TO	Topology Optimization
YASA	Yokeless And Segmented Armature

Symbols

A_{cond}	Conductor cross-sectional area (mm²)
A_s	Specific electrical loading (A/mm)
A_{sp}	Stator pole area (mm²)
A_z	Axial component of magnetic vector potential (Wb/m)
B	Magnetic flux density (T)
B_{bl}	Rotor back iron flux density (T)
B_g	Airgap flux density (T)
B_{mag}	Magnitude of magnetic flux density (T)
B_{magnet}	Normal magnetic flux density in the magnet (T)
B_n	Normal component of magnetic flux density (T)
B_r	Permanent-magnet remanent flux density (T)
B_s	Saturation flux density (T)
B_{sh}	Pole-shoe flux density (T)
B_{st}	Stator-tooth flux density (T)
B_x	x-component of magnetic flux density (T)
B_y	y-component of magnetic flux density (T)
$b_i(x)$	Normalized Gaussian basis function (–)
d	Axial magnet length (mm)
d_c	Copper density (kg/m³)
d_i	Iron density (kg/m³)
d_w	Wire diameter (mm)
D_{avg}	Average active diameter (mm)
D_i	Inner diameter (mm)
D_o	Outer diameter (mm)
$e_k(t)$	Back EMF of phase k (V)
F_{exc}	Excitation magnetomotive force (A·turn)
F_{ripple}	Thrust-force ripple (%)
F_x	Thrust force (N)
g	Physical airgap length (mm)
g_{eff}	Effective airgap length (mm)
$G_i(x)$	Gaussian basis function (–)
H	Magnetic field strength (A/m)
H_j	Magnetic field strength in region j (A/m)
i	Instantaneous phase current (A)
i_m	Peak phase current (A)
I	Current (A)
I_{rms}	RMS phase current (A)
j	Equivalent magnet surface-current density (A/m)
J_{flux}	Magnetic-flux objective term (Wb/m)
J_{free}	Impressed current density (A/m²)
J_m	Equivalent magnetization current density (A/m²)
J_{rms}	RMS current density (A/mm²)
J_{tot}	Total current density (A/m²)
J_{vol}	Material-volume objective term (m²)

k_1	Machine coefficient (–)
k_2	Machine coefficient (–)
k_3	Machine coefficient (–)
k_c	Airgap correction coefficient (–)
k_d	Duty cycle (–)
k_f	Copper fill factor (–)
k_i	Magnetic stacking factor (–)
l_{eff}	Effective out-of-plane depth (mm)
l_j	Length of magnetic region j along the flux path (m)
l_z	Axial stack length (m)
L_{act}	Active length of one turn (mm)
L_{as}	Aligned saturated inductance (H)
L_{avg}	Developed circumference at the average radius (mm)
L_{bl}	Rotor back-iron axial length (mm)
$L_{\mathrm{end},i}$	Inner end-winding length (mm)
$L_{\mathrm{end},o}$	Outer end-winding length (mm)
L_{rp}	Rotor-pole axial length (mm)
L_{sh}	Pole-shoe axial length (mm)
L_{st}	Stator-tooth axial length (mm)
L_t	Mean length of one turn (mm)
L_u	Unaligned inductance (H)
m	Number of phases (–)
M	Permanent-magnet magnetization vector (A/m)
M_0	Magnetization magnitude (A/m)
M_m	Permanent-magnet magnetization magnitude (A/m)
M_x	x-component of magnetization (A/m)
M_y	y-component of magnetization (A/m)
M_z	z-component of magnetization (A/m)
n	Unit normal vector (–)
n_x	x-component of the unit normal vector (–)
n_y	y-component of the unit normal vector (–)
N_p	Number of evaluation positions (–)
N_{ph}	Number of turns per phase (–)
N_r	Number of rotor poles (–)
N_{rpm}	Rotor speed (r/min)
N_s	Number of stator teeth (–)
N_t	Number of turns per coil
N_{turns}	Number of turns per phase (–)
p	SIMP penalization factor (–)
P_c	Copper loss (W)
P_d	Power density (W/kg)
P_{out}	Output power (W)
q	Number of simultaneously conducting phases (–)
r	Radial coordinate (mm)
r_{avg}	Average active radius (mm)
r_t	Airgap torque-integration contour radius (m)

R_{ph}	Phase resistance (Ω)
S_e	Element material state (–)
$s_k(x)$	Phase sign function over the winding region (–)
t_x	x-component of the Maxwell stress vector (Pa)
t_y	y-component of the Maxwell stress vector (Pa)
T	Electromagnetic torque (N·m)
T'	Torque per unit axial length (N)
T_{avg}	Average torque (N·m)
T_d	Torque density (N·m/kg)
v_m	Translator velocity (m/s)
V	Phase voltage (V)
V_{dc}	DC-link voltage (V)
w_{cut}	Back-iron cut width (mm)
w_{cu}	Coil width (mm)
w_d	Pole-shoe depth (mm)
w_g	Minimum gap between adjacent coils (mm)
w_i	Weight of the ith Gaussian basis function (–)
w_{min}	Minimum back-iron width (mm)
w_{rp}	Rotor-pole width (mm)
w_{sh}	Pole-shoe width (mm)
w_{ss}	Stator-slot width in the linearized model (mm)
w_{st}	Stator-tooth width (mm)
w_{ts}	Rotor-track slot width in the linearized model (mm)
W	Total active-material mass (kg)
W_{bl}	Rotor back-iron mass (kg)
W_{cu}	Copper mass (kg)
W_{rp}	Rotor-pole mass (kg)
W_{sh}	Pole-shoe mass (kg)
W_{st}	Stator-tooth mass (kg)
x_i	Centre position of the ith Gaussian basis function (m)
x_k	Translator displacement at evaluation point k (m)
y	y-coordinate (m)
$y(x, w)$	NGNet shape function (–)
β_r	Rotor pole-arc angle (rad)
β_s	Stator pole-arc angle (rad)
β_{sh}	Pole-shoe arc angle (rad)
β_{st}	Stator-tooth arc angle (rad)
Γ_t	Flux target line (–)
Δt	Time step (s)
Δx	Translator displacement step (m)
$\Delta\theta$	Rotor angular step (rad)
η	Efficiency (%)
θ	Angular position (rad)
θ_i	Phase conduction angle (deg)
θ_m	Mechanical rotor angle (rad)
λ_k	Flux linkage of phase k (Wb·turn)

μ_0	Permeability of free space (H/m)
μ_r	Relative permeability (–)
ν	Magnetic reluctivity (m/H)
ν_{air}	Air reluctivity (m/H)
ν_{Fe}	Iron reluctivity (m/H)
$x_{i,1}$	First corner point of the flux target region (m)
$x_{i,2}$	Second corner point of the flux target region (m)
$x_{i,3}$	Third corner point of the flux target region (m)
$x_{i,4}$	Fourth corner point of the flux target region (m)
ρ	Material density design variable (–)
ρ_{cu}	Copper resistivity (Ω·m)
σ	Gaussian basis-function standard deviation (m)
σ_s	Aligned saturation inductance ratio (–)
σ_u	Aligned-to-unaligned inductance ratio (–)
τ	Electromagnetic torque (N·m)
τ_p	Rotor pole-pitch angle (rad)
τ_r	Rotor pole pitch in the linearized model (mm)
τ_s	Stator pole pitch in the linearized model (mm)
ϕ	Aligned magnetic flux (Wb)
Φ_{in}	Incoming magnetic flux (Wb)
Φ_{out}	Outgoing magnetic flux (Wb)
$\Phi_{b,L}$	Left back-iron branch magnetic flux (Wb)
$\Phi_{b,R}$	Right back-iron branch magnetic flux (Wb)
Φ_{rp}	Rotor-pole magnetic flux (Wb)
ω_m	Mechanical angular speed (rad/s)
Ω	Winding domain area (–)

2 State of the Art in Topology Optimization and Additive Manufacturing

Electrical machine design involves the selection of geometric, material, and operating parameters under electromagnetic, thermal, mechanical, and manufacturing constraints [2], [14]. Conventional design procedures commonly rely on established machine configurations that are refined through analytical calculations and Finite Element Analysis (FEA). Although this approach provides practical and manufacturable solutions, the resulting performance depends strongly on the selected initial geometry and the experience of the designer [14]. Optimization techniques provide a more systematic means of exploring the available design space and identifying configurations that satisfy specified performance requirements.

The design freedom offered by an optimization method depends on how the machine geometry is represented. Parametric optimization varies predefined dimensions while maintaining the basic machine topology, whereas shape optimization modifies the boundaries of existing regions [15]. TO provides greater design freedom by determining the distribution of material within a prescribed design domain, thereby enabling more efficient material utilization, weight reduction, and improved torque density. It can therefore identify nonuniform magnetic structures and flux paths that may not be obtained through conventional design procedures. However, the increased design freedom is accompanied by greater computational requirements and additional considerations related to manufacturability [16], [17], [18].

This chapter reviews the optimization techniques used in electrical machine design, with particular emphasis on TO. The main TO approaches, including ON/OFF, level-set, density-based, and machine learning assisted methods, are discussed together with their applications to PM and reluctance machines. The chapter subsequently examines the use of AM, particularly LPBF, for producing electrical machine magnetic components. Finally, the reviewed studies are assessed to identify the remaining challenges in connecting electromagnetic TO, AM, and experimental validation.

2.1 Electrical Machine Optimization Techniques

Electrical machine optimization techniques can be classified according to the type and extent of the permitted design modification. As illustrated in Figure 2.1, the major categories are parametric, shape, and TO. Parametric optimization varies a prescribed set of dimensions or operating variables while retaining the original geometric configuration. Shape optimization modifies the boundaries of existing material regions but generally preserves their connectivity. TO determines the material distribution within a design domain and can therefore introduce, remove, or reconnect material regions during the optimization process [2].

2.1.1 Parametric Optimization

Parametric optimization is the most traditional approach in electrical machine design. A fixed machine template is selected first, and a set of geometrical, winding, or control variables is then optimized. Examples include pole arc, tooth width, airgap length, stack length, magnet dimensions, flux-barrier widths, rotor bridge thickness, number of turns, and current advance angle. Because the number of variables is limited, parametric

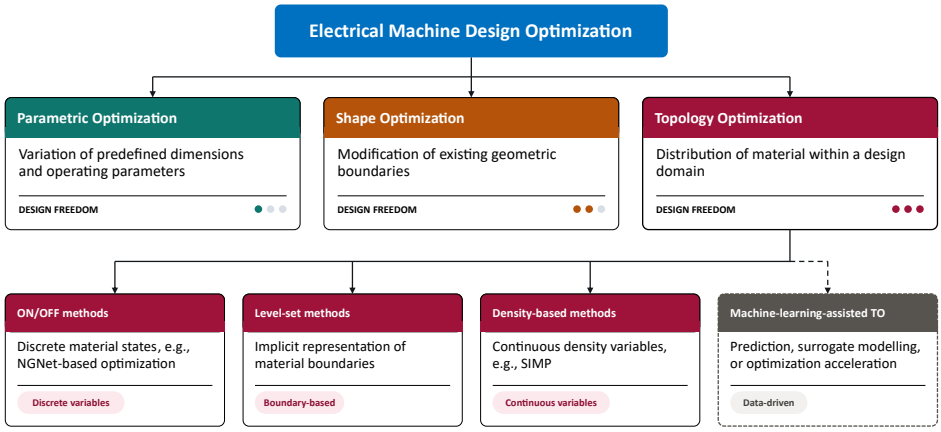


Figure 2.1. Classification of electrical machine design optimization techniques

optimization can be coupled efficiently with FEA, response surface models, genetic algorithms, particle swarm optimization, or gradient based methods [2]. The author in [3] demonstrate this approach for a SynRM, as shown in Figure 2.2, where selected rotor dimensions are defined as design variables. The seven parameters numbered 29–35 and highlighted in red represent the variables adjusted during the optimization, whereas the remaining parameters define the fixed rotor geometry and associated geometrical constraints.

The strength of parametric optimization is that the resulting design usually remains manufacturable, because the topology is known in advance. This is important for industrial machines, where geometric features such as rotor bridges, minimum tooth width, lamination constraints, and assembly tolerances must remain feasible. However, the same advantage is also its limitation. The final design is restricted by the initial human defined template. If a beneficial flux path, hole, barrier, or material distribution is not included in the original parameterization, the algorithm cannot discover it. To provide greater geometrical flexibility beyond varying predefined dimensions, shape optimization modifies the boundaries of existing material regions.

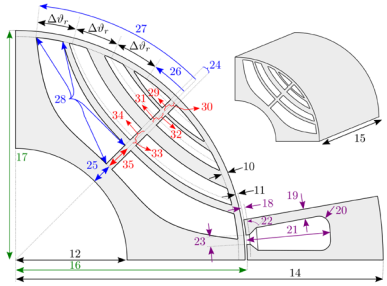


Figure 2.2. Rotor geometry of one pole of SynRM [3]

2.1.2 Shape Optimization

Shape optimization increases the design freedom by allowing the boundaries of the machine geometry to move. Instead of changing only a small number of dimensions, the contour of a rotor pole, stator tooth, flux barrier, or magnet cavity can be modified. This is useful for reducing cogging torque, torque ripple, local saturation, and harmonic content while preserving the main structure of the machine.

Shape optimization commonly represents material boundaries using splines, control points, Fourier descriptors, level-set functions, or free-form deformation variables. These representations enable smooth and continuous modification of the existing geometry, providing greater flexibility to refine the magnetic flux paths than conventional parametric optimization. Brun et al. [19] demonstrated this approach for a SynRM rotor, as presented in Figure 2.3. However, shape optimization generally cannot introduce entirely new holes, material regions, or disconnected flux paths unless such features are already present in the initial geometry. Despite offering greater flexibility than parametric optimization, its results remain dependent on the predefined topology, thereby motivating the use of TO for broader design space exploration.

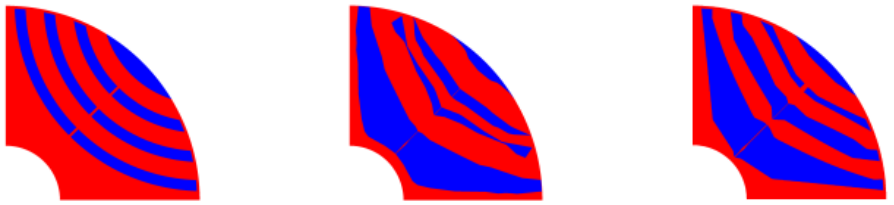


Figure 2.3. Example from the literature of shape optimization of SynRM [19]

2.1.3 Topology Optimization

TO searches for the best material distribution within a predefined design domain. The design domain is discretized, usually by the Finite Element Method (FEM), and each element is associated with a design variable describing whether the element behaves as iron, air, PM, copper, or an intermediate material state. The optimizer updates these variables iteratively until the selected objective function and constraints are satisfied.

The modern form of TO originated in structural mechanics through homogenization and material distribution methods [20][21]. In electromagnetics, one of the early applications was the automated design of magnetic devices by optimizing the material distribution [4]. Since then, TO has been applied to motors, actuators, magnetic bearings, inductors, and other electromagnetic devices. For electrical machines, TO is attractive because it can create flux barriers, flux guides, ribs, holes, and unconventional magnetic paths without requiring them to be parameterized in advance [9][22].

The main benefit of TO is design freedom. It is especially useful for PM machines, where iron, air, and magnet regions can be optimized together, and for reluctance machines, where torque production depends strongly on the saliency and the distribution of high and low reluctance paths. However, the final geometry may contain thin members, isolated islands, checkerboard patterns, rough boundaries, or intermediate densities. Therefore, filtering, projection, minimum length scale control, mechanical constraints, and manufacturability rules are essential when TO results are intended for fabrication.

Parametric, shape, and TO represent a progression from the adjustment of predefined variables to the free redistribution of material. The following sections review the numerical approaches to TO, their application to different electrical machine configurations, and the use of AM to manufacture the resulting optimized geometries.

2.2 Topology Optimization Methods for Electrical Machines

Several TO methods have been developed for electromagnetic devices and electrical machines. The most frequently used families are ON/OFF methods, level-set methods, and density-based methods. The choice of method depends on the number of materials, expected geometry complexity, required smoothness, computational budget, and the availability of sensitivity information.

2.2.1 ON/OFF Method

The ON/OFF method employs a discrete material representation in which each element of the design domain is assigned one of two states, such as iron or air. During the optimization process, the material distribution is updated using sensitivity information, evolutionary rules, or global search algorithms. Because the design variables are binary, the final geometry contains no intermediate density regions.

The method has been applied to electrical machine design using both deterministic and stochastic optimization strategies. In synchronous motors and switched reluctance machines, for example, it has been used to optimize the material distribution within the rotor or stator [23], [24], [25], [26]. Figure 2.4 presents an example of its application to the rotor of an Interior Permanent Magnet (IPM) machine. The principal advantages of the ON/OFF method are its conceptual simplicity and clear distinction between material and void regions. However, its discrete formulation may produce checkerboard patterns, show sensitivity to mesh size, or generate rough and disconnected features. Filtering or regularization techniques are therefore often required to obtain smooth and manufacturable geometries.

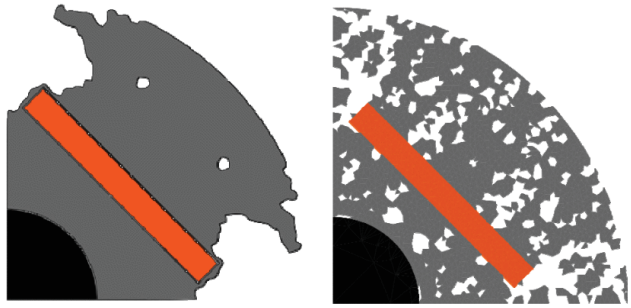


Figure 2.4. Rotor TO of an IPM machine using the ON/OFF method [26]

2.2.2 Level-Set Method

The level-set method represents material boundaries implicitly using a scalar function, whose zero-level contour defines the interface between different materials. During optimization, this boundary evolves according to shape or topological derivatives, commonly through a Hamilton Jacobi equation. This representation produces well defined and relatively smooth boundaries, avoiding the intermediate-density regions associated with element-wise density methods.

In electrical machine design, level-set methods have been applied to SynRM and SRM, particularly when smooth flux barriers or rotor-pole geometries are required [27], [28], [29], [30]. Figure 2.5 shows the application of this method to the rotor TO of an SRM [28]. A key advantage is its ability to generate clearly defined boundaries, which can improve manufacturability. However, the resulting design may depend strongly on the initial

topology unless specialized procedures are introduced to create new holes or disconnected features during optimization.

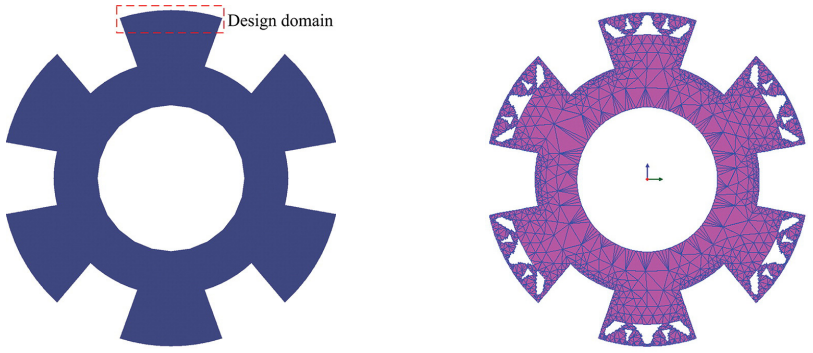


Figure 2.5. Level-set-based rotor TO of an SRM (a) initial model and design domain (b) optimized geometry with the FE mesh [28]

2.2.3 Density Based Method

Density based TO assigns each FE a continuous design variable, usually ranging between 0 and 1. The material property is interpolated between the candidate materials. In structural mechanics this approach is often associated with the SIMP method, where penalization is used to push intermediate densities toward solid or void states [21]. In electromagnetic machines, interpolation is applied to magnetic reluctivity, permeability, magnetization, conductivity, or other material properties depending on the problem formulation.

Density based methods are attractive because they are compatible with gradient based algorithms such as Method of Moving Asymptotes (MMA) and Globally Convergent Method of Moving Asymptotes (GCMMA) and because adjoint sensitivity analysis can be used to handle large numbers of design variables. They are also suitable for multi-material problems, such as the simultaneous distribution of air, iron, and PM material. Recent studies have applied multi-material density-based optimization to PM machines, allowing the rotor structure, magnet distribution, magnetization direction, and operating parameters to be considered within a unified optimization framework [31], [32]. Figure 2.6 presents an example of a PMSM rotor generated using density based multi-material TO [33]. Despite its flexibility, the method requires careful treatment of intermediate densities, checkerboard patterns, mesh dependency, and filter radius selection. The resulting density distribution must generally be converted into a smooth, mechanically robust, and manufacturable geometry.

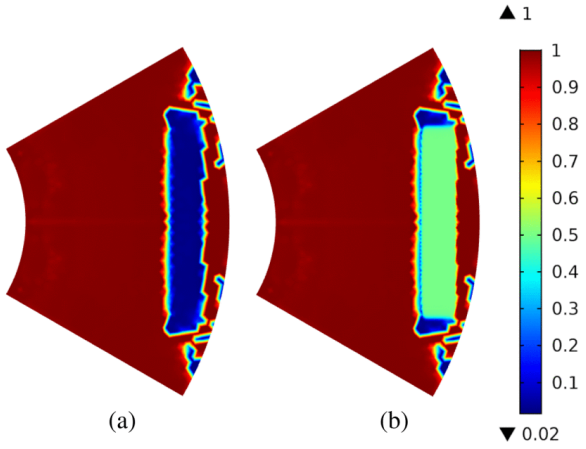


Figure 2.6. Magneto-structural combined dimensional and TO result (a) electrical steel and (b) PM and electrical steel normalized density distributions [33]

2.2.4 Machine learning assisted TO

Physics based TO is computationally demanding because each candidate design generally requires FEA. Machine learning can reduce this burden by serving as a surrogate within the optimization loop. For example, Convolutional Neural Network (CNN) trained using cross-sectional images of IPM rotors have been used to predict torque characteristics, allowing FEA to be restricted to promising candidates and final verification [34].

Transfer learning has reduced the computational cost to less than 15% of that required by conventional optimization [35], while simultaneous learning across different magnet configurations reduced the required FEA evaluations to approximately 5% [36]. CNN surrogates have also been applied to multi-material IPM TO by predicting magnet flux and d and q-axis inductances at different current phase angles [37]. Other approaches include reinforcement learning for sequential topology modification [38] and variational autoencoders for latent-space optimization of PM motor geometries [39].

Despite these advantages, such methods require representative FEA generated training data, and their accuracy may deteriorate outside the training distribution. The final designs should still be verified using high fidelity multi-physics simulations and, where possible, experimental measurements.

The reviewed methods describe how TO is performed, but they do not by themselves indicate where the resulting material redistribution is most beneficial within an electrical machine. The next section therefore shifts from optimization methodology to machine configuration and reviews the application of these approaches to PM and reluctance machines.

2.3 Applications of Topology Optimization in Electrical Machines

Building on the methodological classification in the previous section, this section reviews how TO has been applied to different electrical machine configurations. The literature is dominated by PMSM and SynRM, while SRM have received increasing attention because of their magnet free structure, simple rotor, robustness, and suitability for harsh environments. The following subsections distinguish PM machines, in which iron and magnet regions may be optimized. From reluctance machines, in which torque

production is governed primarily by the distribution of high and low reluctance flux paths.

2.3.1 TO for PM Machines

PM machines are widely used because of their high torque density, high efficiency, and suitability for variable speed drives. However, they also introduce design challenges related to magnet cost, rare-earth supply, demagnetization risk, magnetization direction, cogging torque, torque ripple, and mechanical retention of magnets. TO has therefore been used to optimize the distribution of rotor iron, air cavities, PM, and stator teeth.

Early work focused on reducing cogging torque and improving torque production by modifying the stator or rotor topology [26], [40], [41]. More recent studies include the drive control strategy inside the optimization loop, for example by considering maximum torque per ampere and flux weakening operation [42], [43]. Multi-material formulations have also been developed to optimize iron, air, and magnet distribution simultaneously, including the direction of magnetization [31], [44]. These studies show that TO can improve machine performance beyond conventional parameterized rotor designs, but they also highlight the difficulty of manufacturing complex magnet shapes and enforcing mechanical constraints.

Table 2.1 shows that PM machine TO has moved from single material iron redistribution toward multi-material air, iron, and PM formulations. Recent studies also include control constraints and magnetization direction. This trend is directly relevant for PM and BLDC machines because the optimized rotor back iron, magnet support, and flux path must satisfy electromagnetic, mechanical, and manufacturing constraints at the same time.

Table 2.1. Summary of TO studies for PM machines

Reference	Machine configuration	TO approach	Design space	Main objective(s)	Validation / remarks
[40]	IPM	SIMP based density method	Stator pole shoe	Minimize cogging torque	Simulation study
[41]	SMPM machine	Level-set	Stator and rotor pole	Mitigate cogging torque and reduce losses	Simulation study
[26]	IPM motor	ON/OFF method with filtering	Rotor	Torque	Simulation study
[42]	IPM motor	NGNet based ON/OFF	Rotor	Reduce iron losses	Simulation study
[45]	Skewed IPM motor	NGNet based ON/OFF	Rotor	Reduce torque ripples	Simulation study
[31]	PM-assisted SynRM	Density based multi-material TO	Rotor core, and PM regions	Maximize average torque	Simulation study
[44]	PMSM	Density based multi-material TO	Rotor core, and PM regions	Maximize average torque	Simulation study
[43]	IPM motor	SIMP based density method	Rotor	Maximize average torque	Experimental validation
[46]	IPM motor	Level set and topological derivatives	Rotor	Maximize average torque	Simulation study

2.3.2 Reluctance Machines

Reluctance machines produce torque by the tendency of the rotor to move toward a position of minimum magnetic reluctance. The most important reluctance machine

family for this thesis is SRM. Their doubly salient structure, concentrated stator windings, and sequential phase excitation provide a simple and robust construction. However, their performance is strongly influenced by the geometry of the stator teeth, rotor poles, airgap, and surrounding air regions. SRMs are therefore well suited to TO, which can identify unconventional material distributions and flux paths that are difficult to obtain through conventional parameter optimization.

TO of SRMs generally aims to increase average torque, reduce torque ripple and mass, and mitigate radial force, vibration, or acoustic noise [25], [28], [47], [48]. The design domain may include the stator teeth, rotor poles, magnetic core, or combined rotor and stator regions. Both binary ON/OFF and continuous density-based methods have been applied, together with level-set, evolutionary, gradient based, and multi-physics optimization approaches. Table 2.2 shows that most published results remain simulation based, which leaves room for experimentally validated AM designs.

Table 2.2. Summary of TO studies for SRM

Reference	Machine / configuration	Optimization approach	Design space	Main objective(s)	Validation / remarks
[49]	SRM	TO using mutual energy method	SRM magnetic core	Improve torque-related performance	Early SRM TO study
[27]	6/4 SRM	Level-set method	Stator structure	Reduce vibration	Simulation study
[50]	3-phase 6/4 SRM	Material-density-based TO	Stator teeth and rotor	Desired torque profile / torque ripple	Experimental validation
[25]	6/14 SRM	Interior-point and ON/OFF TO	Stator teeth	Average torque and torque ripple	Simulation study
[24]	6/4 SRM	ON/OFF TO using GA and simulated annealing	Rotor, stator, and copper regions	Average torque improvement	Simulation study
[51]	8/6 SRM	Material-density-based TO / GCMMA	Rotor teeth	Average torque and mass reduction	Simulation study
[23]	SRM with new rotor topology	ON/OFF TO with immune algorithm	Rotor	Average torque and torque ripple	Simulation study
[28]	8/6 SRM	Level-set method	Rotor pole / teeth	Torque ripple minimization and average torque	Simulation study
[47]	SRM	Electromagnetic-structural multiphysics TO	SRM magnetic structure	Balance electromagnetic and structural response	Simulation study

Across both machine groups, TO has demonstrated the ability to improve torque related performance, reduce mass, and control ripple or losses. Nevertheless, Tables 2.1 and 2.2 show that most reported studies remain simulation based. The transition from an optimized numerical material distribution to a mechanically sound and manufacturable magnetic component therefore remains a central limitation. This requirement provides the link to AM, which is reviewed in the following section as a manufacturing route for complex TO geometries.

2.4 Additive Manufacturing of Electrical Machine Magnetic Components

The above section showed that TO can generate non-uniform material distributions that are difficult to realize using conventional punched and stacked laminations. AM, particularly LPBF of soft magnetic alloys, offers a manufacturing route for components with complex contours, internal cavities, and 3D flux paths. This section first examines studies that directly combine TO with AM and then broadens the review to 3D manufactured rotor and stator cores. Particular attention is given to whether the manufactured components were experimentally evaluated.

2.4.1 Integration of Topology Optimization and Additive Manufacturing

Among these few works, the research chain at the VTT Technical Research Centre of Finland is the most complete example. Starting from the printing of a TO soft magnetic core [52] and TO studies of SRM [53] the work culminated in an 8/6 SRM whose, TO stator and rotor cores were both manufactured by LPBF from an Fe-Co-V alloy and experimentally tested [54]. The measurements confirmed that the printed machine delivered the mechanical power predicted by 2D FEA, although the solid printed cores suffered from high eddy current losses.

Similarly, [55] used AM to realize an asymmetric rotor skew of a 6/4 switched reluctance motor that was designed to reduce torque ripple and would have been virtually impossible to manufacture with traditional methods, while [56] developed a dedicated free-form design methodology for rotor cores intended for production by LPBF. On the simulation side, [57] incorporated the measured properties of printed FeSi6.5% material directly into a multi-material TO formulation, explicitly anticipating an AM outcome. These works demonstrate the feasibility of the combined design-to-print workflow, but they also underline how rare experimentally validated combinations of TO and AM still are, which is precisely the gap addressed in this thesis.

2.4.2 Additively Manufactured Rotor and Stator Cores

Beyond the TO driven studies, a considerably larger body of literature has investigated AM of the active magnetic parts of electrical machines as such, i.e., the rotor core, the stator core, or both. The earliest prototypes appeared in 2016, when [58] printed a lightweight rotor for a PMSM from H13 tool steel, [59] printed a maraging steel SynRM rotor, and [60] proposed a high-end SynRM rotor design based on 3D printing. Subsequent rotor-oriented work concentrated on soft magnetic Fe-Si alloys and design features that exploit the freedom of the process continuously skewed and surface grooved PMSM rotors with integrated lightweight structures and hollow shafts [61], [62], [63] free-form rotor cores [56] and printed SynRM rotors with optimized flux barriers [64], [65], [66], [67]. [68], [69] developed a high-silicon Fe-5 wt%Si material for LPBF, printed a complete SRM rotor, and characterized the whole machine over its full torque speed envelope against an identical laminated benchmark, reporting comparable low speed behaviour but significantly increased core losses at high speed due to the solid, non-laminated construction.

Stator oriented studies have mainly targeted axial flux machines, whose 3D flux paths are difficult to realize with laminations. Printed soft magnetic composite cores [70] shape-profiled Yokeless And Segmented Armature (YASA) core segments [71], [72] and stators with eddy current limiting Hilbert space filling cross sections in Fe-6.5 wt%Si [73],

[74] have all been demonstrated. The Hilbert structured stators are particularly relevant because they address the main weakness of printed cores, namely eddy current losses, achieving loss levels comparable to conventional laminations at moderate frequencies while improving stator torque density. A smaller number of works have printed the complete magnetic circuit of a machine. [75] produced a fully printed axial flux SRM and later a complete induction motor with printed stator and rotor cores together with the associated production and characterization workflow [76], [77]. [78], [79] combined an Selective Laser Melting (SLM) printed Fe-3Si stator with an AM NdFeB-PPS bonded magnet rotor. [80] printed the rotor, stator, and casing of a lightweight aerospace actuator in stainless steel. Table 2.3 summarizes these works, grouped by which active part of the machine was manufactured through AM.

Table 2.3. Summary of AM rotor and stator prototypes in electrical machines

Reference	Machine type	AM part	AM technique
[58]	PMSM	Rotor	LPBF/SLM
[59]	SynRM	Rotor	SLM
[60]	SynRM	Rotor	Metal 3D printing (process not specified)
[55]	6/4 SRM	Rotor	SLM
[61]	PMSM	Rotor	LBM
[62]	PMSM	Rotor + shaft	LBM
[56]	PM machine	Rotor	LPBF
[68]	SRM	Rotor	LPBF
[69]	SRM	Rotor	LPBF
[63]	IPMSM	Rotor	LBM
[64]	SynRM	Rotor	LPBF
[81]	BLDC	Rotor	FDM
[65]	SynRM	Rotor	LPBF
[66]	SynRM	Rotor	LPBF
[67]	Axial-flux SynRM	Rotor	Metal 3D printing (process not specified)
[70]	Hybrid axial-flux motor	Stator	SLM
[71]	10 kW YASA AFM	Stator	3D micro-extrusion
[79]	Brushless PM motor	Stator	SLM followed by EDM slicing
[74]	AFM	Stator	LPBF
[73]	AFM	Stator	SLM
[72]	YASA AFM	Stator	3D micro-extrusion
[82]	BLDC (drone)	Stator	SLM
[75]	4/6 axial flux SRM	Both	SLM
[76]	Induction motor	Both	SLM
[77]	Induction motor	Both	SLM
[54]	8/6 SRM	Both	LPBF
[78]	Brushless PM motor	Both	SLM (stator) + BAAM/FDM (rotor magnets)
[80]	PM electric actuator	Both	LPBF/SLM

2.5 Summary

In summary, this chapter has reviewed the progression from parametric and shape optimization to TO, which provides greater design freedom for improving magnetic-material utilization, reducing mass, and increasing torque density. The suitability of ON/OFF, level-set, density-based, and machine-learning-assisted methods depends on their material representation, boundary quality, sensitivity requirements, and computational cost. Most reported electromagnetic TO studies rely on 2D models and focus mainly on airgap facing geometries, while the removal of weakly utilized back iron material remains underexplored. Research on inherently 3D TO is also limited by simulation complexity and the limitations imposed by conventional manufacturing. These gaps motivate the TO and experimental validation of the quasi-static rotor back iron presented in Chapter 3, followed by the optimization and material reduction of an inherently 3D axial flux reluctance machine enabled by AM in Chapter 4.

3 From Numerical Search to Physics Guided Design: Topology Optimization of a Permanent Magnet Machine

The previous chapter demonstrated that TO provides a higher level of geometrical freedom than conventional parametric and shape optimization methods. Taking advantage of this design freedom, this chapter focuses on applying 2D TO methods to improve the utilization of magnetic material in the rotor back iron of a permanent-magnet machine. The objective is to remove weakly utilized material while preserving the magnetic flux paths and maintaining the airgap flux density, back Electromotive Force (EMF), and electromagnetic torque of the original machine.

The optimization problem is formulated using a nonlinear 2D magnetostatic model. To reduce the computational cost, each case topology is evaluated at one representative rotor position rather than at multiple positions covering a complete electrical cycle. The complete rotor position analysis is performed after optimization to verify the airgap flux density, back EMF, and torque characteristics. The chapter first establishes and validates the commercial e-scooter motor used as the benchmark. It then presents the physical basis of the material reduction problem and applies the NGNet, density-based, and physics guided analytical TO methods. Finally, the three methods are compared, and the selected rotor geometry is adapted for LPBF manufacturing and experimentally validated in the assembled motor.

3.1 Motivation for Rotor Back Iron Topology Optimization

In Surface Mounted PM, and in several other PM machine configurations, the dominant rotor magnetic field is quasi static under steady state operation. The PMs establish a comparatively stable magnetic flux pattern, while the rotor back iron provides the return path for the magnet flux. Although the back iron is normally designed using a uniform radial thickness, the magnetic loading within it is not uniform. Some regions carry a large proportion of the pole flux and may operate close to the selected flux density limit, whereas other regions carry considerably less flux as shown in Figure 3.1. Consequently, a noticeable portion of the rotor core material can be weakly utilized from an electromagnetic perspective.

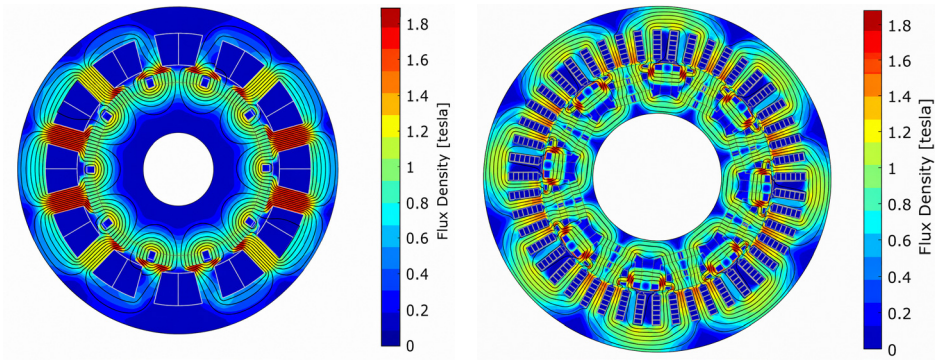


Figure 3.1. Non-uniform flux distribution in the rotor back iron, indicating inefficient material utilization (a) SMPM motor (b) IPM motor

This non-uniform utilization is particularly important in PM machines, including IPM and SMPM configurations. The rotor back iron contributes directly to the moving mass and inertia, yet a conventional design usually retains a constant back iron thickness throughout the active region. The thickness is commonly selected from the most highly loaded section of the magnetic circuit so that local saturation is avoided. Applying this worst-case requirement everywhere produces a robust and easily manufactured machine, but it also leaves excess material in regions where the local magnetic flux is lower. The conventional design is therefore magnetically safe but not necessarily material efficient.

The presence of weakly utilized material creates an opportunity for TO. Instead of treating the back iron thickness as one global parameter, TO permits the material distribution to vary spatially within a prescribed rotor design domain. Material can then be retained along the principal magnetic flux paths and removed from regions that make only a small contribution to torque production or flux conduction. If this redistribution is performed without increasing magnetic saturation or disturbing the airgap field, the rotor mass can be reduced while the back EMF and torque characteristics are preserved. The torque density of the machine may therefore be improved without increasing the PM volume or the electrical loading.

The difficulty is that the desired material distribution is not known in advance. It depends on the magnet flux, rotor geometry, magnetic nonlinearity, operating point, and the performance constraints imposed on the machine. Different TO techniques represent and update the material distribution in fundamentally different ways. A method that provides very high geometrical freedom may require many FE evaluations. A computationally efficient gradient based method may depend strongly on interpolation, filtering, and penalization parameters. A direct analytical method may be extremely fast and physically transparent, but its application may be restricted to components for which the dominant flux paths can be described with sufficient accuracy.

3.2 Commercial E-Scooter Motor

The three-phase outer rotor SMPM BLDC motor from a commercial electric scooter application is selected as a benchmark. The motor has 18 stator slots and 20 rotor poles. Its inner stator carries concentrated windings, while the PM are mounted on the inner surface of a ferromagnetic outer rotor. The large pole number and outer rotor arrangement provide the low-speed torque required for compact scooter application. The cross-section view of the three-phase BLDC is shown in Figure 3.2 and based on the dimension extracted from it is presented in Table 3.1.

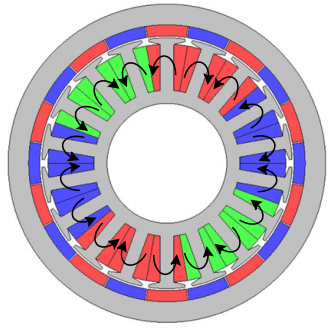


Figure 3.2. 2D-cross sectional view of three phase benchmark motor

Table 3.1. Main parameters of the benchmark BLDC motor

Parameter	Value
Number of stator slots	18
Number of rotor poles	20
Stator outer diameter	64 mm
Rotor outer diameter	85 mm
Rotor inner diameter	65 mm
Active stack length	30 mm
Rated speed	900 rpm
Rated voltage	24 V
Turns per coil	12
Number of parallel strands	5

3.2.1 FE Model

The benchmark motor is analyzed with a nonlinear 2D magnetostatic FE model built directly in JMAG. JMAG solves the field using the magnetic vector potential formulation in the planar model the unknown reduces to the axial component A_z, and the flux density follows from $\mathrm{B} = \nabla \times A_z$. The ferromagnetic regions are assigned the nonlinear B–H characteristic of M400-50A electrical steel, and the rotor magnets are defined with alternating radial magnetization. The mesh is refined in the air gap, at the magnet edges, and within the rotor back iron to resolve the useful flux path and local saturation.

The no-load analysis is performed without stator current, such that the PMs constitute the only magnetic field source. The airgap flux density and flux linkage waveforms are presented in Figure 3.3. The corresponding phase back EMF waveforms and magnetic flux density contour are shown in Figure 3.4. The loaded performance is then evaluated under rated three-phase excitation. The current waveforms and the resulting electromagnetic torque waveform are presented in Figure 3.5. These results characterize the magnetic loading and torque performance of the benchmark motor. The next section examines the rotor flux distribution to establish the physical basis for rotor back iron optimization.

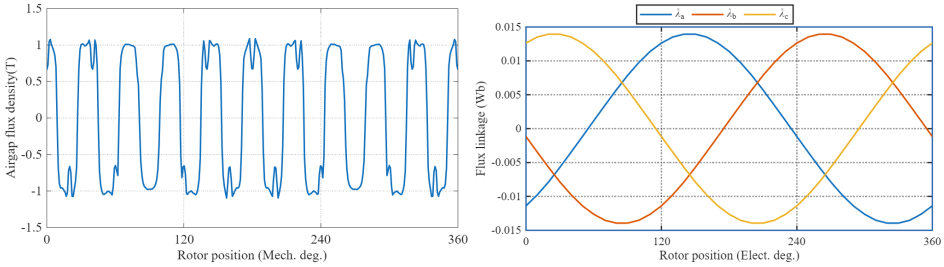


Figure 3.3. Airgap flux density and flux linkage of benchmark motor

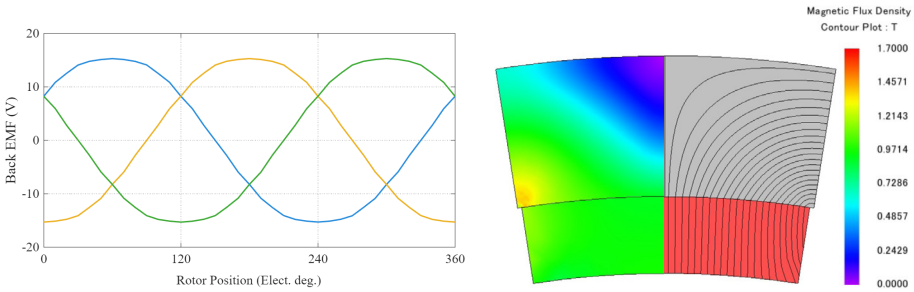


Figure 3.4. Three phase back EMF and flux contour of benchmark motor

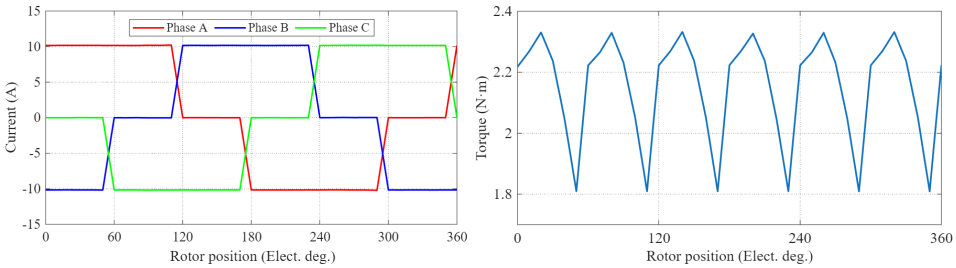


Figure 3.5. Current and torque waveform of benchmark motor

3.3 Physical Basis for Rotor Back Iron Optimization

3.3.1 Quasi-Static Rotor Field

The validated benchmark model provides a reliable basis for assessing the utilization of the rotor core material. During steady state operation, the fundamental magnetic field distribution remains nearly stationary relative to the rotor. Each back iron sector primarily carries the flux associated with its corresponding PM pole, whereas the stationary stator teeth and yoke experience a time varying field as successive rotor poles pass. This periodically repeated flux pattern enables the material requirement of one rotor pole sector to be evaluated and reproduced around the complete rotor.

3.3.2 Optimization Problem

The rotor back iron is selected as the design domain, while the remaining machine geometry, material properties, winding configuration, and operating conditions are kept unchanged. The objective is to minimize the rotor core material without compromising the useful magnetic flux. Each case design must preserve the airgap flux density, back EMF, and average electromagnetic torque of the benchmark machine. The resulting geometry must provide a continuous magnetic return path and prevent unacceptable local saturation. These requirements establish a consistent basis for evaluating the different material representations and optimization procedures. The following TO techniques are therefore employed to identify efficient material distribution within the rotor back iron.

3.4 NGNet Based TO

This section presents the application of the NGNet based TO method to the rotor back iron, including its material representation, genetic-algorithm search process, and resulting electromagnetic performance.

3.4.1 Material Representation Using NGNet

Efficient utilization of the rotor back iron requires identification of the regions that actively carry magnetic flux. TO enables the material distribution within the prescribed design domain to be determined without explicitly defining the dimensions or boundaries of the resulting geometry. In the NGNet method, Gaussian basis functions are distributed throughout the rotor back iron design domain, and their superposition defines the material topology.

For the spatial position vector x and the design variable vector w, the NGNet shape function is expressed as

$$y(x,w)=\sum_{i=1}^{N} w_i \; b_i(x), \tag{3.1}$$

where the normalized basis function is

$$b_i(x)=\frac{G_i(x)}{\sum_{k=1}^{N} G_k(x)}, \tag{3.2}$$

$$G_i(x)=\frac{1}{2\pi\sigma^2}\exp\left(-\frac{\|x-x_i\|^2}{2\sigma^2}\right). \tag{3.3}$$

Normalization makes the local field independent of the number of overlapping functions. The element material state is

$$S_e=\begin{cases}0 & \text{(air)},\ y<0\\ 1 & \text{(iron)},\ y\geq 0.\end{cases} \tag{3.4}$$

Thus, the optimized parameter vector w controls the topology without requiring a predefined rotor boundary. Only one pole pitch is optimized. Gaussian functions are distributed over one side of the back iron sector and mirrored to the other side, reducing the number of independent variables while maintaining a symmetric flux path as shown in Figure 3.6. With Γ_t denoting a target line and n its unit normal, the constrained optimization problem is

$$\max_{w} \int_{\Gamma_t} (B\cdot n)\, dl, \tag{3.5}$$

$$0.5 \leq \|B\| \leq 1.4. \tag{3.6}$$

The lower limit discourages retention of weakly utilized iron, while the upper limit prevents the remaining flux path from being driven into excessive saturation. The detailed optimization parameters are summarized in Table 3.2.

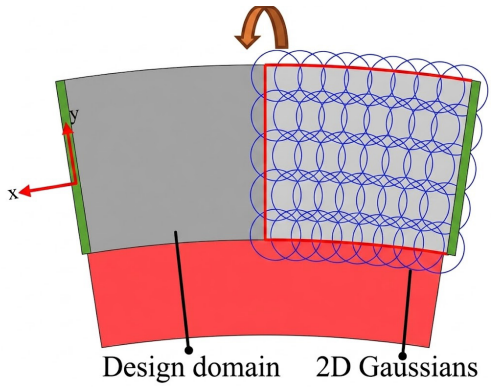


Figure 3.6. Gaussian distribution over design domain

Table 3.2. NGNet optimization settings

Parameter	Value
Number of generations	50
Population size	47
Number of children	47
Number of Gaussian functions	46
Gaussian basis width	0.8 mm
Gaussian basis height	0.8 mm
Optimization method	Genetic algorithm

3.4.2 Genetic Algorithm Search

The NGNet weights form the chromosome used by the genetic algorithm. Each population member produces a binary material distribution, which is transferred to the magnetostatic FEM model. Each case fitness is determined from the transported target line flux while enforcing the admissible flux density interval. Selection, reproduction, and mutation generate the next population. Because the thresholder topology may change discontinuously, the derivative free genetic algorithm is appropriate and can explore substantially different layouts. Its disadvantage is computational cost because every individual requires a field solution.

The optimization was executed on a computer with an Intel® Core™ i7-12700 CPU processor operating at 2.1 GHz and 64 GB of memory. Fifty generations required approximately 6 h 40 min. Material was removed principally from the regions that exhibited low flux density in the benchmark, while the essential flux path remained connected. The optimized one pole geometry was repeated periodically to form the complete rotor. Reanalysis showed no problematic saturation in the retained active regions.

3.4.3 NGNet Performance

The NGNet optimization redistributes the rotor back iron according to its contribution to magnetic flux conduction. Material is retained along the flux carrying paths, while weakly utilized regions are removed. The relationship between the target flux and the iron area retained in the design domain is presented in Figure 3.7, showing the different material

layouts explored by the genetic algorithm. The resulting optimized topology and its flux distribution are shown in Figure 3.8. The retained back iron forms a continuous and symmetric magnetic return path without problematic local saturation.

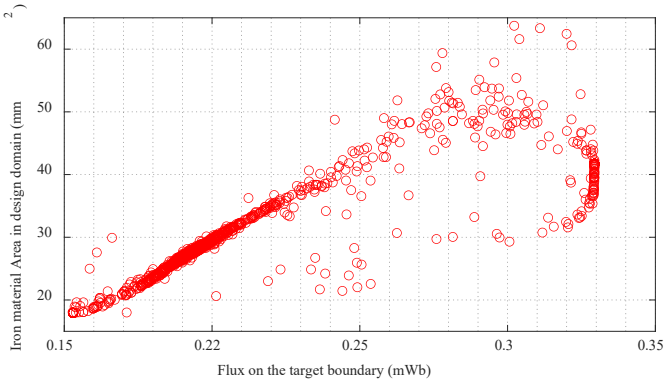


Figure 3.7. Relation between target flux and iron material in the design region

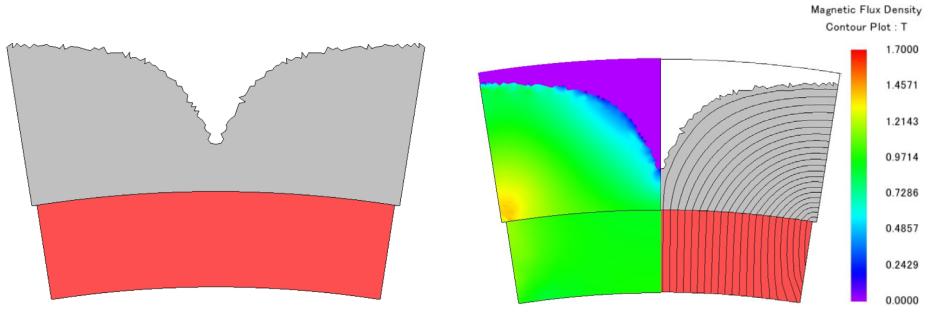


Figure 3.8. TO back iron of the one pole pitch rotor

This material redistribution reduces the rotor back iron volume by 25.67%, corresponding to a 7.32% reduction in the complete motor volume. With the required average torque maintained, the reduction in motor volume increases the torque density by 7.84%. Although the genetic algorithm provides a global search capability, some weakly utilized regions with low flux density remain in the optimized topology. This is mainly because the software does not allow the parameterized iron volume to be imposed directly as a constraint during the topology optimization. Furthermore, the NGNet method is computationally expensive because each candidate topology requires a separate FE evaluation. To address these limitations, the following section investigates a gradient based density TO method.

3.5 Density Based TO

To address the software limitations encountered in the NGNet approach, a fully customized gradient based density TO framework is developed in NGSolve, enabling direct control over the material volume.

3.5.1 SIMP Material Interpolation

The density method assigns a continuous variable ρ in [0,1] to every FE of the design domain. Enable TO using continuous density variables an interpolation scheme is required to model the transition between air and ferromagnetic material. In electromagnetic TO, the most critical material parameter is the magnetic permeability μ or equivalently the magnetic reluctivity v =1/μ. The element reluctivity is interpolated using the SIMP formulation

$$v(\rho)=v_{\text{air}}+\rho^{p}[v_{\text{fe}}\text{-}v_{\text{air}}]. \tag{3.7}$$

The penalization factor p is introduced to suppress intermediate densities and encourage nearly binary material distribution. For the linear material case study, the interpolation smoothly transitions between air and iron depending on ρ. Increasing the p makes intermediate densities energetically unfavorable, forcing the solution toward a clear 0–1 material distribution. This behavior is illustrated in Figure 3.9, where higher penalization values result in a sharper transition near $\rho = 1$.

When magnetic saturation is considered, the permeability of the ferromagnetic material depends on the local magnetic flux density magnitude. In this case, the interpolation is applied to nonlinear reluctivity.

$$v(\rho,\|B\|)=v_{\text{air}}+\rho^{p}[v(\|B\|)\text{-}v_{\text{air}}]. \tag{3.8}$$

The nonlinear discretized problem is solved by Newton iteration. After each Newton iteration, the local flux density B is evaluated, and the corresponding reluctivity is updated. This updated reluctivity is then used both in the state equation and in the sensitivity analysis.

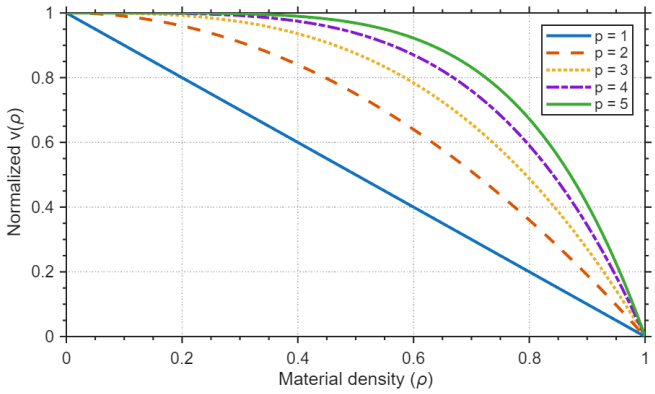


Figure 3.9. SIMP interpolation with different values of penalization

3.5.2 2D Magnetostatic Formulation

In the 2D model, the magnetic vector potential has only an axial component A_z. Maxwell's magnetostatic equation and the reluctivity relation are written as

$$B=\nabla\times A, \tag{3.9}$$

$$J_{\text{tot}}=J_{\text{free}}+J_{m}, \tag{3.10}$$

$$\nabla\times(v\,\nabla\times A)=J_{\text{tot}}. \tag{3.11}$$

No impressed current density is used in the optimization state problem, so J_{free} = 0. The PMs enter through the equivalent magnetization current density

$$J_m = \nabla \times M, \tag{3.12}$$

$$\nabla \times (v\, \nabla \times A) = \nabla \times M. \tag{3.13}$$

Taking the z component gives

$$(\nabla \times M)_z = \frac{\partial M_y}{\partial x} - \frac{\partial M_x}{\partial y}, \tag{3.14}$$

$$\frac{\partial}{\partial x}\left(v \frac{\partial A_z}{\partial x}\right) + \frac{\partial}{\partial y}\left(v \frac{\partial A_z}{\partial y}\right) = \frac{\partial M_y}{\partial x} - \frac{\partial M_x}{\partial y}. \tag{3.15}$$

Radial magnetization of magnitude M_0 is assigned in the magnet regions with alternating polarity. At an element barycentre (x, y),

$$\begin{cases} M_x = M_0 \times \left(\dfrac{x}{r}\right) \\ M_y = M_0 \times \left(\dfrac{y}{r}\right) \\ r = \sqrt{(x^2 + y^2)} \end{cases} \tag{3.16}$$

3.5.3 Objective Function Evaluation

The objective function is formulated to increase the useful magnetic flux passing through the prescribed flux target regions while penalizing the amount of retained rotor back iron material. In the 2D magnetostatic formulation, the magnetic vector potential has only the axial component A_z, and the flux density is

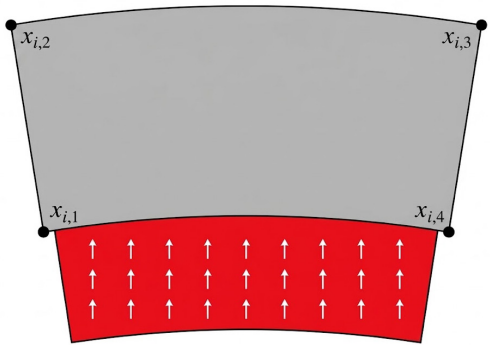


Figure 3.10. TO design domain for the density method

$$B = \left(\frac{\partial A_z}{\partial y}, -\frac{\partial A_z}{\partial x}\right)^T. \tag{3.17}$$

For the *i-th* rotor segment, four corner points are defined around the flux target region, as shown in Figure 3.10. The points $x_{i,1}$ and $x_{i,2}$ lie on one side of the flux region, while $x_{i,3}$ and $x_{i,4}$ lie on the opposite side. The flux crossing on each side can be evaluated from the difference of the magnetic vector potential at the corresponding endpoints. Therefore, the flux objective is written as

$$J_{flux}(A_z) = \sum_{i=1}^{N_s} (-1)^i \left[A_z(x_{i,1}) - A_z(x_{i,2}) - A_z(x_{i,3}) + A_z(x_{i,4}) \right], \tag{3.18}$$

where the coefficient accounts for the alternating magnetization direction of adjacent PMs. The material volume term is defined over design domain as

$$J_{vol}(\rho) = \int_{design\ domain} \rho \, dx, \tag{3.19}$$

the total optimization objective is

$$J(A_z, \rho) = J_{flux}(A_z) + wJ_{vol}(\rho), \tag{3.20}$$

where w is the weighting factor controlling the trade-off between flux performance and material reduction. The first term drives the magnetic flux through the desired flux target regions, while the second term penalizes the amount of iron material retained in the design domain. The standard form of the objective function is

$$\begin{cases} min. \;\; J(A_z, \rho) = J_{flux}(A_z) + wJ_{vol}(\rho) \\ 0 \le \rho \le 1, \end{cases} \tag{3.21}$$

3.5.4 Adjoint Sensitivity Analysis

In the gradient based TO methods, the sensitivity of the objective function, with respect to the material density (ρ) can be obtained in the following way: Consider the reduced cost function

$$J(\rho) = J(A_z(\rho), \rho). \tag{3.22}$$

By chain rule

$$\frac{dJ}{d\rho} = \frac{\partial J}{\partial \rho} + \frac{\partial J}{\partial A_z} \frac{dA_z}{d\rho}. \tag{3.23}$$

Differentiating the constraint residual $R(A_z, \rho) = 0$ with respect to ρ, gives

$$\frac{\partial R}{\partial A_z} \frac{dA_z}{d\rho} + \frac{\partial R}{\partial \rho} = 0, \tag{3.24}$$

$$\frac{dA_z}{d\rho} = -\left(\frac{\partial R}{\partial A_z} \right)^{-1} \frac{\partial R}{\partial \rho}, \tag{3.25}$$

$$\frac{dJ}{d\rho} = \frac{\partial J}{\partial \rho} - \frac{\partial J}{\partial A_z} \left(\frac{\partial R}{\partial A_z} \right)^{-1} \frac{\partial R}{\partial \rho}. \tag{3.26}$$

This is the chain rule expression in which the explicit term plus implicit term is eliminated by solving the adjoint. Define the adjoint λ by the linear system

$$\left(\frac{\partial R}{\partial A_z} \right)^T \lambda = -\left(\frac{\partial J}{\partial A_z} \right)^T, \tag{3.27}$$

$$\frac{dJ}{d\rho} = \frac{\partial J}{\partial \rho} + \left(\lambda^T \frac{\partial R}{\partial \rho} \right). \tag{3.28}$$

3.5.5 Electromagnetic Performance Evaluation

After the optimization, analyzing the airgap flux density in the initial and optimized design the above calculation gives it directly by using

$$\begin{cases} B_x = \dfrac{\partial A_z}{\partial_y} \\ B_y = -\dfrac{\partial A_z}{\partial_x} \\ B_{mag} = \sqrt{B_x^2 + B_y^2}. \end{cases} \tag{3.28}$$

The phase flux linkage is computed directly from vector potential. For each phase $k \in \{A, B, C\}$, the flux linkage is calculated as

$$\lambda_k(\theta_m) = N_{turns} l_z \int_{\Omega} A_z(\theta_m)\, s_k(x) dx, \tag{3.29}$$

where the ρ is fixed after the optimization, A_z is treated as a function of the rotor angular position only, and no sensitivity of A_z with respect to ρ is considered. The phase back EMF is obtained from the time derivate of the flux linkage.

$$e_k(t) = -\frac{d\lambda_k}{dt} = -\frac{d\lambda_k}{d\theta_m} w_m. \tag{3.30}$$

The electromagnetic torque is computed using the Maxwell stress tensor method. The Maxwell stress tensor in magnetostatics is given by

$$T = \frac{1}{\mu_0}\left(B \otimes B - \frac{1}{2}|B|^2 I\right). \tag{3.31}$$

The stress vector acting on a circular contour of radius r_t in the airgap is

$$t = T \cdot n, \tag{3.32}$$

where the torque per unit axial length is obtained from the contour integral

$$T' = \int_{\Gamma_{rt}} \left(x t_y - y t_x\right) ds, \tag{3.33}$$

$$t_x = \frac{1}{\mu_0}\left(B_x B_n - \frac{1}{2} B^2 n_x\right), \tag{3.34}$$

$$t_y = \frac{1}{\mu_0}\left(B_y B_n - \frac{1}{2} B^2 n_y\right), \tag{3.35}$$

$$B_n = B_x n_x + B_y n_y. \tag{3.36}$$

The integration is performed numerically by sampling 360 angular points along the circular airgap contour. The total electromagnetic torque is then obtained by multiplying the per length torque by the stack length

$$T = T' l_z. \tag{3.37}$$

3.5.6 Density Method Performance

The formulation is progressively refined to assess how the objective function and regularization influence the material distribution within the design domain. The density optimization is initially performed using only the flux maximization objective. As shown in Figure 3.11, the optimizer removes material mainly from the central part of the design domain. Because the objective contains no penalty on retained material, it provides little incentive to eliminate all low sensitivity iron. Considerable amount of back iron materials therefore remains near the domain boundaries, and the available design space is not used efficiently for weight reduction.

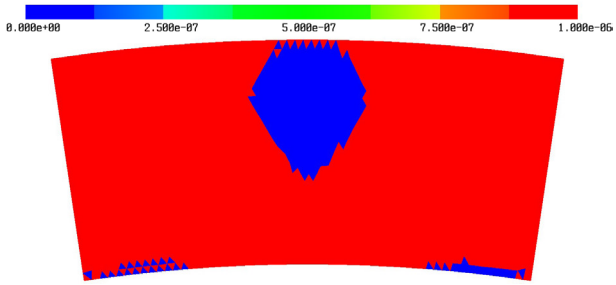


Figure 3.11. Flux maximization objective

Introducing the volume reduction term changes the optimization behaviour. The optimizer becomes more selective and removes additional inactive material while preserving the principal magnetic return path. The unfiltered topology nevertheless contains fragmented regions, local voids, and thin connections shown in Figure 3.12. These features can create locally saturated flux paths and are difficult to manufacture, showing that regularization is required in addition to the combined flux and volume objective.

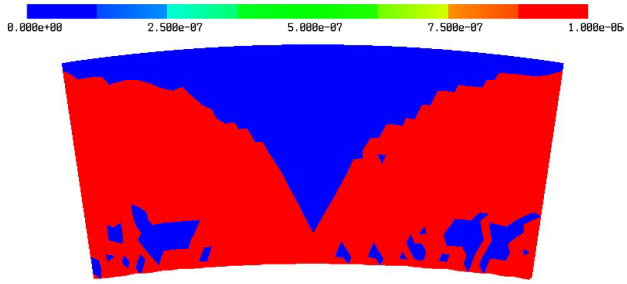


Figure 3.12. Flux maximization objective with volume penalization

A Helmholtz-type Partial Differential Equation (PDE) filter is applied to suppress numerical oscillations and impose a minimum length scale, after which projection sharpens the transition between iron and air. The filtered and projected distribution in Figure 3.13 is more continuous, and the isolated features present in the unfiltered result are removed. The resulting boundary is therefore easier to interpret and more suitable for subsequent manufacturing-oriented reconstruction. The convergence response in Figure 3.14 shows a short oscillatory transient during the first iterations, reflecting the rapid redistribution of material at the start of the optimization. The flux objective then improves steadily and levels off. At the same time, the retained volume ratio decreases rapidly and approaches a nearly constant value after approximately 22 iterations. These complementary trends indicate stable convergence toward a topology that preserves the required magnetic flux with less active material.

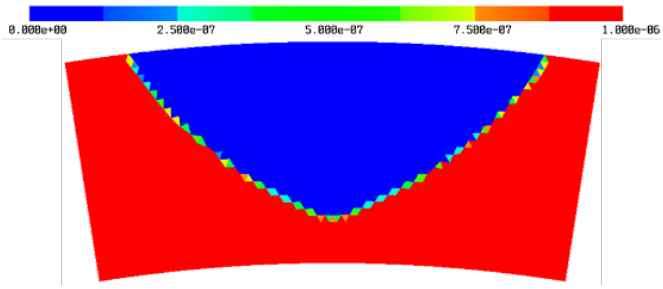


Figure 3.13. Optimal design including the density filter and projection

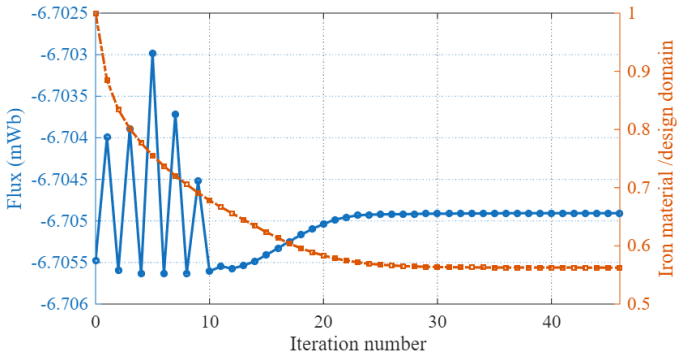


Figure 3.14. Objective function response with respect to iteration numbers

Figure 3.15 compares the magnetic flux density distributions of the initial and optimized rotors. The initial back iron exhibits a non-uniform contour, whereas the optimized design distributes the flux more evenly through the retained material. This redistribution does not weaken the airgap excitation, and the average airgap flux density remains the same. These results demonstrate that the gradient based density method reduces the rotor back iron while preserving the required magnetic performance. However, the method still relies on iterative FE solutions and the appropriate selection of penalization, filtering, and projection parameters. The following section therefore develops a physics guided analytical TO approach that determines the required back iron geometry directly from the magnetic flux path.

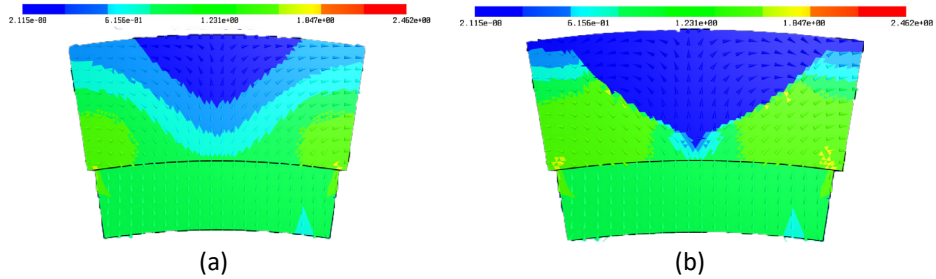


Figure 3.15. Flux density distribution (a) Initial design (b) Optimized design

3.6 Physics Guided Analytical TO

This section presents a physics guided analytical TO approach, covering the magnetic flux model, derivation of the minimum back iron width, and evaluation of the resulting optimized geometry.

3.6.1 Magnetic Flux Model

The analytical method replaces iterative material updates with a direct calculation of the minimum flux carrying geometry. The back iron is assumed to have very high relative permeability μ_r up to saturation flux density B_s. Beyond saturation its magnetization is taken as constant in the applied field direction. The PM has remanence B_r and uniform magnetization

$$M_m = \frac{B_r}{\mu_0}. \tag{3.38}$$

It is also assumed that the back iron remains unsaturated at its outer perimeter. To calculate the magnetic field produced by the magnet using Ampere's law, the magnet has a uniform magnetization, its bound currents can be treated as a free solenoidal surface current around its circumference. Choosing an Ampere contour on the outer perimeter of the back iron where the material is not saturated allows one to assume

$$B = \mu_r \mu_0 H. \tag{3.39}$$

Since $\mu_r \gg 1$, the contribution from the portion of the contour inside the back iron can be neglected. The total current enclosed is

$$I = j\ t = \frac{B_r\ t}{\mu_0}. \tag{3.40}$$

The airgap thickness is much smaller than the magnet and back iron diameters, the magnetic field in the gap and in the magnet is nearly homogeneous. Figure 3.16 shows that the magnetic field lines exit ferromagnetic materials almost perpendicular, so they enter the air gap nearly parallel and therefore remain uniform similarly, the magnet field remains homogeneous at both ends of the magnet and thus within the magnet itself. Under these conditions Ampère's law yields a uniform magnetic flux density of magnitude

$$B = \frac{B_r\ t}{g + t}. \tag{3.41}$$

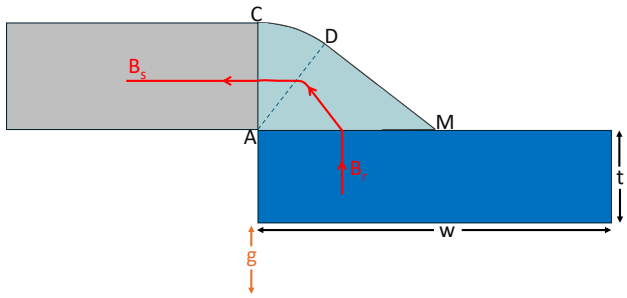


Figure 3.16. Geometrical representation of analytical topology optimized back iron for quasi-static PM machine

3.6.2 Minimum Back Iron Width

To determine how much iron is needed, consider a "cut" through the back iron that encompasses the entire cross-section touching one side of the magnet. Let w be the magnet width and d its axial length. Gauss's law (the divergence theorem) is used to equate the magnetic flux entering this volume (half the magnet's flux) to the flux exit through the cut in the back iron. The flux entering is

$$\emptyset_{in} = \frac{B_r t}{(g+t)} \cdot \frac{wd}{2}. \tag{3.42}$$

However, the back iron can only carry so much flux before saturating. The maximum flux it can transport is limited by the saturation flux density B_s multiplied by its cross-sectional area $w_{cut}d$. In order to carry all of the flux, the cut width must satisfy

$$\emptyset_{out} \leq B_s w_{cut} d. \tag{3.43}$$

Solving for the minimum width yields

$$w_{min} = \frac{B_r}{B_s} \frac{t}{g+t} \cdot \frac{w}{2}. \tag{3.44}$$

If the back iron is thinner than w_{min}, some magnetic flux will drop out because the iron cannot carry the entire flux. In this regard w_{min} as a strict necessity for any viable design. The lengths of AC and AD are both w_{min}. The contour between C and D follows the arc of the circle and the line DM is tangent to the circle at D. The quarter circle centered at A of radius w_{min} must exist in any valid back iron because it provides the necessary width around the magnet edge.

To demonstrate that the proposed shape contains the smallest possible amount of iron, consider an arbitrary cross-section A'D'M formed by intersecting the ADM triangle with a line parallel to AD as shown in Figure 3.17 By similarity of triangles, the ratio of the widths AD/AM equals the ratio A'D'/A'M. Since AD represents the minimum width needed to transport all of the flux from AM, A'D' must be the minimum width required to transport the flux from A'M. Because this argument holds for any parallel intersection, the entire triangle ADM must be included in any valid back iron. Thus, no design that removes material from the ADM triangle can carry the full magnetic flux, proving the minimality of the chosen shape.

The final check is that the minimal iron design satisfies Maxwell's equations and the refraction conditions at the magnet and iron interface. First, Gauss's law for magnetism

$$\nabla \cdot B = 0, \tag{3.45}$$

requires magnetic field lines to form closed loops. In the proposed design, the field lines travel almost vertically through

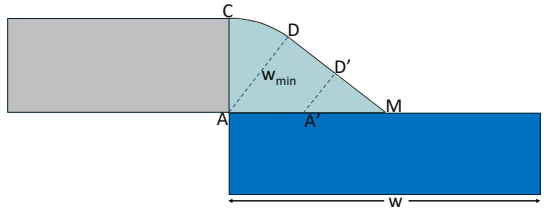


Figure 3.17. Analytical TO with new contour of A'D'M to maintain flux continuity

the magnet path parallel to the straight segment DM through the back iron, follow the circular arc until reaching point C and then complete the loop through the outer region

back to the magnet. Maxwell's other equation

$$\nabla \times \mathrm{H} = \mu_0 j, \tag{3.46}$$

is satisfied because inside the back iron $H \approx B - B_s \approx 0$ and there are no free currents. At the interface between the magnet and the back iron, the continuity of the normal component of B and the tangential component of H must be respected. Tangential H in the magnet must be nearly zero because the magnetization in the magnet is fixed and the permeability of the iron is large. The normal component of B in the magnet is

$$B_{magnet} = \frac{B_r t}{(g+t)}. \tag{3.47}$$

On the flux guide side, the flux density is approximately B_s, but it meets the interface at an angle determined by the geometry. By constructing the right triangle ADM, the cosine of this angle is $\frac{2w_{min}}{w}$. Equating the normal components on both sides requires

$$\frac{B_r t}{g+t} = B_s \frac{2w_{min}}{w}, \tag{3.48}$$

which is exactly the definition of w_{min} derived earlier. Thus, the design also satisfies the magnetic refraction condition. To conclude, the shape shown in Figure 3.16 is minimal, transports the maximum possible magnetic flux and is physically valid.

3.6.3 Analytical TO Result

A single magnetostatic FEM evaluation was used to verify the analytically obtained geometry. The resulting design removes 39.29% of the rotor back iron material and increases the torque density by 14.36%. The optimized geometry and its magnetic field distribution are presented in Figure 3.18. The flux density contours show that material is removed mainly from the weakly utilized central region, while the principal return path between adjacent magnets is retained. The flux lines remain continuous through the analytically determined circular and tangential boundaries. No excessive flux concentration is observed in the active parts of the optimized back iron, confirming that the minimum retained cross-section is sufficient to transport the magnet flux without producing a harmful magnetic bottleneck.

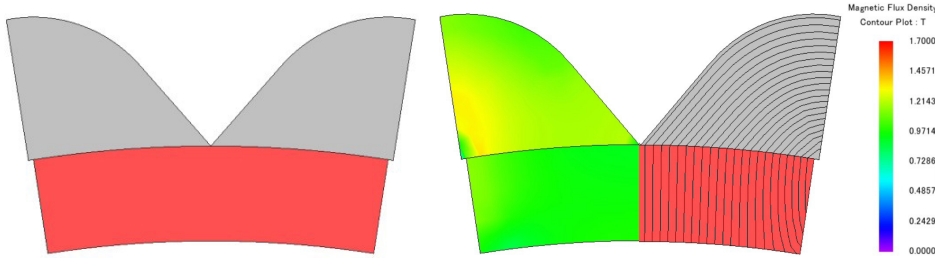


Figure 3.18. (a) TO back iron using analytical approach (b) Contour of flux density and flux lines in analytical TO back iron

Figures 3.19–3.21 compare the airgap flux density, three-phase back EMF, and electromagnetic torque of the initial and analytical TO designs. The airgap flux density and back EMF waveforms are identical, while the torque waveform retains the same average value and ripple pattern. These results confirm that the removed back iron material was magnetically underutilized and analytical TO improves torque density without significantly affecting electromagnetic performance.

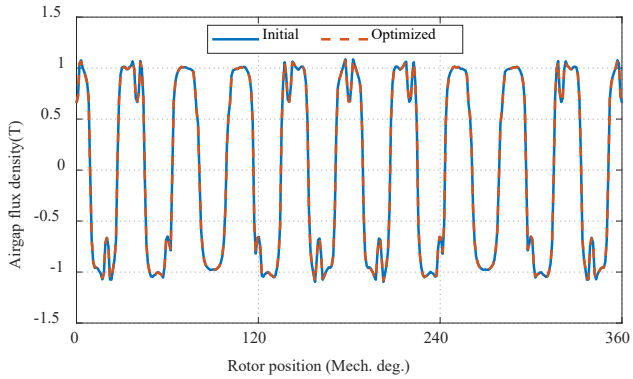


Figure 3.19. Airgap flux density comparison of initial and analytical TO

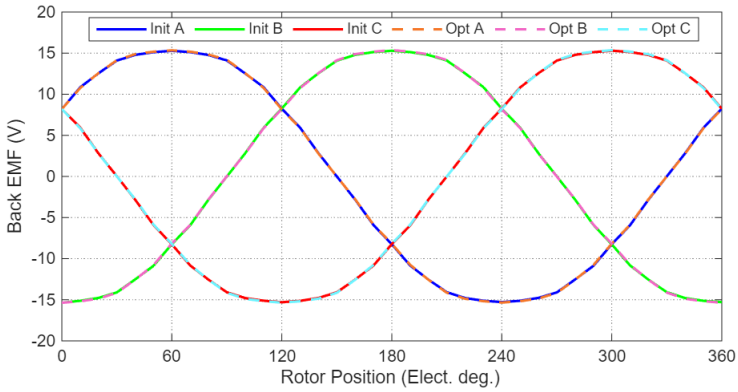


Figure 3.20. Back EMF comparison of initial and analytical TO

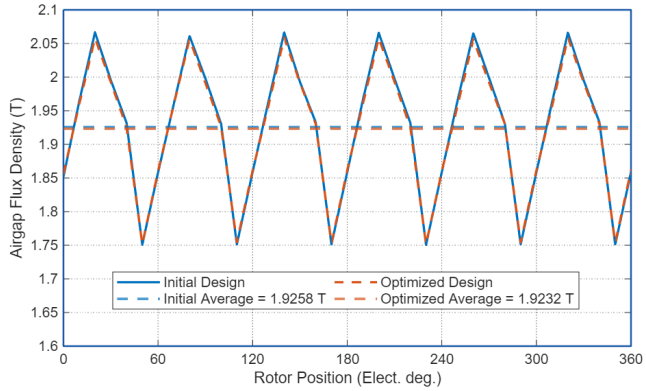


Figure 3.21. Torque waveform comparison of initial and analytical TO

3.7 Comparison of the Three Back Iron Material Reduction Techniques

Table 3.3 consolidates the principal quantitative and methodological differences among NGNet, density-based SIMP, and analytical TO. Since the formulations and individual results have already been presented, only their comparative implications are discussed here.

Table 3.3. Quantitative and methodological comparison of the three back iron material reduction techniques

Criterion	NGNet	Density-based SIMP	Analytical TO
Material representation	Gaussian ON/OFF basis; 46 functions mirrored over one pole sector	Element-wise density variable with nonlinear SIMP reluctivity interpolation	Flux derived boundary governed by continuity and saturation
Search or solution strategy	Derivative free genetic algorithm; population 47 over 50 generations	Gradient-based optimization using adjoint sensitivity and nonlinear FEM	Closed-form, non-iterative construction followed by FEM verification
Design freedom	Moderate; controlled by Gaussian placement, width, and number	High; one design variable per finite element	Problem specific; geometry constrained by the assumed dominant flux path
Regularization and reconstruction	Binary material description; no density filter, although geometric smoothing may be required	SIMP penalization, Helmholtz filter, projection, and final boundary reconstruction	No numerical regularization; mechanical bridge and magnet pockets added during post processing
Numerical effort	Approximately 6 h 40 min; many FEM evaluations	Stable after approximately 20-25 iterations; wall-clock time not separately reported	One field evaluation; negligible optimization computation
Rotor back-iron reduction	25.67%	39%	39.29%
Total motor volume reduction	7.32%	12%	-
Torque-density increase	7.84%	Approximately 14%	14.36%
Electromagnetic performance	Airgap flux density, back EMF, and torque preserved	Airgap flux density, back EMF, and torque preserved	Airgap flux density, back EMF, and torque preserved
Manufacturing and validation status	Numerical benchmark	Numerical result with filtered and projected topology	Manufactured by LPBF after geometric adaptation and experimentally tested
Advantage	Robust global exploration without sensitivity derivatives	Maximum geometric freedom with efficient gradient evaluation	Highest speed, direct physical interpretation, and nearly identical reduction to the density method
Limitation	High computational cost and basis dependent resolution	Parameter sensitivity, intermediate densities, and reconstruction dependence	Limited to problems with a dominant quasi-static flux path

The density based and analytical TO approaches produce almost identical back iron reduction and torque density improvement, whereas NGNet achieves a smaller reduction at substantially greater computational cost. The close agreement between the density based and analytical results indicates that approximately 39% of the original back

iron is unnecessary for the specified electromagnetic operating condition. The three methods consequently serve different purposes. NGNet is suitable for derivative free binary searches, while density based TO offers the greatest geometric freedom but requires regularization and iteration. Analytical TO provides the fastest and most physically transparent solution when a dominant quasi-static flux path is identified.

3.7.1 Manufacturing Oriented Design Modifications

After completing the optimization process, the design was prepared for the manufacturing stage, which required several practical modifications. During optimization, arc shaped magnets were used. However, these magnets are relatively expensive for practical implementation. To reduce the manufacturing cost, straight N35 magnets were selected as an alternative. The use of straight magnets introduces small gaps between the magnets and the rotor back iron as shown in Figure 3.22(a), which results in the reduction of electromagnetic performance. In Figure 3.22(b) small pockets were incorporated behind the magnets, allowing the magnets to fit properly and maintain close contact with the back iron structure. An outer circular iron bridge is also introduced to improve mechanical strength and structural stability of the rotor as shown in Figure 3.23(a), while the 3D Computer-Aided-Design (CAD) model of the optimized rotor back iron is shown in Figure 3.23(b) for better realization of the rotor back iron. Although the resulting back iron geometry has a relatively complex shape, it can be effectively manufactured using AM technique. The comparison of torque waveforms obtained from different back iron configurations and magnet arrangements is presented in Figure 3.24.

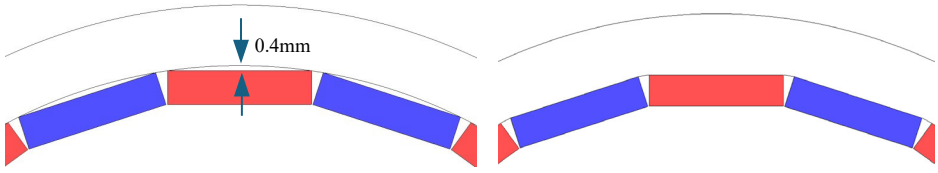


Figure 3.22. Different design configuration with straight magnets (a) With air region behind magnets (b) Iron filled behind magnets

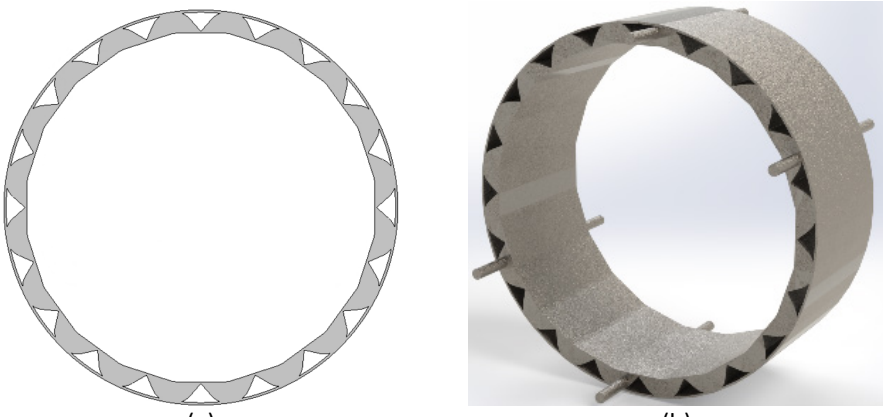


Figure 3.23. Optimized back iron having mechanically feasible (a) 2D cross sectional back iron (b) 3D CAD model of back iron

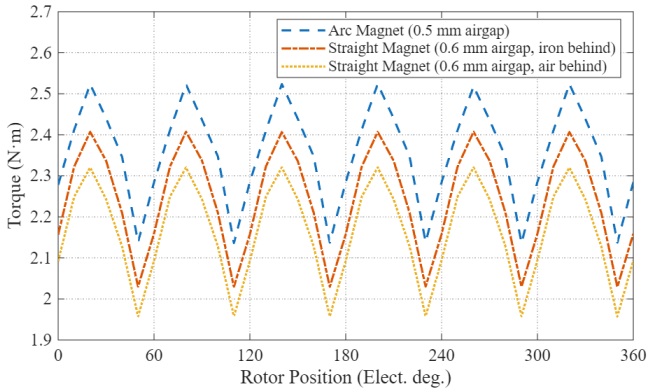


Figure 3.24. Comparison of torque on different magnets shape configuration

3.8 Rotor Back Iron Fabrication Through AM

The initial and topology optimized rotor back iron prototypes were manufactured by LPBF using pre-alloyed, gas-atomized Fe–Si powder supplied by Sandvik Group. The chemical composition of the powder was verified using Energy Dispersive X-ray Spectroscopy and Spark Atomic Emission Spectroscopy [13]. The powder consisted of spherical particles with sizes ranging from 29-58 µm, with a median diameter of 38 µm. The printing process was carried out using an SLM Solutions Realizer SLM-280 system equipped with a 350 W infrared laser.

To prevent density degradation during large volume printing, the scanning strategy was modified from a stripe pattern to a chessboard pattern, which improves printing stability and structural uniformity, as reported in previous studies. Additionally, the re-melting scanning strategy was disabled because it increased surface roughness and reduced powder flowability, resulting in uneven layer formation. The key printing parameters used in the process are summarized in Table 3.4.

The printing time for each back iron was approximately 5 hours. After printing, the prototypes were heat treated in RD-G vacuum furnace at 1200 °C, with a heating rate of 5 °C/min and a holding time of one hour. The parts were then cooled inside the furnace at an initial cooling rate of 50 °C/min, gradually decreasing over time. During the heat treatment process, the vacuum level was maintained between 0.04 and 0.4 mbar. The fabricated AM rotors, including the initial and optimized designs, are shown in Figure 3.25(a) and Figure 3.25(b) respectively.

Table 3.4. Summary of printing parameters

Parameter	Value
Layer thickness	50 µm
Hatch distance	120 µm
Laser Power	350 W
Scanning velocity	0.75 m/s
Volumetric energy density	83 J/mm³



(a) (b)

Figure 3.25. AM based rotor prototype (a) Initial rotor (b) Optimized rotor

3.9 Experimental Testing and Validation

To validate the electromagnetic performance of the proposed outer rotor BLDC motor, experimental measurements were carried out on the fabricated prototype. The experimental setup was designed to evaluate both the no load back EMF characteristics and the machine performance under load conditions. The prototype motor was mounted on a rigid platform and mechanically coupled to a servo motor through a shaft coupling to control the rotational speed. For no load testing, the servo motor was operated at the rated speed of 900 rpm, while the BLDC motor terminals were kept open to measure the induced phase voltages. The three-phase back EMF waveforms were recorded using a digital oscilloscope as shown in Figure 3.26.

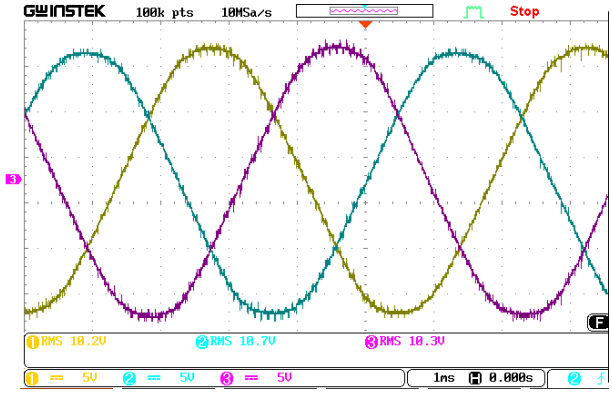


Figure 3.26. Experimental three phase back EMF

For load analysis, the BLDC motor shaft was connected to a DYN-200 torque sensor, and a powder brake was coupled to the torque sensor to apply a controllable mechanical load to the prototype motor. For signal visualization and data acquisition, a Dewesoft SIRIUS isolated data acquisition system was employed. The complete experimental setup is illustrated in Figure 3.27. The motor phase currents were measured using three PR200 current clamps (10 mV/A). The measurements were acquired with a sampling rate

corresponding to a bandwidth of 1 MHz. The measured three-phase motor currents and torque waveform are presented in Figure 3.28(a) and Figure 3.28(b) respectively.

Due to the absence of magnetic property data for the AM rotor back iron material in the simulation software database, the numerical analysis was performed using the M400-50A electrical steel model. However, the practical prototype was fabricated using a Fe–3.7%Si magnetic material, as reported in [14]. The simulated torque is around 5.09% lower than the measured. This discrepancy is mainly attributed to the difference between the magnetic material properties used in the simulations and those of the AM Fe–3.7%Si back iron, as well as manufacturing tolerances and experimental measurement uncertainties.

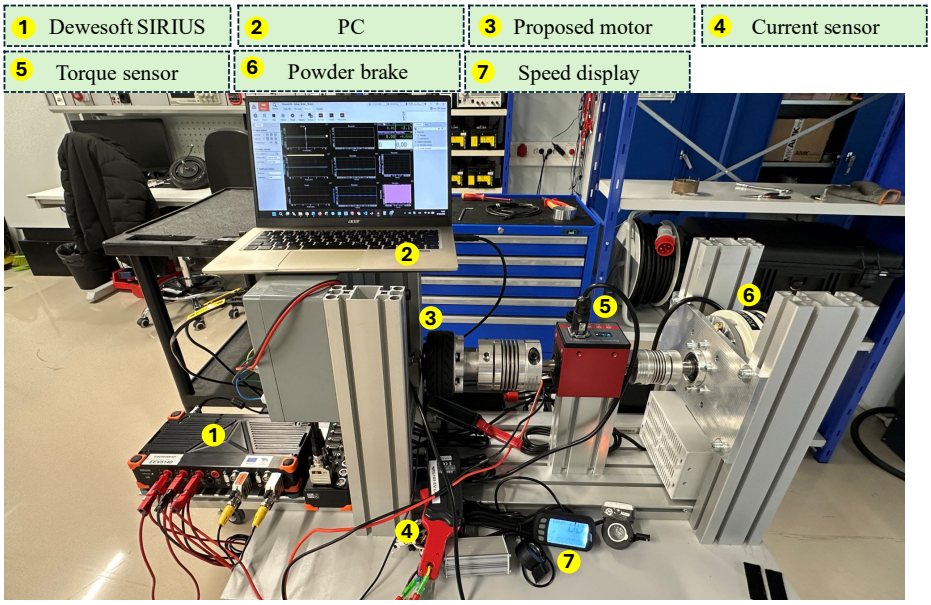
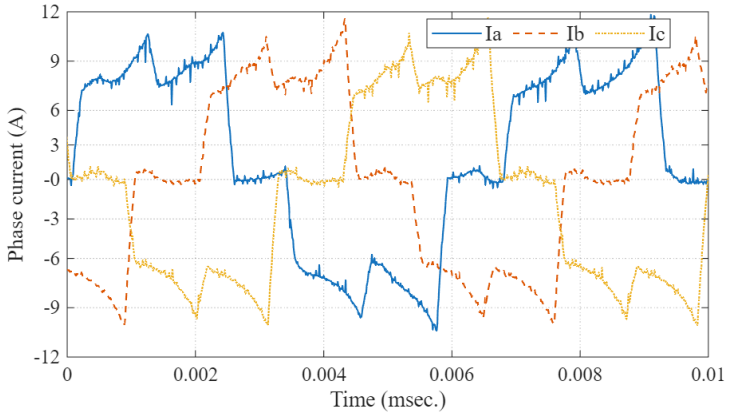


Figure 3.27. Experimental test setup for outer rotor BLDC



(a)

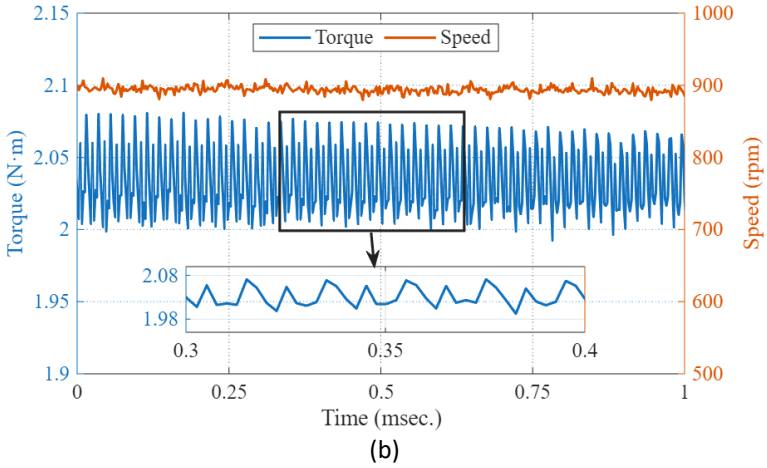


Figure 3.28. Experimental results (a) Three phase motor currents (b) Torque and speed waveform

3.10 Summary

This chapter demonstrated that TO substantially improves magnetic material utilization in the rotor back iron of a PM machine without compromising its performance. The NGNet method reduced the back iron volume by 25.67%, whereas the density based and physics guided analytical methods achieved reductions of approximately 39% and increased torque density by approximately 14%. The analytical method produced a result comparable to the density-based method while requiring only one FEM evaluation, demonstrating its computational advantage for machines with dominant quasi-static flux paths. After manufacturing oriented modifications, the optimized rotor was fabricated using LPBF and experimentally tested, confirming its electromagnetic functionality. These results establish a basis for applying physics guided material reduction, with suitable modifications, to machines having more complex 3D flux paths.

4 Design and TO of an AFDR-SRM

AFSRM are attractive for propulsion systems in which a short axial length, a mechanically robust rotor, high speed capability, and fault tolerant phase operation are required. Their torque is produced by the tendency of the excited magnetic circuit to move toward a position of higher phase inductance. Therefore, neither PMs nor rotor windings are required. The absence of rotor excitation simplifies the electromagnetic rotor, but the axial 3D flux path, the double air gap, and the end effects make direct numerical optimization computationally expensive.

This chapter combines the design and TO stages of a 6/4 AFDR-SRM. The benchmark machine is first sized analytically and validated using nonlinear 3D FEM analysis. The circular machine is then unwrapped at its mean radius to obtain a 2D linearized model suitable for NGNet TO. The optimized linear topology is mapped back to the annular rotor, after which a physics guided analytical procedure reduces the rotor back iron volume. Manufacturing, experimental testing of the optimized design is presented in the final section of this chapter.

The sequence is intentionally hierarchical. Analytical sizing establishes feasible dimensions, 3D FEM defines the numerical benchmark, the linear model provides computationally efficient optimization environment, and the reconstructed 3D model remains the final authority.

4.1 Benchmark AFDR-SRM Design and Numerical Validation

A benchmark AFDR-SRM is established by describing its configuration and operating principle, determining its main dimensions analytically, and verifying the design through 3D FEM simulation.

4.1.1 Machine Configuration and Operating Principle

A three-phase 6/4 AFDR-SRM is selected as the benchmark machine for a high-speed propulsion system. Six trapezoidal stator teeth are arranged as a segmented yokeless stator between two four pole rotors. Diametrically opposite stator teeth are connected in series to form one phase, giving three magnetically and electrically independent phase pairs as shown in Figure 4.1. Concentrated coils maximize the available slotless winding area and allow a phase fault to be isolated without disabling the remaining phases. The two rotors provide two active airgaps and act on opposite axial faces of the stator, increasing the effective airgap area within a compact outside diameter.

Excitation is applied according to rotor position. When a phase is energized near its unaligned position, its inductance increases as the rotor poles approach the corresponding stator teeth as presented in Figure 4.2. Positive torque is obtained while the phase current overlaps the positive inductance slope interval. The rotor is constructed entirely from ferromagnetic material and contains no magnets or conductors. Consequently, its shape can be modified more freely than that of a wound or PM rotor. This freedom motivates the pole shoe and back iron TO developed later in the chapter.

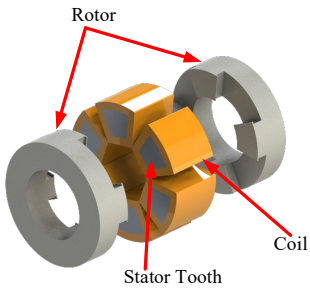


Figure 4.1. Proposed AFDR-SRM

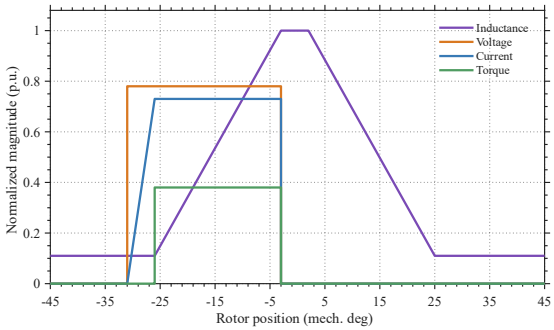


Figure 4.2. Inductance profile of SRM for one phase excitation

4.1.2 Analytical Sizing Formulation

An analytical sizing procedure is used to determine the machine's geometric parameters from the specified performance requirements, thereby providing a physically consistent starting point for the subsequent 3D FE analysis. The required output power, terminal voltage, rotational speed, current density, number of phases, and permissible magnetic and electrical loadings are used as the main design inputs. Following the AFSRM sizing formulation, the output power is expressed in terms of the electrical input during the conduction interval as

$$P_{out} = \eta k_d V I m, \tag{4.1}$$

where the duty cycle is

$$k_d = \frac{\theta_i \, m \, N_r}{360}. \tag{4.2}$$

During the rising inductance interval, the applied voltage is related to the change between the aligned saturated inductance ${L_a}^s$ and the unaligned inductance L_u by

$$V = \frac{({L_a}^s - L_u) i}{t}. \tag{4.3}$$

The time available for the rotor to traverse the effective stator pole arc βs is

$$t = \frac{\beta_s}{\omega_m}. \tag{4.4}$$

Introducing the aligned saturation ratio σ_s and the aligned to unaligned inductance ratio σ_u gives the voltage relation

$$V = \frac{\omega_m}{\beta_s} {L_a}^s i \left(1 - \frac{1}{\sigma_s \sigma_u}\right). \tag{4.5}$$

At alignment, the phase flux linkage can be expressed either through the aligned flux or through the average airgap flux density and stator pole area. For the annular active region this becomes

$$L_a{}^s i = \varphi N_{ph} = B_g A_{sp} N_{ph} = \frac{1}{8} B_g \left(D_o{}^2 - D_i{}^2\right) \beta_s N_{ph}, \tag{4.6}$$

where the electrical loading at the average diameter D_{avg} is

$$A_s = \frac{2N_{ph} im}{\pi D_{avg}}. \tag{4.7}$$

Substitution the flux linkage and electrical loading relations into the voltage equation gives the rated voltage expression

$$V = \frac{\pi^2}{480} \frac{1}{im} B_g A_s D_{avg} \left(D_o{}^2 - D_i{}^2\right) \left(1 - \frac{1}{\sigma_s \sigma_u}\right) N_{rpm}. \tag{4.8}$$

The corresponding output power equation is

$$P_{out} = \eta k_d k_1 k_2 B_g A_s D_{avg} \left(D_o{}^2 - D_i{}^2\right) N_r, \tag{4.9}$$

where the two machine coefficients are

$$k_1 = \frac{\pi^2}{480}, \qquad k_2 = \left(1 - \frac{1}{\sigma_s \sigma_u}\right). \tag{4.10}$$

The average torque follows from the mechanical angular speed and can also be written directly in terms of the electromagnetic and geometric loadings

$$\tau = \frac{P_{out}}{\omega_m}, \tag{4.11}$$

$$\tau = \eta k_d k_2 k_3 B_g A_s D_{avg} \left(D_o{}^2 - D_i{}^2\right), \tag{4.12}$$

$$k_3 = \frac{\pi}{16}. \tag{4.13}$$

For fixed electrical loading, magnetic loading, and aligned to unaligned inductance ratio, the annular dimensions dominate the achievable torque. Based on [83], the maximum average torque can be achieved by maintaining an inner to outer diameter ratio of 0.577. The remaining stator, rotor, winding, resistance, loss, and mass calculations are completed as follows. The geometrical parameters used in the following sizing relations are defined in Figure 4.3, where Figure 4.3(a) presents the stator and rotor parameters, while Figure 4.3(b) shows the coil parameters.

With stacking factor k_i, the average stator tooth width required to carry the airgap flux is

$$w_{st} = \frac{B_g}{k_i B_{st}} \times \frac{\pi D_{avg}}{N_s}. \tag{4.14}$$

For a minimum inner side coil to coil clearance w_g, the available average copper width around each tooth is

$$w_{cu} = \frac{(\pi D_{avg}) - (N_s w_g) - (N_s w_{st})}{2N_s}. \tag{4.15}$$

The average width of the rotor pole, back iron length of the rotor, pole shoe width, pole shoe depth and length of pole shoe can be expressed as

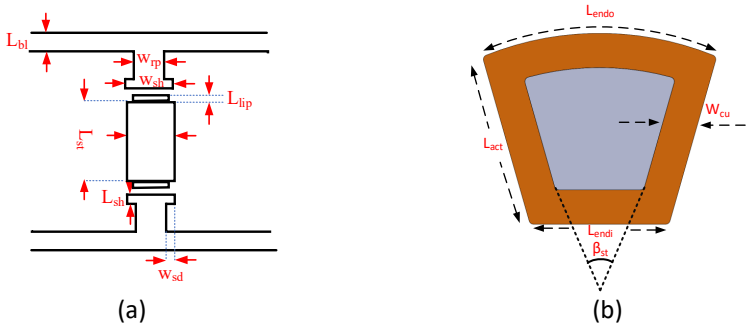


Figure 4.3. Representation of geometrical parameters (a) Stator and rotor parameters (b) Coil parameters

$$\begin{cases} w_{rp} = \dfrac{B_g}{B_{st}} \times \dfrac{\pi D_{avg}}{N_r} \\ L_{bl} = \dfrac{B_g}{B_{bl}} \times \dfrac{\pi D_{avg}}{2N_r} \\ w_{sh} = \dfrac{\pi D_{avg}}{N_r} \times \dfrac{\beta_{sh}}{\tau_p} \\ w_d = \dfrac{w_{sh} - w_{st}}{2} \\ L_{sh} = \dfrac{B_g}{B_{sh}} \times w_d. \end{cases} \tag{4.16}$$

The required stator tooth axial length follows from electrical loading, Root Mean Square (RMS) current density, available copper width, fill factor, and tooth number

$$L_{st} = \frac{A_s \pi D_{avg}}{2 J_{rms} w_{cu} k_f N_s}. \tag{4.17}$$

The active and end-winding lengths give the mean length of one turn

$$\begin{cases} L_{act} = \frac{D_o - D_i}{2} + w_{cu} \\ L_{endo} = (\frac{D_o + w_{cu}}{2}) \times (\beta_{st}) + w_{cu} \\ L_{endi} = \left(\frac{D_i - w_{cu}}{2}\right) \times (\beta_{st}) + w_{cu} \\ L_t = (2L_{act}) + L_{endo} + L_{endi}. \end{cases} \tag{4.18}$$

The conductor cross-section, selected wire diameter, and phase resistance are

$$\begin{cases} A_{cond} = \frac{L_{st} w_{cu} k_f}{N_{tc}} \\ d_w = \sqrt{\frac{4A_{cond}}{\pi}} \end{cases} \tag{4.19}$$

$$R = \frac{\rho_{cu} L_t}{A_{cond}}. \tag{4.20}$$

The three-phase copper loss is

$$P_c = 3{I_{rms}}^2 \times R_{ph}. \tag{4.21}$$

For mass and density evaluation, the component masses are calculated from their volumes and the iron and copper densities

$$\begin{cases} W_{st} = d_i h_{st} w_{st} L_{st} N_s \\ W_{cu} = d_c L_t w_{cu} L_{st} k_f N_s \\ W_{sh} = d_i h_{st} w_{sh} L_{sh} N_r \\ W_{rp} = d_i h_{st} w_{rp} L_{rp} N_r \\ W_{bl} = d_i h_{st} \pi D_{avg} L_{bl} N_r \end{cases} \tag{4.22}$$

$$W = W_{st} + W_{cu} + 2W_{sh} + 2W_{rp} + 2W_{bl}. \tag{4.23}$$

The torque density and power density can be calculated from the output torque and power equation with respect to the whole machine weight and can be expressed as

$$\begin{cases} P_d = \frac{P_{out}}{W} \\ T_d = \frac{T_{avg}}{W} \end{cases} \tag{4.24}$$

The iron loss is not evaluated from a single frequency empirical expression because the local SRM flux density is non-sinusoidal and position dependent. It is therefore obtained from the transient 3D FEM solution. Equations (4.1)–(4.24) provide the complete analytical formulation used to calculate the machine dimensions and parameters summarized in Table 4.1.

These analytical relations provide the initial machine dimensions. The stator tooth and rotor pole widths are verified against the prescribed flux density limits, the winding window is checked against the specified current density requirement, and the rotor back iron is conservatively sized to prevent saturation. Because the axial magnetic circuit is inherently 3D, the analytical model provides an initial design rather than the final geometry. The resulting dimensions are therefore implemented in a nonlinear 3D FE model for refinement and validation in the following section.

Table 4.1. Design and Electrical Parameters of AFDR-SRM

Parameter	Value	Unit
Phase / pole configuration	3-phase, 6/4	—
Rated terminal voltage	96	V
Rated speed	7000	r/min
Rated output power	150	W
Peak phase current	4	A
Current density	5	A/mm²
Turns per coil	150	turns
Electrical loading	28.485	A/mm
Air gap on each side	0.25	mm
Outer diameter	60.0	mm
Inner diameter	33.6	mm
Stator tooth width	13.1	mm
Coil width	3.7	mm

Parameter	Value	Unit
Stator tooth height	13.2	mm
Stator axial length	25.3	mm
Rotor pole width	19.6	mm
Initial rotor back-iron thickness	12.3	mm
Pole-shoe length / depth	0.6 / 1.2	mm
Phase resistance	0.7535	Ω

4.1.3 3D Benchmark FEM Validation

To validate the analytical design and assess the electromagnetic performance of the AFDR-SRM under various operating conditions, a 3D FEM model was constructed in JMAG Designer directly from the machine parameters obtained analytically. The validation follows the sequential procedure outlined in Figure 4.4, beginning with a set of fixed inputs e.g. rated voltage, speed, current density, magnetic loading, pole numbers, and manufacturing constraints. The static field distributions, flux linkage profiles, inductance curves, and static torque characteristics obtained from this analysis guide the adjustment of any free geometric dimensions. Once the magnetic geometry is refined, dynamic simulations operated in single pulse and current chopping modes are performed to map the full operating envelope.

The FEM model itself implements a complete axial 3D magnetic circuit in JMAG. Nonlinear magnetic material properties are assigned to the stator teeth and both rotor discs, while the concentrated phase coils are modelled by their series turns, resistance, and per-phase excitation sequence. A fine mesh is applied to 0.25 mm airgaps. Static solutions step the rotor from the unaligned to the aligned position at a set of prescribed currents. Dynamic solutions incorporate the asymmetric half bridge converter, position dependent phase commutation, and a speed dependent iron loss post-processing step. This two-stage approach deliberately decouples the geometric and field verification from the influence of the converter and motion dynamics.

4.1.4 Magnetic Flux Density Validation

The magnetic flux density distribution is evaluated at the aligned and unaligned rotor positions to verify the analytical sizing and identify any local saturation at the rated current. Figure 4.5 presents the flux distributions when phase A is excited with its rated current of 4 A. At the unaligned position, the magnetic flux density at the stator tooth is 0.28T, while it achieves approximately 0.53T and 0.17T at the rotor pole shoe and at back iron respectively as shown in Figure 4.5(a).

The magnetic flux density at the stator teeth is around 1.52T in the aligned position shown in Figure 4.5(b). The value increases to 1.65T at the rotor pole shoe, which causes a red spot to appear on the edge of the pole shoe. This observation is noteworthy as the pole shoe was originally designed to accommodate a magnetic flux density of 1.6T, and the FEA simulations closely approximate this designed value. These flux density distributions confirm that the machine operates close to its intended design values at currents up to 4 A.

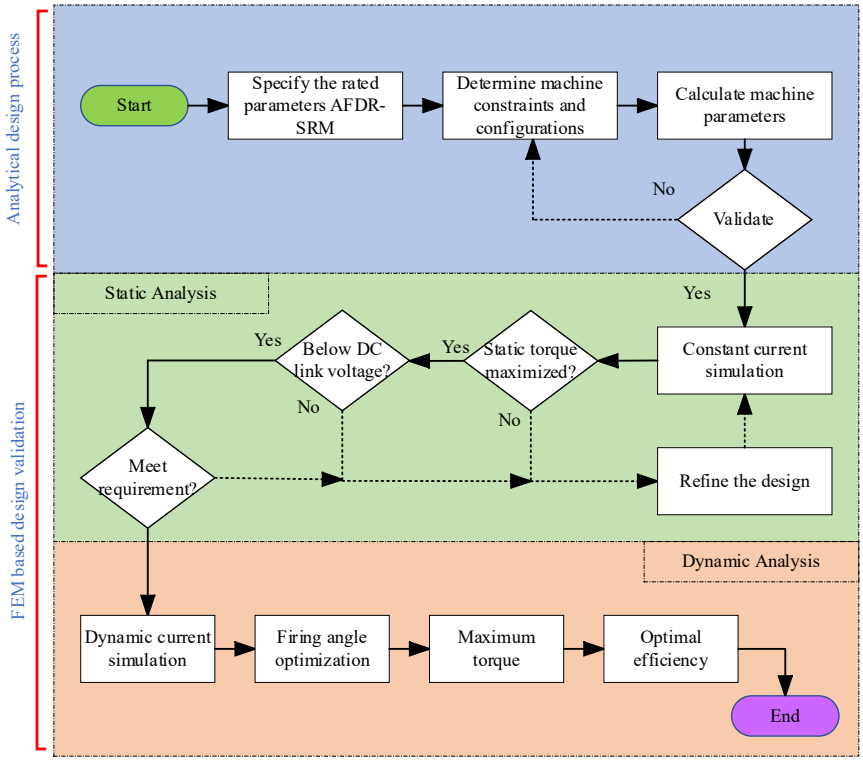


Figure 4.4. Design flow of AFDR-SRM

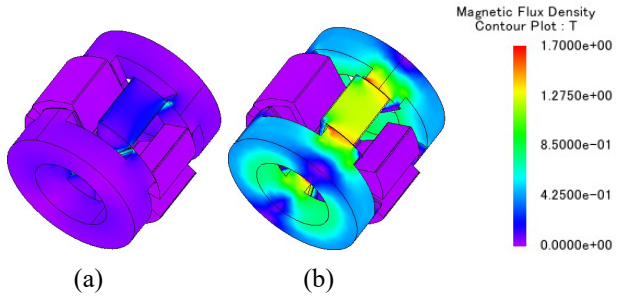


Figure 4.5. Magnetic flux distribution (a) Unaligned position (b) Aligned position

4.1.5 Flux Linkage and Inductance Characteristics

The flux linkage and inductance characteristics are evaluated to determine the machine's magnetic saturation, saliency, and torque producing capability. The analysis begins by calculating the phase flux linkage from the unaligned to the aligned rotor position over a current range of 1 A to 10 A as shown in Figure 4.6. In the unaligned position, the linkage remains low because the combined reluctance of the two axial airgaps and the absence of pole overlap dominate the magnetic circuit. As the rotor pole start overlapping with the stator tooth, the flux linkage rises steeply, and the aligned position curves become progressively nonlinear beyond the knee point, indicating the onset of magnetic saturation near the rated operating current of 4 A.

Phase inductance, derived from these flux linkage characteristics, decreases with increasing current at both aligned and partially aligned positions. At low currents, the iron paths present a low reluctance, leaving the airgaps as the primary magnetic impedance. As shown in Figure 4.7, increasing the current drives the iron toward saturation, thereby increasing the magnetic reluctance and reducing the incremental inductance. The maximum simulated inductance is 21.1 mH at 2 A, the minimum is 2.52 mH, yielding a maximum to minimum ratio of 8.37. This ratio confirms a sufficiently large saliency for effective reluctance torque production and supports the commutation interval adopted in the dynamic model.

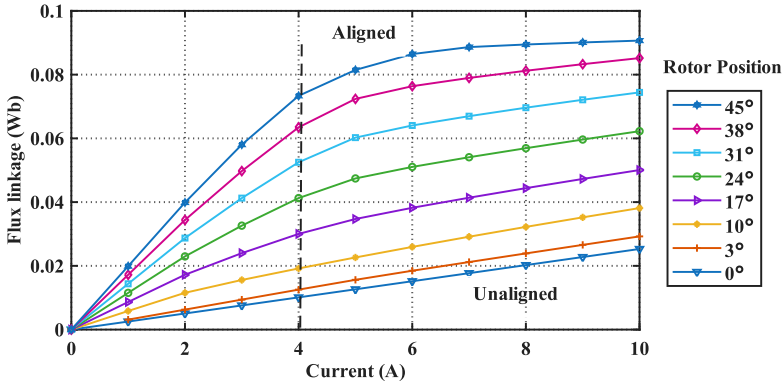


Figure 4.6. Phase flux linkage at different current levels

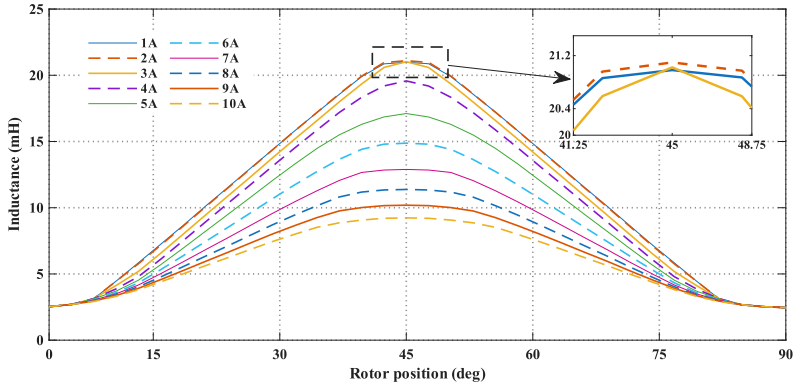


Figure 4.7. Inductance characteristic at different rotor position

4.1.6 Static Flux Linkage and Torque Characteristics

To characterize the machine's electromagnetic behaviour and identify its effective torque producing region, the static flux linkage and torque characteristics are evaluated at different rotor positions and phase current levels. The phase flux linkage increases as the rotor moves from the unaligned position toward the aligned position because the overlap between the stator and rotor poles increases, thereby reducing the magnetic circuit reluctance. At low current levels, the flux linkage curves rise almost proportionally with current. At higher currents, the curves become more closely grouped near alignment, indicating magnetic saturation in the stator tooth and rotor pole regions as shown in Figure 4.8(a). Consequently, increasing the current beyond approximately 7–8 A produces only a limited additional increase in flux linkage.

The static torque characteristics presented in Figure 4.8(b) show that torque increases strongly with phase current. For each current level, the torque rises rapidly after the unaligned position, remains relatively high over the pole overlap region, and then decreases to approximately zero as full alignment is reached. This behaviour agrees with the reluctance torque principle, since positive torque is produced while the phase inductance increases with rotor position. At full alignment, the inductance gradient approaches zero and no further reluctance torque is generated. The positive torque region also identifies the useful phase conduction interval for selecting the turn-on and turn-off angles in the dynamic model.

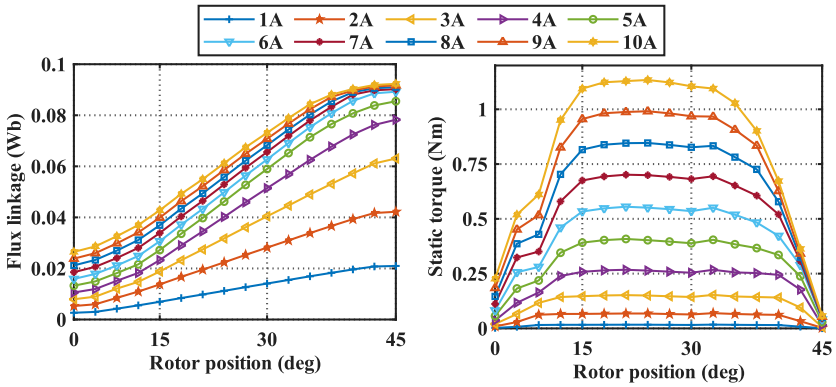


Figure 4.8. Static flux linkage and static torque at different current levels

4.1.7 Dynamic Performance Under Single Pulse and Current Chopping Control

Static analysis alone cannot account for phase commutation, current regulation, and torque ripple during continuous rotation. Therefore, the dynamic performance of the AFDR-SRM is evaluated using Single Pulse Control (SPC) at the rated speed and Current Chopping Control (CCC) at low speed by determining the phase current response, commutation behaviour, instantaneous torque, and torque ripple. The analysis explores the effects of changing the axial length of the rotor poles from 1mm to 10mm, with the corresponding impact on rotor positioning and torque is shown in Figure 4.9.

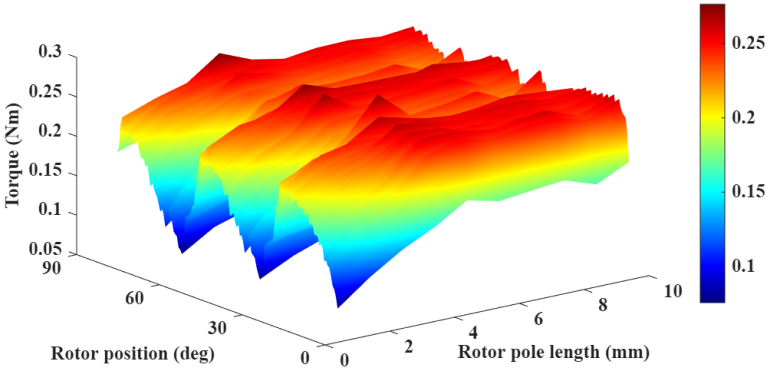


Figure 4.9. Effect on average torque due to rotor pole length

At the rated speed of 7000 r/min and a dc-link voltage of 96 V, the machine was operated using single-pulse control. As shown in Figure 4.10, the phases are excited sequentially in the order A–C–B, with each phase conducting over an interval of

approximately 30°. The phase current increases rapidly after turn-on and reaches approximately 4 A. Following turn-off, the current decreases gradually because of the stored magnetic energy in the phase winding.

At the lower operating speed of 1000 r/min, the back EMF is considerably smaller, and the current would rise above its reference value if the full dc-link voltage were applied continuously. CCC was therefore employed to regulate each phase current at approximately 4 A. As depicted in Figure 4.11, the asymmetric half bridge converter repeatedly switches the phase voltage between positive, zero or freewheeling, and negative demagnetization states. The rapid switching between $+V_{dc}$ and $-V_{dc}$ produces the visible current ripple around the reference value. The dynamic analysis confirm that both control strategies maintain the required phase current response and deliver the expected torque under their respective operating conditions.

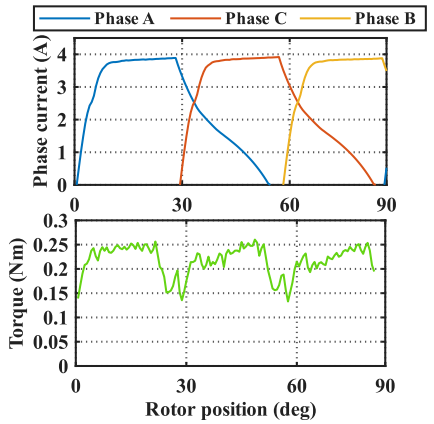


Figure 4.10. Steady state current and torque waveform under SPC

4.1.8 Torque–Speed, Loss, and Efficiency Characteristics

Following the dynamic performance at selected operating points, the torque–speed capability, power output, and efficiency are evaluated over the complete operating range. Figure 4.12 presents the torque–speed and power–speed characteristics of the AFDR-SRM. From standstill to the rated speed of 7000 rpm, the torque remains nearly constant, indicating the machine's ability to maintain consistent torque in the low-to-mid speed range. As the speed approaches the rated value, the machine's output power increases linearly due to the combination of constant torque and rising speed, reaching its peak at the rated speed. This optimal operating point is where the machine achieves maximum efficiency, as seen in Figure 4.13.

Beyond the rated speed, the torque begins to decline, this decline is attributed to the increasing back EMF, which limits the effective current flowing through the windings. With reduced current, the torque output drops, leading to a decrease in power output. Additionally, higher speeds result in increased core (iron) losses due to eddy currents and hysteresis within the magnetic materials, as shown in Figure 4.14. In Figure 4.13, the efficiency map highlights the SRM's performance across various operating conditions. The results indicate that the machine operates with peak efficiency near the rated speed, where the power output is highest. In the constant torque region (up to the rated speed), iron losses remain relatively low due to limited eddy currents and magnetic hysteresis within the core.

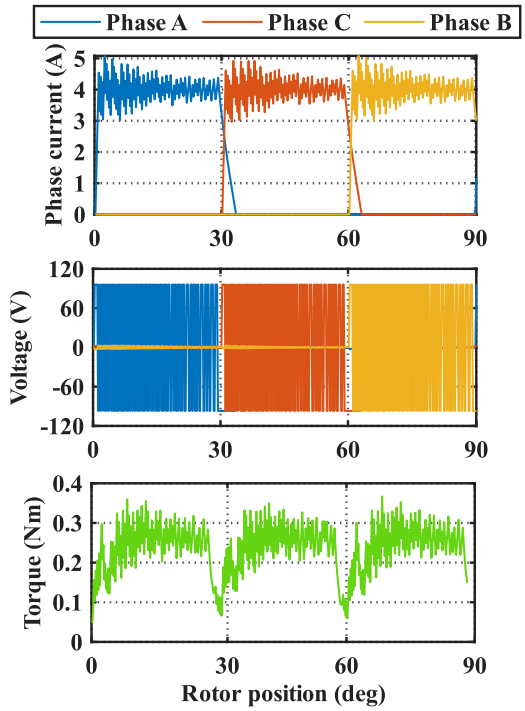


Figure 4.11. Steady state current, voltage and torque waveform under CCC

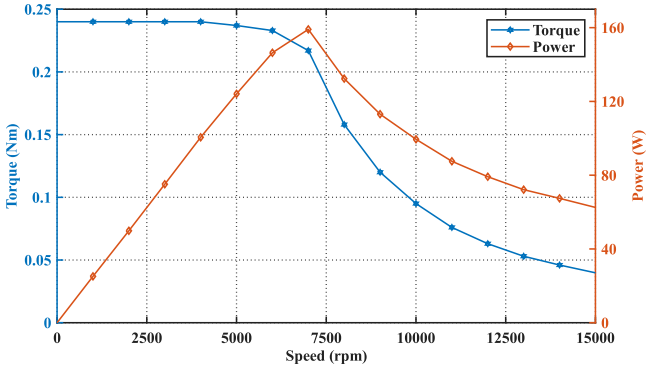


Figure 4.12. Torque speed and power characteristics curve

As the speed exceeds the rated value, the iron losses increase significantly. This increase in iron losses at high speeds reduces the machine's efficiency, as more input power is lost as heat rather than being converted to useful torque and power. Figure 4.15 presents the copper losses map which is high in the constant torque region due to the high current required to maintain steady torque. Copper losses are calculated using Eq. (20), which incorporates the resistivity of copper that varies with the machine's working temperature. Beyond the rated speed, the machine cannot achieve the reference current due to the increased back EMF, which leads to a significant reduction in current. As the current decreases, copper losses also decline, contrasting with the trend in iron losses. This behaviour highlights the shift in loss mechanisms from copper losses in the constant

torque region to iron losses at higher speeds. Overall, the results define the AFDR-SRM operating envelope, with peak efficiency near the rated speed and a transition from copper loss dominance in the constant torque region to iron loss dominance at higher speeds.

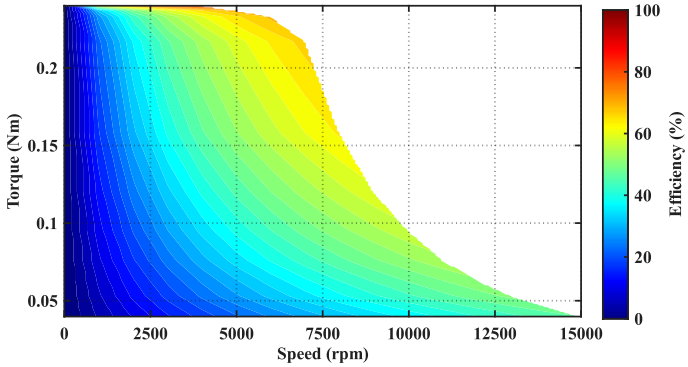


Figure 4.13. Efficiency map of AFDR-SRM

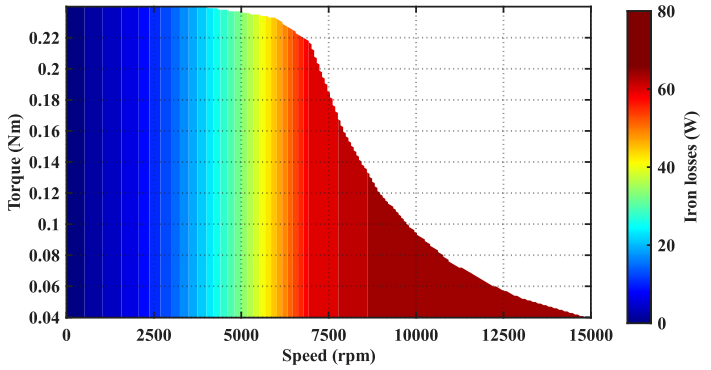


Figure 4.14. Iron losses at different operating regions of AFDR-SRM

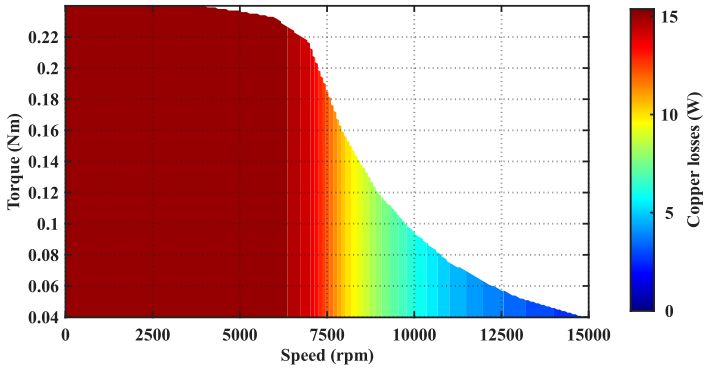


Figure 4.15. Copper losses at different operating regions of AFDR-SRM

4.2 Equivalent 2D Linearized Model

The preceding analysis establish the electromagnetic performance of the AFDR-SRM and provide the baseline for further improvement. However, applying TO directly to the 3D axial flux geometry would require a computationally intensive FE solution at every iteration. To make the optimization more practical, this section investigates an equivalent 2D linearized transformation to reduce the simulation time per iteration.

4.2.1 Basis of the Rotary to Linear Transformation

A linear SRM can be obtained from its rotary counterpart by cutting the stator and rotor along a radial plane and unrolling the circumferential airgap surfaces into straight tracks [84]. A rotary machine with a radial flux path produces a longitudinal flux Linear Switched Reluctance Motor (LSRM), whereas unrolling a rotary machine with an axial flux path produces a transverse flux LSRM. The present AFDR-SRM therefore becomes a double-sided transverse flux linear SRM as shown in Figure 4.16. Following the conventional conversion rule, the originally stationary wound part becomes the mover, and the rotating part becomes the stationary track. Accordingly, the wound segmented stator of the rotary machine forms the active translator, while the two magnetically passive rotors become the upper and lower stationary iron tracks, positioned on either side of the translator.

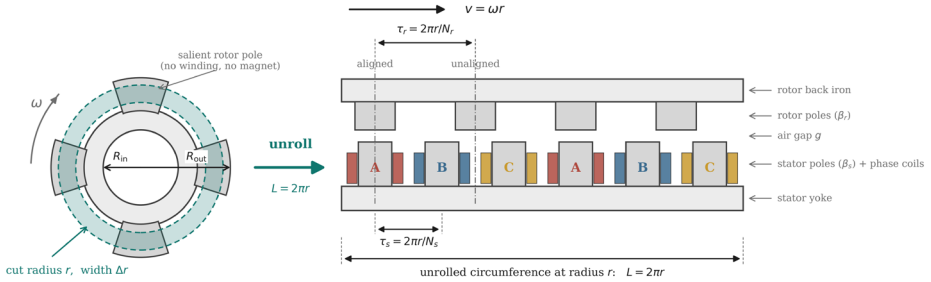


Figure 4.16. Transformation from rotary to linear motor

4.2.2 Mean Radius Geometric Mapping

An AFM has a circumferential pitch that varies with radius. A single exact rectangular development is therefore impossible over the complete annulus. The benchmark is linearized at the average active diameter, which preserves the average circumferential pole pitch and gives equal radial extent on either side of the representative surface. The developed length of the complete mean radius circumference is

$$L_{avg} = 2\pi r_{avg} = \pi D_{avg}, \tag{4.25}$$

where the stator tooth and rotor pole pitches of the 6/4 machine are

$$\begin{cases} \tau_s = \dfrac{L_{avg}}{N_s} = \dfrac{\pi D_{avg}}{N_s} \\ \tau_r = \dfrac{L_{avg}}{N_r} = \dfrac{\pi D_{avg}}{N_r}. \end{cases} \tag{4.26}$$

Stator and rotor pole arcs are converted into linear pole widths, while the remaining pitch becomes the corresponding slot width

$$\begin{cases} w_{st} = r_{avg}\beta_s \\ w_{rp} = r_{avg}\beta_r \\ w_{ss} = \tau_s - w_{st} \\ w_{ts} = \tau_r - w_{rp}. \end{cases} \tag{4.27}$$

Since the 2D FEM model gives force per unit out of plane depth, the model depth must be chosen to preserve the actual annular pole face area. Equating the annular sector area of a pole to its rectangular development at the mean radius shows that the effective depth is simply the radial thickness

$$l_{eff} = \frac{D_o - D_i}{2}. \tag{4.28}$$

4.2.3 Conversion from Rotational Speed to Linear Velocity

In the LSRM design procedure, the linear velocity is commonly expressed in terms of the speed of an equivalent rotary machine through the bore radius. For the present developed model, the inverse transformation is applied. The rotational speed is related to the mechanical angular velocity used in the sizing relation by Eq. (4.4). Differentiating the displacement relation with respect to time gives the translator velocity at the average diameter

$$v_m = \frac{\mathrm{d}x}{\mathrm{d}t} = \frac{\pi D_{avg} N_{rpm}}{60}, \tag{4.29}$$

where the rotary position step and its corresponding time step are converted according to

$$\Delta x = r_{avg}\Delta\theta, \quad \Delta t = \frac{\Delta\theta}{\omega_m} = \frac{\Delta x}{v_m}. \tag{4.30}$$

For a given mechanical conduction angle, the corresponding translator displacement and conduction time follow directly from these relationships.

4.2.4 FEM Simulation of Linear Flux SRM

The 2D linearized model is developed in JMAG Designer using the geometrical transformation and the motion conversion presented in the above section. As illustrated in Figure 4.17, the wound stator of the original AFDR-SRM is represented as a moving translator located between two stationary ferromagnetic tracks corresponding to the upper and lower tracks. The phase windings are arranged sequentially along the direction of motion, while the rotor poles are repeated according to the developed pole pitch. This configuration preserves the double-sided magnetic circuit and the relative movement between the excited mover poles and the passive stator poles.

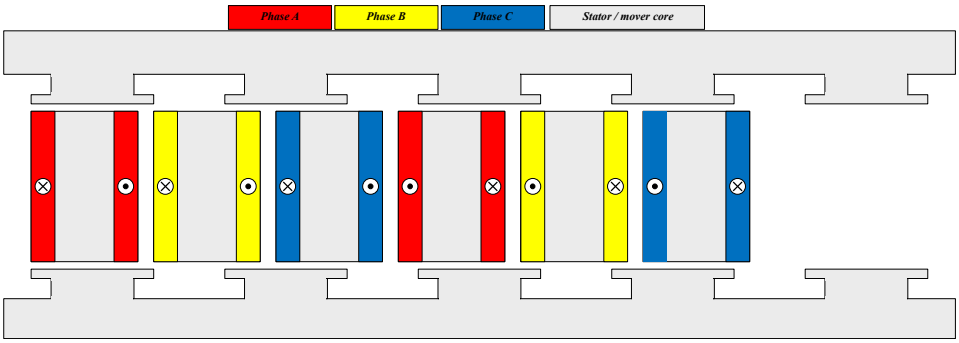


Figure 4.17. Cross-sectional view of the proposed double-sided LSRM

The magnetic field distribution obtained during phase excitation is presented in Figure 4.18. The flux produced by the excited winding crosses both airgaps and enters the upper and lower stationary tracks. The symmetrical flux distribution between the two sides confirms that the linearized model preserves the principal double-sided flux path of the original AFDR-SRM. The thrust force waveform was obtained using the same asymmetric half bridge converter employed in the 3D AFDR-SRM model. However, in the linearized model, the converter switching signals were defined as functions of translator displacement rather than rotor angle. The translator was moved at a constant linear velocity corresponding to the selected rotational operating speed, and the phases were energized sequentially according to their respective displacement intervals. This position dependent switching reproduced the phase excitation and commutation sequence of the original rotary machine and generated the thrust force waveform shown in Figure 4.19. When this thrust is converted to torque using the average diameter, it yields the same average value as the original rotary machine.

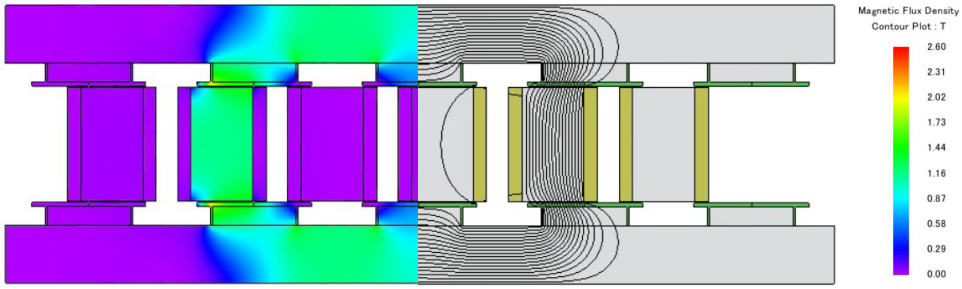


Figure 4.18. Magnetic flux density distribution and flux lines of LSRM

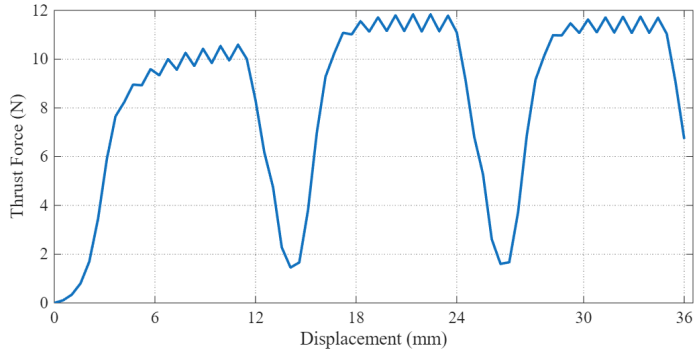


Figure 4.19. Thrust force waveform of LSRM for one pole pitch

4.3 NGNet-Based Topology Optimization

The equivalent linearized model enables NGNet based TO to be performed with considerably less computational time per iteration than applying the same optimization directly to the full 3D AFDR-SRM model.

4.3.1 Design Domain and Material Representation

Improving the thrust response requires the optimization to focus on the region that governs the variation of magnetic reluctance with translator position. Therefore, the airgap facing pole shoe region is selected as the design domain because its geometry

directly influences the inductance gradient and thrust characteristics. The selected design domain is presented in Figure 4.20. All other model parameters, including the windings, airgaps, magnetic materials, constant translator velocity, and displacement dependent switching signals, were kept unchanged.

The material distribution within one periodic pole pitch design domain was represented by overlapping Gaussian basis functions, as shown in Figure 4.21. Their weighting parameters determined whether each region was assigned magnetic material or air. Periodic and reflection symmetries reproduced the optimized geometry across the remaining pole pitches and the opposite magnetic track, thereby reducing the required number of design variables and FEM evaluations. The NGNet optimization parameters used in the topology search are summarized in Table 4.2.

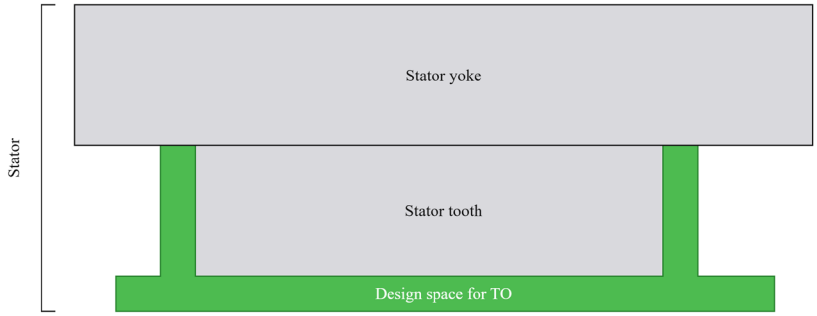


Figure 4.20. Design domain of LSRM TO

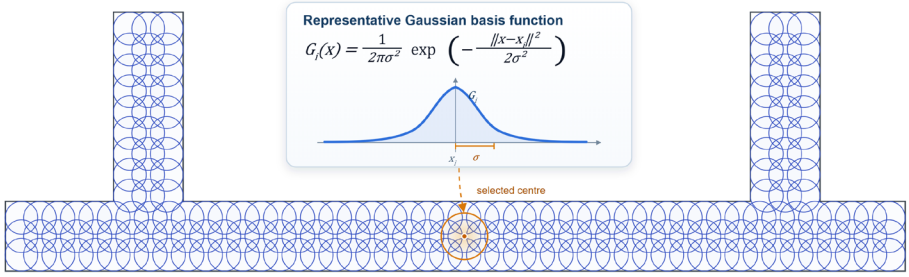


Figure 4.21. Gaussian basis function distribution on design domain

Table 4.2. NGNet optimization parameters of LSRM

Parameter	Value
Number of generations	25
Population size	133
Number of children	133
Number of Gaussian basis functions	132
Gaussian basis width	1.2 mm
Gaussian basis height	1.2 mm
Optimization method	Genetic algorithm

4.3.2 Optimization Objective and Symmetry Reduction

The TO was formulated to improve the thrust characteristics of the LSRM over the complete active displacement interval. Maximizing the force at only one translator position could produce a locally high peak without improving the useful output over the remaining stroke. Therefore, each candidate topology was evaluated at several displacement points, and its performance was determined from the resulting thrust force waveform. To maximize the average thrust and minimize the thrust ripples expressed as

$$\overline{F}_x(\mathrm{w}) = \frac{1}{N_p}\sum_{k=1}^{N_p} F_x\,(x_k, \mathrm{w}), \tag{4.31}$$

$$F_{\mathrm{ripple}}(\mathrm{w}) = \frac{F_{x,\max}(\mathrm{w}) - F_{x,\min}(\mathrm{w})}{\overline{F}_x(\mathrm{w})} \times 100\%, \tag{4.32}$$

where the optimization problem can be stated as

$$\max.\ \overline{F}_x(\mathrm{w}), \qquad \min.\ F_{\mathrm{ripple}}(\mathrm{w}). \tag{4.33}$$

These objectives introduce a balance between electromagnetic output and force smoothness. The average thrust objective favours topologies that maintain an effective magnetic path throughout the active stroke, whereas the ripple objective prevents the optimization from producing a narrow force peak at a particular displacement. Thus, preference is given to material distributions that generate a high and comparatively uniform thrust over the useful force producing region.

For every case generated by the genetic algorithm, the NGNet weighting parameters were converted into the corresponding iron or air distribution and evaluated by FEM. The calculated objective values were then used to rank the candidate solutions and generate the subsequent population. This procedure is continued using the optimization settings described in chapter 3, until the final pole shoe topology was obtained.

4.3.3 Optimized Linear Topology and Thrust Performance

The TO produces an asymmetrical pole shoe structure in which the additional iron is retained only on the left side of the stator pole, as shown in Figure 4.22. This result is consistent with the direction of translator motion. As the translator approaches the aligned position, the phase excitation is removed. Therefore, the iron on the right side of the pole makes only a limited contribution to useful thrust production. The optimization identifies this weakly utilized region and removes it from the design domain while retaining the material required on the left side to establish an effective magnetic path during excitation.

The magnetic flux density distribution and field lines presented in Figure 4.23 demonstrate how the flux passes through the optimized pole shoe and crosses the airgap towards the translator pole. Despite the removal of material from one side of the pole, the remaining structure provides a continuous low reluctance path for the main flux. The flux density distribution also indicates that the optimized pole shoe does not introduce magnetic saturation.



Figure 4.22. Optimized topology obtained from TO LSRM

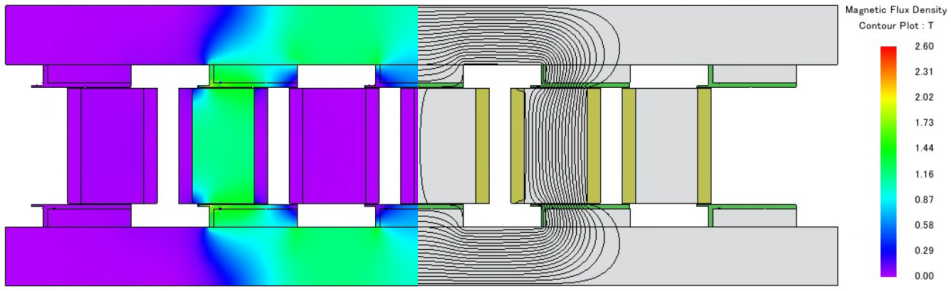


Figure 4.23. Magnetic flux density distribution and flux lines of optimized LSRM

The most suitable candidate solutions obtained from the TO process are compared in Figure 4.24 in terms of their average thrust and thrust force ripple. The distribution of these solutions demonstrates the competing relationship between the two objectives. Some cases generate a higher average thrust but also exhibit considerably greater force pulsations. Consequently, selecting the topology solely on the basis of maximum thrust would not provide the desired improvement in force smoothness.

The case highlighted in orange has the lowest thrust ripple among the presented solutions, while maintaining an average thrust approximately equal to that of the initial design. It was therefore selected as the final topology. This solution provides a more appropriate compromise than the higher thrust cases because it improves the uniformity of the force waveform without reducing the required mean electromagnetic output. The thrust force waveforms of the initial and optimized designs are compared in Figure 4.25. The optimized topology maintains nearly the same average thrust as the initial LSRM while reducing the thrust ripple by approximately 11.2%. After TO process completed, the selected pole profile is mapped onto the rotary AFDR-SRM and repeated for all rotor poles.

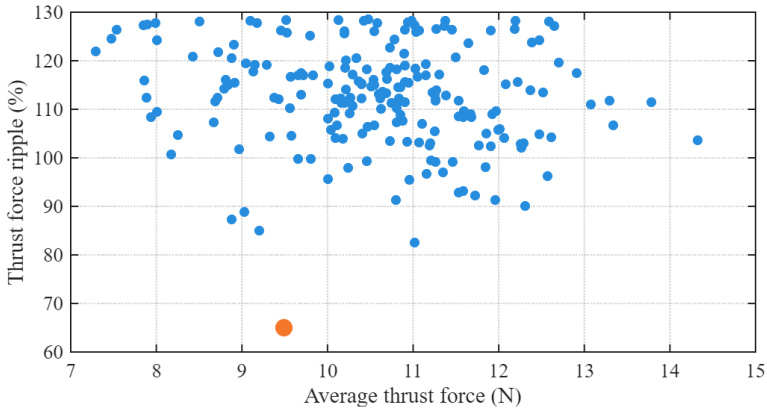


Figure 4.24. Comparison of the best performing case topologies in terms of average thrust and thrust force ripple

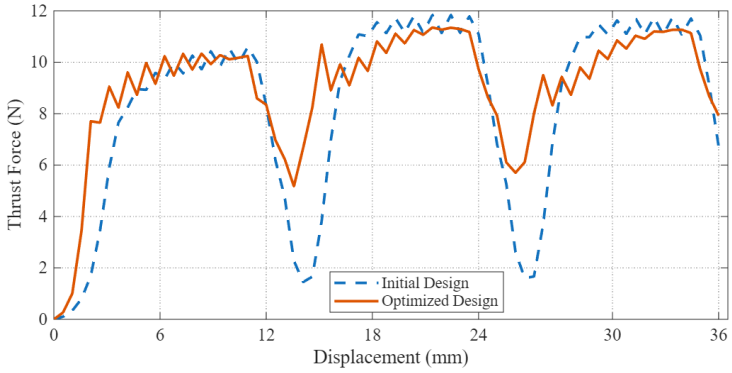


Figure 4.25. Comparison of thrust-force waveforms of LSRM designs

4.4 Analytical TO of Back Iron of AFDR-SRM

After completing the NGNet based pole-shoe optimization, the rotor back iron is considered separately for material reduction. The equivalent magnetic model is established to derive the minimum required back iron width and obtain the analytically reduced rotor geometry.

4.4.1 2D Equivalent Rotor Model

The physics guided analytical procedure developed for the PM rotor in Chapter 3 is extended to the AFDR-SRM. The same geometrical flux continuity principle is retained, while the PM excitation is replaced by the magnetomotive force generated by the excited stator coil. The derivation considers one rotor side and one rotor pole pitch. Therefore, the airgap flux density represents the local value in the selected rotor side airgap, and no additional factor of one half is introduced for the opposite rotor. The geometrical representation used for the analytical rotor back-iron optimization is shown in Figure 4.26.

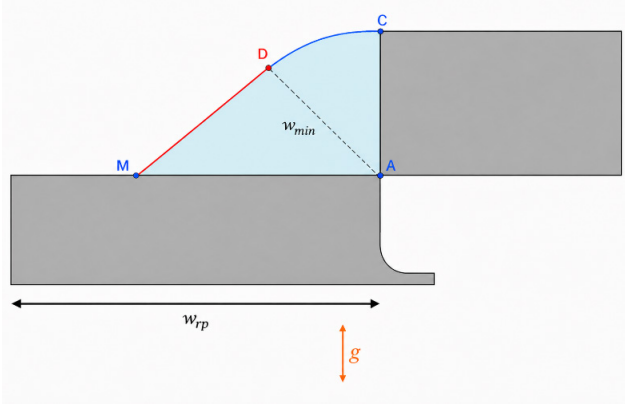


Figure 4.26. Geometrical representation for analytical TO of the AFDR-SRM rotor back iron

At the maximum current aligned condition, the flux entering one rotor pole on the selected rotor side is approximated by the pole face average airgap flux density acting over the pole width and radial depth.

$$\Phi_{\text{in}} = B_g w_{\text{rp}} l_{eff}. \tag{4.34}$$

For the symmetric pole considered in the analytical construction, this flux divides equally into the left- and right-hand circumferential return paths of the same rotor back iron. Point M in Figure 4.26 is the pole centreline and point A is the pole edge. Hence MA is the half of the width rotor pole. The flux passes from MA towards the minimum section AD is consequently

$$\Phi_{b,R} = \frac{\Phi_{\text{in}}}{2} = \frac{B_g w_{\text{rp}} l_{eff}}{2}. \tag{4.35}$$

4.4.2 Minimum Rotor Back Iron Width

Let AD = w_{min} be the shortest flux carrying section of one back iron branch. At the limiting design condition, the flux density at AD is equal to the permissible back iron value. Equating the flux entering one half of the pole to the maximum flux that can be transported through AD gives

$$B_g \frac{w_{\text{rp}}}{2} l_{eff} = B_s k_i w_{\text{min}} l_{eff}. \tag{4.36}$$

After cancellation of the radial depth, the strict analytical minimum becomes

$$w_{\text{min}} = \frac{B_{g,\text{max}}}{B_s k_i} \cdot \frac{w_{\text{rp}}}{2}. \tag{4.37}$$

In the PM machine, the airgap source was expressed using remanence and magnet thickness. In the SRM, the source is the effective coil magnetomotive force. Although only one rotor side is modelled, a complete magnetic loop on that side crosses the airgap twice. First from the excited stator pole to the rotor and again from the rotor return pole to the return stator pole. The magnetic circuit equation is therefore

$$\mathcal{F}_{\text{exc}} = N_c I = 2\frac{B_g}{\mu_0} g_{\text{eff}} + \sum_j H_j(B_j) l_j. \tag{4.38}$$

The term $g_{eff} = k_c g$ represents the effective length of one physical airgap crossing, and the summation represents the nonlinear Magnetomotive Force (MMF) drop in the stator teeth, rotor poles, and rotor back iron.

For preliminary sizing, the iron MMF drop may be neglected because the two airgaps dominate the reluctance before strong saturation occurs. This gives

$$B_g \approx \frac{\mu_0 N_c I}{2 g_{\text{eff}}}. \tag{4.39}$$

Substitution of Eq. (4.39) into Eq. (4.37) yields the minimum width

$$w_{\text{min}} \approx \frac{\mu_0 N_c I w_{\text{rp}}}{4 g_{\text{eff}} B_s k_i}. \tag{4.40}$$

4.4.3 Analytically Reduced Rotor Geometry

Unlike the PM machine considered in Chapter 3, the AFDR-SRM generates its airgap field through the combined magnetomotive force of the two series connected phase coils. The analytically optimized rotor shown in Figure 4.27 preserves the essential flux carrying paths while removing magnetically underutilized material from the back iron. The resulting reduction in rotor volume does not introduce magnetic saturation within the retained rotor structure. Figure 4.28 compares the torque waveforms of the initial design and the design obtained after NGNet based TO of the rotor pole shoe. The smoother torque waveform is attributed to the NGNet optimization, which modifies the pole shoe geometry and consequently reshapes the rotor position dependent inductance gradient. The optimization reduces torque pulsations while maintaining approximately the same average electromagnetic torque. The analytical back iron TO serves a different purpose. It is applied after the pole shoe optimization to remove magnetically underutilized material from the rotor back iron. Therefore, the torque ripple improvement is attributed to the NGNet method, whereas the analytical method is responsible for the rotor volume and mass reduction. The electromagnetic and active mass results are summarized in Table 4.3.

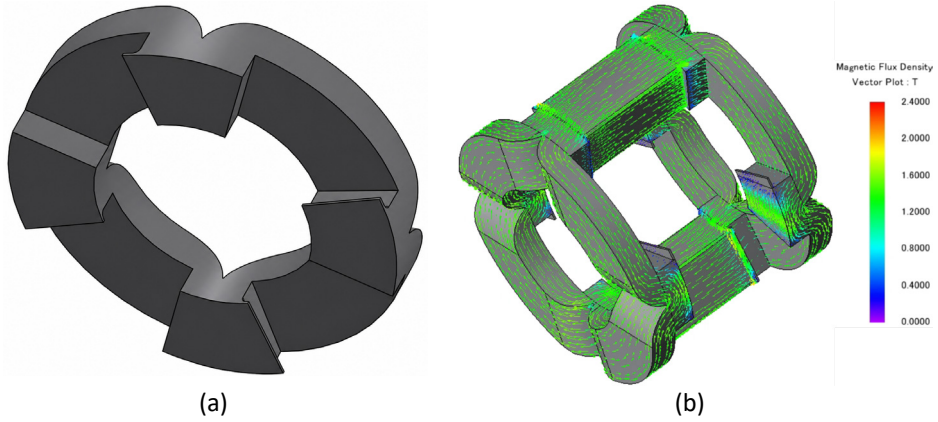


Figure 4.27. Rotor geometry after physics guided analytical back iron optimization (a) Optimized rotor geometry (b) Flux flow in the optimized AFDR-SRM

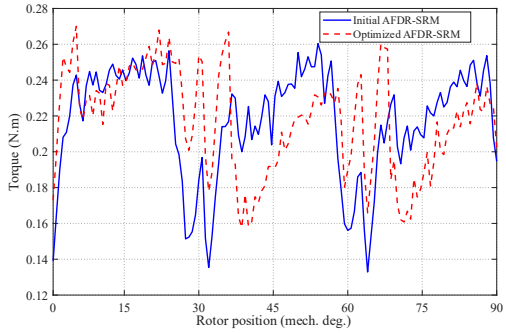


Figure 4.28. Comparison of initial and optimized torque waveform of AFDR-SRM

Table 4.3. Comparison of initial and optimized AFDR-SRM designs

Parameter	Initial design	Optimized design	Change	Associated method
Average torque (N·m)	0.218	0.216	-0.92%	NGNet pole shoe TO
Torque ripple (%)	58.48	51.93	-11.20%	NGNet pole shoe TO
Volume of one rotor (mm^3)	10,255.24	9,306.34	-9.25%	Analytical back iron TO
Mass of one rotor (g)	77.940	70.728	-9.25%	Analytical back iron TO
Total active material mass (g)	567.455	553.031	-2.54%	Analytical back iron TO
Torque density (N·m/kg)	0.3842	0.3906	+1.67%	Combined result

The analytical method produces a considerable reduction at the rotor level, its influence on the complete active material mass is comparatively small because the stator and winding masses remain unchanged. This limited reduction is attributed to the relatively short radial pole depth of the AFDR-SRM, which restricts the volume of back iron available for removal. In contrast, the optimized back iron profile of the outer rotor BLDC machine in Chapter 3 extends over its full axial stack length, resulting in a larger volume reduction.

4.5 Additive Manufacturing of the AFDR-SRM

The manufacturing route for the AFDR-SRM was developed concurrently with the electromagnetic design because the segmented stator, 3D flux path, and compact double rotor arrangement cannot be produced conveniently by conventional punching and stacking alone. LPBF was therefore used to manufacture the magnetic components from Fe-Si alloy. The procedure described in this section corresponds to the experimentally demonstrated AFDR-SRM prototype and defines the manufacturing constraints that must subsequently be applied to the TO rotor.

4.5.1 Manufacturing Oriented Core Design

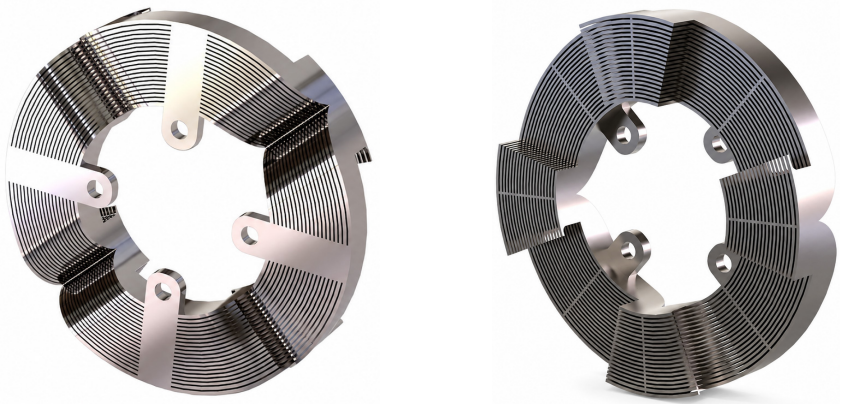
A fully solid AM magnetic core permits large electrically continuous paths and therefore substantial eddy-current loss. Before printing, each stator tooth was therefore divided into parallel ferromagnetic layers 0.4 mm thick, separated by 0.25 mm airgaps. The layer orientation preserves the principal useful flux path while interrupting the dominant circulating current loops. A continuous 0.4 mm wide solid connecting rib bridges the airgaps and joins the separated ferromagnetic layers, as shown in Figure 4.29. This rib consolidates the laminated stator tooth into a single integral component that can be printed, handled, and assembled as one piece.

The same electrical segmentation principle was applied conceptually to the TO rotor. Figure 4.30 retains the rotor geometry and shows the curved parallel layers following the optimized pole shoe and back iron profile. The four solid hub bridges provide the shaft connection regions and mechanically link the laminated pole sectors. The exploded view

in Figure 4.31 shows the assembly arrangement of the AFDR-SRM. The wound stator teeth are positioned at equal angular intervals using spacers and secured between two Printed Circuit Board (PCB) sheets, forming a single stator assembly. The bearings support the central shaft, while the two rotors are connected to it through rotor supports. Overall, this configuration enables the segmented stator and optimized rotors to be manufactured as structurally connected components while reducing the continuous conductive paths responsible for eddy currents.



Figure 4.29. CAD model of parallel laminated stator tooth



(a) (b)

Figure 4.30. CAD model of laminated TO rotor (a) rear view (b) front view

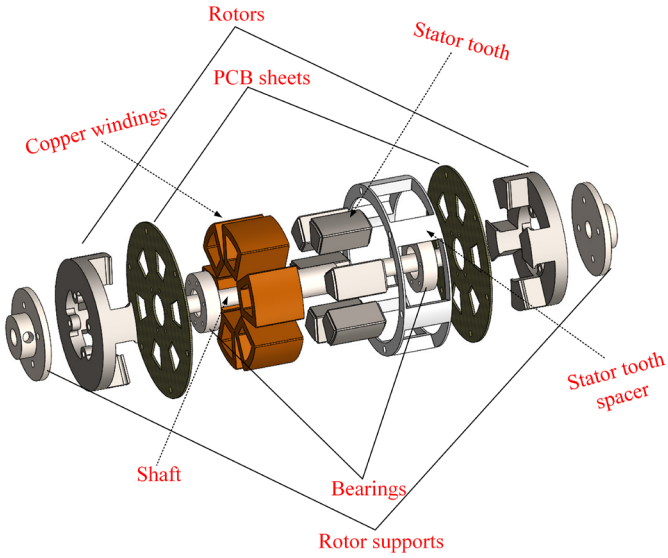


Figure 4.31. Exploded view of AFDR-SRM

4.5.2 LPBF Printing Process

The AFDR-SRM stator and rotor cores were manufactured by LPBF using pre-alloyed, gas-atomized Fe-Si powder supplied by Sandvik Group. Before fabrication, the powder chemistry was verified using energy-dispersive X-ray spectroscopy and spark atomic emission spectroscopy. The predominantly spherical particles ranged from 29 to 58 µm, with a median diameter of 38 µm. Printing was performed on an SLM Solutions Realizer SLM-280 equipped with a 350 W infrared laser.

For the comparatively large magnetic components, the scan strategy was changed from stripes to a chessboard pattern to improve part completion and density uniformity. Re-melting was disabled because it increased surface roughness, impaired powder flow, and promoted uneven layer growth. The process parameters used for the prototype are summarized in Table 4.4. Each four-pole rotor required approximately 6 h of build time, while the six stator segments required approximately 10 h in total. Figure 4.32. LPBF fabrication of the AFDR-SRM magnetic components in the SLM-280 build chamber shows the LPBF process during fabrication of the magnetic parts. The visible melt pool region illustrates the localized layer-by-layer consolidation used to form the thin magnetic features.

Table 4.4. LPBF parameters used for the AFDR-SRM magnetic components

Parameter	Value
Layer thickness	50 µm
Hatch distance	120 µm
Laser power	350 W
Scanning velocity	0.75 m/s
Volumetric energy density	83 J/mm³

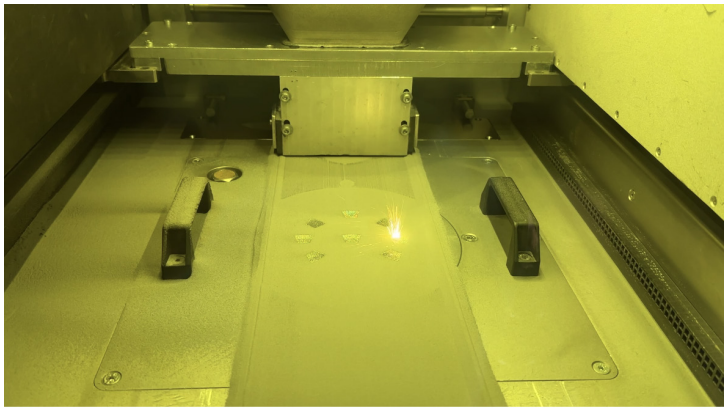


Figure 4.32. LPBF fabrication of the AFDR-SRM magnetic components in the SLM-280 build chamber

4.5.3 Heat Treatment and Component Preparation

After printing, the magnetic parts were heat treated at 1200 °C. The temperature was increased at 5 °C/min, held at the target temperature for one hour, and followed by furnace cooling with an initial rate of approximately 50 °C/min that decreased progressively. Vacuum was maintained between 0.04 and 0.4 mbar throughout the treatment. This post-process relieves residual stress and restores the soft-magnetic response of the printed Fe-Si material.

The manufactured components are shown in Figure 4.33. The exposed parallel layers are visible in the printed tooth, while the wound component shows how the concentrated coil is located around the segmented core. The outer and inner lips on the stator segment control the winding position and connect the PCB sheet to circumferentially assemble the six stator segments between the two rotors.

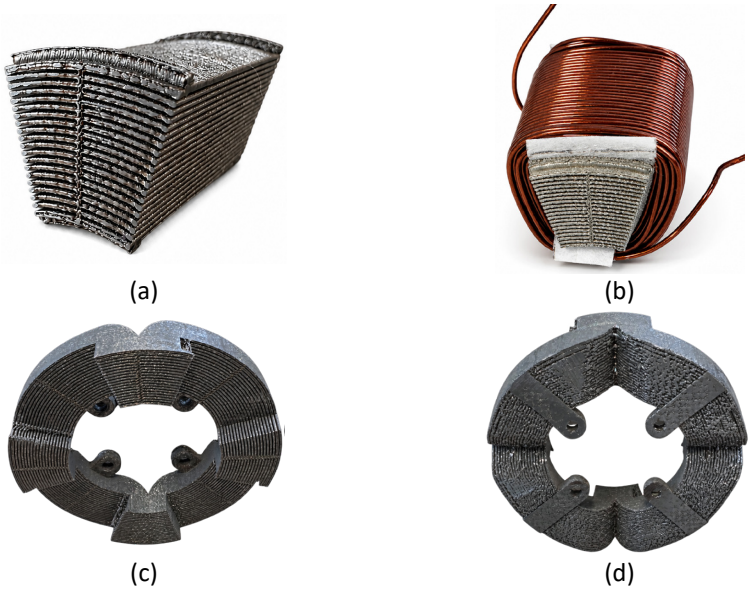


Figure 4.33. AM AFDR-SRM parts (a) stator tooth (b) stator winding (c) rotor front (d) rotor back

4.6 Experimental Setup and Test Results

Experimental testing was performed using a dedicated test bench configured for dynamic operation of the manufactured prototype. The complete test arrangement is presented in Figure 4.34. The AFDR-SRM was driven by two TI BOOSTXL-DRV8305EVM inverter modules controlled using a TI LAUNCHXL-F28379D development board. The controller generated the required phase switching signals based on the rotor position and speed feedback. A rotary encoder was coupled to the left-hand side of the AFDR-SRM shaft to provide this feedback for electronic commutation and closed loop speed control.

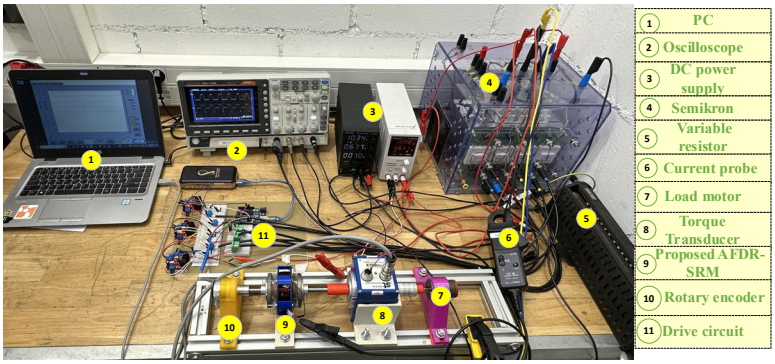


Figure 4.34. Experimental setup for the dynamic testing of the proposed AFDR-SRM

4.6.1 Dynamic Operation Under Load

Dynamic testing under an adjustable mechanical load was performed to evaluate the prototype's speed tracking response and phase commutation. Figure 4.35 presents the reference and measured rotor speeds together with the three-phase currents. The measured speed closely follows the reference command, while the phase current waveforms indicate the required sequential commutation. Small deviations during acceleration and deceleration are attributed to the combined inertia of the AFDR-SRM and load machine, together with the discrete phase commutation process.

The transducer measured the transmitted shaft torque during operation. The BLDC machine was operated as a generator, and its three-phase output was connected to a

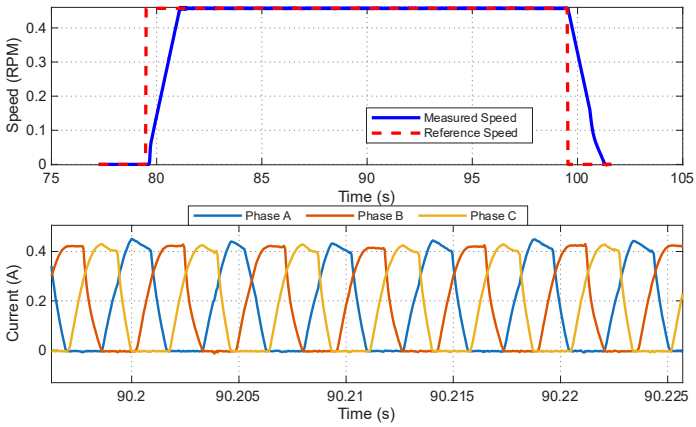


Figure 4.35. Reference and measured speeds together with the measured phase currents during dynamic operation

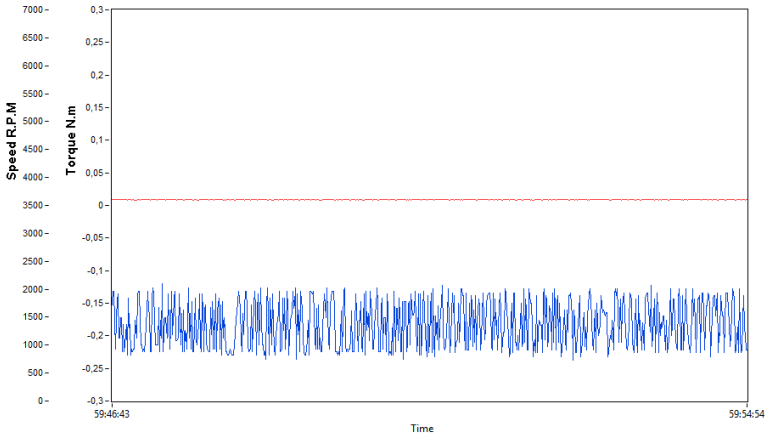


Figure 4.36. Measured speed and shaft torque of the AFDR-SRM under load

Semikron rectifier. The rectifier converted the generated three-phase voltage into DC, which was then supplied to a variable resistive load. Consequently, the mechanical loading applied to the AFDR-SRM could be adjusted by varying the resistance.

The prototype was tested at a maximum DC-link voltage of 45 V because the DRV8305-based inverter has an operating voltage limit of approximately 48 V. At this voltage, the AFDR-SRM achieved a maximum speed of approximately 3500 r/min. The experimentally measured average torque in Figure 4.36 was 8.7% lower than that predicted by the FEM model. This discrepancy can be attributed mainly to mechanical imperfections in the assembled prototype, variations in the manufactured airgaps from the specified value of 0.25 mm, and differences between the actual magnetic material properties and those assumed in the FEM analysis. Nevertheless, the close agreement between the FEM and experimental results validates the proposed motor design and confirms its operation under dynamic loading.

4.7 Summary

This chapter presented the design, optimization, AM process, and experimental validation of the proposed AFDR-SRM. The NGNet based pole shoe optimization reduced torque ripple by 11.2% while maintaining approximately the same average torque. The analytical back iron method reduced the rotor volume by 9.25%, resulting in a 1.67% increase in torque density. The optimized magnetic components were manufactured and assembled into a complete prototype, for which the measured average torque was 8.7% lower than the FEM prediction, primarily because of manufacturing tolerances, variations in material properties and airgap dimensions, and mechanical misalignment. The results confirm the feasibility and successful operation of the proposed motor topology.

5 Conclusions and Future Work

This thesis investigated the integration of TO and AM for electrical machines, addressing the research gaps identified in Chapter 1. The limited application of TO to reluctance machines, the computational cost of 3D TO for axial flux topologies, the shortage of experimentally validated AM built magnetic components, and the need for computationally efficient TO methods. Two machine platforms were investigated across Chapters 3 and 4. An outer rotor PM BLDC motor for electric scooter propulsion, and AFDR-SRM for high-speed propulsion. This chapter summarizes the main findings of the thesis, revert to the research hypotheses formulated in Chapter 1, and outlines directions for future research.

5.1 Conclusion of the Thesis

Chapter 3 applied three TO methods, NGNet with a genetic algorithm, density based SIMP with adjoint sensitivity analysis, and a newly derived closed form analytical method, to the rotor back iron of an outer rotor BLDC motor. The NGNet method reduced the back iron material by 25.67% and increased the torque density by 7.84%. The density based SIMP and analytical methods achieved greater material reductions of 39% and 39.29%, resulting in torque density increases of approximately 14% and 14.36%, respectively. In all three cases, the airgap flux density, back EMF, and average torque remained essentially unchanged. The close agreement between the density based and analytical results indicated that approximately 39% of the original back iron was magnetically redundant for the specified operating condition, and the analytical method reached this result through a single field evaluation rather than the many FE iterations required by SIMP or the population-based search required by NGNet. The optimized geometry was adapted for manufacturing, fabricated from Fe-3.7wt%Si powder by LPBF, assembled into a complete motor, and tested experimentally. The measured and simulated torque agreed within 5.09%, confirming that the AM built, TO rotor performs as predicted by simulation.

Chapter 4 presented the analytical design and 3D FEM validation of a 6/4 AFDR-SRM with a segmented, yokeless stator. The machine was transformed into an equivalent 2D linear model, which reduced the simulation time from hours to minutes and enabled NGNet based TO of the rotor pole shoe. The optimized topology reduced torque ripple by 11.2% while maintaining approximately the same average torque. The analytical back iron reduction method developed in Chapter 3 was extended to the electrically excited stator and reduced the rotor volume and mass by 9.25%, increasing torque density by 1.67% without introducing saturation. The stator teeth and rotor poles were divided into parallel laminations to limit eddy current losses, joined by a lip feature that mechanically assembles the segmented stator into a single ring without additional fixtures or adhesives. The manufactured prototype, comprising six laminated stator segments and two four-pole rotors printed from Fe-3.7wt%Si powder, was tested under dynamic load. The measured and simulated average torque agreed within 8.7%, confirming the feasibility of the proposed design and manufacturing approach.

5.2 Future Work

The methods and results developed in this thesis point to several directions for further research.

- Develop a full 3D TO framework for axial flux machines to account for 3D flux paths. The equivalent 2D model could be retained for initial design screening, while machine-learning-assisted surrogate models could reduce the number of computationally expensive 3D FE evaluations.
- Extending the optimization objective beyond electromagnetic performance to include thermal and mechanical criteria, such as stress in the laminated rotor and heat dissipation from the segmented stator, in a coupled multiphysics TO formulation.
- Formulating a multi-material TO that simultaneously distributes soft-magnetic material, PM and non-magnetic material within the same design domain, rather than adding mechanical bridges, magnet pockets, and lip joints as manual post-processing steps.

List of Figures

Figure 2.1. Classification of electrical machine design optimization techniques 20
Figure 2.2. Rotor geometry of one pole of SynRM [2] 20
Figure 2.3. Example from the literature of shape optimization of SynRM [3] 21
Figure 2.4. Rotor TO of an IPM machine using the ON/OFF method [11] 22
Figure 2.5. Level-set-based rotor TO of an SRM (a) initial model and design domain (b) optimized geometry with the FE mesh [13] 23
Figure 2.6. Magneto-structural combined dimensional and TO result (a) electrical steel and (b) PM and electrical steel normalized density distributions [18] 24
Figure 3.1. Non-uniform flux distribution in the rotor back iron, indicating inefficient material utilization (a) SMPM motor (b) IPM motor 30
Figure 3.2. 2D-cross sectional view of three phase benchmark motor 31
Figure 3.3. Airgap flux density and flux linkage of benchmark motor 32
Figure 3.4. Three phase back EMF and flux contour of benchmark motor 33
Figure 3.5. Current and torque waveform of benchmark motor 33
Figure 3.6. Gaussian distribution over design domain 35
Figure 3.7. Relation between target flux and iron material in the design region 36
Figure 3.8. TO back iron of the one pole pitch rotor 36
Figure 3.9. SIMP interpolation with different values of penalization 37
Figure 3.10. TO design domain for the density method 38
Figure 3.11. Flux maximization objective 41
Figure 3.12. Flux maximization objective with volume penalization 41
Figure 3.13. Optimal design including the density filter and projection 42
Figure 3.14. Objective function response with respect to iteration numbers 42
Figure 3.15. Flux density distribution (a) Initial design (b) Optimized design 42
Figure 3.16. Geometrical representation of analytical topology optimized back iron for quasi-static PM machine 43
Figure 3.17. Analytical TO with new contour of A'D'M to maintain flux continuity 44
Figure 3.18. (a) TO back iron using analytical approach (b) Contour of flux density and flux lines in analytical TO back iron 45
Figure 3.19. Airgap flux density comparison of initial and analytical TO 46
Figure 3.20. Back EMF comparison of initial and analytical TO 46
Figure 3.21. Torque waveform comparison of initial and analytical TO 46
Figure 3.22. Different design configuration with straight magnets (a) With air region behind magnets (b) Iron filled behind magnets 48
Figure 3.23. Optimized back iron having mechanically feasible (a) 2D cross sectional back iron (b) 3D CAD model of back iron 48
Figure 3.24. Comparison of torque on different magnets shape configuration 49
Figure 3.25. AM based rotor prototype (a) Initial rotor (b) Optimized rotor 50
Figure 3.26. Experimental three phase back EMF 50
Figure 3.27. Experimental test setup for outer rotor BLDC 51
Figure 3.28. Experimental results (a) Three phase motor currents (b) Torque and speed waveform 52
Figure 4.1. Proposed AFDR-SRM 54
Figure 4.2. Inductance profile of SRM for one phase excitation 54
Figure 4.3. Representation of geometrical parameters (a) Stator and rotor parameters (b) Coil parameters 56

Figure 4.4. Design flow of AFDR-SRM 59
Figure 4.5. Magnetic flux distribution (a) Unaligned position (b) Aligned position 59
Figure 4.6. Phase flux linkage at different current levels 60
Figure 4.7. Inductance characteristic at different rotor position 60
Figure 4.8. Static flux linkage and static torque at different current levels 61
Figure 4.9. Effect on average torque due to rotor pole length 61
Figure 4.10. Steady state current and torque waveform under SPC 62
Figure 4.11. Steady state current, voltage and torque waveform under CCC 63
Figure 4.12. Torque speed and power characteristics curve 63
Figure 4.13. Efficiency map of AFDR-SRM 64
Figure 4.14. Iron losses at different operating regions of AFDR-SRM 64
Figure 4.15. Copper losses at different operating regions of AFDR-SRM 64
Figure 4.16. Transformation from rotary to linear motor 65
Figure 4.17. Cross-sectional view of the proposed double-sided LSRM 66
Figure 4.18. Magnetic flux density distribution and flux lines of LSRM 67
Figure 4.19. Thrust force waveform of LSRM for one pole pitch 67
Figure 4.20. Design domain of LSRM TO 68
Figure 4.21. Gaussian basis function distribution on design domain 68
Figure 4.22. Optimized topology obtained from TO LSRM 70
Figure 4.23. Magnetic flux density distribution and flux lines of optimized LSRM 70
Figure 4.24. Comparison of the best performing case topologies in terms of average thrust and thrust force ripple 71
Figure 4.25. Comparison of thrust-force waveforms of LSRM designs 71
Figure 4.26. Geometrical representation for analytical TO of the AFDR-SRM rotor back iron 72
Figure 4.27. Rotor geometry after physics guided analytical back iron optimization (a) Optimized rotor geometry (b) Flux flow in the optimized AFDR-SRM 73
Figure 4.28. Comparison of initial and optimized torque waveform of AFDR-SRM 73
Figure 4.29. CAD model of parallel laminated stator tooth 75
Figure 4.30. CAD model of laminated TO rotor (a) rear view (b) front view 75
Figure 4.31. Exploded view of AFDR-SRM 76
Figure 4.32. LPBF fabrication of the AFDR-SRM magnetic components in the SLM-280 build chamber 77
Figure 4.33. AM AFDR-SRM parts (a) stator tooth (b) stator winding (c) rotor front (d) rotor back 77
Figure 4.34. Experimental setup for the dynamic testing of the proposed AFDR-SRM 78
Figure 4.35. Reference and measured speeds together with the measured phase currents during dynamic operation 78
Figure 4.36. Measured speed and shaft torque of the AFDR-SRM under load 79

List of Tables

Table 2.1. Summary of TO studies for PM machines 25
Table 2.2. Summary of TO studies for SRM..... 26
Table 2.3. Summary of AM rotor and stator prototypes in electrical machines..... 28
Table 3.1. Main parameters of the benchmark BLDC motor 32
Table 3.2. NGNet optimization settings 35
Table 3.3. Quantitative and methodological comparison of the three back iron material reduction techniques 47
Table 3.4. Summary of printing parameters 49
Table 4.1. Design and Electrical Parameters of AFDR-SRM..... 57
Table 4.2. NGNet optimization parameters of LSRM 68
Table 4.3. Comparison of initial and optimized AFDR-SRM designs 74
Table 4.4. LPBF parameters used for the AFDR-SRM magnetic components 76

References

[1] IEA 4E Electric Motor Systems Platform (EMSA), “Electric Motor Systems: Why Are They Important?,” Dec. 2025.

[2] G. Bramerdorfer, J. A. Tapia, J. J. Pyrhonen, and A. Cavagnino, “Modern Electrical Machine Design Optimization: Techniques, Trends, and Best Practices,” *IEEE Transactions on Industrial Electronics*, vol. 65, no. 10, 2018, doi: 10.1109/TIE.2018.2801805.

[3] B. Ban, S. Stipetic, and T. Jercic, “Minimum set of rotor parameters for synchronous reluctance machine and improved optimization convergence via forced rotor barrier feasibility,” *Energies (Basel).*, vol. 14, no. 10, 2021, doi: 10.3390/en14102744.

[4] M. U. Naseer, A. Kallaste, B. Asad, T. Vaimann, and A. Rassõlkin, “A review on additive manufacturing possibilities for electrical machines,” 2021. doi: 10.3390/en14071940.

[5] F. Wu and A. M. El-Refaie, “Toward Additively Manufactured Electrical Machines: Opportunities and Challenges,” *IEEE Trans. Ind. Appl.*, vol. 56, no. 2, 2020, doi: 10.1109/TIA.2019.2960250.

[6] V. Chaudhary *et al.*, “Additive manufacturing of functionally graded Co–Fe and Ni–Fe magnetic materials,” *J. Alloys Compd.*, vol. 823, 2020, doi: 10.1016/ j.jallcom.2020.153817.

[7] M. Sarap, A. Kallaste, P. S. Ghahfarokhi, H. Tiismus, and T. Vaimann, “Utilization of Additive Manufacturing in the Thermal Design of Electrical Machines: A Review,” *Machines*, vol. 10, no. 4, 2022, doi: 10.3390/machines10040251.

[8] S. Hussain, A. Kallaste, and T. Vaimann, “Recent Trends in Additive Manufacturing and Topology Optimization of Reluctance Machines,” 2023. doi: 10.3390/en16093840.

[9] M. R. Mahmoud, M. N. Ibrahim, and P. Sergeant, “Topology Optimization for Enhancing Electric Machine Performance: A Review,” in *2024 International Conference on Electrical Machines, ICEM 2024*, 2024. doi: 10.1109/ICEM60801. 2024.10700505.

[10] F. N. U. Nishanth, J. Van Verdeghem, and E. L. Severson, “A Review of Axial Flux Permanent Magnet Machine Technology,” *IEEE Trans. Ind. Appl.*, vol. 59, no. 4, 2023, doi: 10.1109/TIA.2023.3258933.

[11] R. Wrobel and B. Mecrow, “A Comprehensive Review of Additive Manufacturing in Construction of Electrical Machines,” 2020. doi: 10.1109/TEC.2020.2964942.

[12] A. Shoeb and S. Xue, “Topology Optimization of Axial Flux Machines with a Simplified 2D Finite Element Approximation,” in *2023 IEEE Energy Conversion Congress and Exposition, ECCE 2023*, 2023. doi: 10.1109/ECCE53617. 2023.10362222.

[13] N. Taran, V. Rallabandi, D. M. Ionel, G. Heins, D. Patterson, and P. Zhou, “Design optimization of electric machines with 3D FEA and a new hybrid DOE-DE numerical algorithm,” in *2019 IEEE International Electric Machines and Drives Conference, IEMDC 2019*, 2019. doi: 10.1109/IEMDC.2019.8785088.

[14] Y. Duan and D. M. Ionel, “A review of recent developments in electrical machine design optimization methods with a permanent-magnet synchronous motor benchmark study,” 2013. doi: 10.1109/TIA.2013.2252597.

[15] E. Kuci, F. Henrotte, P. Duysinx, and C. Geuzaine, “Combination of topology optimization and Lie derivative-based shape optimization for electro-mechanical design,” *Structural and Multidisciplinary Optimization*, vol. 59, no. 5, 2019, doi: 10.1007/s00158-018-2157-2.

[16] A. Credo, G. Fabri, M. Villani, and M. Popescu, “Adopting the Topology Optimization in the Design of High-Speed Synchronous Reluctance Motors for Electric Vehicles,” *IEEE Trans. Ind. Appl.*, vol. 56, no. 5, 2020, doi: 10.1109/TIA.2020.3007366.

[17] F. Guo and I. P. Brown, “Simultaneous Magnetic and Structural Topology Optimization of Synchronous Reluctance Machine Rotors,” *IEEE Trans. Magn.*, vol. 56, no. 10, 2020, doi: 10.1109/TMAG.2020.3014289.

[18] E. Kuci, M. Jansen, and O. Coulaud, “Level set topology optimization of synchronous reluctance machines using a body-fitted mesh representation,” *Structural and Multidisciplinary Optimization*, vol. 64, no. 6, 2021, doi: 10.1007/s00158-021-03049-0.

[19] O. Brun *et al.*, “Mechanical Free Shape Optimization of Synchronous Reluctance Machines,” 2023. [Online]. Available: https://hal.science/hal-04214785v1

[20] M. P. Bendsøe and N. Kikuchi, “Generating optimal topologies in structural design using a homogenization method,” *Comput. Methods Appl. Mech. Eng.*, vol. 71, no. 2, 1988, doi: 10.1016/0045-7825(88)90086-2.

[21] M. P. Bendsøe, “Optimal shape design as a material distribution problem,” *Structural Optimization*, vol. 1, no. 4, 1989, doi: 10.1007/BF01650949.

[22] F. N. U. Nishanth and B. Wang, “Topology Optimization of Electric Machines: A Review,” in *2022 IEEE Energy Conversion Congress and Exposition, ECCE 2022*, 2022. doi: 10.1109/ECCE50734.2022.9948073.

[23] F. Shiyang and K. Watanabe, “Topology optimization of rotor design in switched reluctance motor using immune algorithm,” in *International Journal of Applied Electromagnetics and Mechanics*, 2020. doi: 10.3233/JAE-209347.

[24] D. Jonathan, D. Bruno, and B. A. Hamid, “Simulated annealing and genetic algorithms in topology optimization tools: A comparison through the design of a switched reluctance machine,” in *SPEEDAM 2010 - International Symposium on Power Electronics, Electrical Drives, Automation and Motion*, 2010. doi: 10.1109/SPEEDAM.2010.5545100.

[25] E. Sayed, M. H. Bakr, B. Bilgin, and A. Emadi, “Gradient-based design optimization of a switched reluctance motor for an HVAC application,” in *2020 IEEE Transportation Electrification Conference and Expo, ITEC 2020*, 2020. doi: 10.1109/ITEC48692.2020.9161741.

[26] K. Watanabe, T. Suga, and S. Kitabatake, “Topology optimization based on the ON/OFF method for synchronous motor,” *IEEE Trans. Magn.*, vol. 54, no. 3, 2018, doi: 10.1109/TMAG.2017.2751653.

[27] J. Yoo, “Reduction of vibration caused by magnetic force in a switched reluctance motor by topology optimization,” *Journal of Applied Mechanics, Transactions ASME*, vol. 69, no. 3, 2002, doi: 10.1115/1.1467093.

[28] H. Zhang and S. Wang, “Topology Optimization of Rotor Pole in Switched Reluctance Motor for Minimum Torque Ripple,” *Electric Power Components and Systems*, vol. 45, no. 8, 2017, doi: 10.1080/15325008.2017.1310769.

[29] Y. Yamashita and Y. Okamoto, “Design Optimization of Synchronous Reluctance Motor for Reducing Iron Loss and Improving Torque Characteristics Using

Topology Optimization Based on the Level-Set Method," *IEEE Trans. Magn.*, vol. 56, no. 3, 2020, doi: 10.1109/tmag.2019.2954468.

[30] O. Brun *et al.*, "A Level-Set-Based Topology Optimization for Maximizing the Torque of Synchronous Reluctance Machines," *IEEE Trans. Magn.*, vol. 60, no. 3, 2024, doi: 10.1109/TMAG.2023.3326878.

[31] T. Gauthey, P. Gangl, and M. H. Hassan, "Multi-Material Topology Optimization with Continuous Magnetization Direction for motors design," in *2022 International Conference on Electrical Machines, ICEM 2022*, 2022. doi: 10.1109/ICEM51905.2022.9910654.

[32] F. Guo, N. Tang, and I. P. Brown, "Magneto-Structural Combined Dimensional and Topology Optimization of Interior Permanent Magnet Synchronous Machine Rotors," *IEEE Trans. Ind. Appl.*, vol. 58, no. 6, 2022, doi: 10.1109/TIA.2022.3203020.

[33] F. Guo, N. Tang, and I. P. Brown, "Combined Dimensional and Topology Optimization of Synchronous Machine Rotors Using a Material Density Interpolation Method," *IEEE Trans. Ind. Appl.*, vol. 59, no. 6, 2023, doi: 10.1109/TIA.2023.3292214.

[34] H. Sasaki and H. Igarashi, "Topology optimization accelerated by deep learning," *IEEE Trans. Magn.*, vol. 55, no. 6, 2019, doi: 10.1109/TMAG.2019.2901906.

[35] J. Asanuma, S. Doi, and H. Igarashi, "Transfer Learning through Deep Learning: Application to Topology Optimization of Electric Motor," *IEEE Trans. Magn.*, vol. 56, no. 3, 2020, doi: 10.1109/TMAG.2019.2956849.

[36] H. Sasaki, Y. Hidaka, and H. Igarashi, "Topology Optimization using Deep Learning ——Comparison of Simultaneous and Additional Learning——," *IEEJ Transactions on Power and Energy*, vol. 140, no. 12, 2020, doi: 10.1541/ieejpes.140.858.

[37] H. Sato and H. Igarashi, "Deep learning-based surrogate model for fast multi-material topology optimization of IPM motor," *COMPEL - The International Journal for Computation and Mathematics in Electrical and Electronic Engineering*, vol. 41, no. 3, 2022, doi: 10.1108/COMPEL-03-2021-0086.

[38] A. Khan, C. Midha, and D. Lowther, "Reinforcement Learning for Topology Optimization of a Synchronous Reluctance Motor," *IEEE Trans. Magn.*, vol. 58, no. 9, 2022, doi: 10.1109/TMAG.2022.3184246.

[39] H. Sato and H. Igarashi, "Fast Topology Optimization for PM Motors Using Variational Autoencoder and Neural Networks With Dropout," *IEEE Trans. Magn.*, vol. 59, no. 5, 2023, doi: 10.1109/TMAG.2023.3242288.

[40] J. S. Choi, K. Izui, S. Nishiwaki, A. Kawamoto, and T. Nomura, "Topology optimization of the stator for minimizing cogging torque of IPM motors," *IEEE Trans. Magn.*, vol. 47, no. 10, 2011, doi: 10.1109/TMAG.2011.2158572.

[41] P. A. Putek, "Mitigation of the cogging torque and loss minimization in a permanent magnet machine using shape and topology optimization," *Engineering Computations (Swansea, Wales)*, vol. 33, no. 3, 2016, doi: 10.1108/EC-01-2015-0007.

[42] S. Hayashi, Y. Kubota, S. Soma, M. Ohtani, and H. Igarashi, "Topology Optimization of Permanent Magnet Synchronous Motor Considering the Control System," *IEEE Trans. Magn.*, vol. 58, no. 9, 2022, doi: 10.1109/TMAG.2022.3172718.

[43] C. Lee and I. G. Jang, “Topology Optimization of the IPMSMs Considering Both the MTPA and FW Controls under the Voltage and Current Limitations,” *IEEE Transactions on Industrial Electronics*, vol. 70, no. 8, 2023, doi: 10.1109/TIE.2023.3234136.

[44] T. Cherriere *et al.*, “A Multimaterial Topology Optimization Considering the PM Nonlinearity,” *IEEE Trans. Magn.*, vol. 59, no. 5, 2023, doi: 10.1109/TMAG.2023.3256003.

[45] S. Hayashi, Y. Kubota, S. Soma, S. Oya, and H. Igarashi, “Topology-Parameter Hybrid Optimization of Skewed Permanent Magnet Motor,” *IEEE Trans. Magn.*, vol. 59, no. 5, 2023, doi: 10.1109/TMAG.2023.3239620.

[46] P. Gangl, T. Komann, N. Krenn, and S. Ulbrich, “Robust Topology Optimization of Electric Machines using Topological Derivatives,” Apr. 2025, [Online]. Available: http://arxiv.org/abs/2504.05070

[47] Z. Sun, H. Otsuki, T. Sato, and K. Watanabe, “Topology Optimization of a Switched Reluctance Machine by Electromagnetic-Structural Multiphysics Finite Element Analysis,” *IEEE Trans. Magn.*, vol. 60, no. 3, 2024, doi: 10.1109/TMAG.2023.3301903.

[48] E. Andriushchenko, M. H. Mohammadi, D. A. Lowther, H. Heidari, A. Kallaste, and A. Khan, “Topology Optimization of a 3D-Printed Switched Reluctance Motor,” in *2022 International Conference on Electrical Machines, ICEM 2022*, 2022. doi: 10.1109/ICEM51905.2022.9910829.

[49] J. K. Byun and S. Y. Hahn, “Topology optimization of switched reluctance motor using mutual energy method,” *International Journal of Applied Electromagnetics and Mechanics*, vol. 13, no. 1-4 SPEC., 2001, doi: 10.3233/jae-2002-349.

[50] J. Lee, J. H. Seo, and N. Kikuchi, “Topology optimization of switched reluctance motors for the desired torque profile,” *Structural and Multidisciplinary Optimization*, vol. 42, no. 5, 2010, doi: 10.1007/s00158-010-0547-1.

[51] A. Manninen, J. Keranen, J. Pippuri-Makelainen, T. Riipinen, S. Metsa-Kortelainen, and T. Lindroos, “Impact of Topology Optimization Problem Setup on Switched Reluctance Machine Design,” in *COMPUMAG 2019 - 22nd International Conference on the Computation of Electromagnetic Fields*, 2019. doi: 10.1109/COMPUMAG45669.2019.9032826.

[52] S. Metsä-Kortelainen *et al.*, “Manufacturing of topology optimized soft magnetic core through 3D printing,” 2016.

[53] A. Manninen, J. Keränen, J. Pippuri-Mäkeläinen, S. Metsä-Kortelainen, T. Ripinen, and T. Lindroos, “Topology optimization of 3D printed switched reluctance motor,” Dec. 2018.

[54] A. Manninen, J. Pippuri-Mäkeläinen, T. Riipinen, J. Keränen, S. Metsä-Kortelainen, and T. Lindroos, “DESIGN AND TESTING OF A SWITCHED RELUCTANCE MOTOR WITH ADDITIVELY MANUFACTURED FERROMAGNETIC CORES,” in *IET Conference Proceedings*, 2023. doi: 10.1049/icp.2023.1992.

[55] G. M. Tseng, K. J. Jhong, M. C. Tsai, P. W. Huang, and W. H. Lee, “Application of additive manufacturing for low torque ripple of 6/4 switched reluctance motor,” in *19th International Conference on Electrical Machines and Systems, ICEMS 2016*, 2017.

[56] M. Garibaldi, C. Gerada, I. Ashcroft, and R. Hague, “Free-Form Design of Electrical Machine Rotor Cores for Production Using Additive Manufacturing,” *Journal of Mechanical Design*, vol. 141, no. 7, 2019, doi: 10.1115/1.4042621.

[57] M. Hage-Hassan *et al.*, “Multi-Material BESO Topology Optimization for SynRM based on printed FeSi6.5%,” 2023. [Online]. Available: https://centralesupelec.hal.science/hal-04246986v1

[58] S. Lammers *et al.*, “Additive Manufacturing of a lightweight rotor for a permanent magnet synchronous machine,” in *2016 6th International Electric Drives Production Conference, EDPC 2016 - Proceedings*, 2016. doi: 10.1109/EDPC. 2016.7851312.

[59] Z. Y. Zhang, K. J. Jhong, C. W. Cheng, P. W. Huang, M. C. Tsai, and W. H. Lee, “Metal 3D printing of synchronous reluctance motor,” in *Proceedings of the IEEE International Conference on Industrial Technology*, 2016. doi: 10.1109/ICIT.2016. 7474912.

[60] H. S. Hong, H. C. Liu, G. C. Jeong, and J. Lee, “Design of high-end SynRM based on 3D printing technology,” in *IEEE CEFC 2016 - 17th Biennial Conference on Electromagnetic Field Computation*, 2017. doi: 10.1109/CEFC.2016.7816043.

[61] S. Urbanek and B. Ponick, “Surface Eddy Current Loss Reduction in Additively Manufactured Permanent Magnet Rotor Active Parts,” in *Proceedings - 2018 23rd International Conference on Electrical Machines, ICEM 2018*, 2018. doi: 10.1109/ICELMACH.2018.8507151.

[62] S. Urbanek *et al.*, “Additive Manufacturing of a Soft Magnetic Rotor Active Part and Shaft for a Permanent Magnet Synchronous Machine,” in *2018 IEEE Transportation and Electrification Conference and Expo, ITEC 2018*, 2018. doi: 10.1109/ITEC.2018.8450250.

[63] S. Urbanek *et al.*, “Design and Experimental Investigation of an Additively Manufactured PMSM Rotor,” in *2021 IEEE International Electric Machines and Drives Conference, IEMDC 2021*, 2021. doi: 10.1109/IEMDC47953.2021.9449566.

[64] D. Michieletto and L. Alberti, “Design and Realization of a Synchronous Reluctance Motor with Printed Rotor,” in *IECON Proceedings (Industrial Electronics Conference)*, 2022. doi: 10.1109/IECON49645.2022.9968455.

[65] D. Michieletto, L. Alberti, and A. Belahcen, “Optimization of Printed Synchronous Reluctance Rotor Based on Bézier Curves,” in *2024 International Conference on Electrical Machines, ICEM 2024*, 2024. doi: 10.1109/ICEM60801.2024.10700207.

[66] M. Di Nardo *et al.*, “Experimental Assessment of a Synchronous Reluctance Machine Featuring an Additive Manufactured Rotor,” in *Proceedings of the IEEE Workshop on Electrical Machines Design, Control and Diagnosis, WEMDCD*, 2025. doi: 10.1109/WEMDCD61816.2025.11014166.

[67] Y. Zhou *et al.*, “Development and Manufacturing of Axial-Flux Synchronous Reluctance Motors With 3-D Printing Technology,” *IEEE Transactions on Industrial Electronics*, vol. 73, no. 1, 2026, doi: 10.1109/TIE.2025.3585047.

[68] L. Gargalis *et al.*, “Development and Testing of Soft Magnetic Rotor for a Switched Reluctance Motor Built through Additive Manufacturing Technology,” in *23rd International Conference on Electrical Machines and Systems, ICEMS 2020*, 2020. doi: 10.23919/ICEMS50442.2020.9290893.

[69] L. Gargalis *et al.*, “Additive manufacturing and testing of a soft magnetic rotor for a switched reluctance motor,” *IEEE Access*, vol. 8, 2020, doi: 10.1109/ACCESS.2020.3037190.

[70] H. J. Pyo, J. W. Jeong, J. Yu, S. G. Lee, and W. H. Kim, “Design of 3D-Printed Hybrid Axial-Flux Motor Using 3D-Printed SMC Core,” *IEEE Transactions on Applied Superconductivity*, vol. 30, no. 4, 2020, doi: 10.1109/TASC.2020.2973364.

[71] A. Selema, M. N. Ibrahim, H. Vansompel, and P. Sergeant, “Development of Yokeless Axial Flux Machine Using 3D-Printed Shape-Profiled Core,” in *2022 International Conference on Electrical Machines, ICEM 2022*, 2022. doi: 10.1109/ICEM51905.2022.9910661.

[72] A. Selema *et al.*, “New Measurement Approach and Development of 3-D-Printed Core for Yokeless Axial-Flux Machine,” *IEEE Sens. J.*, vol. 24, no. 12, 2024, doi: 10.1109/JSEN.2024.3395890.

[73] F. N. U. Nishanth, A. D. Goodall, I. Todd, and E. L. Severson, “Characterization of an Axial Flux Machine With an Additively Manufactured Stator,” *IEEE Transactions on Energy Conversion*, vol. 38, no. 4, 2023, doi: 10.1109/TEC.2023.3285539.

[74] A. D. Goodall, F. N. U. Nishanth, E. L. Severson, and I. Todd, “Loss performance of an additively manufactured axial flux machine stator with an eddy-current limiting structure,” *Mater. Today Commun.*, vol. 35, 2023, doi: 10.1016/j.mtcomm.2023.105978.

[75] H. Tiismus, A. Kallaste, T. Vaimann, A. Rassolkin, and A. Belahcen, “Additive Manufacturing of Prototype Axial Flux Switched Reluctance Electrical Machine,” in *2021 28th International Workshop on Electric Drives: Improving Reliability of Electric Drives, IWED 2021 - Proceedings*, 2021. doi: 10.1109/IWED52055.2021.9376337.

[76] H. Tiismus, A. Kallaste, M. U. Naseer, T. Vaimann, and A. Rassolkin, “Design and Performance of Laser Additively Manufactured Core Induction Motor,” *IEEE Access*, vol. 10, 2022, doi: 10.1109/ACCESS.2022.3173317.

[77] H. Tiismus, *Production and Properties of Additively Manufactured Electrical Machine Cores*.

[78] T. N. Lamichhane *et al.*, “An Additively Manufactured Fe-3Si Stator for a High-Performance Electrical Motor,” *Applied Sciences (Switzerland)*, vol. 15, no. 4, 2025, doi: 10.3390/app15041706.

[79] T. N. Lamichhane *et al.*, “Additively Manufactured Fe-3si Stator for High-Performance Electrical Motor,” *SSRN Electronic Journal*, 2022, doi: 10.2139/ssrn.4086824.

[80] B. Lizarribar Carrillo, B. Prieto, M. Martínez-Iturralde, J. García Goikoetxea, S. Montes, and E. San José, “Design and additive manufacturing of a lightweight aerospace electric actuator,” *Open Research Europe*, vol. 4, 2025, doi: 10.12688/openreseurope.17752.2.

[81] V. S. R. P. Akula, K. K. Goyal, O. P. Verma, and V. Gupta, “Feasibility study of a 3D printed BLDC outrunner rotor,” in *Materials Today: Proceedings*, 2023. doi: 10.1016/j.matpr.2022.11.090.

[82] A. Bibi *et al.*, “Performance comparison of additively manufactured and conventional stators in permanent magnet brushless direct current motor,” *Electrical Engineering*, vol. 108, no. 2, 2026, doi: 10.1007/s00202-025-03472-2.

[83] J. Ma *et al.*, “Optimal Design of an Axial-Flux Switched Reluctance Motor with Grain-Oriented Electrical Steel,” *IEEE Trans. Ind. Appl.*, vol. 53, no. 6, 2017, doi: 10.1109/TIA.2017.2727438.

[84] R. Krishnan, “Switched Reluctance Motor Drives: Modeling, Simulation, Analysis, Design, and Applications.”

Acknowledgements

I would like to express my sincere gratitude to my supervisor, Prof. Ants Kallaste, for his invaluable guidance, encouragement, and continuous support throughout my doctoral studies. His expertise, constructive feedback, and confidence in my work played a central role in shaping the direction of this research and bringing the thesis to completion.

I am also sincerely grateful to Dr. Muhammad Usman Naseer for his valuable mentorship, technical guidance, and insightful discussions throughout my doctoral research.

I am also grateful to all my co-authors and colleagues for their technical discussions, collaboration, and assistance throughout this journey.

I extend my deepest gratitude to my parents and family for their constant encouragement and belief in me. I am especially thankful to my wife for their patience, understanding, love, and sacrifices throughout this demanding journey. Their unwavering support provided me with the strength and motivation needed to complete this thesis.

This research was supported by the Estonian Research Council through project PRG1827, “Additively Manufactured Electrical Machines.” This financial support is gratefully acknowledged.

Abstract

Topology Optimization for Improved Magnetic Core Utilization and Torque Density in Additively Manufactured Electrical Machines

Electrical machines account for a substantial share of global electricity consumption, and the increasing demand for higher power density and application specific customization in electric vehicles, drones, and aerospace propulsion is difficult to satisfy with conventional manufacturing. AM, particularly LPBF, removes many of the geometric restrictions of conventional lamination and casting, but exploiting this freedom requires a systematic method for determining which shape to build. TO provides this method, yet its integrated application with AM to electrical machines remains fragmented. PM machines dominate the TO literature, reluctance machines and axial flux topologies are comparatively unexplored because of their 3D flux paths and computational cost, and experimentally validated results after AM fabrication remain scarce.

This thesis addresses these gaps by developing, comparing, and experimentally validating TO methods for two AM machines, an outer rotor PM BLDC motor for electric scooter propulsion, and an AFDR-SRM for high-speed propulsion. For the BLDC rotor back iron, three methods, an ON/OFF NGNet optimized by genetic algorithm, a density based SIMP method with adjoint sensitivity analysis, and a newly derived closed-form analytical method based on Ampere's and Gauss's laws, are applied to the same design domain and benchmarked for material reduction, torque density, and computational cost. For the AFDR-SRM, an analytical output-power-based sizing procedure is combined with an NGNet based pole shoe optimization performed on a computationally efficient 2D linear equivalent of the axial flux machine, and the analytical back iron reduction method developed for the PM rotor is extended to the coil-excited rotor.

The three back iron optimization methods for the BLDC motor achieve back iron reductions of 25.67% (NGNet), 39% (SIMP), and 39.29% (analytical), with the analytical method requiring a single field evaluation instead of tens of thousands of FE solves, confirming that a physics based closed-form design can match numerically optimized results at negligible computational cost. For the AFDR-SRM, pole-shoe optimization reduces torque ripple by 11.2%, while the analytical back iron reduction lowers rotor mass by 9.25% and raises torque density by 1.67%, without introducing magnetic saturation. Prototypes of both machines were fabricated from Fe-3.7wt%Si powder by LPBF, including a TO outer rotor back iron and for the AFDR-SRM, a fully laminated, segmented stator and rotor assembled through a mechanical lip feature, and heat treated to restore soft-magnetic properties. Experimental testing shows that the measured and simulated torque of the BLDC prototype agree within 5.09%, and that the measured and simulated average torque of the AFDR-SRM agree within 8.7%, with the remaining discrepancies attributable to material property assumptions, manufacturing tolerances, and mechanical assembly effects.

The results confirm the four research hypotheses, TO of a quasi-static PM magnetic core substantially reduces back iron material without compromising electromagnetic performance, a physics guided analytical method reproduces near optimal designs at a fraction of the computational effort of numerical TO. The TO of the AFDR-SRM rotor simultaneously improves material utilization and reduces torque ripple. Together, the thesis establishes a reproducible design-to-prototype workflow linking analytical and

numerical TO, design for LPBF, and experimental validation, extending TO beyond PM machines to reluctance and axial flux topologies and demonstrating that AM, and TO magnetic cores can be fabricated and operated with performance consistent with simulation.

Lühikokkuvõte

Kihtlisandus meetodil valmistatud elektrimasinate topoloogia optimeerimine pöördemomendi tiheduse ja magnetsüdamike tõhususe suurendamiseks

Elektrimasinate arvele langeb märkimisväärne osa maailma elektritarbimisest, samas kui kasvavat nõudlust suurema võimsustiheduse ja rakenduspõhise kohandatavuse järele elektrisõidukites, droonides ja lennunduse seadmetes on tavapäraste tootmismeetoditega järjest keeruline rahuldada. Lisandtootmine (AM), eelkõige pulberkihtide laseriga sulatamine (LPBF), kõrvaldab paljud traditsiooniliste tootmismeetoditega seotud geomeetrilised piirangud, kuid selle projekteerimisvabaduse ärakasutamine eeldab süsteemset meetodit valmistatava geomeetria määramiseks. TO pakub sellist meetodit, ent selle integreeritud rakendamine koos AM-iga elektrimasinatele on siiani killustatud. TO-alases kirjanduses domineerivad PM masinad, samas kui reluktantsmasinaid ja aksiaalvoo topoloogiaid on võrdlemisi vähe uuritud ning prototüübitud nende 3D magnetvoost tuleneva arvutusliku mahukuse tõttu.

Käesolev doktoritöö täidab need lüngad, arendades, võrreldes ja eksperimentaalselt valideerides TO meetodeid kahe AM masina jaoks: välisrootoriga PM BLDC mootor elektritõukeratta rakenduse jaoks ning AFDR-SRM suure kiirusega veorakenduste jaoks. BLDC mootori rootori ikke jaoks rakendati samale disainipiirkonnale kolme meetodit: geneetilise algoritmiga optimeeritud ON/OFF NGNet, tihedusepõhine SIMP meetod koos adjunkt-tundlikkusanalüüsiga, ning uudne Ampère'i ja Gaussi seadustel põhinev suletud kujuga analüütiline lähenemine. Meetodeid võrreldi materjalikulu vähendamise, pöördemomendi tiheduse ja arvutusliku mahukuse osas. AFDR-SRM jaoks kombineeriti analüütiline väljundvõimsusel põhinev mõõtmestamismenetlus NGNet-põhise pooluskinga optimeerimisega, mis viidi läbi arvutuslikult tõhusal kahemõõtmelisel lineaarsel ekvivalendil. Lisaks laiendati püsimagnetrootori jaoks välja töötatud analüütilist tagaraua vähendamise meetodit mähisergastusega rootorile.

BLDC mootori kolm optimeerimismeetodit vähendasid masina ikke materjalikulu vastavalt 25,67% (NGNet), 39% (SIMP) ja 39,29% (analüütiline meetod), kusjuures analüütiline meetod nõudis kümnete tuhandete lõplike elementide arvutuste asemel vaid ühte väljaarvutust, kinnitades, et füüsikapõhine suletud kujuga disain suudab saavutada numbriliselt optimeeritud tulemustega võrreldava tulemuse tühise arvutusliku kuluga. AFDR-SRM puhul vähendas pooluskinga optimeerimine pöördemomendi lainetust 11,2%, samal ajal kui analüütiline ikke vähendamine vähendas rootori massi 9,25% ja suurendas pöördemomendi tihedust 1,67%, ilma magnetküllastust tekitamata. Mõlema masina prototüübid valmistati Fe-3,7 mass%Si pulbrist LPBF-meetodil: sealhulgas PM BLDC välisrootori ike ning AFDR-SRM õhupiludega lamineeritud staator ja rootor. Eksperimentaalne testimine näitas, et BLDC prototüübi mõõdetud ja simuleeritud pöördemoment olid kooskõlas 5,09% täpsusega ning AFDR-SRM mõõdetud ja simuleeritud keskmine pöördemoment olid kooskõlas 8,7% täpsusega. Erinevused on seletatavad materjaliomaduste varieeruvuse, tootmistolerantside ja mehaanilise kokkupanekuga seotud mõjudega.

Lõputöö tulemused kinnitavad kolme uurimishüpoteesi: kvaasistaatilise PM magnetsüdamiku TO võimaldab vähendada oluliselt tagaraua materjalivajadust ilma elektromagnetilist toimivust kahjustamata; analüütiline meetod võimaldab saavutada sarnase ehituse murdosa arvutusliku kuluga võrreldes numbrilise TO-ga; AFDR-SRM

rootori TO parandab samaaegselt materjali kasutust ja vähendab pöördemomendi lainetust. Kokkuvõttes loob käesolev doktoritöö korratava disainist prototüübini viiva töövoo, mis ühendab analüütilise ja numbrilise TO, LPBF-i jaoks kohandatud disaini ning eksperimentaalse valideerimise, laiendades TO-d PM masinatelt reluktants- ja aksiaalvoo topoloogiatele ning näidates, et AM ja TO magnetsüdamikke saab valmistada ja käitada simulatsiooniga kooskõlas oleva toimivusega.

Publication I

S. Hussain, A. Kallaste, and T. Vaimann, “Recent Trends in Additive Manufacturing and Topology Optimization of Reluctance Machines,” *Energies*, vol. 16, no. 9, p. 3840, 2023, doi: 10.3390/en16093840.

energies

MDPI

Review

Recent Trends in Additive Manufacturing and Topology Optimization of Reluctance Machines

Shahid Hussain *, Ants Kallaste and Toomas Vaimann

Department of Electrical Power Engineering and Mechatronics, Tallinn University of Technology, 19086 Tallinn, Estonia; ants.kallaste@taltech.ee (A.K.)
* Correspondence: shahid.hussain@taltech.ee

Abstract: Additive manufacturing (AM) or 3D printing has opened up new opportunities for researchers in the field of electrical machines, as it allows for more flexibility in design and faster prototyping, which can lead to more efficient and cost-effective production. An overview of the primary AM techniques utilized for designing electrical machines is presented in this paper. AM enables the creation of complex and intricate designs that are difficult or impossible to achieve using traditional methods. Topology Optimization (TO) can be used to optimize the design of parts for various purposes such as weight, thermal, material usage and structural performance. This paper primarily concentrates on the most recent studies of the AM and TO of the reluctance machines. The integration of AM with TO can enhance the design and fabrication process of magnetic components in electrical machines by overcoming current manufacturing limitations and enabling the exploration of new design possibilities. The technology of AM and TO both have limitations and challenges which are discussed in this paper. Overall, the paper offers a valuable resource for researchers and practitioners working in the field of AM and TO of electrical machines.

Keywords: additive manufacturing; topology optimization; level set; synchronous reluctance machine; switch reluctance machine; ON-OFF method; material density; genetic algorithm; power bed fusion; binder jetting; soft magnetic materials

check for updates

Citation: Hussain, S.; Kallaste, A.; Vaimann, T. Recent Trends in Additive Manufacturing and Topology Optimization of Reluctance Machines. *Energies* **2023**, *16*, 3840. https://doi.org/10.3390/en16093840

Academic Editor: Lorand Szabo

Received: 19 March 2023
Revised: 12 April 2023
Accepted: 18 April 2023
Published: 29 April 2023

Copyright: © 2023 by the authors. Licensee MDPI, Basel, Switzerland. This article is an open access article distributed under the terms and conditions of the Creative Commons Attribution (CC BY) license (https://creativecommons.org/licenses/by/4.0/).

1. Introduction

The future goal of reducing carbon emissions in transportation can only be achieved by exploring and implementing new technologies and innovative designs for drive-train components. This will require a change in the traditional approach to electrification, as outlined in various roadmaps [1–3]. Additive Manufacturing (AM) or 3D printing technology is one of the developing technologies of the current contemporary era. AM is a technique for fabricating physical objects in which the substrate or powdered materials are deposited layer by layer to build the 3D object [4,5]. Compared to conventional manufacturing techniques, AM has several advantages over traditional manufacturing processes, such as the potential to decrease material waste and trash parts coupled with the conventional method [6].

In recent years, the use of additive manufacturing has grown in the field of electrical machines, providing new possibilities for design and production of these machines, although the technology is still maturing and has the potential to progress significantly. The manufacturers are able to save the vital resources that would be greatly wasted in the traditional subtraction-based production since AM allows for freeform limitless shape complexity. In addition, AM technology could provide the most affordable and frequent prompts to fabricate small volumes of extremely complicated shapes [7]. However, a fully assembled AM electrical machine is still a dream for large-scale manufacturing and industrial applications due to a number of challenges, including slow manufacturing speed, inner structural imperfections, constrained multi-material printing potential, and the requirement for postprocessing printed parts [8].

In order to maximize performance and efficiency while reducing size, weight, and losses, optimization is required in the design of electrical machines. The two primary sub parts in the design process for an electrical machine are design and preliminary design optimization [9,10]. By investigating several topologies and doing muti-disciplinary study of the machine, engineers use design optimization to determine the best essential performance parameters for a specific application [11,12]. The objective of conventional optimization techniques for the design of electric machines is to find the optimum values of the parameterized geometric variables by altering them within a defined range. However, conventional optimization is limited to optimizing shapes within predefined boundaries and cannot change the topology of the design. Topology optimization, on the other hand, overcomes these limitations by allowing the design of the structure to be changed during the optimization process, resulting in more optimal solutions [13].

Furthermore, the advantages of using AM for Topology Optimization (TO) include the ability to create complex geometries and internal structures that would be difficult or impossible to fabricate using traditional manufacturing techniques. TO is a design method that aims to find the optimal layout of a structure or system in order to meet certain design objectives, such as minimizing weight or maximizing average torque. Compared to the geometric parameterization and optimization of rotor flux barriers, TO provides a smoother barrier design by allowing for flexible material distribution within the design space [14]. However, the manufacturability level of the TO is lower than the conventional optimization, but thanks to the AM technique, it makes possible the fabrication of these complicated geometries.

Researchers work on the different techniques of AM and TO, but there is limited literature available on the integration of AM and TO. This paper reviews the use of TO and AM with regard to magnetic components for electrical machines. In order to provide background for further discussing the integration of TO in a later section of the paper, the paper initially highlights the primary AM techniques, with a particular focus on those pertaining to electrical machines. Additionally, various soft magnetic material types are examined for possible use in AM. The state-of-the-art current literature of AM and TO, particularly with regard to iron cores and windings in reluctance machines, is also covered in more detail. Some challenges and limitations in the AM and TO are also summarized in this paper. These case studies emphasize the innovative integration of these cutting-edge technologies and demonstrate their potential for use in electrical machine design in the future.

2. AM Technologies Suitable for Electrical Machines

Despite being designed for low-volume manufacturing with a low manufacturing rate (0.01–1 kg/h) and high cost (USD 0.1–10 per gram) [15], the potential for AM's application to expand exponentially is expected to grow. This is due to its rapid development in terms of material accessibility and process quality, which indicates a significant increase in the extent and diversity of its utilization. There are several printer types used for additive manufacturing; among these, the four AM technologies listed below are the most well-known and developed for commercial applications.

- Powder Bed Fusion (PBF)
- Binder Jetting Technology (BJT)
- Direct Energy Deposition (DED)
- Resistance Heat or Joule Printing (JP)

The Powder Bed Fusion (PBF) is also known as Selective Laser Melting (SLM) or Electron Beam Melting (EBM). The majority of current metal additive manufacturing systems use PBF technology [16]. For building full-density products, current PBF AM techniques often employ melting rather than sintering. However, rather than using a laser or other energy source to fuse the powder together, binder jetting uses a liquid binding agent to join the powder particles together [17]. Binder jetting is generally considered to be a more cost-effective method of fabricating parts compared to electron beam melting (EBM)

and selective laser melting (SLM). However, binder jetting typically requires extensive post-processing after the 3D printing process is complete. The binder-bonded parts produced by binder jetting are typically weak and brittle and require additional processing steps to achieve the desired strength, hardness, and surface finish. In order to create high-performance superalloys, direct energy deposition (DED) has been developed. DED employs a laser or electron beam as an energy source that is simultaneously utilized to melt feedstock material (powder or wire) and is narrowly focused on a small area of the platform. The difference between DED and PBF technologies is that DED does not employ a powder bed and melts the feedstock layer by layer before deposition while using a much larger amount of energy to melt metals. This technique enables the simultaneous deposition of different materials and various axis [18]. When compared to PBF, it can construct less complicated components and has a lower precision, surface quality, and manufacturing capacity [19,19,20]. Joule heating uses direct electrical current with resistance heating for melting and layer bonding; it is somewhat comparable to other wire feed technologies like DED. Compared to other techniques, this method uses a single feed and melt process and a far more basic raw material. As a result, this simplicity reduces expenses and time saving [21–23].

Figure 1 shows the overall comparison of the aforementioned techniques. Both PBF and BJT provide higher resolution, which is needed in most applications, but are limited by printing speed. Further, DED and Joule printing are faster while having a lower resolution. On the other hand, EBM and SLM are typically more expensive 3D printing methods that use high-power lasers to melt metal, ceramic, or polymer powders into solid objects. However, EBM and SLM can produce high-quality, high-density parts with high mechanical strength and fine resolution, making them suitable for applications where high performance is required.

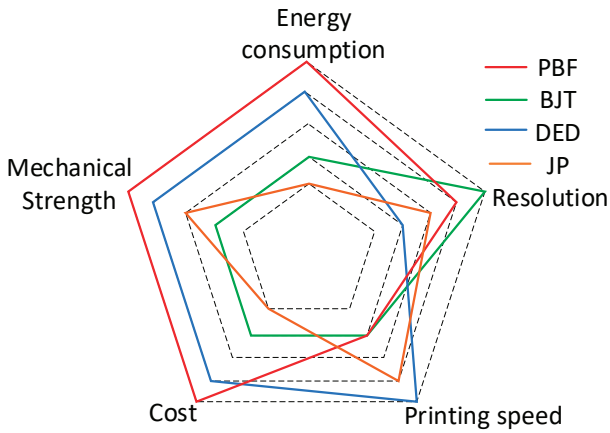


Figure 1. Different AM techniques comparison.

3. Soft Magnetic Materials for AM Machines

Iron cores for electrical machines are traditionally made from non-oriented electric steel laminations and these laminations are stacked together to form the core of the electrical machine [24]. However, the problem of low mechanical strength in thin sheets causes bending during stamping, which in turn reduces the ability to stack the laminations at a high stacking coefficient. Another problem is that electrical steel laminations can only be stacked in flat sheets and cannot be molded into intricate 3D patterns, which limits its application in 3D iron cores [25,26].

AM has the potential to bring advancements in the field of magnetic materials by allowing for the 3D printing of high-quality powdered soft magnetic materials, resulting in the creation of complex-shaped iron cores with improved control over the electromagnetic

and mechanical properties [5,27]. Furthermore, these materials are typically iron-based alloys such as iron–nickel, iron–cobalt, and iron–silicon alloys can be printed. In [28] the author demonstrated that using Fe–6.5Si alloys in the AM process of the iron cores of electric machine components results in better magnetization properties compared to using Fe–3Si alloys with a lower silicon content. The use of Fe–6.5Si alloys also leads to a reduction of more than 50% in eddy current losses at 50 Hz frequency. Iron cores for electrical machine may be 3D-printed using Fe–Ni alloys with high nickel compositions (up to 80%). The magnetic characteristics of these alloys include low saturation magnetic flux density but exceptional properties regarding permeability and losses. Among soft magnetic materials, Fe–Co alloys have the greatest saturation magnetic flux density, with the 50–50% Fe–Co alloy having a saturation magnetic flux density of 2.45 T [29]. The magnetic properties of commonly used soft magnetic materials for AM is summarized in Table 1.

Table 1. Different soft magnetic material properties used for AM.

Material Compositions	Max. Saturation (T)	Relative Permeability (μ_r)	Resistivity $\rho(\mu\Omega cm)$	Density (g/cc)	AM Technique	Reference
Fe–Si6.5	1.8	10,700	82	7.3–7.7	BJT	[30]
Fe–Co-based alloy	2.4	20,000–66,000	40	8.12	SLM	[31,32]
Fe–49Co-2V	2.23	-	49.4	-	PBF	[33]
20%Fe–80%Ni	1.08	8000–120,000			SLM	[34]

4. Electrical Machines Manufacturing Using AM Techniques

With the use of 3D computer-aided design, AM is rapidly developing a collection of new manufacturing technologies that allows for the direct manufacture of components from powder or wire filament. AM technology should make it unnecessary to do extra processing in order to produce intricate 3D geometries [35]. Furthermore, AM may reduce or even eliminate the material waste and scrap components that are common in many conventional manufacturing techniques. In general, the 3D printing process recycles wasted wire and powder to fully use the raw material [36]. Although some efforts have been made to bring a more holistic approach, where multiple parts are produced using AM, it is noteworthy that the majority of work linked to the AM of electrical machines is focused on the individual machine components and materials. In this section, the focus is on the electrical machine's active parts, and it includes the core and windings of the machine.

4.1. Stator and Rotor Core of Reluctance Machines

In order to build contemporary electrical machines with high specific output, magnetic materials are necessary. There are several electrical steels and soft magnetic composites (SMCs) used in the current procedures for creating magnetic cores. The most common method for producing a magnetic core is to stack a number of electrical steel profiles or lamination sheets that have been properly prepared, or to compress a mixture of metal powder and an insulating material [37]. However, these materials are often challenging to address using traditional methods because of their poor mechanical properties and limitations on the manufacturing of complex geometries.

With respect to the fabrication of magnetic parts and components, AM offers a compelling alternative to the well-established methods. The optimized switch reluctance machine rotor, which has six poles of the salient type, is shown in Figure 2a. This rotor was constructed using the PBF technique from an iron–cobalt alloy with a magnetic flux density of 2.3T. The authors also indicate that to decrease the specific power loss, the electrical resistivity of the developed design might be further enhanced [29]. Moreover, Figure 2b depicts the synchronous reluctance machine's rotor, which was fabricated using the PBF AM approach [38].

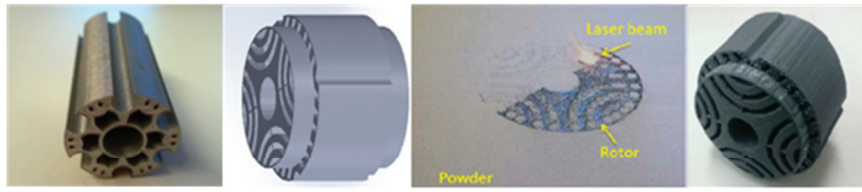


Figure 2. Electrical machine cores manufactured through AM techniques: (**a**) Rotor prototype of switched reluctance machine [37]; (**b**) Rotor core of synchronous reluctance machine [38].

In [39], the 3D-printed rotor of switched reluctance machine was compared with the benchmark machine. Due to the focus being on the material performance, both rotor prototypes' designs and dimensions were the same. Moreover, the rotor prototype was also manufactured in three segments owing to the height limitations of the 3D printer. The two segments' axial lengths are 25 mm each, the third segment is 54 mm long, and the rotor's total axial length is 104 mm, as shown in Figure 3a. Due to the segmentation, the 3D-printed rotor was also ensured to have lower eddy current losses than the solid component. In Figure 3b the fully assembled 3D-printed rotor is shown and was compared with the laminated benchmark rotor. This study demonstrates that the 3D-printed rotor produces results similar to those of the benchmark rotor while yet leaving a significant opportunities for performance improvement [40].

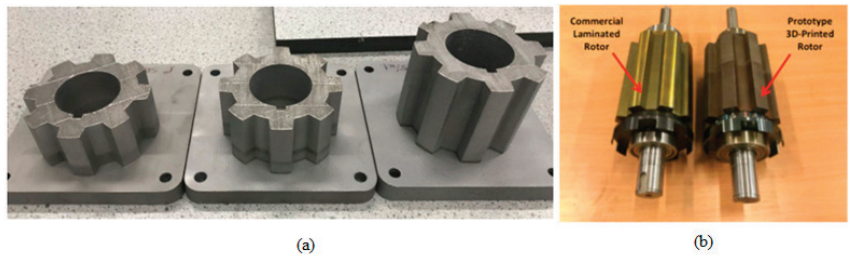


Figure 3. 3D-printed SRM rotor: (**a**) 3D-printed segments of rotor; (**b**) Commercial and 3D-printed assembled rotor [39,40].

In order to lessen the torque ripples and windage loss, a novel skew rotor design for switched reluctance machines was proposed. It has 2 mm thick ribs with 0.4 mm diameter holes in a honeycomb structure as shown in Figure 4. Using the conventional process, it was challenging to construct this rotor design. The AM method of PBF is used to build the prototype for this rotor design. Additionally, the 45% decrease in the machine's torque ripples profile was shown by the experimental results [41].

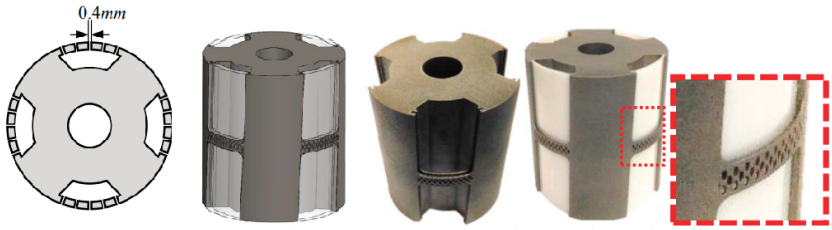


Figure 4. 3D-printed SRM rotor with honeycomb rib [41].

As the type of reluctance machine is most suited for PBF fabrication because it only needs one alloy powder, a fully assembled, fully functional axial flux switched reluctance

was developed utilizing this technology. Other machine types, such as permanent magnet machines or induction machines, need several materials, making it challenging to print them using AM owing to the use of many materials. Due to the disparity in component sizes, the suggested machine was printed in five phases. For the whole machine with stator halves, the printing process takes 57 h. Figure 5 [42] depicts the different parts and fully assembled machine. Additionally, annealing was done to enhance the magnetic characteristics. In order to do this, the toroid was heated for one hour at a temperature of 1150 C with a heating rate of 300 K/h, and then gradually cooled [43].



Figure 5. Printed axial machine having stator halved embedded teeth [42].

In addition to emphasizing the internal design and manufacture of electrical machines, the author of [44] showed a prototype of an induction machine that was manufactured employing additive manufacturing. The author introduces airgaps in the core in the form of crack-like printed regions to enhance the internal resistance of the core, and these airgaps were placed perpendicular to the core axis. The rotor and stator core were manufactured using metal rods, and the author stated that it is the first 3D-printed machine in scientific literature whose performance has been assessed. Figure 6 depicts the stator and rotor of a printed induction machine. Despite the irregular airgaps between the thick material layers, the 3D-printed induction machine exhibited the nominal torque of 0.5 N-m at an efficiency of 34% when compared to the benchmark machine [45] whose efficiency was 52%.

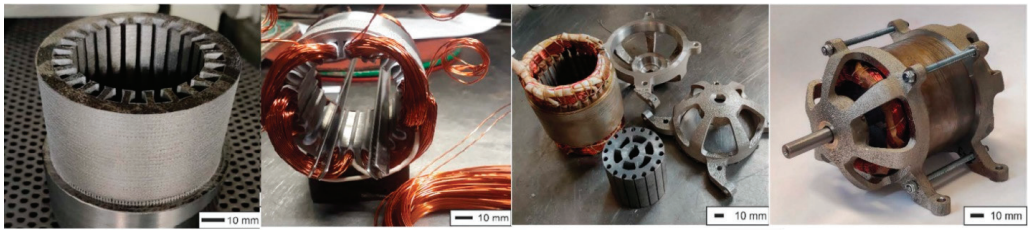


Figure 6. Fully assembled AM induction machine [44].

According to [46], a line start synchronous reluctance machine was designed with a novel, robust structure for less copper losses and vibration. As shown on the left side of Figure 7, the flux barriers include small ribs that go both in the xy and z directions to create a grid-like structure. Aluminum paste was placed within the cage of the line start synchronous reluctance machine, which was then heated to produce a solid aluminum cage as shown in Figure 7. The filling of the barriers lessens the machine's vibration, but this impact also lowers the saliency ratio, which reduces the torque.

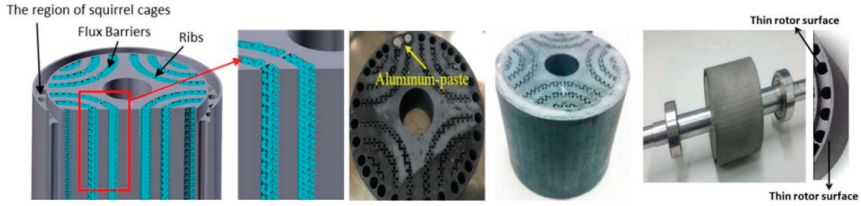


Figure 7. 3D-printed rotor of line start synchronous reluctance machine [46].

4.2. Windings

Electrical machine windings refer to the coils of wire that are used in electrical machines, to generate or utilize electromagnetic fields. These windings can be made of copper or aluminum and are typically wound around a core made of iron or other magnetic material. The development of modern electrical machine windings continues to be an active area of research and development, with the goal of creating more efficient and cost-effective electrical machines. In addition, AM is a promising technology for creating electrical machine windings, as it allows for the creation of complex geometries and can improve the performance and efficiency of the machine. It is important to note that the use of additive manufacturing for winding production is still in its early stages and there are not yet many examples in the industry, but it is considered a promising technology for the future.

In addition, the use of AM in electrical machines may serve a variety of goals, such as improving power density by improving the fill factor [47,48], optimizing end-winding [49,50], or integrating conductors with cooling channels [51]. The advancement in AM is the 3D multi-material printing which offers more design freedom and a faster and unique structure of fabricating different machines. Some examples of multi material printing are shown in Figure 8 [52–55]. This comprises ceramic materials that, in terms of various physical characteristics like heat resistance or thermal conductivity, outperform more traditional organic insulating materials composed of plastic. In this approach, electrical coils with much greater temperature resistance may be produced.

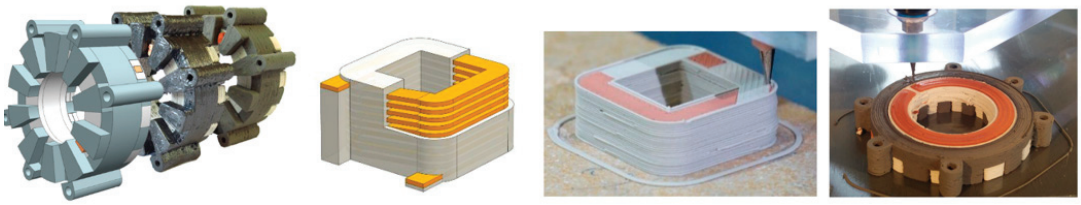


Figure 8. 3D-multi material printing technology [53–55].

The hybrid stranded concentrated winding of a high-speed traction machine is shown in Figure 9a, the resulted machine yields 60% reduction in the overall losses [56]. These improvements can be utilized to enhance the power density and reliability of the machine. The author in [57] demonstrated different types of AM coils prototype using different materials for low weight and low losses applications and was compared with the conventional manufactured coils. All four coils are shown in Figure 9b, which are then placed in the E-core. The performance comparison of different cores is illustrated in Table 2. The high fill factor and low AC losses were achieved as compared to the traditional one. Additionally, AM introduced new materials that gained attention in the enhanced thermal management method. In [58,59], the authors provide a detailed explanation about the advanced thermal management for AM machines.

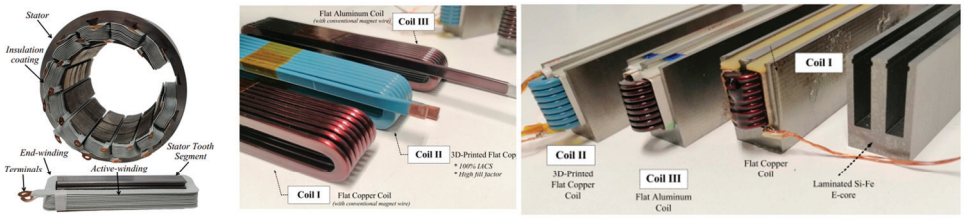


Figure 9. AM-based coils: (**a**) Concentrated AM copper coils [56]; (**b**) Solid flat shaped coils using different materials [57].

Table 2. Different coils comparison using different materials [57].

Type of Conductor	Flat Copper Coil	AM Shaped Copper Coil	Flat Aluminum Coil	AM Shaped Aluminum Coil
Material	Commercial copper	Pure copper powder	Commercial aluminum	Aluminum alloy powder
Insulation	Enameled	Class H-resin	Enameled	Class H-resin
Manufacturing	Commercial wire	3D printed	Commercial wire	3D printed
Fill factor	72.7%	77.96%	71.3%	62.4%
Cycle time	<one hour	9–10 h	<one hour	4–5 h
Mass density	8.96 g/cm^3	8.95 g/cm^3	2.7 g/cm^3	2.67 g/cm^3
Coil weight	171.2 gm	183.6 gm	55.2 gm	47.8 gm
DC losses	1 p.u	0.83 p.u	1.6 p.u	2.68 p.u
AC losses	81.6%	76.5%	64.5%	31.4%
Total losses	4.155 p.u	4.343 p.u	4.371 p.u	3.902 p.u
Efficiency	98.04%	97.76%	97.52%	98.71%
Frequency	Up to 900 Hz	Up to 900 Hz	Above 1.2 kHz	Above 900 Hz

5. Optimization of AM Electrical Machines

Optimization in electrical machine design refers to the process of making improvements to the design of an electrical machine in order to maximize its performance and/or cost-effectiveness. To examine and optimize several aspects of the machine, including various parameters such as the shape of the machine, mathematical models and algorithms are often used. The goal is to find the optimal trade-off between design objectives and constraints, such as power density, torque density, efficiency, size, weight, cost, and materials. Generally, optimization techniques can be classified as deterministic and stochastic optimization. Deterministic optimization techniques, such as gradient-based methods, use a specific mathematical formula to find the optimal solution. They are fast and reliable but may be trapped in a local minimum while stochastic optimization techniques, such as genetic algorithms and particle swarm optimization use random processes to explore the solution space. They are less likely to get trapped in a local minimum but may be slower and less reliable [60]. The choice of method depends on the specific problem and requirements of the application.

Moreover, commonly used machine geometry templates and mathematical models for optimization are used to shape magnetic structures in electrical machines. These methods are well established and have been used for many years in the design and optimization of electrical machines. The use of these methods can make the design process more efficient and manageable, but it also restricts the design options to the predefined parameters, limiting the possible shapes and forms that can be generated. On the other hand, topology optimization (TO) is a more recent technique that involves the optimization of the overall layout and structure of the magnetic components in an electrical machine, rather than just the shape of individual components. For example, in the design of electrical machines, flux barriers inside the rotor or stator design spaces can be added and optimized for performance improvement. If the geometry optimization is utilized for the flux barriers, it increases the optimization variables and is not flexible to get the optimal shape [61–64]. Nevertheless, the TO approach can lead to more efficient and lightweight designs, but it is

generally more computationally intensive and requires specialized software [65–67]. The integration of TO and AM is demonstrated in the flowchart depicted in Figure 10.

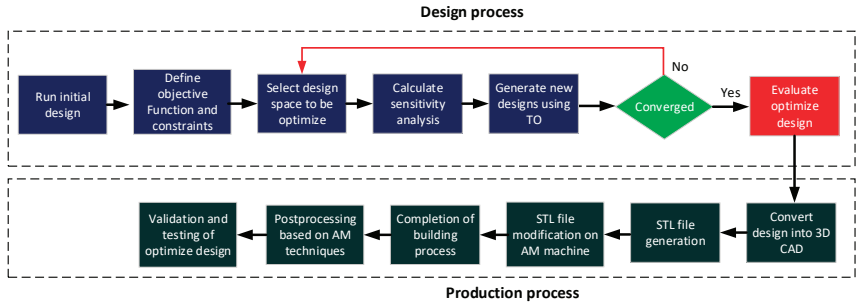


Figure 10. Steps involved for the TO and AM integration.

5.1. Topology Optimization of Reluctance Machines

The main objective of most TO studies for electric machines is to improve torque density and optimize the torque profile or cogging torque by adjusting the material distribution in the rotor. This can be achieved by using advanced optimization techniques and algorithms to find the optimal distribution of material in the rotor that results in the highest torque density or the desired torque profile [13]. Additionally, reluctance machines such as synchronous reluctance and switch reluctance machines have a simple construction compared to other types of electric machines, which makes them a good candidate for TO [13,68–71]. Despite receiving less attention, the TO of electric machine stator design has been reported in [72,73]. Different TO methods have been developed in the field of electrical machines during the last few years and these techniques may be broadly categorized into three groups: (i) the ON–OFF method, (ii) the Level set method, and (iii) the Material density method.

5.1.1. ON–OFF Method

The ON–OFF-based TO technique divides the design space into smaller cells and assigns each cell as either air (OFF) or iron (ON) through a discretization process using triangular or rectangular mesh structure [74]. This technique can be combined with various numerical optimization methods, such as evolutionary and gradient-based algorithms, to find approximate optimal solutions. In [75–78], evolutionary-based methods that do not require gradient information have been used. However, it may result in complex and non-intuitive shapes with isolated or disconnected regions of material, as shown in Figure 11a. This can lead to difficulties in fabrication or reduced performance of the final design. To overcome this issue, the author in [79–82] proposed the ON–OFF method with an immune algorithm to optimize the rotor of SRM, in which the filtering process is introduced to obtain the feasible shapes and improve the torque property as shown in Figure 11b.

In [64,83], ON–OFF-based normalized Gaussian network (NGNet) is presented to improve the torque density and reduce the iron losses. The output of the NGNet is determined by:

$$y(x) = \sum_{i=1}^{N} w_i b_i(x) \tag{1}$$

$$b_i(x) = G_i(x) \Big/ \sum_{j=1}^{N} G_j(x) \tag{2}$$

where G_i is the Gaussian function, w_i and b_i are the weight coefficient and normalized function, respectively. N represents the number of Gaussian functions and i, j is the number of cells. The state of the cells can be determined by:

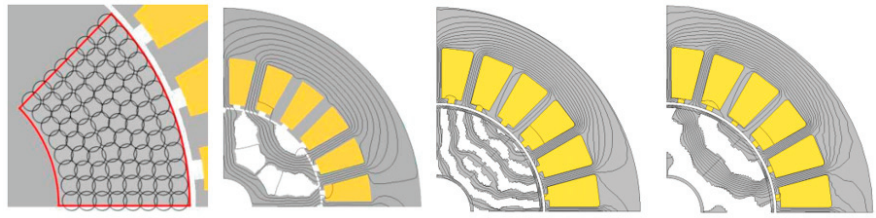
$$S_e = \begin{cases} on & y(x_e) \geq 0 \\ off & y(x_e) < 0 \end{cases} \quad (3)$$



(**a**) (**b**)

Figure 11. ON–OFF TO results: (**a**) without filter; (**b**) with filter using immune algorithm.

The material is configured to iron when the cell is in the on state, whereas it is configured to air when the cell is in the off state. Three different optimization problems were studied to improve the performance of the machine: (i) maximize torque; (ii) minimize iron losses with constraint of average torque; (iii) maximize average torque with constraint of iron losses. Furthermore, the Gaussian function distribution and the optimized design is shown in Figure 12a. There should be a tradeoff between the average torque and the iron losses because the wider rotor surface increases the torque, but also, the latter should be made smaller to reduce the iron losses. Another filtering technique, Gabor filter combined with ON–OFF method based on NGNet, is presented in [84]. The authors concluded that the proposed filter provided lower torque ripples as compared to the conventional NGNet, and the optimized design using filter gives the thinner flux barriers as depicted in Figure 12b. The main disadvantage of the abovementioned methods is the high computational cost because the FEA computation is needed at each generation [85].



(**a**) (**b**)

Figure 12. (**a**) Gaussian function distribution and optimized resulted shape; (**b**) Gabor filter and without filter [84].

The gradient based ON–OFF TO solves the problem of high computational cost but has the probability that it may stop on a local optimal solution. In [86], the gradient-based TO are applied to a 6/14 SRM to enhance the dynamic torque of the machine. The stator tooth is selected for the design space of the TO, then utilizes the method of adjoint gradients with respect to the material properties to optimize the material distribution for the reduction of torque ripples. The main drawback of this method is the difficulty in the evaluation of the non-differentiable functions [64].

5.1.2. Level Set Method

The level set method uses an implicit function known as the "level set function" to handle interfaces and shapes numerically. The level set method was first introduced in [87]

for the purpose of using it in TO to represent material boundaries. They demonstrated that this method can be used to design a cantilever beam with distinct boundaries without being dependent on a mesh or grayscale elements. Furthermore, the level set technique, which is based on gradients, produces a solution that is more practical for the given problem but lower convergence rate. In the level set TO, the material boundaries are shown in Figure 13a and computationally it can be defined as [88]:

$$\varphi(x,t) = \begin{cases} \varphi(x,t) > 0 & ferromagnetic\ material \\ \varphi(x,t) = 0 & boundary\ edge \\ \varphi(x,t) < 0 & Air \end{cases} \quad (4)$$

The objective of level set topology optimization is to find the optimal distribution of material in a design space to meet specific design objectives, by determining the value of $\varphi(x,t)$ at each location (x,t). In [89], the rotor of the synchronous reluctance machine was optimized using the level set method combined with the continuum sensitivity analysis. The objective function of the problem was to improve the torque of the machine by redistributing the magnetic material throughout the rotor design. The torque ripples profile of 8/6 pole SRM is enhanced by using the level set method, and sensitivity analysis having the adjoint variable method is utilized in [90]. In the optimized design, the average torque is improved by 12% with also the reduction in the torque ripples. The initial and optimized model with the torque waveform comparison is shown in Figure 13b. For reducing the iron losses and improving the torque of the synchronous reluctance machine, the level set method with sensitivity analysis of adjoint variable method is employed [91].

Additionally, this technique does not need the creation of intermediary materials or rely on the mesh that is used to discretize the design domain [92]. The level set approach for TO of EM devices has become quite well-liked as a result of these benefits [93]. However, this approach has certain limitations, including the need for an initial definition for the level set representation, convergence to local optima, and difficulties in computing the form gradients necessary to develop the interface [94].

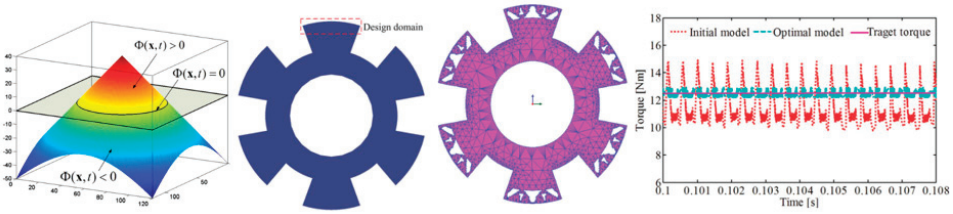


Figure 13. Level set TO: (**a**) Different domain of level set method [90]; (**b**) Initial and optimized model with torque waveform.

5.1.3. Material Density Method

The density method is a technique that was originally developed for solid mechanics TO [14]. It is a simple method that has recently gained popularity for electromagnetic TO, even for multi-material problems. This method is based on the idea of using a density function to represent the material distribution in the design domain, then using optimization algorithms to find the optimal density distribution that satisfies certain design constraints and objectives. This method has been found to be effective for a wide range of electromagnetic optimization problems and has been applied to a variety of different types of electromagnetic structures [70,73,95–98]. It is based on interpolation, filtering, and projection schemes, and originally used the simple power-law as the material penalization function. This leads to the SIMP (Solid Isotropic Material with Penalization) approach [99]. A schematic flowchart of procedures in the material density method is presented in Figure 14.

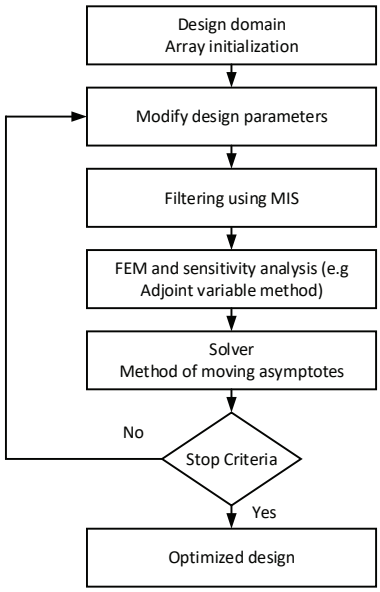


Figure 14. Flowchart of the TO using the material density-based method.

By solving the magnetic flux density and integrating the Maxwell tensor stress using (5) to determine torque, the material density approach is used to optimize the 8/6 pole rotor of the SRM [100].

$$T = \iint dAr \times (S.n) \tag{5}$$

The objective of the optimization problem is to determine the function density and is defined as:

$$\rho(x) = \begin{cases} 1 & x \epsilon \Omega_m \\ 0 & x \epsilon \Omega_a \end{cases} \tag{6}$$

where Ω_m and Ω_a represents the ferromagnetic region and air region, respectively. In the material density method, the $\rho(x)$ gives the values between 0 and 1 but practically, the distribution of the material is either 0 or 1, due to which the discontinuity exists in the final shape. To make the material distribution feasible, the magnetic reluctivity is defined by the smooth heaviside function [101]:

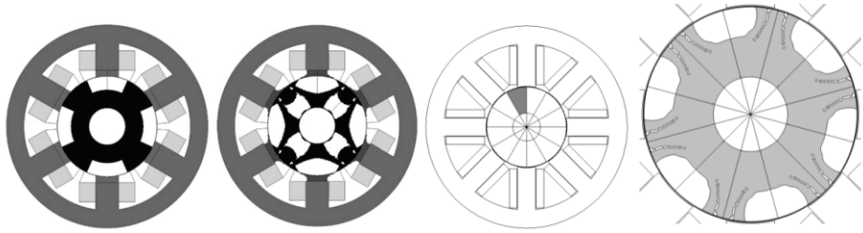
$$\rho(\psi) = \frac{3}{16}\left(\frac{\psi}{h}\right)^5 - \frac{5}{8}\left(\frac{\psi}{h}\right)^3 + \frac{3}{16}\left(\frac{\psi}{h}\right) + \frac{1}{2} \quad (-h \le \psi \le h) \tag{7}$$

where h represents the one half of the transition width between $\rho(-h) = 0$ and $\rho(h) = 1$. The magnetic reluctivity is defined as:

$$v_i\left(\psi_i, \left|B^2\right|\right) = (1 - \rho(\psi_i))^p * v_{air} + (\rho(\psi_i))^p \times v_F\left(\left|B^2\right|\right) \tag{8}$$

where $v_F\left(\left|B^2\right|\right)$ is the magnetic reluctivity and is a function of the mgnetic flux density and v_i, v_{air} is the reluctivity of the i^{th} element and reluctivity of air, respectively. The penalization coefficient is represented by the variable p. By choosing the proper value of p, the gray elements can be eliminated. In [102], the material density-based TO was utilized for the torque ripple minimization and the design space include the stator teeth and rotor poles. The optimized design showed a significant amount of reduction in the profile of torque ripple with the cost of a slight reduction of 7.22% in the average torque. In addition, the initial and optimized design of 6/4 pole SRM is depicted in Figure 15a. The TO of

material density was applied in [103] to minimize the torque ripple and the final design reach to the target torque value. The design space includes the half of the rotor pole as shown in Figure 15b, and after optimization, the torque reached the target value. The overview of TO applied to the reluctance machine for performance enhancement is shown in Table 3.



(**a**) (**b**)

Figure 15. (**a**) Initial and optimized design of 6/4 SRM; (**b**) Initial design geometry and optimized design.

Table 3. Summary of TO used in reluctance machines for performance improvement.

Machine Type	Optimization Method	Design Space	Objective Function	Prototype Fabrication	Reference
SRM	Material density method	Stator teeth and rotor poles	Min. torque ripples	Yes	[101]
SRM	Level set method	Rotor poles	Max. average torque and min. torque ripples	No	[89]
SynRM	Level set method	The rotor	Max. average torque	No	[88]
SynRM	ON-OFF	The rotor	Max. torque	No	[63]
SRM	NGNet	Stator teeth	Min. iron losses	No	[85]
SRM	Gradient based ON-OFF	The rotor	Min. torque ripples	No	[99]
SRM	Material density + GCMMA	The rotor	Max. torque	No	[102]
SynRM	Material density + GCMMA	The rotor	Max. torque	No	[83]
SRM	ON-OFF NGNet	The rotor	Max. torque	No	[78]
SynRM	Using Gabor filter	The rotor	Min. torque ripples	No	[74]

6. Challenges and Opportunities

AM and TO have the potential to revolutionize the way electrical machines are designed and manufactured. However, there are several challenges associated with the AM and TO of electrical machines, including:

Simulation Time and Geometry Complexity

The use of AM technology in the manufacturing of electrical machines is now facing significant challenges due to simulation time and geometric complexity. Additionally, the design of electrical machines is a non-convex optimization problem, meaning that gradient-based optimization techniques may not always produce the global optimal solution. In order to confront these challenges, researchers have come up with methods that utilize machine learning and deep learning to reduce simulation time and improve the accuracy of the global optimal solution. These techniques utilize the power of machine learning algorithms and deep neural networks to improve the simulation process and reduce the time required to find the optimal solution [85,104–107]. However, while these techniques have shown promise in reducing simulation time and improving the accuracy of the solution, they also require significant computational resources and specialized expertise to implement effectively.

Manufacturability

AM offers a solution to the challenges posed by TO designs with unpredictable characteristics, rough faces, and uneven material distribution that are difficult to manufacture using traditional methods. However, the current state of AM technology presents a challenge in achieving the desired performance, especially when it comes to magnetic materials,

which have low magnetic properties. Therefore, further development and improvement of AM technology is necessary to fully realize its potential in overcoming the limitations of optimized designs in traditional manufacturing methods.

Structural Integrity

TO is an important tool in the design of electromagnetic performance, but it has a significant limitation. It focuses primarily on improving electromagnetic performance and may result in designs that are not mechanically robust. Especially when it comes to synchronous reluctance machines, where the optimum design may have excessively thin ribs that are not practical from a structural integrity perspective. To overcome this limitation, it is necessary to perform a TO with structure analysis, which takes into account the mechanical restrictions of the machine. This will ensure that the optimized design is not only optimal in terms of electromagnetic performance but also has sufficient structural integrity.

Multi-Materials

To optimize different materials and manufacture multi-material machines, AM and TO are still in their early stages of development. As in case of reluctance machines, the materials are homogenous and the optimization process may be simplified. However, TO can become more difficult when dealing with multi-material machines, such as permanent magnet machines, since it is necessary to take into account various materials and their interactions. The usage of several materials may also lead to additional possible design alternatives and better performance characteristics, making it a desirable challenge for TO efforts. Despite notable developments in the area of AM, it is still very difficult for researchers to fabricate whole machines using this technology. Even while multi-material AM has been the subject of a few reports, it has not lived up to expectations. Future growth of this technology depends on the development of AM for manufacturing multi-material electrical machines.

To enhance the implementation of AM and TO in the design of electrical machines, research should focus on addressing these challenges. This could include developing new manufacturing techniques to produce the optimized designs, exploring new materials and designs to achieve the desired properties, and developing new optimization algorithms to reduce simulation time and complexity. Additionally, guidelines and design rules for the AM-based electric machine TO should be developed to assist designers in applying these techniques.

7. Conclusions

The paper reviewed various techniques used in modern AM and compared them, with a focus on the application of AM in the manufacturing of electric machines. In addition to highlighting examples of multi-material AM, also covered were various core and winding types that can be produced using AM. The paper also presented a detailed discussion on TO and how it can be used to optimize the design of electric machines for improved performance and reduced weight. Both gradient- and non-gradient-based TO methods are discussed, with an emphasis on reluctance machines. The ON–OFF TO produces complex geometries that are impossible to manufacture. To address these problems, various filtering techniques were used, and these were discussed in the study. The paper concluded that while the combination of AM and TO has the potential to fundamentally change the design of electrical machines, certain challenges such as manufacturability, geometric complexity, and structural integrity must be addressed before this technique can be feasibly adopted in practical machine designs. Overall, the paper suggests that there are many opportunities for future research in AM and TO to improve the design and manufacture of electric machines.

Author Contributions: Conceptualization, S.H. and A.K.; methodology, S.H. and A.K.; validation, S.H. and A.K.; writing—original draft preparation, S.H.; writing—review and editing, A.K. and T.V.; visualization, A.K. and S.H.; supervision, A.K.; project administration, A.K. All authors have read and agreed to the published version of the manuscript.

Funding: This work was supported by the Estonian Research Council grant (PRG-1827).

Data Availability Statement: All data related to this work are included in this article.

Conflicts of Interest: The authors declare no conflict of interest.

References

1. Madonna, V.; Migliazza, G.; Giangrande, P.; Lorenzani, E.; Buticchi, G.; Galea, M. The Rebirth of the Current Source Inverter: Advantages for Aerospace Motor Design. *IEEE Ind. Electron. Mag.* **2019**, *13*, 65–76. [CrossRef]
2. Madonna, V.; Giangrande, P.; Migliazza, G.; Buticchi, G.; Galea, M. A Time-Saving Approach for the Thermal Lifetime Evaluation of Low-Voltage Electrical Machines. *IEEE Trans. Ind. Electron.* **2019**, *67*, 9195–9205. [CrossRef]
3. Giangrande, P.; Madonna, V.; Nuzzo, S.; Galea, M. Moving Toward a Reliability-Oriented Design Approach of Low-Voltage Electrical Machines by Including Insulation Thermal Aging Considerations. *IEEE Trans. Transp. Electrification* **2020**, *6*, 16–27. [CrossRef]
4. Guo, N.; Leu, M.C. Additive manufacturing: Technology, applications and research needs. *Front. Mech. Eng.* **2013**, *8*, 215–243. [CrossRef]
5. Naseer, M.U.; Kallaste, A.; Asad, B.; Vaimann, T.; Rassõlkin, A. A Review on Additive Manufacturing Possibilities for Electrical Machines. *Energies* **2021**, *14*, 1940. [CrossRef]
6. Ian, G.; Rosen, D.; Stucker, B. Rapid tooling. In *Additive Manufacturing Technologies: 3D Printing, Rapid Prototyping, and Direct Digital Manufacturing*; Springer: Berlin/Heidelberg, Germany, 2015; pp. 437–449.
7. Wu, F.; El-Refaie, A.M. Towards fully additively manufactured permanent magnet synchronous machines: Opportunities and challenges. In Proceedings of the 2019 IEEE International Electric Machines & Drives Conference (IEMDC), San Diego, CA, USA, 12–15 May 2019; IEEE: Piscataway, NJ, USA, 2019; pp. 2225–2232.
8. Tiismus, H.; Kallaste, A.; Belahcen, A.; Rassõlkin, A.; Vaimann, T. Challenges of additive manufacturing of electrical machines. In Proceedings of the 2019 IEEE 12th International Symposium on Diagnostics for Electrical Machines, Power Electronics and Drives (SDEMPED), Toulouse, France, 27–30 August 2019; IEEE: Piscataway, NJ, USA, 2019; pp. 44–48.
9. Abetti, P.A.; Cuthbertson, W.J.; Williams, S.B. Philosophy of applying digital computers to the design of electric apparatus. *Trans. Am. Inst. Electr. Eng. Part I Commun. Electron.* **1958**, *77*, 367–379. [CrossRef]
10. Bramerdorfer, G.; Tapia, J.A.; Pyrhönen, J.J.; Cavagnino, A. Modern electrical machine design optimization: Techniques, trends, and best practices. *IEEE Trans. Ind. Electron.* **2018**, *65*, 7672–7684. [CrossRef]
11. Orosz, T. Evolution and Modern Approaches of the Power Transformer Cost Optimization Methods. *Period. Polytech. Electr. Eng. Comput. Sci.* **2019**, *63*, 37–50. [CrossRef]
12. Sizov, G.Y.; Ionel, D.M.; Demerdash, N.A.O. Modeling and design optimization of PM AC machines using computationally efficient—Finite element analysis. In Proceedings of the 2010 IEEE Energy Conversion Congress and Exposition, Atlanta, GA, USA, 12–16 September 2010; IEEE: Piscataway, NJ, USA, 2010; pp. 578–585.
13. Wang, B. Topology Optimization of Electric Machines: A Review. In Proceedings of the 2022 IEEE Energy Conversion Congress and Exposition (ECCE), Detroit, MI, USA, 9–13 October 2022; IEEE: Piscataway, NJ, USA, 2022; pp. 1–8.
14. Bendsøe, M.P. Optimal shape design as a material distribution problem. *Struct. Multidiscip. Optim.* **1989**, *1*, 193–202. [CrossRef]
15. Wu, F.; El-Refaie, A.M. Toward Additively Manufactured Electrical Machines: Opportunities and Challenges. *IEEE Trans. Ind. Appl.* **2019**, *56*, 1306–1320. [CrossRef]
16. Wohlers, T.T. *Wohlers Report: 3D Printing and Additive Manufacturing, State of the Industry, Annual Worldwide Progress Report*; Wohlers Associates Incorporated: Washington, DC, USA, 2014.
17. Lamichhane, T.N.; Sethuraman, L.; Dalagan, A.; Wang, H.; Keller, J.; Paranthaman, M.P. Additive manufacturing of soft magnets for electrical machines—A review. *Mater. Today Phys.* **2020**, *15*, 100255. [CrossRef]
18. Ngo, T.D.; Kashani, A.; Imbalzano, G.; Nguyen, K.T.; Hui, D. Additive manufacturing (3D printing): A review of materials, methods, applications and challenges. *Compos. Part B Eng.* **2018**, *143*, 172–196. [CrossRef]
19. Available online: https://www.interempresas.net/FeriaVirtual/Catalogos_y_documentos/244423/pl1uk14-lasertec-65-3d-pdf-data.pdf (accessed on 12 April 2023).
20. Gibson, I.; Rosen, D.; Stucker, B. Directed energy deposition processes. In *Additive Manufacturing Technologies*; Springer: Berlin/Heidelberg, Germany, 2015; pp. 245–268.
21. Chen, X.; Shang, X.; Zhou, Z.; Chen, S.-G. A Review of the Development Status of Wire Arc Additive Manufacturing Technology. *Adv. Mater. Sci. Eng.* **2022**, *2022*, 1–28. [CrossRef]
22. Available online: https://3dprinting.com/news/joule-printing-by-digital-alloys-fast-and-low-cost-metal-printing/ (accessed on 12 April 2023).
23. Klobcar, D.; Baloš, S.; Bašic, M.; Djuric, A.; Lindic, M.; Ščetinec, A. WAAM and Other Unconventional Metal Additive Manufacturing Technologies. *Adv. Technol. Mater* **2020**, *45*, 1–9. [CrossRef]
24. Bali, M. Magnetic material degradation due to different cutting techniques and its modeling for electric machine design. In Proceedings of the More Drive 2017: "Megatrend Effizienz" in Industrie und Mobilität, Wien, Austria, 26 January 2017.
25. Jack, A.; Mecrow, B.; Dickinson, P.; Stephenson, D.; Burdess, J.; Fawcett, N.; Evans, J. Permanent-magnet machines with powdered iron cores and prepressed windings. *IEEE Trans. Ind. Appl.* **2000**, *36*, 1077–1084. [CrossRef]

26. Szabó, L.; Fodor, D. The Key Role of 3D Printing Technologies in the Further Development of Electrical Machines. *Machines* **2022**, *10*, 330. [CrossRef]
27. Tiismus, H.; Kallaste, A.; Vaimann, T.; Rassõlkin, A. State of the art of additively manufactured electromagnetic materials for topology optimized electrical machines. *Addit. Manuf.* **2022**, *55*, 102778. [CrossRef]
28. Stornelli, G.; Faba, A.; Di Schino, A.; Folgarait, P.; Ridolfi, M.R.; Cardelli, E.; Montanari, R. Properties of Additively Manufactured Electric Steel Powder Cores with Increased Si Content. *Materials* **2021**, *14*, 1489. [CrossRef]
29. Metsä-Kortelainen, S.; Lindroos, T.; Savolainen, M.; Jokinen, A.; Revuelta, A.; Pasanen, A.; Ruusuvuori, K.; Pippuri, J. Manufacturing of topology optimized soft magnetic core through 3D printing. In Proceedings of the NAFEMS Exploring the Design Freedom of Additive Manufacturing through Simulation, Helsinki, Finland, 22–23 November 2016.
30. Cramer, C.L.; Nandwana, P.; Yan, J.; Evans, S.F.; Elliott, A.M.; Chinnasamy, C.; Paranthaman, M.P. Binder jet additive manufacturing method to fabricate near net shape crack-free highly dense Fe-6.5 wt.% Si soft magnets. *Heliyon* **2019**, *5*, e02804. [CrossRef]
31. Kustas, A.B.; Susan, D.F.; Johnson, K.L.; Whetten, S.R.; Rodriguez, M.A.; Dagel, D.J.; Michael, J.R.; Keicher, D.M.; Argibay, N. Characterization of the Fe-Co-1.5 V soft ferromagnetic alloy processed by Laser Engineered Net Shaping (LENS). *Addit. Manuf.* **2018**, *21*, 41–52.
32. Kustas, A.B.; Fancher, C.M.; Whetten, S.R.; Dagel, D.J.; Michael, J.R.; Susan, D.F. Controlling the extent of atomic ordering in intermetallic alloys through additive manufacturing. *Addit. Manuf.* **2019**, *28*, 772–780. [CrossRef]
33. Riipinen, T.; Metsä-Kortelainen, S.; Lindroos, T.; Keränen, J.S.; Manninen, A.; Pippuri-Mäkeläinen, J. Properties of soft magnetic Fe-Co-V alloy produced by laser powder bed fusion. *Rapid Prototyp. J.* **2019**, *25*, 699–707. [CrossRef]
34. Nam, Y.G.; Koo, B.; Chang, M.S.; Yang, S.; Yu, J.; Park, Y.H.; Jeong, J.W. Selective laser melting vitrification of amorphous soft magnetic alloys with help of double-scanning-induced compositional homogeneity. *Mater. Lett.* **2020**, *261*, 127068. [CrossRef]
35. Pham, T.Q.; Foster, S.N. Additive Manufacturing of Non-homogeneous Magnetic Cores for Electrical Machines Opportunities and Challenges. In Proceedings of the 2020 International Conference on Electrical Machines (ICEM), Gothenburg, Sweden, 23–26 August 2020; 2020; Volume 1, pp. 1623–1629.
36. Gibson, I.; Rosen, D.; Stucker, B.; Khorasani, M. *Additive Manufacturing Technologies*; Springer: Berlin/Heidelberg, Germany, 2021.
37. Shokrollahi, H.; Janghorban, K. Soft magnetic composite materials (SMCs). *J. Mater. Process. Technol.* **2007**, *189*, 1–12. [CrossRef]
38. Zhang, Z.-Y.; Jhong, K.J.; Cheng, C.-W.; Huang, P.-W.; Tsai, M.-C.; Lee, W.-H. Metal 3D printing of synchronous reluctance motor. In Proceedings of the 2016 IEEE International Conference on Industrial Technology (ICIT), Taipei, Taiwan, 14–17 March 2016; IEEE: Piscataway, NJ, USA, 2016; pp. 1125–1128.
39. Gargalis, L.; Madonna, V.; Giangrande, P.; Rocca, R.; Hardy, M.; Ashcroft, I.; Galea, M.; Hague, R. Additive Manufacturing and Testing of a Soft Magnetic Rotor for a Switched Reluctance Motor. *IEEE Access* **2020**, *8*, 206982–206991. [CrossRef]
40. Gargalis, L.; Madonna, V.; Giangrande, P.; Rocca, R.; Ashcroft, I.; Hague, R.; Galea, M. Development and Testing of Soft Magnetic Rotor for a Switched Reluctance Motor Built Through Additive Manufacturing Technology. In Proceedings of the 2020 23rd International Conference on Electrical Machines and Systems (ICEMS), Hamamatsu, Japan, 24–27 November 2020; IEEE: Piscataway, NJ, USA, 2020; pp. 263–268.
41. Tseng, G.-M.; Jhong, K.-J.; Tsai, M.-C.; Huang, P.-W.; Lee, W.-H. Application of additive manufacturing for low torque ripple of 6/4 switched reluctance motor. In Proceedings of the 2016 19th International Conference on Electrical Machines and Systems (ICEMS), Chiba, Japan, 13–16 November 2016; IEEE: Piscataway, NJ, USA, 2016; pp. 1–4.
42. Tiismus, H.; Kallaste, A.; Vaimann, T.; Rassõlkin, A.; Belahcen, A. Additive Manufacturing of Prototype Axial Flux Switched Reluctance Electrical Machine. In Proceedings of the 2021 28th International Workshop on Electric Drives: Improving Reliability of Electric Drives (IWED), Moscow, Russia, 27–29 January 2021; IEEE: Piscataway, NJ, USA, 2021; pp. 1–4.
43. Tiismus, H.; Kallaste, A.; Belahcen, A.; Rassõlkin, A.; Vaimann, T. Hysteresis loss evaluation of additively manufactured soft magnetic core. In Proceedings of the 2020 International Conference on Electrical Machines (ICEM), Gothenburg, Sweden, 23–26 August 2020; IEEE: Piscataway, NJ, USA, 2020; Volume 1, pp. 1657–1661.
44. Tiismus, H.; Kallaste, A.; Naseer, M.U.; Vaimann, T.; Rassolkin, A. Design and Performance of Laser Additively Manufactured Core Induction Motor. *IEEE Access* **2022**, *10*, 50137–50152. [CrossRef]
45. Elektrimootor, F. Available online: https://www.felandia.eu/media/veelandia/product/eu.erply.com/1052-ms-561-4-0-06_tehnilised_andmed_v1.pdf (accessed on 9 May 2022).
46. Huang, P.-W.; Tsai, M.-C.; Jiang, I.-H. 3-D structure line-start synchronous reluctance motor design based on selective laser melting of 3-D printing. *IEEE Trans. Magn.* **2018**, *54*, 1–4.
47. Lorenz, F.; Rudolph, J.; Werner, R. High temperature operation and increased cooling capabilities of switched reluctance machines using 3D printed ceramic insulated coils. In Proceedings of the 2018 IEEE transportation electrification conference and expo (ITEC), Long Beach, CA, USA, 13–15 June 2018; IEEE: Piscataway, NJ, USA, 2018; pp. 400–405.
48. Lynch, M.E.; Tangudu, J.; Jagdale, V.; El-Wardany, T.I.; Schmidt, W.R.; Veronesi, W.A. Strand Cross-Section for High Fill-Factor Electric Machine Windings. U.S. Patent Application 14/450,520, 4 February 2016.
49. Jagdale, V.; Tangudu, J. *Topology Optimized End Winding for Additively Manufactured Induction Motor with Distributed Winding*; SAE Technical Paper; SAE: Warrendale, PA, USA, 2016.
50. Wawrzyniak, B.I.; Tangudu, J. *Design Analysis of High Power Density Additively Manufactured Induction Motor*; SAE Technical Paper; SAE: Warrendale, PA, USA, 2016.

51. Wohlers, C.; Juris, P.; Kabelac, S.; Ponick, B. Design and direct liquid cooling of tooth-coil windings. *Electr. Eng.* **2018**, *100*, 2299–2308. [CrossRef]
52. Ayat, S.; Simpson, N.; Daguse, B.; Rudolph, J.; Lorenz, F.; Drury, D. Design of Shaped-Profile Electrical Machine Windings for Multi-Material Additive Manufacture. In Proceedings of the 2020 International Conference on Electrical Machines (ICEM), Gothenburg, Sweden, 23–26 August 2020; 2020; Volume 1, pp. 1554–1559.
53. Lorenz, F.; Rudolph, J.; Wemer, R. Design of 3D printed High Performance Windings for switched reluctance machines. In Proceedings of the 2018 XIII International Conference on Electrical Machines (ICEM), Alexandroupoli, Greece, 3–6 September 2018; IEEE: Piscataway, NJ, USA, 2018; pp. 2451–2457.
54. Trnka, N.; Rudolph, J.; Werner, R. Magnetic properties of ferromagnetic materials produced by 3D multi-material printing. In Proceedings of the 2020 IEEE 29th International Symposium on Industrial Electronics (ISIE), Delft, The Netherlands, 17–19 June 2020; IEEE: Piscataway, NJ, USA, 2020; pp. 326–331.
55. Available online: https://www.tu-chemnitz.de/etit/ema/AMMM/ (accessed on 12 April 2023).
56. Simpson, N.; Jung, J.; Helm, A.; Mellor, P. Additive manufacturing of a conformal hybrid-strand concentrated winding topology for minimal AC loss in electrical machines. In Proceedings of the 2021 IEEE Energy Conversion Congress and Exposition (ECCE), Vancouver, BC, Canada, 10–14 October 2021; IEEE: Piscataway, NJ, USA, 2021; pp. 3844–3851.
57. Selema, A.; Ibrahim, M.N.; Sergeant, P. Additively-Manufactured Ultra-Light Shaped-Profile Windings for HF Electrical Machines and Weight-Sensitive Applications. *IEEE Trans. Transp. Electrif.* **2022**, *8*, 4313–4324. [CrossRef]
58. Ghahfarokhi, P.S.; Podgornovs, A.; Kallaste, A.; Cardoso, A.J.M.; Belahcen, A.; Vaimann, T.; Tiismus, H.; Asad, B. Opportunities and challenges of utilizing additive manufacturing approaches in thermal management of electrical machines. *IEEE Access* **2021**, *9*, 36368–36381. [CrossRef]
59. Sarap, M.; Kallaste, A.; Ghahfarokhi, P.S.; Tiismus, H.; Vaimann, T. Utilization of Additive Manufacturing in the Thermal Design of Electrical Machines: A Review. *Machines* **2022**, *10*, 251. [CrossRef]
60. Cavazzuti, M. *Optimization Methods: From Theory to Design Scientific and Technological Aspects in Mechanics*; Springer: Berlin/Heidelberg, Germany, 2012.
61. Cupertino, F.; Pellegrino, G.; Gerada, C. Design of synchronous reluctance motors with multiobjective optimization algorithms. *IEEE Trans. Ind. Appl.* **2014**, *50*, 3617–3627. [CrossRef]
62. Barta, J.; Ondrusek, C. Rotor Design And Optimization Of Synchronous Reluctance Machine. *MM Sci. J.* **2015**, *2015*, 555–559. [CrossRef]
63. Pellegrino, G.; Cupertino, F.; Gerada, C. Barriers shapes and minimum set of rotor parameters in the automated design of Synchronous Reluctance machines. In Proceedings of the 2013 International Electric Machines & Drives Conference, Chicago, IL, USA, 12–15 May 2013; IEEE: Piscataway, NJ, USA, 2013; pp. 1204–1210.
64. Sato, S.; Sato, T.; Igarashi, H. Topology Optimization of Synchronous Reluctance Motor Using Normalized Gaussian Network. *IEEE Trans. Magn.* **2015**, *51*, 8200904. [CrossRef]
65. Kano, Y.; Terahai, T.; Kosaka, T.; Matsui, N.; Nakanishi, T. A new flux-barrier design of torque ripple reduction in saliency-based sensorless drive IPM motors for general industrial applications. In Proceedings of the 2009 IEEE Energy Conversion Congress and Exposition, San Jose, CA, USA, 20–24 September 2009; IEEE: Piscataway, NJ, USA, 2009; pp. 1939–1945.
66. Fei, W.; Luk, P.C.K.; Shen, J.X.; Xia, B.; Wang, Y. Permanent-magnet flux-switching integrated starter generator with different rotor configurations for cogging torque and torque ripple mitigations. *IEEE Trans. Ind. Appl.* **2011**, *47*, 1247–1256.
67. Valavi, M.; Nysveen, A.; Nilssen, R. Characterization of radial magnetic forces in low-speed permanent magnet wind generator with non-overlapping concentrated windings. In Proceedings of the 2012 XXth International Conference on Electrical Machines, Marseille, France, 2–5 September 2012; IEEE: Piscataway, NJ, USA, 2012; pp. 2943–2948.
68. Credo, A.; Fabri, G.; Villani, M.; Popescu, M. Adopting the Topology Optimization in the Design of High-Speed Synchronous Reluctance Motors for Electric Vehicles. *IEEE Trans. Ind. Appl.* **2020**, *56*, 5429–5438. [CrossRef]
69. Guo, F.; Brown, I.P. Simultaneous Magnetic and Structural Topology Optimization of Synchronous Reluctance Machine Rotors. *IEEE Trans. Magn.* **2020**, *56*, 1–12. [CrossRef]
70. Korman, O.; Di Nardo, M.; Degano, M.; Gerada, C. On the Use of Topology Optimization for Synchronous Reluctance Machines Design. *Energies* **2022**, *15*, 3719. [CrossRef]
71. Cederlund, J.; Nategh, S.; Lennström, D. Topology Optimization of Electrical Machines for NVH Purposes in E-mobility Applications-Part 1. In Proceedings of the IECON 2021–47th Annual Conference of the IEEE Industrial Electronics Society, online, 13–16 October 2021; IEEE: Piscataway, NJ, USA, 2021; pp. 1–6.
72. Choi, J.S.; Izui, K.; Nishiwaki, S.; Kawamoto, A.; Nomura, T. Topology Optimization of the Stator for Minimizing Cogging Torque of IPM Motors. *IEEE Trans. Magn.* **2011**, *47*, 3024–3027. [CrossRef]
73. Thabuis, A.; Ren, X.; Burnand, G.; Perriard, Y. Density-Based Topology Optimization of Conductor Paths for Windings in Slotted Electrical Machines. In Proceedings of the 2019 22nd International Conference on Electrical Machines and Systems (ICEMS), Harbin, China, 11–14 August 2019; IEEE: Piscataway, NJ, USA, 2019; pp. 1–6.
74. Zhao, F.; Yan, R. Topology Optimization of Magnetic Actuator Using the Improved ON/OFF Method. In Proceedings of the 2012 Sixth International Conference on Electromagnetic Field Problems and Applications, Dalian, China, 19–21 June 2012; IEEE: Piscataway, NJ, USA, 2012; pp. 1–4.

75. Watanabe, K.; Suga, T.; Kitabatake, S. Topology Optimization Based on the ON/OFF Method for Synchronous Motor. *IEEE Trans. Magn.* **2017**, *54*, 1–4. [CrossRef]
76. Ishikawa, T.; Nakayama, K.; Kurita, N.; Dawson, F.P. Optimization of Rotor Topology in PM Synchronous Motors by Genetic Algorithm Considering Cluster of Materials and Cleaning Procedure. *IEEE Trans. Magn.* **2014**, *50*, 637–640. [CrossRef]
77. Takahashi, N.; Yamada, T.; Shimose, S.; Miyagi, D. Optimization of rotor of actual IPM motor using ON/OFF method. *IEEE Trans. Magn.* **2011**, *47*, 1262–1265. [CrossRef]
78. Choi, N.-S.; Kim, D.-H.; Lee, H.-B.; Byun, J.-K. Topology Optimization of Dielectric Resonator in 3-D Waveguide Structure Considering Higher Mode Incidence. *IEEE Trans. Magn.* **2012**, *48*, 559–562. [CrossRef]
79. Shiyang, F.; Watanabe, K. Topology optimization of rotor design in switched reluctance motor using immune algorithm. *Int. J. Appl. Electromagn. Mech.* **2020**, *64*, 413–420. [CrossRef]
80. Watanabe, K.; Campelo, F.; Igarashi, H. Topology optimization based on immune algorithm and multigrid method. *IEEE Trans. Magn.* **2007**, *43*, 1637–1640. [CrossRef]
81. Watanabe, K.; Campelo, F.; Iijima, Y.; Kawano, K.; Matsuo, T.; Mifune, T.; Igarashi, H. Optimization of Inductors Using Evolutionary Algorithms and Its Experimental Validation. *IEEE Trans. Magn.* **2010**, *46*, 3393–3396. [CrossRef]
82. Midha, C.; Mohammadi, M.H.; Silva, R.C.P.; Lowther, D.A. Selection of Spatial Filters for ON/OFF Based Topology Optimization of a C-Core Electromagnetic Actuator. *IEEE Trans. Magn.* **2019**, *55*, 1–4. [CrossRef]
83. Sato, T.; Watanabe, K.; Igarashi, H. Multimaterial Topology Optimization of Electric Machines Based on Normalized Gaussian Network. *IEEE Trans. Magn.* **2015**, *51*, 7202604. [CrossRef]
84. Otomo, Y.; Igarashi, H. Topology Optimization Using Gabor Filter: Application to Synchronous Reluctance Motor. *IEEE Trans. Magn.* **2021**, *57*, 1–4. [CrossRef]
85. Sasaki, H.; Igarashi, H. Topology Optimization Accelerated by Deep Learning. *IEEE Trans. Magn.* **2019**, *55*, 7401305. [CrossRef]
86. Sayed, E.; Bakr, M.H.; Bilgin, B.; Emadi, A. Gradient-Based Design Optimization of a Switched Reluctance Motor for an HVAC Application. In Proceedings of the 2020 IEEE Transportation Electrification Conference & Expo (ITEC), Detroit, MI, USA, 23–26 June 2020; IEEE: Piscataway, NJ, USA, 2020; pp. 1031–1037.
87. Sethian, J.A.; Wiegmann, A. Structural Boundary Design via Level Set and Immersed Interface Methods. *J. Comput. Phys.* **2000**, *163*, 489–528. [CrossRef]
88. Osher, S.; Fedkiw, R.P. Level Set Methods: An Overview and Some Recent Results. *J. Comput. Phys.* **2001**, *169*, 463–502. [CrossRef]
89. Kim, Y.S.; Park, I.H. Topology Optimization of Rotor in Synchronous Reluctance Motor Using Level Set Method and Shape Design Sensitivity. *IEEE Trans. Appl. Supercond.* **2010**, *20*, 1093–1096.
90. Zhang, H.; Wang, S. Topology Optimization of Rotor Pole in Switched Reluctance Motor for Minimum Torque Ripple. *Electr. Power Components Syst.* **2017**, *45*, 905–911. [CrossRef]
91. Yamashita, Y.; Okamoto, Y. Design Optimization of Synchronous Reluctance Motor for Reducing Iron Loss and Improving Torque Characteristics Using Topology Optimization Based on the Level-Set Method. *IEEE Trans. Magn.* **2020**, *56*, 1–4. [CrossRef]
92. Park, S.-I.; Min, S.; Yamasaki, S.; Nishiwaki, S.; Yoo, J. Magnetic Actuator Design Using Level Set Based Topology Optimization. *IEEE Trans. Magn.* **2008**, *44*, 4037–4040. [CrossRef]
93. Campelo, F.; Ramirez, J.; Igarashi, H. A survey of topology optimization in electromagnetics: Considerations and current trends. *Academia* **2010**, *46*, 2010.
94. Midha, C. *A Study of Topology Optimization Methods for the Design of Electromagnetic Devices*; McGill University: Quebec City, QC, Canada, 2019.
95. Luo, J.; Luo, Z.; Chen, L.; Tong, L.; Wang, M.Y. A semi-implicit level set method for structural shape and topology optimization. *J. Comput. Phys.* **2008**, *227*, 5561–5581. [CrossRef]
96. Sanogo, S.; Messine, F.; Henaux, C.; Vilamot, R. Topology Optimization for Magnetic Circuits Dedicated to Electric Propulsion. *IEEE Trans. Magn.* **2014**, *50*, 1–13. [CrossRef]
97. Mohamodhosen, B.B.S.; Gillon, F.; Tounzi, M.; Chevallier, L. Topology optimisation using nonlinear behaviour of ferromagnetic materials. *COMPEL Int. J. Comput. Math. Electr. Electron. Eng.* **2018**, *37*, 2211–2223. [CrossRef]
98. Gauthey, T.; Gangl, P.; Hassan, M.H. Multi-Material Topology Optimization with Continuous Magnetization Direction for Permanent Magnet Synchronous Reluctance Motors. *arXiv* **2021**, arXiv:2107.04825.
99. Rozvany, G.I.; Zhou, M.; Birker, T. Generalized shape optimization without homogenization. *Struct. Optim.* **1992**, *4*, 250–252. [CrossRef]
100. Manninen, A.; Keränen, J.; Pippuri-Mäkeläinen, J.; Metsä-Kortelainen, S.; Riipinen, T.; Lindroos, T. Topology Optimization for Additive Manufacturing of Switced Reluctance Machines. In Proceedings of the 18th Biennial IEEE Conference Electromagnetic Field Computation (CEFC), Hangzhou, China, 28–31 October 2018.
101. Okamoto, Y.; Hoshino, R.; Wakao, S.; Tsuburaya, T. Improvement of Torque Characteristics For a Synchronous Reluctance Motor Using MMA-based Topology Optimization Method. *IEEE Trans. Magn.* **2017**, *54*, 1–4. [CrossRef]
102. Lee, J.; Seo, J.H.; Kikuchi, N. Topology optimization of switched reluctance motors for the desired torque profile. *Struct. Multidiscip. Optim.* **2010**, *42*, 783–796. [CrossRef]
103. Manninen, A.; Keränen, J.; Pippuri-Mäkeläinen, J.; Riipinen, T.; Metsä-Kortelainen, S.; Lindroos, T. Impact of topology optimization problem setup on switched reluctance machine design. In Proceedings of the 2019 22nd International Conference on the Computation of Electromagnetic Fields (COMPUMAG), Paris, France, 15–19 June 2019; IEEE: Piscataway, NJ, USA, 2019; pp. 1–4.

104. Tahkola, M.; Keranen, J.; Sedov, D.; Far, M.F.; Kortelainen, J. Surrogate Modeling of Electrical Machine Torque Using Artificial Neural Networks. *IEEE Access* **2020**, *8*, 220027–220045. [CrossRef]
105. Sasaki, H.; Igarashi, H. Topology optimization of IPM motor with aid of deep learning. *Int. J. Appl. Electromagn. Mech.* **2019**, *59*, 87–96. [CrossRef]
106. Asanuma, J.; Doi, S.; Igarashi, H. Transfer Learning Through Deep Learning: Application to Topology Optimization of Electric Motor. *IEEE Trans. Magn.* **2020**, *56*, 1–4. [CrossRef]
107. Doi, S.; Sasaki, H.; Igarashi, H. Multi-Objective Topology Optimization of Rotating Machines Using Deep Learning. *IEEE Trans. Magn.* **2019**, *55*, 7202605. [CrossRef]

Disclaimer/Publisher's Note: The statements, opinions and data contained in all publications are solely those of the individual author(s) and contributor(s) and not of MDPI and/or the editor(s). MDPI and/or the editor(s) disclaim responsibility for any injury to people or property resulting from any ideas, methods, instructions or products referred to in the content.

Publication II

S. Hussain, A. Kallaste, M. U. Naseer, Z. Ahmad, and T. Vaimann, "Topology Optimization of Outer Rotor BLDC Motor for Electric Scooter Application," in *2026 IEEE International Magnetic Conference—Short Papers (INTERMAG Short Papers)*, Manchester, United Kingdom, 2026, pp. 1–2, doi: 10.1109/INTERMAGShortPapers68882.2026.11596512.

2026 IEEE International Magnetic Conference - Short Papers (INTERMAG Short Papers) | 979-8-3315-5762-1/26/$31.00 ©2026 IEEE | DOI: 10.1109/INTERMAGSHORTPAPERS68882.2026.11596512

Topology Optimization of Outer Rotor BLDC Motor for Electric Scooter Application

Shahid Hussain[1], Ants Kallaste[1], Muhammad Usman Naseer[1], Zahoor Ahmad[1] and Toomas Vaimann[1]

[1]Department of Electrical Power Engineering and Mechatronics, Tallinn University of Technology, Estonia

This paper presents a topology optimization method for the rotor back iron of outer rotor permanent magnet BLDC motors especially for EV scooter applications. The method uses a normalized Gaussian network to parametrically represent material distribution and to remove iron from regions of low flux utilization while preserving practical manufacturability. For the benchmark machine, the proposed optimization yields a distinctly lighter rotor and improved torque density while preserving back-EMF and torque waveform performance. The proposed methodology and the corresponding results are discussed in detail.

***Index Terms*—Brushless DC motor, genetic algorithm, NGNet, topology optimization**

I. Introduction

Electric two-wheeler applications, particularly EV scooters, increasingly adopt outer rotor BLDC motors due to their high torque density and compact wheel hub integration. However, lightweight design and high efficiency requirements under urban driving cycles impose stringent constraints on rotor magnetic material utilization and saturation behavior, motivating the need for advanced design methodologies beyond conventional parametric optimization approaches.

Topology Optimization (TO) provides a systematic approach for improving electromagnetic performance by allowing non-uniform magnetic material distribution based on magnetic field characteristics. Among various TO methods, the on–off approach based on the Normalized Gaussian Network (NGNet) represents design geometries using Gaussian basis functions and has been successfully applied to electric machine design, including permanent magnet motors and synchronous reluctance motors [1] [2]. To reduce magnetic saturation and improve torque performance, this method exhibits the global optimal shapes without the need of filtering process [3][4].

This paper presents a back iron optimization of an outer rotor BLDC motor, in which magnetic material is removed from regions with low flux utilization to reduce rotor weight. By maintaining electromagnetic performance while decreasing rotor mass, the proposed approach improves torque density and enables more efficient utilization of magnetic material.

II. Optimization Method

Efficient utilization of magnetic material requires careful identification and design of the rotor flux-carrying regions. TO is employed to determine the optimal material distribution without prescribing explicit geometric parameters. In the proposed approach, Gaussian basis functions are distributed over the design domain, and the resulting material layout is governed by a shape function expressed as

$$y(x,w) = \sum_{i=1}^{N} w_i b_i(x) \tag{1}$$

where w_i denotes the weighting factor, x represents the spatial position vector, and N is the total number of Gaussian basis functions. The term refers to the normalized Gaussian basis function, which is defined as

$$b_i(x) = \frac{G_i(x)}{\sum_{k=1}^{N} G_k(x)} \tag{2}$$

$$G_k(x) = \frac{1}{2\pi\sigma^2} exp\left[-\frac{||x - x_i||^2}{2\sigma^2}\right] \tag{3}$$

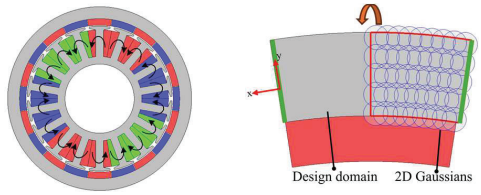
where x_i denote the center location of the kth Gaussian basis function and σ^2 represents the variance, respectively. Based on this formulation, the material property S_e can be

$$S_e = \begin{cases} 0, & air, \quad y < 0 \\ 1, & iron, \quad y \geq 0 \end{cases} \tag{4}$$

The resulting material layout is governed by the parameter vector w, which is optimized to maximize the objective function.

III. Problem Setting

To optimize the rotor back iron, an 18-slot, 20-pole outer rotor permanent magnet motor is considered as a benchmark, as shown in Fig. 1(a). Owing to the periodic symmetry of the machine, only one sector of the rotor is modeled for the optimization study, as illustrated in Fig. 1(b). The design domain corresponds to the rotor back iron region, where finer mesh is applied to accurately capture magnetic flux distribution and local saturation effects. Line boundaries as green are defined on both sides of the rotor back iron sector, and a local coordinate system is introduced along these boundaries to express the normal vector parallel to the flux lines. The objective of the optimization is to maximize the magnetic flux passing through the back iron by advocating efficient flux



(a) (b)

Fig. 1. 2D cross-sectional view (a) Three phase 18/20 baseline PM motor (b) Design domain of TO

979-8-3315-5762-1/26/$31.00 ©2026 IEEE
Authorized licensed use limited to: Tallinn University of Technology. Downloaded on October 26,2026 at 09:05:01 UTC from IEEE Xplore. Restrictions apply.

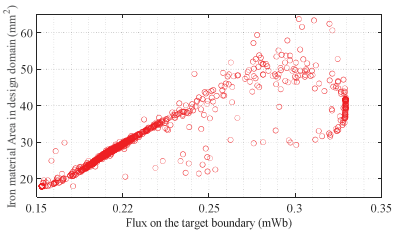


Fig. 2. Relation between target flux and iron material in the design region

utilization between the defined boundaries. The objective function is formulated as

$$max. \int_{target\ line} B \cdot \hat{n}\, dx \qquad (5)$$

$$s.t. \quad 0.5 \leq B \geq 1.4$$

where B denotes the magnetic flux density on the target line and $\hat{n}$ is the unit normal vector perpendicular to the target line. Since the dominant flux crossing the back iron is oriented along the normal direction, this formulation effectively maximizes the usable magnetic flux through the back iron. To avoid excessive magnetic saturation and ensure practical material utilization, the magnetic flux density within the back iron is constrained to remain within a prescribed flux density range. Regions where the flux density falls outside this range are identified as inefficient for flux conduction and are therefore contenders for material removal during the optimization process.

As shown in Fig. 1(b), the Gaussian basis functions are distributed over the rotor back iron on the right side of the sector. Due to the geometric and magnetic symmetry of the rotor, the material distribution defined by these Gaussian basis functions is mirrored to the left side. This symmetry reduces the number of design variables while preserving physically consistent magnetic flux paths across the rotor back iron. The detailed optimization parameters are summarized in Table I.

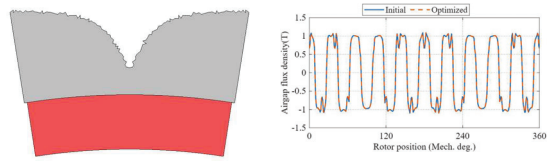
IV. Optimization Results

The optimization was performed on a computer equipped with an Intel® Core™ i7-12700 CPU operating at 2.1 GHz with 64 GB of installed memory. The optimization takes 6 hours and 40 minutes to complete after 50 generations of magnetostatic study. The relation between the target flux and iron material in the design region is shown in Fig. 2. Following optimization, the magnetic flux density distributions were analyzed and found to be consistent with those of the initial design, with material removal occurring primarily in regions of low flux density. The optimal shape of the rotor back iron and airgap flux density waveforms are shown in Fig. 3(a) and 3(b) respectively. The flux density contour and field lines are depicted in Fig. 4(a) and Fig. 4(b), where no magnetic saturation can be seen in the active regions of the rotor back iron.

The back EMF, and torque waveforms of the initial and optimized designs are compared in Fig. 5(a), and 5(b) respectively. The optimized rotor exhibits a volume reduction of 25.67%, corresponding to a 7.32% reduction relative to the total motor volume. As a result, the torque density increased by 7.84% without degradation of key performance indicators,

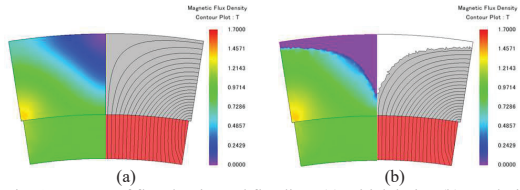
TABLE I
NGNet Optimization Setup

Parameters	Value
Number of generations	50
Population size	47
Number of children	47
Number of Gaussians	46
Gaussian basis width	0.8 (mm)
Gaussian basis height	0.8 (mm)
Optimization method	Genetic algorithm



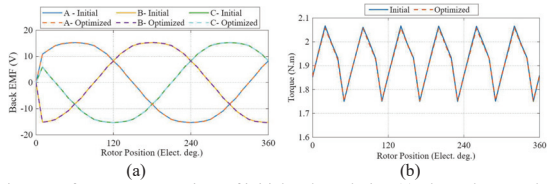
(a) (b)

Fig. 3. (a) TO design of the one pole pitch rotor (b) Airgap flux density waveform



(a) (b)

Fig. 4. Contour of flux density and flux lines (a) Initial design (b) TO design



(a) (b)

Fig. 5. Performance comparison of initial and TO design (a) Three phase Back EMF (b) Electromagnetic torque waveform

demonstrating improved material utilization and lightweight rotor design.

V. Acknowledgement

This work was supported by the Estonian Research Council grant (PRG-1827).

References

[1] Y. Fu, W. Liu, C. Zhang, J. Chen, S. Qiu, and X. Li, "NGnet-Based Sequential Optimization Technique of Variable Flux Memory Machines Considering Multimagnetization State Ripple Suppression," *IEEE Transactions on Transportation Electrification*, vol. 11, no. 2, 2025, doi: 10.1109/TTE.2024.3477597.

[2] S. Hayashi, M. Yatsurugi, Y. Kubota, S. Soma, and H. Igarashi, "Topology Optimization of a Surface Permanent Magnet Motor With High Torque Density," *IEEE Trans Magn*, vol. 60, no. 3, 2024, doi: 10.1109/TMAG.2023.3309538.

[3] T. Sato, K. Watanabe, and H. Igarashi, "Multimaterial topology optimization of electric machines based on normalized Gaussian network," *IEEE Trans Magn*, vol. 51, no. 3, 2015, doi: 10.1109/TMAG.2014.2359972.

[4] S. Hayashi, Y. Kubota, S. Soma, M. Ohtani, and H. Igarashi, "Topology Optimization of Permanent Magnet Synchronous Motor Considering the Control System," *IEEE Trans Magn*, vol. 58, no. 9, 2022, doi: 10.1109/TMAG.2022.3172718.

Authorized licensed use limited to: Tallinn University of Technology. Downloaded on October 26,2026 at 09:05:01 UTC from IEEE Xplore. Restrictions apply.

Publication III

S. Hussain, A. Kallaste, M. U. Naseer, Z. Ahmad, H. Tiismus, T. Plopeanu, M. Ibrahim, and T. Vaimann, “Topology Optimization of Additively Manufactured Outer Rotor Permanent Magnet Motor,” *IEEE Transactions on Magnetics*, 2026, doi: 10.1109/TMAG.2026.3701312.

Topology Optimization of Additively Manufactured Outer-Rotor Permanent Magnet Motor

Shahid Hussain[1], Ants Kallaste[1], Muhammad Usman Naseer[1], Zahoor Ahmad[1], Hans Tiismus[1], Tudor Plopeanu[2], Mahmoud Ibrahim[1], and Toomas Vaimann[1,3]

[1]Department of Electrical Power Engineering and Mechatronics, Tallinn University of Technology, Tallinn 19086, Estonia
[2]Department of Cybernetics, Tallinn University of Technology, Tallinn 19086, Estonia
[3]Faculty of Electrical and Electronics Engineering, Ton Duc Thang University, Ho Chi Minh City 758307, Vietnam

This article presents a topology optimization (TO) method for the rotor back iron of outer-rotor permanent magnet brushless DC (BLDC) motors, particularly for electric vehicles (EV) scooter applications. A non-iterative analytical TO method for the rotor back iron that removes low flux utilization regions while preserving the main magnetic flux path. The normalized Gaussian network (NGNet) based TO is used as a benchmark to evaluate the proposed method and highlight the computational advantage of analytical TO. Unlike the NGNet approach, which requires iterative genetic algorithm optimization, the proposed analytical method determines the optimized back iron geometry from magnetic flux continuity and saturation constraints with minimal computational effort. The optimization results in a lighter rotor and improved torque density while preserving the back electromotive force (EMF) and torque waveform characteristics. The initial and optimized rotor back irons were fabricated using additive manufacturing (AM) with a material composition of Fe–3.7%Si. The difference between the simulated and experimentally measured torque was found to be approximately 5.09%.

***Index Terms*—Brushless DC (BLDC) motor, genetic algorithm, normalized Gaussian network (NGNet), topology optimization (TO).**

I. Introduction

ELECTRIC two-wheeler applications, particularly electric vehicles (EV) scooters, increasingly adopt outer-rotor brushless DC (BLDC) motors due to their high torque density and compact wheel hub integration. However, lightweight design and high efficiency requirements under urban driving cycles impose stringent constraints on rotor magnetic material utilization and saturation behavior, motivating the need for advanced design methodologies beyond conventional parametric optimization approaches [1].

Topology optimization (TO) provides a systematic approach for improving electromagnetic performance by allowing nonuniform magnetic material distribution based on magnetic field characteristics. Over the past decade, TO has been extensively applied to structural mechanics problems, and more recently to electromagnetic devices. Recent reviews highlight significant advances in density-based, ON/OFF, level-set, and multi-material TO approaches for electromagnetic systems and rotating machines [2], [3], [4]. Among various TO methods, the ON–OFF approach based on the normalized Gaussian network (NGNet) represents design geometries using Gaussian basis functions and has been successfully applied to electric machine design, including permanent magnet motors and synchronous reluctance motors [5], [6]. To reduce magnetic saturation and improve torque performance, this method exhibits the global optimal shapes without the need for a filtering process [7], [8].

To bridge the gap between TO and advanced manufacturing, additive manufacturing (AM) offers the capability to produce the complex geometries obtained through the TO technique [9], [10]. However, only a limited number of studies have reported the practical fabrication of TO designs using AM. In [11], the authors performed TO of a switched reluctance machine and subsequently manufactured the design using laser powder bed fusion (LPBF). In [12], the power density of PM machines for aerospace applications was improved by utilizing the magnetic material more efficiently in the rotor back iron and stator yoke. Nevertheless, this study did not employ a systematic optimization methodology or algorithm specifically for optimizing the targeted regions.

This article presents rotor back iron optimization techniques for an outer-rotor BLDC motor, where magnetic material is removed from regions with low flux utilization in order to reduce rotor weight. By reducing rotor mass while maintaining electromagnetic performance, the proposed approaches enhance torque density and improve the overall utilization of magnetic material. The remainder of this article is organized as follows. Section II describes the TO method using NGNet. Section III presents the TO problem formulation and the optimization results, and their comparison is described in Section IV. Section V discusses the post processing procedures, and Section VI details the manufacturing of the optimized rotor back iron using AM. Section VII presents the experimental validation, and Section VIII concludes this article.

Received 9 March 2026; revised 28 May 2026; accepted 29 May 2026. Date of publication 8 June 2026; date of current version 21 October 2026. This work was supported by Estonian Research Council under Grant PRG-1827 and Grant PRG-1145. Corresponding author: S. Hussain (e-mail: shahid.hussain@taltech.ee).

Color versions of one or more figures in this article are available at https://doi.org/10.1109/TMAG.2026.3701312.

Digital Object Identifier 10.1109/TMAG.2026.3701312

0018-9464 © 2026 IEEE. All rights reserved, including rights for text and data mining, and training of artificial intelligence and similar technologies. Personal use is permitted, but republication/redistribution requires IEEE permission.
See https://www.ieee.org/publications/rights/index.html for more information.

Authorized licensed use limited to: Tallinn University of Technology. Downloaded on October 26,2026 at 09:06:30 UTC from IEEE Xplore. Restrictions apply.

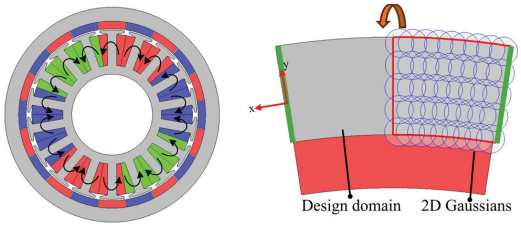


Fig. 1. 2-D cross-sectional view. (a) Three-phase 18/20 baseline PM motor. (b) Design domain of TO.

II. TO Using NGNet

Efficient utilization of magnetic material requires careful identification and design of the rotor flux-carrying regions. TO is employed to determine the optimal material distribution without prescribing explicit geometric parameters. In the proposed approach, Gaussian basis functions are distributed over the design domain, and the resulting material layout is governed by a shape function expressed as

$$y(x,w)=\sum_{i=1}^{N} w_i b_i(x) \tag{1}$$

where w_i denotes the weighting factor, x represents the spatial position vector, and N is the total number of Gaussian basis functions. The term refers to the normalized Gaussian basis function, which is defined as

$$b_i(x)=\frac{G_i(x)}{\sum_{k=1}^{N} G_k(x)} \tag{2}$$

$$G_k(x)=\frac{1}{2\pi\sigma^2} exp\left[-\frac{\|x-x_i\|^2}{2\sigma^2}\right] \tag{3}$$

where x_i denotes the center location of the kth Gaussian basis function and σ^2 represents the variance, respectively. Based on this formulation, the material property S_e can be

$$S_e=\begin{cases}0, & air, \quad y<0\\ 1, & iron, \quad y\geq 0.\end{cases} \tag{4}$$

The resulting material layout is governed by the parameter vector w, which is optimized to maximize the objective function.

III. TO Problem Setting

A. NGNet Problem

To optimize the rotor back iron, an 18-slot, 20-pole outer-rotor permanent magnet motor is considered as a benchmark, as shown in Fig. 1(a). Owing to the periodic symmetry of the machine, only one pole pitch of the rotor is modeled for the optimization study, as illustrated in Fig. 1(b). The design domain corresponds to the rotor back iron region, where a finer mesh is applied to accurately capture magnetic flux distribution and local saturation effects. Line boundaries, as green, are defined on both sides of the rotor back iron sector, and a local coordinate system is introduced along these boundaries to express the normal vector parallel to the flux lines. The objective of the optimization is to maximize the magnetic flux passing through the back iron by advocating efficient flux utilization between the defined boundaries. The objective function is formulated as

$$\begin{aligned} &max. \int_{target\ \ line} B\cdot \hat{n} dx\\ &\text{s.t.} \quad 0.5\leq B\leq 1.4 \end{aligned} \tag{5}$$

where B denotes the magnetic flux density on the target line and $\hat{n}$ is the unit normal vector perpendicular to the target line.

Since the dominant flux crossing the back iron is oriented along the normal direction, this formulation effectively maximizes the usable magnetic flux through the back iron. To avoid excessive magnetic saturation and ensure practical material utilization, the magnetic flux density within the back iron is constrained to remain within a prescribed flux density range. Regions where the flux density falls outside this range are identified as inefficient for flux conduction and are therefore contenders for material removal during the optimization process.

At the start of the optimization process, the material on the left side of the design domain is defined as M400-50A (iron), and air is assigned to the right side. As shown in Fig. 1(b), the Gaussian basis functions are distributed over the rotor back iron on the right side of the sector. Due to the geometric and magnetic symmetry of the rotor, the material distribution defined by these Gaussian basis functions is mirrored to the left side. This symmetry reduces the number of design variables while preserving physically consistent magnetic flux paths across the rotor back iron. The detailed optimization parameters are summarized in Table I.

TABLE I
NGNet Optimization Setup

Parameters	Value
Number of generations	50
Population size	47
Number of children	47
Number of Gaussians	46
Gaussian basis width	0.8 (mm)
Gaussian basis height	0.8 (mm)
Optimization method	Genetic algorithm

B. Proposed Analytical Formulation

The analysis begins by specifying the magnetic properties of the materials. The B–H curve of the soft-magnetic back iron is assumed to be linear with a very high relative permeability. μ_r up to a saturation flux density B_s beyond saturation, the magnetization M is taken to remain constant at B_s in the direction of the applied field. The permanent magnet has a constant magnetization as

$$M_m=\frac{B_r}{\mu_0} \tag{6}$$

corresponding to its remanent flux density B_r. It is also assumed that the back iron remains unsaturated at its outer perimeter. To calculate the magnetic field produced by the

Authorized licensed use limited to: Tallinn University of Technology. Downloaded on October 26,2026 at 09:06:30 UTC from IEEE Xplore. Restrictions apply.

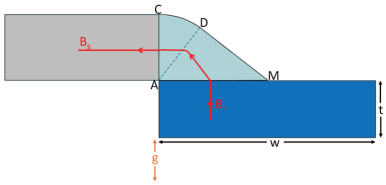


Fig. 2. Illustration of analytical topology-optimized back iron for quasi-static electromagnetic device.

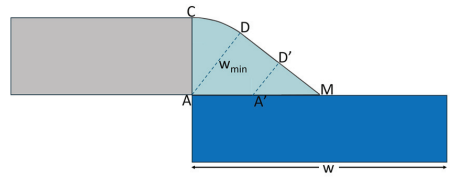


Fig. 3. Analytical TO with new contour of A′ D′ M to maintain flux continuity.

magnet using Ampere's law, the magnet has a uniform magnetization; its bound currents can be treated as a free solenoidal surface current around its circumference. Choosing an Ampere contour on the outer perimeter of the back iron where the material is not saturated allows one to assume

$$B = \mu_r \mu_0 H. \tag{7}$$

Since $\mu_r \gg 1$, the contribution from the portion of the contour inside the back iron can be neglected. The total current enclosed is

$$I = jt = \frac{B_r t}{\mu_0} \tag{8}$$

where t is the magnet thickness. The air gap thickness g is much smaller than the magnet and back iron diameters; the magnetic field in the gap and in the magnet is nearly homogeneous. Fig. 2 shows that the magnetic field lines exit ferromagnetic materials almost perpendicular, so they enter the air gap nearly parallel and therefore remain uniform; similarly, the magnet field remains homogeneous at both ends of the magnet and thus within the magnet itself. Under these conditions Ampère's law yields a uniform magnetic flux density of magnitude

$$B = \frac{B_r t}{(g+t)}. \tag{9}$$

To determine how much iron is needed, consider a "cut" through the back iron that encompasses the entire cross section touching one side of the magnet. Let w be the magnet width and d its axial length. Gauss's law (the divergence theorem) is used to equate the magnetic flux entering this volume (half the magnet's flux) to the flux exiting through the cut in the back iron. The flux entering is

$$\emptyset_{in} = \frac{B_r t}{(g+t)} \cdot \frac{wd}{2}. \tag{10}$$

However, the back iron can only carry so much flux before saturating. The maximum flux it can transport is limited by the saturation flux density B_s multiplied by its cross-sectional area $w_{cut}d$. In order to carry all of the flux, the cut width must satisfy

$$\emptyset_{out} \leq B_s w_{cut} d. \tag{11}$$

Solving for the minimum width yields

$$w_{min} = \frac{B_r}{B_s} \frac{t}{g+t} \cdot \frac{w}{2}. \tag{12}$$

If the back iron is thinner than w_{min}, some magnetic flux will drop out because the iron cannot carry the entire flux. In this regard w_{min} as a strict necessity for any viable design. The lengths of AC and AD are both w_{min}. The contour between C and D follows the arc of the circle, and the line DM is tangent to the circle at D. The quarter circle centered at A of radius w_{min} must exist in any valid back iron because it provides the necessary width around the magnet edge.

To demonstrate that the proposed shape contains the smallest possible amount of iron, consider an arbitrary cross section A′ D′ M formed by intersecting the ADM triangle with a line parallel to AD as shown in Fig. 3. By similarity of triangles, the ratio of the widths AD/AM equals the ratio A′ D′ /A′ M. Since AD represents the minimum width needed to transport all of the flux from AM, A′ D′ must be the minimum width required to transport the flux from A′ M. Because this argument holds for any parallel intersection, the entire triangle ADM must be included in any valid back iron. Thus, no design that removes material from the ADM triangle can carry the full magnetic flux, proving the minimality of the chosen shape.

The final check is that the minimal iron design satisfies Maxwell's equations and the refraction conditions at the magnet and iron interface. First, Gauss's law for magnetism

$$\nabla \cdot B = 0 \tag{13}$$

requires magnetic field lines to form closed loops. In the proposed design, the field lines travel almost vertically through the magnet path parallel to the straight segment DM through the back iron, follow the circular arc until reaching point C, and then complete the loop through the outer region back to the magnet. Maxwell's other equation

$$\nabla \times H = \mu_0 j \tag{14}$$

is satisfied because inside the back iron $H \approx B - B_s \approx 0$ and there are no free currents. At the interface between the magnet and the back iron, the continuity of the normal component of B and the tangential component of H must be respected. Tangential H in the magnet must be nearly zero because the magnetization in the magnet is fixed and the permeability of the iron is large. The normal component of B in the magnet is

$$B_{magnet} = \frac{B_r t}{(g+t)}. \tag{15}$$

On the flux guide side, the flux density is approximately B_s, but it meets the interface at an angle determined by the geometry. By constructing the right triangle ADM, the cosine

Authorized licensed use limited to: Tallinn University of Technology. Downloaded on October 26,2026 at 09:06:30 UTC from IEEE Xplore. Restrictions apply.

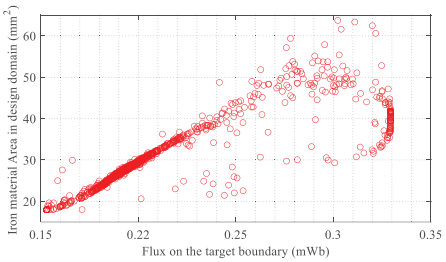


Fig. 4. Relation between target flux and iron material in the design region.

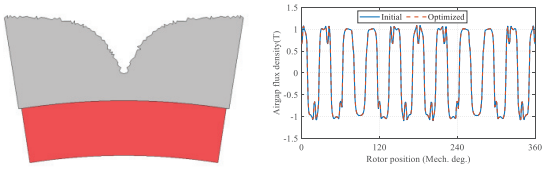


Fig. 5. (a) TO back iron of the one pole pitch rotor. (b) Airgap flux density waveform.

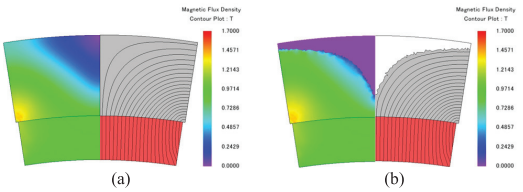


Fig. 6. Contour of flux density and flux lines. (a) Initial back iron. (b) TO back iron.

of this angle is $(2w_{min})/(w)$. Equating the normal components on both sides requires

$$\frac{B_r t}{g+t} = B_s \frac{2w_{min}}{w} \tag{16}$$

which is exactly the definition of w_{min} derived earlier. Thus, the design also satisfies the magnetic refraction condition. To conclude, the shape shown in Fig. 2 is minimal, transports the maximum possible magnetic flux, and is physically valid.

IV. Optimization Results

The optimization was performed on a computer equipped with an Intel[1] Core[2] i7-12700 CPU operating at 2.1 GHz with 64 GB of installed memory. The optimization took 6 h and 40 min to complete after 50 generations of magnetostatic study. The relation between the target flux and iron material in the design region is presented in Fig. 4. Following optimization, the magnetic flux density distributions were analyzed and found to be consistent with those of the initial design, with material removal occurring primarily in regions of low flux density.

[1]Registered trademark.
[2]Trademarked.

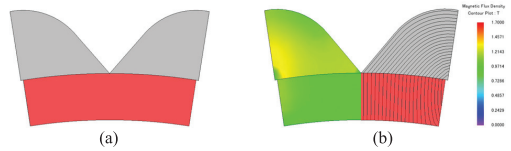


Fig. 7. (a) TO back iron using analytical approach. (b) Contour of flux density and flux lines in analytical TO back iron.

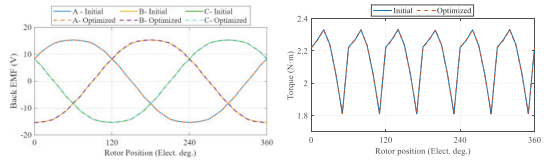


Fig. 8. Performance comparison of initial and TO design. (a) Three-phase back EMF. (b) Electromagnetic torque waveform.

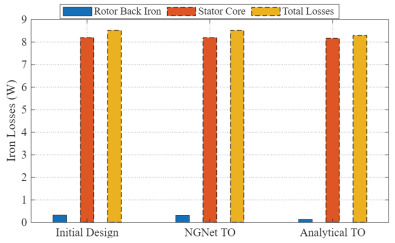


Fig. 9. Comparison of iron losses between different designs.

TABLE II
Performance Comparison of Different Optimization Methods

Aspect	NGNet method	Analytical TO approach
Optimization type	Genetic algorithm	Non-iterative
Back iron reduction	25.67%	39.29%
Increase in torque density	7.84%	14.36%
Computational time	6h	-

The optimized rotor back iron geometry obtained for one pole pitch sector is shown in Fig. 5(a), and this shape is periodically repeated around the rotor to form the complete TO back iron. The corresponding airgap flux density waveform comparison between the initial and optimized back iron is shown in Fig. 5(b). The flux density contour and field lines are depicted in Fig. 6(a) and (b), where no magnetic saturation can be seen in the active regions of the rotor back iron. The back iron design obtained from the analytical-based TO and the contour of flux density and field lines are shown in Fig. 7(a) and (b), respectively. Analytical-based optimization does not require any iterative process; with just one finite element method (FEM) simulation, the optimal design is achieved. The electromagnetic performance, like back electromotive force (EMF) and torque waveforms achieved from both methods, is the same.

Authorized licensed use limited to: Tallinn University of Technology. Downloaded on October 26,2026 at 09:06:30 UTC from IEEE Xplore. Restrictions apply.

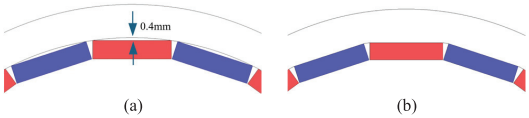


Fig. 10. Different design configurations with straight magnets. (a) With air region behind magnets. (b) Iron filled behind magnets.

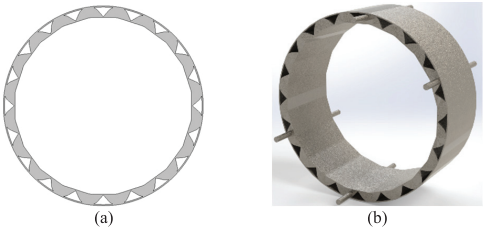


Fig. 11. Optimized back iron having a mechanically feasible design. (a) 2-D cross-sectional back iron. (b) 3-D CAD model of back iron.

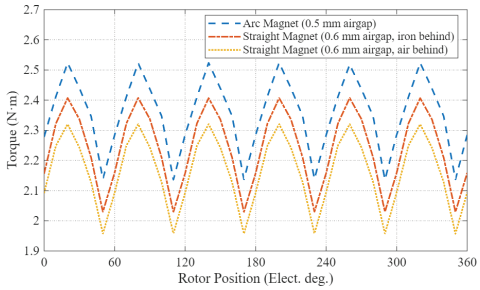


Fig. 12. Comparison of torque on different magnet shape configurations.

Fig. 8(a) and (b) shows the comparison of the initial and optimized back EMF and torque waveforms, which follow the same trend, and also the average torque value is the same. Moreover, the difference in iron losses between the initial and optimized designs is relatively small because the dominant contribution comes from the stator core, which remains unchanged in all cases. As shown in Fig. 9, the rotor back iron losses are very low because the magnetic flux on the rotor side is nearly static and the rotor operates at a relatively low speed, resulting in negligible eddy-current losses. Therefore, only a minor variation in the total iron losses is observed among the different designs. The performance comparison of both optimization methods is presented in Table II.

V. Post Processing

After completing the optimization process, the design was prepared for the manufacturing stage, which required several practical modifications. During optimization, arc-shaped magnets were used. However, these magnets are relatively expensive for practical implementation. To reduce the manufacturing cost, straight N35 magnets were selected as an alternative.

The use of straight magnets introduces small gaps between the magnets and the rotor back iron, as shown in Fig. 10(a), which results in the reduction of electromagnetic performance. In Fig. 10(b), small pockets were incorporated behind the magnets, allowing the magnets to fit properly and maintain close contact with the back iron structure. An outer circular iron bridge is also introduced to improve the mechanical strength and structural stability of the rotor, as shown in Fig. 11(a), while the 3-D CAD model of the optimized rotor back iron is shown in Fig. 11(b) for better realization of the rotor back iron. Although the resulting back iron geometry has a relatively complex shape, it can be effectively manufactured using the AM technique. The comparison of torque waveforms obtained from different back iron configurations and magnet arrangements is presented in Fig. 12.

TABLE III
Summary of Printing Parameters

Parameter	Value
Layer thickness	50 µm
Hatch distance	120 µm
Laser Power	350 W
Scanning velocity	0.75 m/s
Volumetric energy density	83 J/mm³



Fig. 13. AM-based rotor prototype. (a) Initial rotor. (b) Optimized rotor.

VI. Rotor Back Iron Fabrication Through AM

Pre-alloyed, gas-atomized Fe–Si powder supplied by the Sandvik Group was used to manufacture the machine cores using the LPBF process. The chemical composition of the powder was verified using energy-dispersive X-ray spectroscopy (EDX) and spark atomic emission spectroscopy (AES) [13]. The powder consisted of spherical particles with sizes ranging from 29 to 58 μm, with a median diameter of 38 μm. The printing process was carried out using an SLM Solutions Realizer SLM-280 system equipped with a 350 W infrared laser.

To prevent density degradation during large volume printing, the scanning strategy was modified from a stripe pattern to a chessboard pattern, which improves printing stability and structural uniformity, as reported in previous studies. In addition, the re-melting scanning strategy was disabled because it increased surface roughness and reduced powder flowability, resulting in uneven layer formation. The key printing parameters used in the process are summarized in Table III.

The printing time for each back iron was approximately 5 h. After printing, the prototypes were heat treated in an RD-G vacuum furnace at 1200 °C, with a heating rate of

Authorized licensed use limited to: Tallinn University of Technology. Downloaded on October 26,2026 at 09:06:30 UTC from IEEE Xplore. Restrictions apply.

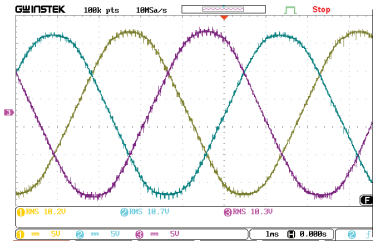


Fig. 14. Experimental three-phase back EMF.

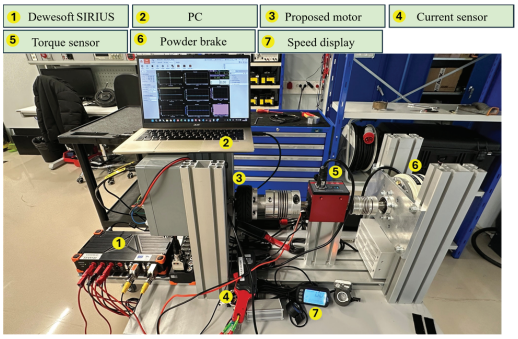


Fig. 15. Experimental test setup for outer-rotor BLDC.

5 °C /min and a holding time of one hour. The parts were then cooled inside the furnace at an initial cooling rate of 50 °C /min, gradually decreasing over time. During the heat treatment process, the vacuum level was maintained between 0.04 and 0.4 mbar. The fabricated AM rotors, including the initial and optimized designs, are shown in Fig. 13(a) and (b), respectively.

VII. Experimental Testing and Validation

To validate the electromagnetic performance of the proposed outer-rotor BLDC motor, experimental measurements were carried out on the fabricated prototype. The experimental setup was designed to evaluate both the no-load back EMF characteristics and the machine performance under load conditions.

A. No Load Measurement

The prototype motor was mounted on a rigid platform and mechanically coupled to a servo motor through a shaft coupling to control the rotational speed. For no-load testing, the servo motor was operated at the rated speed of 900 r/min, while the BLDC motor terminals were kept open to measure the induced phase voltages. The three-phase back EMF waveforms were recorded using a digital oscilloscope as shown in Fig. 14.

B. Load Test Setup and Validation

For load analysis, the BLDC motor shaft was connected to a DYN-200 torque sensor, and a powder brake was coupled to the torque sensor to apply a controllable mechanical load to the

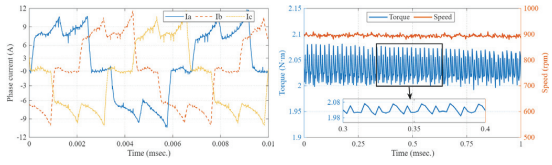


Fig. 16. Experimental results. (a) Three-phase motor currents. (b) Torque and speed waveform.

prototype motor. For signal visualization and data acquisition, a Dewesoft SIRIUS isolated data acquisition system was employed. The complete experimental setup is illustrated in Fig. 15. Motor phase currents were measured using three PR200 current clamps (10 mV/A). The measurements were acquired with a sampling rate corresponding to a bandwidth of 1 MHz. The recorded three-phase motor currents and torque waveform are presented in Fig. 16(a) and (b), respectively.

Due to the absence of magnetic property data for the AM rotor back iron material in the simulation software database, the numerical analysis was performed using the M400-50A electrical steel model. However, the practical prototype was fabricated using a Fe–3.7%Si magnetic material, as reported in [14]. The simulated torque is around 5.09% lower than the measured value. This discrepancy is mainly attributed to the difference between the magnetic material properties used in the simulations and those of the AM Fe–3.7%Si back iron, as well as manufacturing tolerances and experimental measurement uncertainties.

VIII. Conclusion

This article presented a TO approach for the rotor back iron of an outer-rotor BLDC motor intended for EV scooter applications. Two optimization approaches were investigated: the NGNet based on TO and a proposed analytical topology method. The analytical approach enables optimal material utilization without requiring iterative optimization, significantly reducing computational complexity while maintaining electromagnetic performance.

The optimized rotor back iron design achieved substantial material reduction and improved torque density while preserving the back EMF and torque waveform characteristics. The optimized design was fabricated using AM with Fe–3.7%Si material, and experimental validation was performed to verify the proposed method. The measured results showed good agreement with the simulation results, with a torque deviation of approximately 5.09%. Although the proposed TO method significantly reduces computational effort, it does not consider mechanical stress and thermal effects. Future work will focus on extending the method to include these multiphysics constraints and validating its applicability on the motor configuration.

References

[1] D. Fodorean, L. Idoumghar, and L. Szabo, "Motorization for an electric scooter by using permanent-magnet machines optimized based on a hybrid metaheuristic algorithm," *IEEE Trans. Veh. Technol.*, vol. 62, no. 1, pp. 39–49, Jan. 2013, doi: 10.1109/TVT.2012.2215970.

Authorized licensed use limited to: Tallinn University of Technology. Downloaded on October 26,2026 at 09:06:30 UTC from IEEE Xplore. Restrictions apply.

[2] S. Lim, S. Min, and J.-P. Hong, "Level-set-based optimal stator design of interior permanent-magnet motor for torque ripple reduction using phase-field model," *IEEE Trans. Magn.*, vol. 47, no. 10, pp. 3020–3023, Oct. 2011, doi: 10.1109/TMAG.2011.2158201.

[3] J. S. Choi, K. Izui, S. Nishiwaki, A. Kawamoto, and T. Nomura, "Topology optimization of the stator for minimizing cogging torque of IPM motors," *IEEE Trans. Magn.*, vol. 47, no. 10, pp. 3024–3027, Oct. 2011, doi: 10.1109/TMAG.2011.2158572.

[4] F. Guo, N. Tang, and I. P. Brown, "Combined dimensional and topology optimization of synchronous machine rotors using a material density interpolation method," *IEEE Trans. Ind. Appl.*, vol. 59, no. 6, pp. 6591–6600, Nov. 2023, doi: 10.1109/TIA.2023.3292214.

[5] Y. Fu, W. Liu, C. Zhang, J. Chen, S. Qiu, and X. Li, "NGnet-based sequential optimization technique of variable flux memory machines considering multimagnetization state ripple suppression," *IEEE Trans. Transport. Electrific.*, vol. 11, no. 2, pp. 5265–5275, Apr. 2025, doi: 10.1109/TTE.2024.3477597.

[6] S. Hayashi, M. Yatsurugi, Y. Kubota, S. Soma, and H. Igarashi, "Topology optimization of a surface permanent magnet motor with high torque density," *IEEE Trans. Magn.*, vol. 60, no. 3, pp. 1–5, Mar. 2024, doi: 10.1109/TMAG.2023.3309538.

[7] T. Sato, K. Watanabe, and H. Igarashi, "Multimaterial topology optimization of electric machines based on normalized Gaussian network," *IEEE Trans. Magn.*, vol. 51, no. 3, pp. 1–4, Mar. 2015, doi: 10.1109/TMAG.2014.2359972.

[8] S. Hayashi, Y. Kubota, S. Soma, M. Ohtani, and H. Igarashi, "Topology optimization of permanent magnet synchronous motor considering the control system," *IEEE Trans. Magn.*, vol. 58, no. 9, pp. 1–5, Sep. 2022, doi: 10.1109/TMAG.2022.3172718.

[9] L. Sethuraman and G. Vijayakumar, "A new shape optimization approach for lightweighting electric machines inspired by additive manufacturing," in *Proc. Joint MMM-Intermag Conf. (INTERMAG)*, Jan. 2022, pp. 1–7, doi: 10.1109/INTERMAG39746.2022.9827714.

[10] S. Hussain, A. Kallaste, and T. Vaimann, "Recent trends in additive manufacturing and topology optimization of reluctance machines," *Energies*, vol. 16, no. 9, p. 3840, Apr. 2023, doi: 10.3390/en16093840.

[11] A. Manninen, J. Pippuri-Mäkeläinen, T. Riipinen, J. Keränen, S. Metsä-Kortelainen, and T. Lindroos, "Design and testing of a switched reluctance motor with additively manufactured ferromagnetic cores," *IET Conf. Proc.*, vol. 2023, no. 17, pp. 150–157, 2023, doi: 10.1049/icp.2023.1992.

[12] S. Fang, Y. Wang, and H. Liu, "Design study of an aerospace motor for more electric aircraft," *IET Electric Power Appl.*, vol. 14, no. 14, pp. 2881–2890, Dec. 2020, doi: 10.1049/iet-epa.2020.0507.

[13] H. Tiismus, A. Kallaste, M. U. Naseer, T. Vaimann, and A. Rassolkin, "Design and performance of laser additively manufactured core induction motor," *IEEE Access*, vol. 10, pp. 50137–50152, 2022, doi: 10.1109/ACCESS.2022.3173317.

[14] H. Tiismus et al., "Laser additively manufactured magnetic core design and process for electrical machine applications," *Energies*, vol. 15, no. 10, p. 3665, May 2022, doi: 10.3390/en15103665.

Authorized licensed use limited to: Tallinn University of Technology. Downloaded on October 26,2026 at 09:06:30 UTC from IEEE Xplore. Restrictions apply.

Publication IV

S. Hussain, A. Kallaste, P. Gangl, N. Krenn, T. Cherrière, M. U. Naseer, Z. Ahmad, and T. Vaimann, “Electromagnetic Topology Optimization of Brushless DC Motor Based on Density Method," *2026 International Conference on Electrical Machines (ICEM)*, Funchal (Madeira), Portugal, 2026, pp. 1-7, doi: 10.1109/ICEM68283.2026.11757987.

Electromagnetic Topology Optimization of Brushless DC Motor Based on Density Method

Shahid Hussain, Ants Kallaste, Muhmmad Usman Naseer, Zahoor Ahmad, Toomas Vaimann
Department of Electrical Power Engineering and Mechatronics
Tallinn University of Technology
Tallinn, Estonia

Peter Gangl, Nepomuk Krenn,
Johann Radon Institute for Computational and Applied Mathematics, Austrian Academy of Sciences
Linz, Austria

Théodore Cherrière
Group of Electrical Engineering Paris CentraleSupélec, Université Paris-Saclay
Gif-sur-Yvette, France

***Abstract*— A density-based topology optimization method for minimizing inactive magnetic material in the rotor back iron of an outer rotor Brushless DC (BLDC) motor is presented in this paper. While the stator and permanent magnets stay fixed, the magnetic reluctivity between air and ferromagnetic material within the rotor back iron region is interpolated using a Solid Isotropic Material with Penalization (SIMP) formulation. For effective gradient assessment, adjoint based sensitivity analysis is used in conjunction with a nonlinear two-dimensional magnetostatic finite element model. In order to eliminate intermediate densities and reduce oscillatory patterns, Helmholtz type filtering are used to ensure numerical stability and designs that can be manufactured. To maintain electromagnetic performance, a directional flux tracking objective with a volume constraint is developed. The optimized design preserves airgap flux density, back EMF, and torque characteristics while reducing the rotor back iron volume by 39% (or 12% of the overall motor volume). Torque density increases by around 14% as a result, indicating reduced material usage without performance degradation.**

Keywords—Density method, adjoint variable method, Topology optimization, solid isotropic material with penalization, PM motor

I. Introduction

Permanent Magnet (PM) electrical machines are extensively utilized in electric vehicles, robotics, aerospace systems, and industrial drives owing to their high efficiency, compact design, and exceptional torque density. In modern machine design, enhancing torque density while minimizing material usage has emerged as a key goal, influenced by cost, sustainability, and lightweight design criteria [1], [2]. In traditional electrical machine design, predetermined form boundaries are adjusted to optimize the geometry of active components. This method, known as parametric or geometric optimization, changes certain geometric dimensions to obtain the required performance [3], [4].

Parametric optimization is useful for optimizing already existing designs, it is intrinsically constrained by the original geometrical parameters. The optimization procedure is unable to really change the magnetic circuit structure and only allows for variants within a predetermined design configuration [5]. Due to this, potentially more effective material distributions could go neglected, especially in areas where magnetic flux is used unevenly. These restrictions become much more important when seeking substantial weight reduction or increased torque density beyond small geometric changes.

Topology optimization (TO) emerged as a strong computational design tool for identifying optimal material distributions within a specified design space. In contrast to traditional size, TO does not need specified geometry parameterization and instead allows material to be redistributed freely within the domain [6], [7]. Over the past decade, TO has been extensively applied to structural mechanics problems, and more recently to electromagnetic devices. Recent reviews highlight significant advances in density based, ON/OFF, level-set, and multi-material TO approaches for electromagnetic systems and rotating machines [8], [9], [10], [11], [12].

Among the various TO techniques, the density-based approach is the most widely adopted, particularly in electromagnetic device applications. This method relies on gradient based optimization and employs a continuous design variable to represent the material distribution within the domain. A key component of density based TO is the Material Interpolation Scheme (MIS), which governs the transition between different material states. Considerable research efforts have focused on improving the sharpness and clarity of optimized design boundaries through enhanced interpolation strategies. Among these, the SIMP method remains one of the most established and widely used schemes [13].

This paper presents the TO of the rotor back iron in a BLDC motor, with the objective of reducing rotor weight by eliminating magnetically inactive material. The rest of the paper is organized as follows. Section II describes the optimization problem and the specifications of the selected motor. Section III details the material interpolation scheme, including its extension to the nonlinear magnetic case. Section IV presents magnetostatic formulation along with the development of the objective function and the corresponding sensitivity analysis. Section V discusses the post processing quantities of the motor and Section VI presents the results obtained from the optimization. Some conclusions are drawn in Section VI.

II. Optimization Problem description

The design of quasi-static permanent magnet electromagnetic devices yields underutilized magnetic material, specifically in the back iron region. These inactive regions have no substantial impact on electromagnetic performance, nevertheless they do increase their total mass. These extra materials decrease torque density in rotary machines and thrust density in linear machines. Therefore, reducing unnecessary magnetic material while maintaining electromagnetic performance is of great practical relevance.

An outer rotor BLDC motor is chosen as the case study. Table I summarizes the major geometrical and electrical characteristics, whereas two-dimensional cross-section of the machine is shown in Fig. 1(a). During the optimization process, the stator geometry and permanent magnets are kept fixed. Only the rotor back iron is treated as the design domain. The solid back iron is divided into 20 segments. Each segment consists of two distinct subregions, as illustrated in Fig. 1(b).

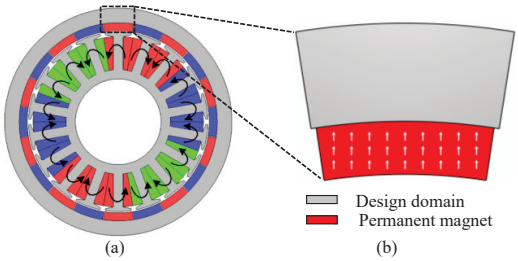


Fig. 1. 2D cross-sectional view (a) Baseline PM motor (b) TO Design domain

TABLE I. BLDC PARAMETERS

Parameter	Unit	Value
Slots number		18
Pole numbers		20
Stator outer diameter	mm	64
Rotor outer diameter	mm	85
Rotor inner diameter	mm	65
Stack length	mm	30
Rated speed	rpm	900
Rated voltage	V	24
Number of turns per coil		12
Number of strands		5

The design domain corresponds exclusively to the rotor back iron region where material redistribution is permitted. The density variable $\rho \in [0,1]$ is assigned to each finite element within this domain. Four predefined target lines, located on the left and right sides of back iron segment, are introduced to evaluate the magnetic flux.

III. Material Interpolation Scheme

To enable TO using continuous density variables an interpolation scheme is required to model the transition between air and ferromagnetic material. In electromagnetic TO, the most critical material parameter is the magnetic permeability μ or equivalently the magnetic reluctivity v =1/μ. The element reluctivity is interpolated using the SIMP formulation

$$v(\rho) = v_{air} + \rho^p\left(v_{fe} - v_{air}\right). \quad (1)$$

The penalization factor p is introduced to suppress intermediate densities and encourage nearly binary material distribution. For the linear material case study, the interpolation smoothly transitions between air and iron depending on ρ. Increasing the penalization factor p makes intermediate densities energetically unfavorable, forcing the solution toward a clear 0–1 material distribution. This behavior is illustrated in Fig. 2, where higher penalization values result in a sharper transition near ρ=1.

When magnetic saturation is considered, the permeability of the ferromagnetic material depends on the local magnetic flux density magnitude. In this case, the interpolation is applied to nonlinear reluctivity.

$$v(\rho, |B|) = v_{air} + \rho^p\,(v(|B|) - v_{air}) \quad (2)$$

We solve the discretized problem by Newton method. After each Newton iteration, the local flux density B is evaluated, and the corresponding reluctivity is updated. This updated reluctivity is then used both in the state equation and in the sensitivity analysis.

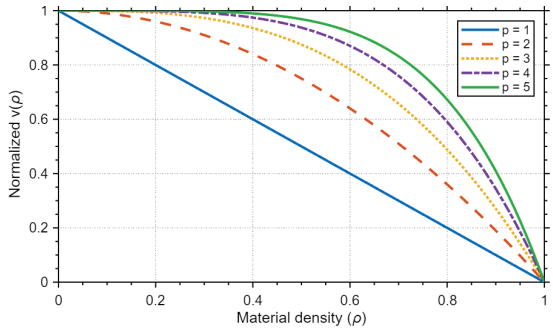


Fig. 2. SIMP interpolation with different values of penalization

IV. Two-Dimensional Magnetostatic Formulation

A. Electromagnetic Model for PM Motor

In the two-dimensional magnetostatic field, Maxwell's equations are expressed as

$$B = \nabla \times A, \quad (3)$$

where B is the magnetic flux density and A is the magnetic vector potential. The total current density can be expressed as

$$J_{tot} = J_{free} + J_m. \quad (4)$$

The magnetic curl reluctivity relation is

$$\nabla \times \left(v(\nabla \times A)\right) = J_{tot}, \quad (5)$$

where J_{tot} is the total current density and in this problem formulation we do not employ any impressed current density (J_{free}) which is zero. Hence the only volumetric source is the magnetization of the permanent magnets, and it becomes a no-load study. The magnetization contributes through the equivalent magnetization current density,

$$J_m = \nabla \times M \quad (6)$$

$$\nabla \times \left(v(\nabla \times A)\right) = \nabla \times M, \quad (7)$$

where M is the permanent magnet magnetization and taking the z-component of the curl reluctivity relation yields

$$(\nabla \times M)_z = \frac{\partial M_y}{\partial_x} - \frac{\partial M_x}{\partial_y} \quad (8)$$

$$\frac{\partial}{\partial_x}\left(v\frac{\partial A_z}{\partial_x}\right) + \frac{\partial}{\partial_y}\left(v\frac{\partial A_z}{\partial_y}\right) = \frac{\partial M_y}{\partial_x} - \frac{\partial M_x}{\partial_y}. \quad (9)$$

B. Magnetization Model and Implementation

Permanent magnets are prescribed magnetization in magnet subdomains. A radial magnetization of magnitude M_0 is utilized and the polarity alternates between adjacent sectors. The base magnetization components are given by

$$\begin{cases} M_x = M_0 \times \left(\frac{x}{r}\right) \\ M_y = M_0 \times \left(\frac{y}{r}\right) \\ r = \sqrt{(x^2 + y^2)} \end{cases} \quad (10)$$

where x,y are the coordinates and r is the radial coordinate of the barycenter of the element.

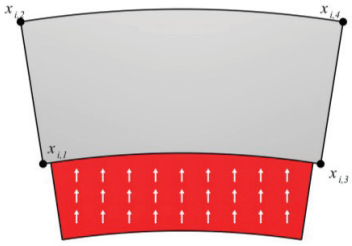


Fig. 3. Flux evaluation points on the back iron sector

C. Objective Function

The objective function is formulated to increase the useful magnetic flux passing through the prescribed flux target regions while penalizing the amount of retained rotor back iron material. In the two-dimensional magnetostatic formulation, the magnetic vector potential has only the axial component A_z, and the flux density is

$$B = \left(\frac{\partial A_z}{\partial y}, -\frac{\partial A_z}{\partial x}\right)^T. \tag{11}$$

For the *i-th* rotor segment, four corner points are defined around the flux target region, as shown in Fig. 3. The points $x_{i,1}$ and $x_{i,2}$ lie on one side of the flux region, while $x_{i,3}$ and $x_{i,4}$ lie on the opposite side. The flux crossing on each side can be evaluated from the difference of the magnetic vector potential at the corresponding endpoints. Therefore, the flux objective is written as

$$J_{flux}(A_z) = \sum_{i=1}^{N_s} (-1)^i \left[A_z(x_{i,1}) - A_z(x_{i,2}) - A_z(x_{i,3}) + A_z(x_{i,4})\right] \tag{12}$$

where N_s is the number of repeated rotor segments. The coefficient accounts for the alternating magnetization direction of adjacent permanent magnets. The material volume term is defined over design domain as

$$J_{vol}(\rho) = \int_{design\ domain} \rho\, dx, \tag{13}$$

The total optimization objective is

$$J(A_z, \rho) = J_{flux}(A_z) + wJ_{vol}(\rho), \tag{14}$$

where w is the weighting factor controlling the trade-off between flux performance and material reduction. The first term drives the magnetic flux through the desired flux target regions, while the second term penalizes the amount of iron material retained in the design domain. The standard form of the objective function is

$$\begin{cases} min.\ J(A_z, \rho) = J_{flux}(A_z) + wJ_{vol}(\rho) \\ 0 \le \rho \le 1, \end{cases} \tag{15}$$

D. Adjoint Based Sensitivity Analysis

In the gradient based TO methods, the sensitivity of the objective function, with respect to the material density (ρ) can be obtained in the following way: Consider the reduced cost function

$$J(\rho) = J(A_z(\rho), \rho). \tag{16}$$

By chain rule

$$\frac{dJ}{d\rho} = \frac{\partial J}{\partial \rho} + \frac{\partial J}{\partial A_z}\frac{dA_z}{d\rho}. \tag{17}$$

Differentiating the constraint residual $R(A_z, \rho) = 0$ with respect to ρ, gives

$$\frac{\partial R}{\partial A_z}\frac{dA_z}{d\rho} + \frac{\partial R}{\partial \rho} = 0 \tag{18}$$

$$\frac{dA_z}{d\rho} = -\left(\frac{\partial R}{\partial A_z}\right)^{-1}\frac{\partial R}{\partial \rho} \tag{19}$$

$$\frac{dJ}{d\rho} = \frac{\partial J}{\partial \rho} - \frac{\partial J}{\partial A_z}\left(\frac{\partial R}{\partial A_z}\right)^{-1}\frac{\partial R}{\partial \rho}. \tag{20}$$

Where R is the residual and this is the chain rule expression in which the explicit term plus implicit term is eliminated by solving the adjoint. Define the adjoint λ by the linear system

$$\left(\frac{\partial R}{\partial A_z}\right)^T \lambda = -\left(\frac{\partial J}{\partial A_z}\right)^T \tag{21}$$

$$\frac{dJ}{d\rho} = \frac{\partial J}{\partial \rho} + (\lambda^T \frac{\partial R}{\partial \rho}) \tag{22}$$

V. Post Processed Quantities

A. Airgap Flux Density and Back EMF

After the optimization, analyzing the airgap flux density in the initial and optimized design the above calculation gives it directly by using

$$\begin{cases} B_x = \dfrac{\partial A_z}{\partial_y} \\ B_y = -\dfrac{\partial A_z}{\partial_x} \\ B_{mag} = \sqrt{B_x^2 + B_y^2}, \end{cases} \tag{23}$$

where B_x and B_y are the rectangular coordinates of the flux density and B_{mag} is the magnitude of the flux density. The magnetic field solution is obtained from the 2D magnetostatic formulation using the magnetic vector potential A_z. The phase flux linkage is computed directly from the vector potential. For each phase $k \in \{A, B, C\}$, the flux linkage is calculated as

$$\lambda_k(\theta_m) = N_{turns} l_z \int_{\Omega} A_z(\theta_m)\, s_k(x) dx \tag{24}$$

where N_{turns}, l_z, and s_k are the number of turns per phase, stack length and the phase sign function assigned to each slot region respectively. θ_m is the rotor mechanical angle. Since the ρ is fixed after the optimization, A_z is treated as a function of the rotor angular position only, and no sensitivity of A_z with respect to ρ is considered. The phase back EMF is obtained from the time derivate of the flux linkage.

$$e_k(t) = -\frac{d\lambda_k}{dt} = -\frac{d\lambda_k}{d\theta_m} w_m \tag{25}$$

where w_m is the rotor mechanical speed in rad/sec.

B. Electromagnetic Torque Calculation

The electromagnetic torque is computed using the Maxwell stress tensor method. The Maxwell stress tensor in magnetostatics is given by

$$T = \frac{1}{\mu_0}\left(B \otimes B - \frac{1}{2}|B|^2 I\right) \tag{26}$$

where μ_0 is the permeability of free space and I is the unit or identity matrix. The stress vector acting on a circular contour of radius r_t in the airgap is

$$t = T \cdot n \tag{27}$$

where n is the unit vector. The torque per unit axial length is obtained from the contour integral.

$$T' = \int_{\Gamma_{rt}} \left(x t_y - y t_x\right) ds \tag{28}$$

$$t_x = \frac{1}{\mu_0}\left(B_x B_n - \frac{1}{2} B^2 n_x\right) \tag{29}$$

$$t_y = \frac{1}{\mu_0}\left(B_y B_n - \frac{1}{2} B^2 n_y\right) \tag{30}$$

$$B_n = B_x n_x + B_y n_y. \tag{31}$$

The integration is performed numerically by sampling 360 angular points along the circular airgap contour. The total electromagnetic torque is then obtained by multiplying the per length torque by the stack length

$$T = T' l_z. \tag{32}$$

VI. Results and Discussions

To compare the influence of objective formulation and regularization, three optimization cases were examined. The Figs. below show how the material layout changes when the volume term and filtering are introduced.

A. Effect of Objective Formulation

When only the flux objective is considered, the optimizer removes material mainly from the central part of the design domain, as shown in Fig. 4. However, because no volume penalty is included, the algorithm has little incentive to eliminate all low sensitivity material. A noticeable amount of back iron therefore remains near the boundaries, indicating that the available design space is not used efficiently for weight reduction.

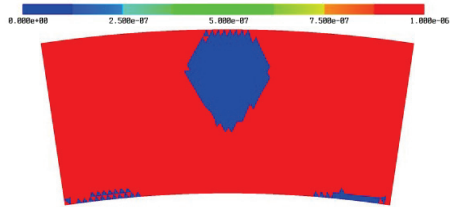


Fig. 4. Flux maximization objective

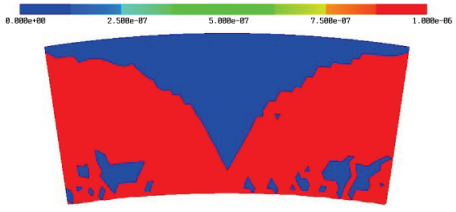


Fig. 5. Flux maximization objective with volume penalization

Adding the volume reduction objective changes the optimization behavior, as shown in Fig. 5. The optimizer becomes more selective and removes additional inactive material while still preserving the main magnetic path required for flux transmission. This confirms that the volume term is necessary when the design target is not only electromagnetic performance but also material saving. Nevertheless, the unfiltered topology contains fragmented regions, local voids, and thin connections. These features are undesirable because they can create locally saturated flux paths and are difficult to manufacture. The combined flux and volume objective improves material utilization, regularization is still required before the topology can be considered a practical rotor back iron design.

B. Filtering and Projection

A PDE based density filter is applied in order to remove oscillations and impose a minimum length scale. The technique of filtering solves a Helmholtz-type equation:

$$-r^2 \nabla^2 \tilde{\rho} + \tilde{\rho} = \rho \tag{33}$$

where $\tilde{\rho}$ and r represent the filter density and filter radius respectively. After filtering and projection techniques, the material distribution in Fig. 6 becomes more continuous, and the small isolated features observed in the unfiltered result are removed. The transition between iron and air is also smoother, which makes the design more suitable for interpretation and subsequent manufacturing oriented refinement.

C. Performance Comparison of Initial and Optimized Design

The evolution of the objective function and the material volume during the optimization process is shown in Fig. 7. The flux objective curve exhibits a short oscillatory transient during the first few iterations, which reflects the rapid redistribution of material at the start of the optimization. After this initial stage, the objective function improves steadily and then levels off, indicating convergence.

The volume ratio follows a complementary trend. It decreases quickly at the beginning as inactive back iron material is removed and then approaches a nearly constant value after approximately 20-25 iterations. This behavior shows that the optimizer first explores the design space aggressively and then converges toward a stable topology that satisfies the magnetic requirement with less material. Overall, the response confirms stable convergence while maintaining the required flux performance with less active material.

Fig. 8 displays the magnetic flux density distributions of the original and optimized designs. The rotor back iron in the baseline design exhibits non-homogenous flux density contour. The optimized design, on the other hand displays a

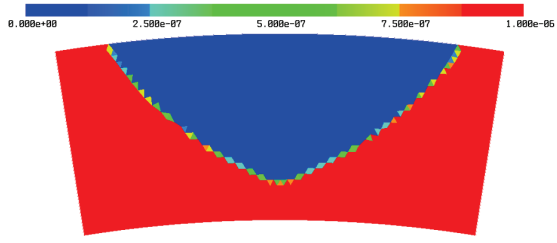


Fig. 6. Optimal design including the density filter and projection

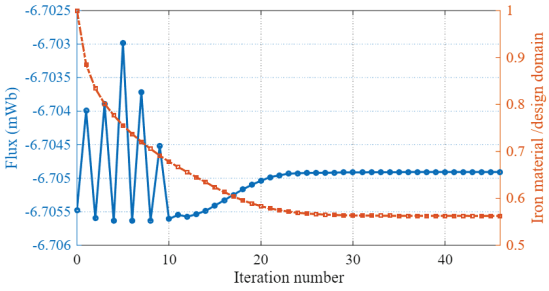


Fig. 7. Objective function response with respect to iteration numbers

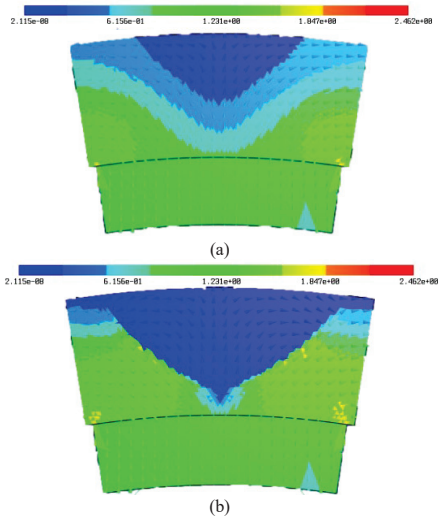


Fig. 8. Flux density distribution (a) Initial design (b) Optimized design

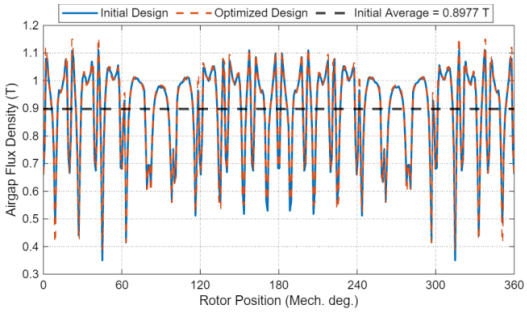


Fig. 9. Airgap flux density of initial and optimized design

magnetic flux pattern that is more uniform and distributed evenly.

Fig. 9 shows a comparison of the absolute airgap flux density waveforms. The results demonstrate that the optimized design maintains the airgap flux density waveform magnitude and shape. The optimization does not reduce the electromagnetic excitation in the airgap, as shown by the average airgap flux density being almost unchanged. Similarly, the three-phase back EMF waveforms in Fig. 10 exhibit the same waveform characteristics and amplitude for both designs. Fig. 11 compares the electromagnetic torque waveforms having no apparent changes in torque ripple

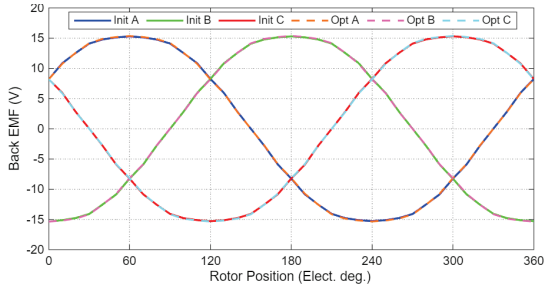


Fig. 10. Three phase Back EMF of initial and optimized design

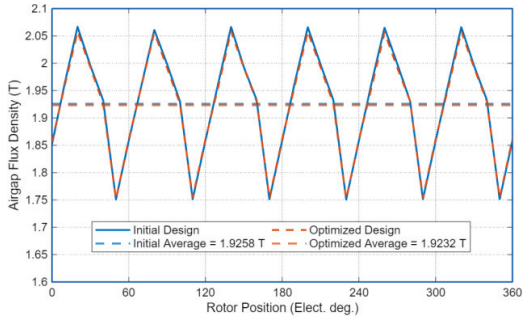


Fig. 11. Torque waveform of initial and optimized design

TABLE II. PERFORMANCE PARAMETERS

Performance	Unit	Initial	Optimized
Average airgap flux density	T	0.89	0.89
Peak phase Back EMF	V	15.35	15.30
Average torque	$N.m$	1.92	1.92
Back iron weight	kg	0.31	0.19
Torque density	$N.m/kg$	1.95	2.23

behavior, the improved design attains the same average torque as the original design. This indicates that the capacity to produce torque is not adversely affected by the removal of inactive back iron material.

In terms of volume reduction, the optimized rotor achieves a 39% decrease in the rotor back iron area, which translates to a 12% reduction in the overall motor volume. As a result, the torque density increases by approximately 14%, demonstrating improved material utilization without compromising key performance indicators. A summary of the main performance metrics is provided in Table II.

VII. CONCLUSIONS

This paper has presented a density based TO approach for material redistribution in the rotor back iron of an outer rotor BLDC motor. Unlike conventional parametric optimization methods that modify predefined geometric boundaries, the proposed framework enables free material redistribution within the rotor back iron domain, allowing identification and removal of magnetically under-utilized regions.

The magnetic reluctivity was interpolated using the SIMP formulation, and nonlinear magnetic behavior was incorporated through iterative updating of the local B–H characteristics. An adjoint based sensitivity formulation enabled computationally efficient gradient evaluation, while Helmholtz-type filtering technique ensured smooth, physically meaningful, and nearly binary material

distributions. Additionally, the impact of objective functions was examined, emphasizing the significance of regularization in attaining stable convergence and removing oscillatory patterns.

The results demonstrate that significant material reductions are possible without compromising electromagnetic performance. The suggested approach shows how density based TO may be used practically for designing high performance and environmentally friendly electrical machines. Incorporating mechanical stress limitations, expanding the framework to three-dimensional models, and investigating multi-objective formulations that take efficiency, thermal behavior, and manufacturability factors into account are the primary objectives of future study.

ACKNOWLEDGEMENT

This work was supported by Estonian Research Council under Grants PRG-1827 and the joint DFG/FWF Collaborative Research Centre CREATOR (DFG Project-ID 492661287/TRR 361; FWF Project-DOI 10.55776/F90) at TU Darmstadt, TU Graz and JKU/RICAM Linz. P.G. is partially supported by the State of Upper Austria.

REFERENCES

[1] W. Geng, J. Wang, L. Li, and J. Guo, "Design and Multiobjective Optimization of a New Flux-Concentrating Rotor Combining Halbach PM Array and Spoke-Type IPM Machine," *IEEE/ASME Transactions on Mechatronics*, vol. 28, no. 1, 2023, doi: 10.1109/TMECH.2022.3196115.

[2] X. Ba, X. Sun, Z. Gong, Y. Guo, C. Zhang, and J. Zhu, "A Generalized Per-Phase Equivalent Circuit Model of the PMSM With Predictable Core Loss," *IEEE/ASME Transactions on Mechatronics*, vol. 28, no. 3, 2023, doi: 10.1109/TMECH.2022.3227271.

[3] S. W. Jung, J. S. Ro, and H. K. Jung, "A Hybrid Algorithm Using Shape and Topology Optimization for the Design of Electric Machines," *IEEE Trans. Magn.*, vol. 54, no. 3, 2018, doi: 10.1109/TMAG.2017.2764753.

[4] S. Ruzbehi and I. Hahn, "Two-level topology optimization of an electromagnetic actuator based on genetic algorithm and neighbourhood method," in *Proceedings of the IEEE International Conference on Industrial Technology*, 2020. doi: 10.1109/ICIT45562.2020.9067305.

[5] X. He *et al.*, "Multimaterial Topology Optimization Method of Surface-Mounted PMSM Rotor Poles Based on Variable Density Representation," *IEEE/ASME Transactions on Mechatronics*, vol. 30, no. 1, 2025, doi: 10.1109/TMECH.2024.3400985.

[6] F. Lucchini, R. Torchio, V. Cirimele, P. Alotto, and P. Bettini, "Topology Optimization for Electromagnetics: A Survey," *IEEE Access*, vol. 10, 2022, doi: 10.1109/ACCESS.2022.3206368.

[7] A. Silvestrini, M. H. Hassan, X. Mininger, G. Krebs, and P. Dessante, "Magneto-Mechanical Topology Optimization With Generalized Optimality Criteria," *IEEE Trans. Magn.*, vol. 60, no. 3, 2024, doi: 10.1109/TMAG.2023.3338422.

[8] S. Lim, S. Min, and J. P. Hong, "Level-set-based optimal stator design of interior permanent-magnet motor for torque ripple reduction using phase-field model," *IEEE Trans. Magn.*, vol. 47, no. 10, 2011, doi: 10.1109/TMAG.2011.2158201.

[9] J. S. Choi, K. Izui, S. Nishiwaki, A. Kawamoto, and T. Nomura, "Topology optimization of the stator for minimizing cogging torque of IPM motors," *IEEE Trans. Magn.*, vol. 47, no. 10, 2011, doi: 10.1109/TMAG.2011.2158572.

[10] F. Guo, N. Tang, and I. P. Brown, "Combined Dimensional and Topology Optimization of Synchronous Machine Rotors Using a Material Density Interpolation Method," *IEEE Trans. Ind. Appl.*, vol. 59, no. 6, 2023, doi: 10.1109/TIA.2023.3292214.

[11] T. Sato, K. Watanabe, and H. Igarashi, "Multimaterial topology optimization of electric machines based on normalized Gaussian network," *IEEE Trans. Magn.*, vol. 51, no. 3, 2015, doi: 10.1109/TMAG.2014.2359972.

[12] T. Cherrière, P. Gangl, and N. Krenn, "Topology optimization with arbitrarily many materials: density versus level-set applied to a hybrid excited rotor," *IEEE Trans. Magn.*, 2025, doi: 10.1109/TMAG.2025.3630504.

[13] M. R. Mahmoud, M. N. Ibrahim, and P. Sergeant, "Evaluating density-based topology optimization using different material interpolation schemes: Magnetic actuator design case study," *J. Magn. Magn. Mater.*, vol. 636, 2025, doi: 10.1016/j.jmmm.2025.173646.

BIOGRAPHIES

Shahid Hussain (Student Member, IEEE) received the B.S. and M.S. degrees in electrical power engineering from COMSATS University Islamabad, Abbottabad Campus, Pakistan, in 2019 and 2022, respectively. He is currently working toward the PhD degree from the Tallinn University of Technology, Tallinn, Estonia. His research interests include the design of linear flux switching machines and topology optimization of additively manufactured switched reluctance machines.

Ants Kallaste was born in Pärnu, Estonia, in 1980 and received his BSc, MSc and PhD degrees in electrical engineering from Tallinn University of Technology, Estonia, in 2004, 2006 and 2013, respectively. He is currently a Professor of Electrical Machines at Tallinn University of Technology, Department of Electrical Power Engineering and Mechatronics. In addition, he holds the position of Head of the Electrical Machines Research Group. He is the senior researcher of IEEE and a member of the Estonian Society of Moritz Hermann Jacobi. He has spent several years in private engineering companies and visited numerous other research institutions.

Peter Gangl studied applied mathematics at Johannes Kepler University in Linz, Austria (BSc 2010, MSc 2012, PhD 2017). Subsequently, he held post-doctoral positions at Graz University of Technology in Graz, Austria, and at Friedrich-Alexander-Universität Erlangen-Nürnberg, Germany. He currently holds a position as a Senior Scientist at the Johann Radon Institute for Computational and Applied Mathematics (RICAM) of the Austrian Academy of Sciences in Linz, Austria. His research focuses on mathematical methods for design optimization. Dr. Gangl received awards from the Austrian Mathematical Society (OMG), the European Consortium for Mathematics in Industry (ECMI) and the Society for Industrial and Applied Mathematics (SIAM) for his PhD thesis.

Nepomuk Krenn received his degree in mathematics from Graz, Austria and is currently pursuing his doctoral research at the Johann Radon Institute for Computational and Applied Mathematics (RICAM) of the Austrian Academy of Sciences, Linz, Austria. His work focuses on topology optimization and topological derivative methods for multiphysics design problems, particularly in the optimization of electric machines under coupled electromagnetic, thermal, and structural constraints.

Théodore Cherrière received the Ph.D. degree in electrical engineering from Université Paris-Saclay, Paris, France, in 2023. After a postdoctoral stay at RICAM (Linz, Austria), he joined CentraleSupélec and the research Group in electrical engineering of Paris (GeePs) as an assistant professor in 2024. His research interests include electromagnetics computing, multiphysics simulations, and topology optimization of electrical actuators.

Muhammad Usman Naseer (Member, IEEE) was born in 1990 in Pakistan. He received the B.Sc. degree in electrical engineering from the Islamia University of Bahawalpur, Bahawalpur, Pakistan, in 2011 and the M.S. degree from the University of Engineering and Technology, Lahore, Pakistan. He is completed the doctoral degree from Tallinn University of Technology, Tallinn, Estonia. Recently, he has been working as a researcher in the Electrical Machine Design Group, in the Department of Electrical Power Engineering and Mechatronics, Tallinn University of Technology, Tallinn, Estonia. His research interest focuses on electrical machine modeling, design, and optimization.

Zahoor Ahmad was born in Khyber Pakhtunkhwa, Pakistan, in 1993. He received a BS degree in Electrical Engineering from the University of Science and Technology, Bannu, Khyber Pakhtunkhwa, in 2016 and an MS. Degree in Electrical Engineering from COMSATS University Islamabad at Abbottabad, Pakistan, in 2020. During his MS degree program, he worked on the Design and Analysis of Moving Magnet Linear Oscillating Actuators. Currently, he is pursuing a PhD at Tallinn University of Technology, Department of Electrical Power Engineering and Mechatronics. His research interests include Advanced Design Methodology for Additively Manufactured Electrical Machines.

Toomas Vaimann (Senior Member, IEEE) was born in Pärnu, Estonia, in 1984. He received the B.Sc., M.Sc., and Ph.D. degrees in electrical engineering from the Tallinn University of Technology, Tallinn, Estonia, in 2007, 2009, and 2014, respectively. He is currently a Senior Researcher with the Department of Electrical Power Engineering and Mechatronics, Tallinn University of Technology. Internationally, he has been a Postdoctoral Researcher with the Department of Electrical Engineering and Automation, Aalto University, Espoo, Finland, and works as a Visiting Professor with the Faculty of Control Systems and Robotics, ITMO University, St. Petersburg, Russia. He has been working in several companies as an Electrical Engineer. He is a member of the Estonian Society of Moritz Hermann Jacobi and Estonian Society for Electrical Power Engineering. His main research interest focuses on the diagnostics of electrical machines.

Publication V

S. Hussain, A. Kallaste, M. U. Naseer, M. Sarap, H. Tiismus, and T. Vaimann, “Preliminary Design Analysis of an Axial Flux Yokeless Stator Switched Reluctance Machine,” in *2023 IEEE 64th International Scientific Conference on Power and Electrical Engineering of Riga Technical University (RTUCON)*, Riga, Latvia, 2023, pp. 1–6, doi: 10.1109/RTUCON60080.2023.10413130.

2023 IEEE 64th International Scientific Conference on Power and Electrical Engineering of Riga Technical University (RTUCON)

2023 IEEE 64th International Scientific Conference on Power and Electrical Engineering of Riga Technical University (RTUCON) | 979-8-3503-1773-2/23/$31.00 ©2023 IEEE | DOI: 10.1109/RTUCON60080.2023.10413130

Preliminary Design Analysis of an Axial Flux Yokeless Stator Switched Reluctance Machine

Shahid Hussain, Ants Kallaste, Muhammad Usman Naseer, Martin Sarap, Hans Tiismus, Toomas Vaimann
Department of Electrical Power Engineering and Mechatronics
Tallinn University of Technology
Tallinn, Estonia
shahid.hussain@taltech.ee

***Abstract*—In this paper a new axial flux yokeless stator switched reluctance machine is designed specifically for drone applications. The machine incorporates a segmented stator and double rotor arrangement, along with a concentrated winding configuration, resulting in enhanced performance. First, the output power equation is derived for the proposed machine and proceeds to discuss the various geometric parameters in detail. The overall design methodology process is described, which leads to the attainment of performance results. To validate the calculated dimensions, a 3D finite element method is utilized to analyze the effectiveness of the machine's performance. The study also focuses on evaluating the performance of the pole shoe on both the stator pole and the rotor. To demonstrate the practicality of the proposed machine, this paper provides a step-by-step explanation of its 3D view, offering insights into its physical appearance and structure.**

Keywords—axial flux switched reluctance machine, additive manufacturing, eddy currents, segmented stator

I. INTRODUCTION

The rapid increase of electrification in transportation sector, along with the available enabling technologies, creates possibilities for the integration of drones, flying cars and air taxi like applications [1]. This trend is reshaping traditional infrastructure requirements and reducing the need for extensive transportation networks and their associated maintenance. As drones become increasingly capable and efficient, they offer a viable alternative for transporting goods, delivering packages, and conducting surveillance operations, eliminating the need for extensive physical infrastructure such as roads or manned vehicles.

Switched Reluctance Machines (SRM) are suitable for the application of drone propulsion system because it offers high speed, low weight and high-power density which are the key requirement for the drone applications. The suitability of SRM as an option is due to their simple and sturdy design, fault tolerance, and high reliability [2-4]. However, these machines suffer from limitations such as low torque density and significant torque ripples, which deter their widespread application [5,6]. In the past few years, various innovative designs have been put forward to address these issues. These include the segmented rotor type [7], double rotor configurations [8,9], double stator type [10,11], and axial flux type [6,12].

Furthermore, existing literature acknowledges that axial flux machines exhibit superior torque densities and efficiencies compared to radial counterparts due to their larger active air-gap surface area. [13]. By using multiple air gaps, it is possible to significantly increase the utilization of the magnetic flux generated by the excitation coils, which will increase the torque density. To further improve the torque density, axial rotor segmented SRM has been introduced in which the author uses the double stator and segmented single rotor topology, and short pitch winding configuration is utilized [14]. In order to improve the torque density, a new double stator and segmented rotor topology is employed and to make the magnetic flux shorter, full pitch winding configuration is utilized [6]. However, the use of full pitch winding increases the end winding length, which leads to higher copper losses due to the high consumption of copper. The higher copper losses in full pitch winding can result in lower motor efficiency compared to motors with short pitch winding. Moreover, the segmented rotor construction can introduce mechanical challenges at higher speeds [15]. As the rotor segments move relative to each other, they can experience increased centrifugal forces, which can lead to higher stresses and potentially reduce the machine's reliability and lifespan.

Moreover, another important aspect which effect the performance of axial machine is to reduce the eddy current losses. For many years, electrical steel laminations have been utilized in electrical machines to minimize eddy current losses. However, these laminations restrict the magnetic flux to a two-dimensional plane. To address these limitations, Soft Magnetic Composites (SMCs) have been employed in 3D magnetic circuits as they exhibit lower core losses, particularly at high frequencies. Nonetheless, SMCs are constrained in terms of shape due to their uniaxial pressing operation. An alternative approach to overcome these limitations is the use of Additive Manufacturing (AM) or 3D printing techniques, which allow for the production of complex geometries while effectively managing eddy current losses. In [17], the author employed selective laser melting to manufacture 3D printed axial flux machines with a 6/4 topology, consisting of two stators and one rotor. The entire rotor and stators were produced in 57 hours using this technique. Further, an axial flux stator is manufactured through additive manufacturing and compared the performance with the identical conventionally manufactured baseline machine [18]. The results demonstrate that using Hilbert pattern can reduce the eddy current losses by approximately 50% compared with a solid structure. Although,

979-8-3503-1773-2/23/$31.00 ©2023 European Union

Authorized licensed use limited to: Tallinn University of Technology. Downloaded on February 28,2024 at 14:34:25 UTC from IEEE Xplore. Restrictions apply.

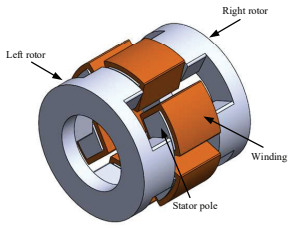


Fig. 1. Axial flux yokeless stator double rotor SRM

the stacking factor of AM stator is lower than the baseline due to which it exhibits 18% lower magnetizing flux. Additionally, advancements in AM technology enable the production of structures with thinner features and improved stacking efficiency, enabling them to achieve comparable performance to laminated structures across a wider range of operating conditions.

In this paper a new 6/4 Axial Flux Yokeless Stator Switched Reluctance Machine (AFYS-SRM) is presented as shown in Fig. 1. The configuration of the machine includes the single stator segments placed between the two rotors. Eliminating stator yoke results in a decrease in the iron component as well as a reduction in the weight and core losses of the machine while maintaining the performance level without any degradation. The following paper is organized as section II comprehensively explain the sizing and design methodology of the presented machine. In section III the Finite Element Method (FEM) is implemented on the basis of the calculated parameters in section II. Section IV discusses the complete assembly of the machine. Conclusion and future work of this machine is explained in section V.

II. Machine Sizing

The output equation for an axial SRM typically relates the machine's output torque or power to its key design parameters, such as the average diameter, speed, and magnetic and electric loadings. It is worth mentioning that the specific form of the output equation for an axial SRM can vary depending on the machine's configuration, control strategy, and the objectives of the design. Therefore, it is crucial to consider these factors while formulating the output equation to accurately represent the SRM's performance characteristics. The general power equation for 6/4 axial SRM can be defined as [19]

$$P_{out} = k_e k_d vim \tag{1}$$

where k_e is the efficiency, k_d represents the duty cycle, v and i are peak values of voltage and current respectively and m denotes the number of phases. The duty cycle can be expressed as

$$k_d = \frac{\theta_i . m P_r}{360} \tag{2}$$

where θ_i is the conduction angle, and P_r is the number of rotor poles. The applied voltage can be determined in terms of inductance and current as

$$v = \frac{(L_a{}^s - L_u)i}{t} \tag{3}$$

where $L_a{}^s$ is the aligned saturated inductance, L_u is the unaligned inductance. The time it takes for the rotor to rotate from an unaligned position to an aligned position is denoted as t and can be expressed as

$$t = \frac{\beta_s}{\omega_m} \tag{4}$$

where β_s, ω_m is the stator pole arc and rotor speed in rad/sec respectively. Substituting Eq. (4) in Eq. (3) and the voltage Eq. becomes

$$v = \frac{\omega_m}{\beta_s} L_a{}^s i(1 - \frac{1}{\sigma_s \sigma_u}) \tag{5}$$

where σ_s, σ_u are the ratio of saturated aligned to unsaturated aligned inductance and ratio of unsaturated aligned and unaligned inductance. The flux linkages in the aligned position can be represented using either the flux and the number of turns, or the flux density and the dimensions of the machine.

$$L_a{}^s i = \varphi N_{ph} = B_g A_{sp} N_{ph} = \frac{1}{8} B_g (D_0{}^2 - D_i{}^2) \beta_s N_{ph} \tag{6}$$

where φ, N_{ph}, B_g and A_{sp} is the aligned flux, number of turns per phase, airgap flux density and stator pole area respectively and D_0, D_i are the outer and internal diameter. Moreover, the electric loading can be expressed as

$$A_s = \frac{2 N_{ph} im}{\pi D_{avg}} \tag{7}$$

where m represents the number of phases conducting simultaneously and D_{avg} is the average diameter of an axial machine. In the case of 6/4, only one phase conducts at a moment. Substituting Eq. (6) and (7) in (5).

$$v = \frac{\pi^2}{480} \frac{1}{im} B_g A_s D_{avg} (D_0{}^2 - D_i{}^2)(1 - \frac{1}{\sigma_s \sigma_u}) N_r \tag{8}$$

where N_r represents the rotor speed in revolution per minute. Putting the Eq. (8) in (1) to get the output power Eq.

$$P_{out} = k_e k_d k_1 k_2 B_g A_s D_{avg} (D_0{}^2 - D_i{}^2) N_r \tag{9}$$

where

$$k_1 = \frac{\pi^2}{480}, k_2 = (1 - \frac{1}{\sigma_s \sigma_u}) \tag{10}$$

The output torque Eq. can be derived from the above output power Eq. and can be expressed as

$$\tau = \frac{P_{out}}{\omega_m} \tag{11}$$

Substituting Eq. (9) in (11), the torque Eq. becomes

$$\tau = k_e k_d k_2 k_3 B_g A_s D_{avg} (D_0{}^2 - D_i{}^2) \tag{12}$$

where

Authorized licensed use limited to: Tallinn University of Technology. Downloaded on February 28,2024 at 14:34:25 UTC from IEEE Xplore. Restrictions apply.

$$k_3 = \frac{\pi}{16} \tag{13}$$

The average torque of the machine also depends on the inner and outer diameters of the stator once the electrical and magnetic loads have been set and the maximum and minimum inductance ratios are specified. It is significant to note that the machine's maximum average output torque may be obtained at a ratio of inner and outer diameter of 0.577 [19]. Further, the geometric parameters of a 6/4 axial SRM can be determined as and the width of copper is defined as [20]

$$w_{cu} = \frac{\pi D_0 (1+k_r)}{4N_s} \times \frac{B_t \alpha_t - B_t \alpha_t \alpha_{cg} - B_g}{B_t} \tag{14}$$

where k_r is the ratio of inner to outer diameter, N_s represents the number of stator poles, B_t is the flux density of stator pole, α_t is the ratio of the reduction in the flux density due to the added radii corners helps to mitigate the effects of end winding and leakage inductance. This reduction is important for improving the performance and efficiency of the motor, α_{cg} is the gap between the coils serves to enhance thermal conductivity between the copper windings and the iron core. Moreover, the stator slot depth, stator pole width and rotor pole width can be expressed as

$$w_{sd} = \frac{\pi D_0 (1+k_r)}{4N_s} \times \frac{B_t \alpha_t \alpha_{sh} - B_g}{B_t \alpha_t} \tag{15}$$

$$w_{sp} = \frac{B_g \pi D_0 (1+k_r)}{2N_s B_t} \tag{16}$$

$$w_{rp} = \frac{B_g \pi D_0 (1+k_r)}{2P_r B_t} \tag{17}$$

where α_{sh} is the ratio between the arc of pole shoe and the stator pole pitch. The length of the stator pole can be determined as

$$L_s = \frac{A_s}{2\alpha J_{rms}} \times \frac{\pi D_0}{2N_s w_{cu}} \times \frac{1+k_r}{2} \tag{18}$$

where α is the filling factor of copper in the stator slot and is consider as 0.75 and J_{rms} is the current density and for natural cooling system it is selected as 4.5 A/mm^2. The width of the stator pole shoe can be expressed as

$$w_{sh} = \frac{\pi D_0 (1+k_r)}{2N_s} \alpha_{sh} \tag{19}$$

And the length of pole shoe is

$$L_{sh} = \frac{B_g w_{sd}}{B_{sh}} \tag{20}$$

where B_{sh} is the allowed flux density in the stator pole shoe. Moreover, the back iron length of rotor can be expressed as

$$L_{bl} = \frac{\pi D_0}{4P_r} \times \frac{(1+k_r)}{2} \times \frac{B_g}{B_{bl}} \tag{21}$$

where B_{bl} is the flux density of back iron. It is noted that the number of turns per phase can be determined using the Eq. (7)

When the geometric parameters have been computed, proceed to create a visual representation of the design in SolidWorks 2023 using these parameters. Subsequently, validate the FEM analysis by comparing it with the results obtained from analytical calculations. The main geometric parameters are shown in Fig. 2.

The preliminary stage of the AFYS-SRM involves introducing the specifications, constraints, and configurations. The rated parameters encompass the base speed set at 3000 rpm, current density, and efficiency. As for the machine configuration, it includes slot/pole combination, stator and rotor pole arcs, and a specific winding arrangement. The AFYS-SRM utilizes a concentrated-type winding, characterized by alternating winding polarities. This design facilitates the controlled flow of flux, allowing it to enter from one rotor pole, passes through stator pole and leave through the other rotor pole within a given phase. The diameters of the machine are determined using the output power Eq. and the initial assumptions are verified through an iterative computation process. Table I presents the geometric parameters associated with the AFYS-SRM. The flowchart of design methodology is shown in Fig. 3.

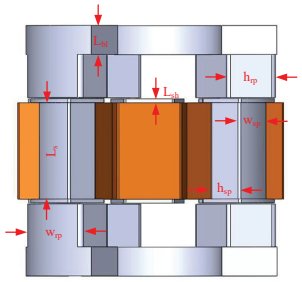


Fig. 2. Geometric parameters of AFYS-SRM

TABLE I. CALCULATED PARAMETERS OF AFYS-SRM

Symbol	Parameter	Value
D_0	Outer diamter (mm)	60
D_i	Inner diamter (mm)	33.6
w_{sp}	Stator pole width (mm)	11.43
h_{sp}	Stator pole height (mm)	13.2
w_{cu}	Copper width (mm)	3.94
w_{sd}	Stator slot depth (mm)	1.68
w_{sh}	Stator pole shoe width (mm)	17.88
L_{sh}	Pole shoe length (mm)	0.896
L_s	Stator pole length (mm)	23
L_{bl}	Back iron length (mm)	6.3

Authorized licensed use limited to: Tallinn University of Technology. Downloaded on February 28,2024 at 14:34:25 UTC from IEEE Xplore. Restrictions apply.

Symbol	Parameter	Value
w_{rp}	Rotor pole width (mm)	19.66
h_{rp}	Rotor pole height (mm)	13.2
N_{ph}	Number of turns	183

III. Simulation Results And Comparison

In this section, a 3-D Finite Element Method (FEM) is utilized to validate the performance of the AFYS-SRM. A motion-coupled analysis is conducted to evaluate the dynamic behavior of the motor. The motor is driven by an asymmetric half-bridge converter.

Fig. 4 illustrates the distribution of flux density in the AFYS-SRM when the A-phase winding carries current, considering both aligned and unaligned positions. The observed magnetic flux path of a single phase predominantly follows a trajectory from the right rotor pole to the stator and subsequently back to the left rotor pole. In the unaligned position, the magnetic flux density at the stator pole measures 0.2T, while it reaches 0.25T at the rotor pole shoe. Conversely, when the rotor pole aligns with the stator pole, the flux density increases to approximately 1.6T at the stator pole and 1.65T at the rotor pole shoe. Additionally, the magnetic flux density at the rotor yoke amounts to 1.04T during the aligned position.

Fig. 5 displays the simulated three-phase currents in the motor. Furthermore, Fig. 6 presents a torque comparison at the rated speed. During the initial stages of machine design, the pole shoe was originally positioned on the stator pole. This configuration offers advantages such as reducing torque ripples and providing support for the windings. However, challenges arose during the assembly process in combining the stator segments. To address this issue, an alternative solution is devised, placing the pole shoe on the rotor pole to mitigate torque ripples. A lip is introduced on the stator pole to attach all the stator poles with a carbon fiber sheet, which would also aid in holding the windings in place.

Additionally, Table II provides a summary of simulated performance parameters under rated operating conditions. These parameters encompass various metrics such as torque, power, power density, and torque density, which serve to characterize the machine's performance.

IV. Complete Assembly of AFYS-SRM

The 3D view of AFYS-SRM is shown in Fig. 7 and explain the advantage and working of each part in steps.

Shaft plate: The shaft plate is a component made of iron. It is fixed with the rotor on both sides using bolts. The shaft plate acts as a support structure and holds the shaft of the machine. It will provide stability and helps transmit the rotational motion from the rotor to the shaft.

Rotor: The rotor is an integral part of the AFYS-SRM and is connected to the shaft plate on both sides. It is typically composed salient type poles for the flow of the magnetic field for machine operation. The rotor rotates along with the shaft and interacts with the stator to produce torque.

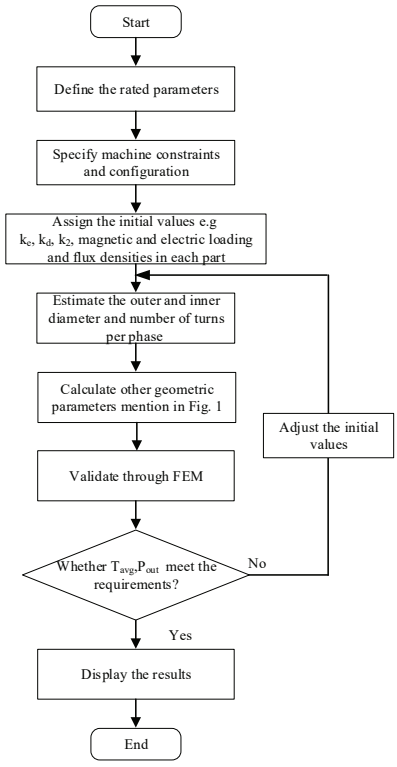


Fig. 3. Flowchart of design methodology of axial flux SRM

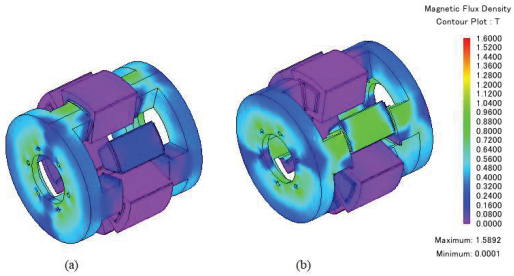


Fig. 4. Flux distribution of AFYS-SRM (a) Unaligned position (b) Aligned position

Shaft keyway: The shaft plate has a keyway, which is a groove or slot that runs the length of the plate. The purpose of the keyway is to secure the shaft and prevent rotational motion between the shaft and the plate. It facilitates the efficient transfer power from the rotor to the shaft.

Authorized licensed use limited to: Tallinn University of Technology. Downloaded on February 28,2024 at 14:34:25 UTC from IEEE Xplore. Restrictions apply.

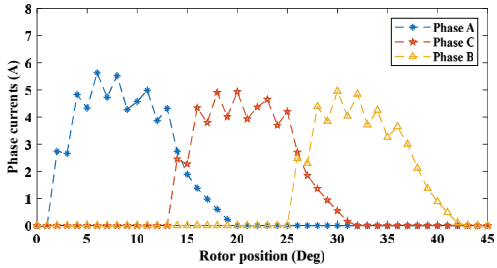


Fig. 5. Three phase currents waveform

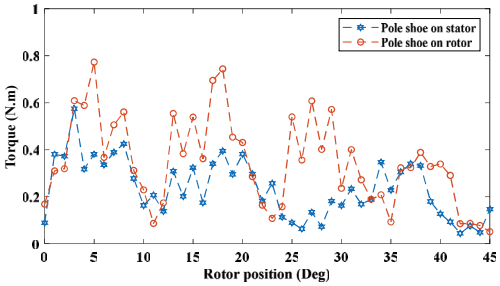


Fig. 6. Comparison of torque of two machines

TABLE II. SIMULATED PERFORMANCE PARAMETERS AT RATED CONDITION

Symbol	Parameter	Value
N_r	Rotor speed (rpm)	3000
P_{out}	Output power (W)	140
τ	Average torque (Nm)	0.45
$\tau_{density}$	Torque density (Nm/kg)	0.59
$P_{density}$	Power density (W/kg)	183.17

Bearing plate: The bearing plate is a distinct component that is attached to the shaft. It serves as a mounting platform for the machine's bearings. The bearing is supported and stabilized by the bearing plate, enabling the shaft to rotate precisely and smoothly.

Carbon fiber sheet: The carbon fiber material is attached to the bearing plate and serves multiple purposes. As a structural component, it holds the stator poles in position. For supporting the stator poles, carbon fiber sheets reduce the need for epoxy resin while providing a durable and lightweight alternative. Additionally, the carbon fiber material aides in heat dissipation and reduces the overall weight of the machine.

Stator pole: The AFYS-SRM stator poles have a lip on both sides, allowing them to be attached to the carbon fiber sheet. By incorporating this configuration, the necessity for epoxy resin bonding is avoided as it ensures a strong connection between all stator poles via the carbon fiber sheet. Furthermore, the gaps establish a mechanical bond between the stator poles and the carbon fiber sheet, ensuring accurate alignment and secure fixation.

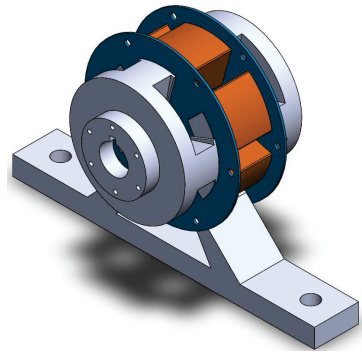


Fig. 7. Complete 3D view of AFYS-SRM

Mounting support: The mounting support serves as a structural element that is affixed lower to the carbon fiber sheet. It provides additional support and stability to the entire machine assembly. The mounting support is responsible for securing the machine in its designated location and preventing unwanted vibrations or movement during operation.

V. CONCLUSION AND FUTURE WORK

The preliminary design procedure for the AFYS-SRM was presented in this study. The geometrical characteristics of the machine were determined, and machine sizing equations were developed. Using 3D-FEM, the effectiveness of the machine was evaluated. By adding pole shoes to the stator and rotor sides, respectively, the torque of two distinct machine designs based on their rotor and stator structures were compared.

The results of the study showed that the average torque was 32.35% greater when the pole shoe was designed on the rotor poles compared to the stator poles. This indicates that placing pole shoe on the rotor side can substantially improve the performance of the machine. In addition, the study provided information regarding the AFYS-SRM's construction. It displayed the initial conditions and highlights improvement areas for the future.

Future work in this area of research will include geometric and topology optimization to enhance the performance of the AFYS-SRM while reducing material consumption through the use of topology optimization techniques. Using these optimization techniques, the design of the machine can be refined and enhanced to attain even greater efficiency and performance.

Moreover, the optimized design will be manufactured utilizing AM techniques. AM-based winding permits greater flexibility, resulting in a greater fill factor, which corresponds to the utilization of available winding space. In addition, this method allows the machine to operate at high current densities, which facilitates the implementation of an effective cooling mechanism.

Authorized licensed use limited to: Tallinn University of Technology. Downloaded on February 28,2024 at 14:34:25 UTC from IEEE Xplore. Restrictions apply.

Future work will leverage topology optimization, AM fabrication, and AM-based winding techniques to construct an AFYS-SRM with increased performance, enhanced efficiency, reduced material consumption, and effective thermal management.

ACKNOWLEDGMENT

This work was supported by the Estonian Research Council grant (PRG-1827).

REFERENCES

[1] Islam, Md Sariful, Rajib Mikail, and Iqbal Husain. "Slotless lightweight motor for aerial applications." *IEEE Transactions on Industry Applications* 55.6 (2019): 5789-5799.

[2] de Paula, Marcelo Vinícius, et al. "A dahlin cruise control design method for switched reluctance motors with minimum torque ripple point tracking applied in electric vehicles." *IEEE Transactions on transportation electrification* 7.2 (2020): 730-740.

[3] Cao, Wenping, et al. "Overview of electric motor technologies used for more electric aircraft (MEA)." *IEEE transactions on industrial electronics* 59.9 (2011): 3523-3531.

[4] Uddin, Wasi, et al. "Design methodology of a switched reluctance machine for off-road vehicle applications." *IEEE Transactions on Industry Applications* 52.3 (2016): 2138-2147.

[5] Kiyota, Kyohei, and Akira Chiba. "Design of switched reluctance motor competitive to 60-kW IPMSM in third-generation hybrid electric vehicle." *IEEE Transactions on Industry Applications* 48.6 (2012): 2303-2309.

[6] Yu, Fengyuan, et al. "Design and multiobjective optimization of a double-stator axial flux SRM with full-pitch winding configuration." *IEEE Transactions on Transportation Electrification* 8.4 (2022): 4348-4364.

[7] Widmer, James D., and Barrie C. Mecrow. "Optimized segmental rotor switched reluctance machines with a greater number of rotor segments than stator slots." *IEEE Transactions on Industry Applications* 49.4 (2013): 1491-1498.

[8] Yang, Yinye, Nigel Schofield, and Ali Emadi. "Double-rotor switched reluctance machine (DRSRM)." *IEEE Transactions on Energy Conversion* 30.2 (2015): 671-680.

[9] Ghaffarpour, Ali, and Mojtaba Mirsalim. "Split-tooth double-rotor permanent magnet switched reluctance motor." *IEEE Transactions on Transportation Electrification* 8.2 (2022): 2400-2411.

[10] Maharjan, Lizon, et al. "Comprehensive report on design and development of a 100-kW DSSRM." *IEEE Transactions on Transportation Electrification* 4.4 (2018): 835-856.

[11] Yan, Wenju, et al. "Design of a low-ripple double-modular-stator switched reluctance machine for electric vehicle applications." *IEEE Transactions on Transportation Electrification* 7.3 (2021): 1349-1358.

[12] Sun, Wei, et al. "Development and investigation of novel axial-field dual-rotor segmented switched reluctance machine." *IEEE Transactions on Transportation Electrification* 7.2 (2020): 754-765.

[13] Torkaman, Hossein, Aghil Ghaheri, and Ali Keyhani. "Axial flux switched reluctance machines: a comprehensive review of design and topologies." *IET Electric Power Applications* 13.3 (2019): 310-321.

[14] Sun, Wei, et al. "Electromagnetic analysis on novel rotor-segmented axial-field SRM based on dynamic magnetic equivalent circuit." *IEEE Transactions on Magnetics* 55.6 (2019): 1-5.

[15] Xu, Zhenyao, et al. "A review on segmented switched reluctance motors." *Energies* 15.23 (2022): 9212.

[16] Goodall, Alexander D., et al. "Loss performance of an additively manufactured axial flux machine stator with an eddy-current limiting structure." *Materials Today Communications* 35 (2023): 105978.

[17] Tiismus, Hans, et al. "Additive manufacturing of prototype axial flux switched reluctance electrical machine." *2021 28th International Workshop on Electric Drives: Improving Reliability of Electric Drives (IWED)*. IEEE, 2021.

[18] Nishanth, Fnu, et al. "Characterization of an Axial Flux Machine with an Additively Manufactured Stator." *IEEE Transactions on Energy Conversion* (2023).

[19] Ma, Jimin, et al. "Optimal design of an axial-flux switched reluctance motor with grain-oriented electrical steel." *IEEE Transactions on Industry Applications* 53.6 (2017): 5327-5337.

[20] Vun, Sook Teng, and Malcolm D. McCulloch. "Optimal design method for large-scale YASA machines." *IEEE Transactions on Energy Conversion* 30, no. 3 (2015): 900-907.

Shahid Hussain received his BS and MS degree in electrical power engineering from COMSATS University Islamabad, Abbottabad Campus, Pakistan in 2019 and 2022 respectively. He is currently pursuing his PhD degree from Tallinn University of Technology, Estonia. His research interests include design of linear flux switching machines and topology optimization of additively manufactured switched reluctance machine.

Authorized licensed use limited to: Tallinn University of Technology. Downloaded on February 28,2024 at 14:34:25 UTC from IEEE Xplore. Restrictions apply.

Publication VI

S. Hussain, A. Kallaste, M. U. Naseer, H. Tiismus, and T. Vaimann, “Development of an Axial Flux SRM Through Additive Manufacturing,” in *2024 International Conference on Electrical Machines (ICEM)*, Torino, Italy, 2024, pp. 1–6, doi: 10.1109/ICEM60801.2024.10700569.

Development of an Axial Flux SRM Through Additive Manufacturing

Shahid Hussain, Ants Kallaste, Muhammad Usman Naseer, Hans Tiismus, Toomas Vaimann
Department of Electrical Power Engineering and Mechatronics
Tallinn University of Technology
Tallinn, Estonia
shahid.hussain@taltech.ee

***Abstract*—Axial-switched reluctance machines have a higher torque density compared to radial-switched reluctance machines, making them a preferred option for applications that require high torque. Due to the intricate three-dimensional design of axial machines, production poses substantial challenges. Additive manufacturing has simplified the process by allowing to produce complex shapes. This paper presents a systematic design approach that utilizes output equations to establish the geometrical parameters of a machine analytically. The proposed machine design was validated using 3D finite element analysis with JMAG software after the analytical phase. The study proposes a design feature to address the challenges associated with the mechanical assembly of machine. This design modification introduces a lip feature on the stator segments to mechanically join all the segments. Furthermore, this study evaluates the impact of this modification on the machine's performance by comparing it to a base design without this feature. The paper outlines the fabrication of a physical prototype utilizing Selective Laser Melting employing an advanced additive manufacturing process.**

Keywords—Axial flux, reluctance machine, additive manufacturing, finite element method, eddy current losses

I. INTRODUCTION

Switched Reluctance Machines (SRMs) are preferred for their durable and magnet-free design, which allows for straightforward temperature control, excellent ability to withstand faults, and a wide range of operating speeds, all at an attractive price limit [1]. As a result, SRMs are considered strong contenders for future drive systems and have already been effectively used in electric vehicles, mining equipment, aircraft, pumps, and more [2], [3], [4], [5], [6]. However, SRM faces significant limitations due to its relatively low torque density and substantial torque ripple, which currently hinder its widespread adoption [7]. Different machines design and control strategies are presented by the researcher to enhance the performance of SRM.

The research on Axial Flux Switched Reluctance Machine (AFSRM) as referenced in [8], [9], [10], [11] have been extensively explored and analyzed. The magnetic field in these types of machines is distributed in three-dimensional space. However, the manufacturing of axial machines is difficult as compared to the radial machine. In radial machines, the eddy current losses are reduced by using the lamination sheets in axial direction and efficiently minimize the eddy currents by aligning the lamination direction perpendicular to the primary flux path. In an axial flux machine, the laminations are arranged in a radial pattern, which makes traditional manufacturing methods challenging. However, utilizing Additive Manufacturing (AM) techniques can address these challenges [12], [13].

AM enables the creation of parts and components with unprecedented geometric freedom without much increasing costs, as it minimizes the material waste [14]. In contrast, the literature on AM for soft-magnetic components primarily concentrates on manufacturing unique geometric designs that emerge from efforts to optimize and study materials to enhance magnetic properties or decrease iron losses. Soft magnetic component fabrication for axial flux machines is an area that is rarely covered in the literature [13], [15], [16]. The validation procedure usually involves analyzing data from FEA along with performing conventional material characterization tests, rather than building an electric machine and physically evaluating its performance as a motor.

According to the author knowledge, in the existing literature, only one AFSRM are fully fabricated through AM [16]. The author proposed a double stator and single rotor AFSRM, which took the printer 57 hours to complete. The materials composition used for the machine were iron (97.05%) and silicon (2.95%), respectively. In [17] the author presented a radial SRM in which he fabricated the rotor through AM. Further, the 8-pole salient type rotor was printed in three segments due to the printer dimension limitations through powder bed fusion. One segment length was 54 mm, and the other two segments' lengths were 25 mm. The samples were heated at 1150 ◦C for one hour to improve the magnetic properties and remove the residual stress.

As mentioned above, the existing literature on the fabrication of reluctance machines through AM is quite limited. However, the studies in [15], [18] fabricated the stator of axial flux PM machine using the SLM technique. For the eddy current loss minimization, the Hilbert pattern was utilized in the AM soft magnetic component [19]. The results show that the AM manufactured stator utilizing 6.5% Si has 34% light weight than the solid stator. Furthermore, the Hilbert structured stator has 13% higher torque density than the laminated stator. In another study, [20] presented the complete AM manufactured induction machine using the lamination thickness of 2 mm having 0.2 mm airgaps between the laminations. Then the lattice structures were added within the airgaps to combine the printed parts in a single core and achieved 34% efficiency at the rated speed. After reviewing different articles on the fabrication of different machines, it appears that a yokeless stator has not yet been produced through AM.

This paper introduces a 6/4 Axial Flux Double Rotor Switched Reluctance Machine (AFDRSRM) featuring a yokeless stator, which is fabricated using AM techniques. Traditionally, machines with yokeless stators pose manufacturing challenges when using conventional methods, primarily because it is difficult to assemble the stator segments into a complete ring. However, the adoption of AM enables the production of yokeless machines with an integrated assembly that is more feasible and efficient. The proposed 6/4 AFDRSRM topology is illustrated in Fig. 1. Furthermore, this

2024 International Conference on Electrical Machines (ICEM) | 979-8-3503-7060-7/24/$31.00 ©2024 IEEE | DOI: 10.1109/ICEM60801.2024.10700569

Authorized licensed use limited to: Tallinn University of Technology. Downloaded on October 26,2026 at 09:07:12 UTC from IEEE Xplore. Restrictions apply.

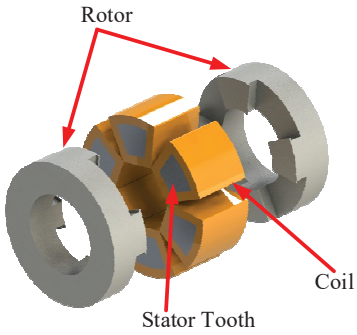


Fig. 1. Topology of 6/4 AFDRSRM

paper is organized as section II describes the analytical formulation for finding the output power and other geometrical parameters. FEM based simulation results are discussed in section III and section IV gives an overview of the printed machine parts. Finally, conclusions are drawn in section V.

II. Output Equation and Design Formulations

A. Output power and Torque

By derivation, the output power equation of AFDRSRM is given by [21]:

$$P_{out} = k_e k_d k_1 k_2 B_g A_s D_{avg} \left({D_o}^2 - {D_i}^2\right) N_{rpm} \quad (1)$$

$$k_1 = \frac{\pi^2}{480} \quad (2)$$

$$k_2 = 1 - \frac{L_u}{L_a} \quad (3)$$

where k_e and k_d are the machine efficiency and the duty cycle for each phase respectively. k_1 and k_2 are the machine coefficients and the ratio of unaligned to aligned inductance. Moreover, B_g and A_s the magnetic and electric loading of the machine respectively, while D_o and D_i are the machine outer and inner diameter. The rated speed of the machine is represented by N_{rpm}. Furthermore, the derivation for the average torque is reported in [21] and is as follows:

$$T_{avg} = k_e k_d k_2 k_3 B_g A_s D_{avg} \left({D_o}^2 - {D_i}^2\right) \quad (4)$$

where

$$k_3 = \frac{\pi}{16} \quad (5)$$

The electrical load equation of AFDRSRM can be obtained as follows:

$$A_s = \frac{2 N_{ph} i m}{\pi D_{avg}} \quad (6)$$

where N_{ph} is the number of turns per phase, i is the peak current value and m represents the number of phases. In the case of 6/4 SRM only one phase conduct at a time. In addition, D_{avg} is the average diameter of the machine and $D_{avg} = (D_o + D_i)/2$. Once the electrical and magnetic loading is fixed and the ratio of unaligned to aligned inductance is determined then the average torque is related to the outer and inner diameter of the AFSRSRM.

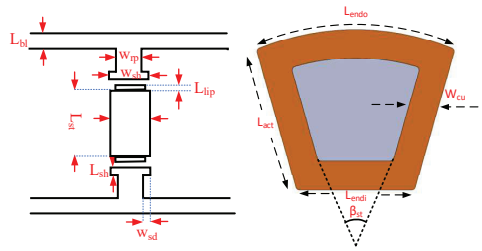


Fig. 2. Representation of geometrical parameters (a) Stator and rotor parameters (b) Coil parameters

B. Geometrical parameters of AFDRSRM

The geometrical parameters for the AFDRSRM can be determined as follows. The geometrical parameters of the stator and rotor are illustrated in Fig. 2(a). However, the average width of the stator tooth can be expressed as:

$$w_{st} = \frac{B_g}{B_{st}} \times \frac{\pi D_{avg}}{N_s} \quad (7)$$

where B_{st} is the magnetic flux density of the core material in the stator tooth and N_s represent the number of stator teeth. Further, the width of copper around the stator tooth is illustrated in Fig. 2(b) and can be formulated as:

$$w_{cu} = \frac{\left(\pi D_{avg}\right) - \left(N_s w_g\right) - \left(N_s w_{st}\right)}{2 N_s} \quad (8)$$

where w_g is the minimum possible gap between the coils and is assumed to be 1mm on the inner side of the coil. Setting up this threshold to a minimum possible gap between the coils at the inner diameter of the coil. Reducing this value will result in joining of the coils at the inner point. Moreover, the average width of the rotor pole, pole shoe width, pole shoe depth and length of pole shoe can be expressed as:

$$\begin{cases} w_{rp} = \dfrac{B_g}{B_{st}} \times \dfrac{\pi D_{avg}}{N_r} \\ w_{sh} = \dfrac{\pi D_{avg}}{N_r} \times \dfrac{\beta_{sh}}{\tau_p} \\ w_d = \dfrac{w_{sh} - w_{st}}{2} \\ L_{sh} = \dfrac{B_g}{B_{sh}} \times w_d \end{cases} \quad (9)$$

where β_{sh}, τ_p are the arc of the pole shoe and pole pitch of the rotor, respectively. w_d and L_{sh} are the depth of the pole shoe and length of the pole shoe, respectively. Moreover, the stator tooth length can be determined as:

$$L_{st} = \frac{A_s \pi D_{avg}}{2 J_{rms} w_{cu} k_f N_s} \quad (10)$$

where J_{rms} is the current density and k_f is the copper filling factor in the stator slot. The number of turns per phase can be calculated from (6) when the electric loading is fixed. However, for the phase resistance calculation the mean length of wire can be calculated as:

Authorized licensed use limited to: Tallinn University of Technology. Downloaded on October 26,2026 at 09:07:12 UTC from IEEE Xplore. Restrictions apply.

$$\begin{cases} L_{act} = \dfrac{D_o - D_i}{2} + w_{cu} \\ L_{endo} = (\dfrac{D_o + w_{cu}}{2}) \times (\beta_{st}) + w_{cu} \\ L_{endi} = \left(\dfrac{D_i - w_{cu}}{2}\right) \times (\beta_{st}) + w_{cu} \\ L_t = (2L_{act}) + L_{endo} + L_{endi} \end{cases} \quad (11)$$

where $L_{act}, L_{endo}, L_{endi}$ are the active length, outer end winding length and inner end winding length, respectively. L_t is the total mean length for one complete turn. Then the calculation for the conductor area and wire diameter can be determined as follows:

$$\begin{cases} A_{cond} = \dfrac{L_{st} w_{cu} k_f}{N_{tc}} \\ d_w = \sqrt{\dfrac{4A_{cond}}{\pi}} \end{cases} \quad (12)$$

where N_{tc} is the number of turns per coil and can be determined from the turns per phase. d_w is the wire diameter for selection of wire according to the wire gauge system, the value close to the system will be selected. The resistance for the one complete turn can be:

$$R = \frac{\rho_{cu} L_t}{A_{cond}} \quad (13)$$

where ρ_{cu} is the resistivity of copper and the phase resistance can simply be determined by multiplying the resistance of one turn to the number of turns per phase as $R_{ph} = R \times N_{ph}$. The geometrical parameters of the AFDRSRM are illustrated in Table I. Furthermore, the copper loss calculation and efficiency can be expressed as:

$$\begin{cases} P_c = 3{I_{rms}}^2 \times R_{ph} \\ \eta = \frac{P_{out}}{P_{out} + P_c + P_{iron}} \times 100\% \end{cases} \quad (14)$$

where I_{rms} is the rms current, P_c and P_{iron} are the copper losses and iron losses respectively. To find the efficiency of AFDRSRM, iron losses though empirical formula does not give the accurate calculation. For this reason, the iron losses are evaluated through Finite Element Method (FEM). Moreover, for the power density or torque density calculation, the weight of each part of AFDRSRM can be determined:

$$\begin{cases} W_{st} = d_i h_{st} w_{st} L_{st} N_s \\ W_{cu} = d_c L_t w_{cu} L_{st} k_f N_s \\ W_{sh} = d_i h_{st} w_{sh} L_{sh} N_r \\ W_{rp} = d_i h_{st} w_{rp} L_{rp} N_r \\ W_{bl} = d_i h_{st} \pi D_{avg} L_{bl} N_r \end{cases} \quad (15)$$

So, the whole weight of the machine can be determined as:

$$W = W_{st} + W_{cu} + 2W_{sh} + 2W_{rp} + 2W_{bl} \quad (16)$$

where W_{st}, W_{cu} are the weight of the stator tooth and the weight of the copper, respectively. d_i and d_c are the densities of the iron and copper, respectively. Further, W_{sh}, W_{rp} and W_{bl} are the weight of pole shoe, weight of the rotor pole and weight of the back iron, respectively. h_{st} is the height of the stator tooth and is same for the rotor pole height also, because the stator tooth height and rotor pole height are same. L_{rp} and L_{bl} are the rotor pole axial length and rotor back iron length, respectively. In addition, the torque density and power density

TABLE I. DESIGN AND ELECTRICAL PARAMETERS OF AFDRSRM

Parameters	Symbols	Values
No. of stator/rotor poles	N_s/N_r	6/4
Rated speed (rpm)	N_{rpm}	7000
Rated voltage (V)	V_{dc}	96
Number of turns per coil	N_{tc}	150
Electrical loading (A/mm)	A_s	28.485
Current density rms (A/mm^2)	J_{rms}	5
Airgap length (single side)	l_g	0.25
Outer diameter (mm)	D_o	60
Inner diameter (mm)	D_i	33.6
Stator tooth width (mm)	w_{st}	13.1
Coil width (mm)	w_{cu}	3.7
Stator tooth height (mm)	h_{st}	13.2
Stator axial length (mm)	L_{st}	25.3
Pole shoe length (mm)	L_{sh}	0.6
Pole shoe depth (mm)	w_d	1.2
Rotor pole width (mm)	w_{rp}	19.6
Rotor back iron (mm)	L_{bi}	12.3
Phase resistance (Ω)	R_{ph}	0.7535

can be calculated from the output torque and power equation with respect to the whole machine and can be expressed as:

$$\begin{cases} P_d = \dfrac{P_{out}}{W} \\ T_d = \dfrac{T_{avg}}{W} \end{cases} \quad (17)$$

III. SIMULATION RESULTS

This section explores the methods and tools used to assess the machine steady-state and transient performance characteristics. Using the implementation of JMAG software, which integrates with 3D FEM, extensive simulations are run in order to get an understanding of the machine behavior under different conditions, including both steady state operations and dynamic behavior.

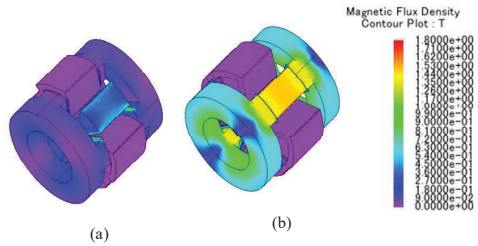


Fig. 3. Magnetic flux distribution (a) Unaligned position (b) Aligned position

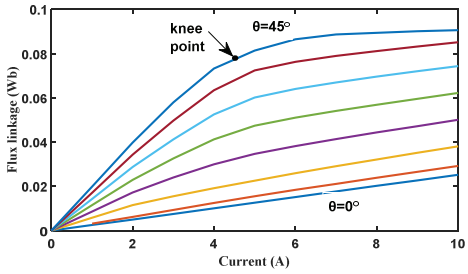


Fig. 4. Phase flux linkage at different current levels

Authorized licensed use limited to: Tallinn University of Technology. Downloaded on October 26,2026 at 09:07:12 UTC from IEEE Xplore. Restrictions apply.

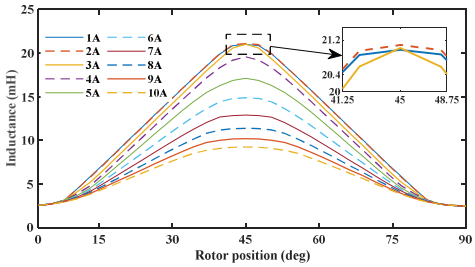


Fig. 5. Inductance characteristic at different rotor position

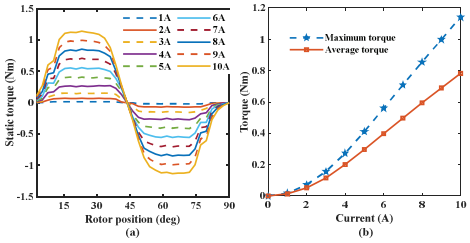


Fig. 6. Static torque characteristics of AFDRSRM (a) Torque with different rotor position (b) Average torque and maximum torque

A. Static Analysis

The flux-linkage and torque characteristics of SRMs, which are dependent on the position of the rotor and the current flowing through the coil, have a significant impact on the machine's performance as well as control methods. To derive these characteristics, 3D Finite Element Analysis (FEA) is utilized. The distribution of magnetic flux density for both the aligned and unaligned positions of the rotor is shown in Fig. 3(a) and 3(b), respectively, when a single-phase current of 4A is supplied. The illustrations demonstrate how the magnetic flux lines cross over from the stator tooth to one rotor, then from that rotor, they proceed to the stator tooth that is diametrically opposite of it and finally to the other rotor pole. Further, at the unaligned position, the magnetic flux density at the stator tooth measures 0.28T, while it achieves approximately 0.53T and 0.17T at the rotor pole shoe and at back iron respectively as illustrated in Fig 3(a).

The magnetic flux density at the stator teeth is around 1.52T in the aligned position shown in Fig. 3(b). The value increases to 1.65T at the rotor pole shoe, which causes a red spot to appear on the edge of the pole shoe. This observation is noteworthy as the pole shoe was originally designed to accommodate a magnetic flux density of 1.6T, and the FEA simulations closely approximate this designed value. Moreover, the flux linkage characteristics of AFDRSRM at unaligned to the aligned position at different current levels are studied in Fig. 4. It can be observed that the flux linkage at unaligned position is significantly smaller and at the aligned position it gets saturated after the knee point at the rated current of 4A. The phase A inductance variations as the applied current varies from 1A to 10A are shown in Fig. 5. It has been noted that when applied current increases, inductance decreases. This phenomenon happens because iron components have higher reluctance to the magnetic flux at higher currents, which lowers the inductance value. Since the iron cores are not yet saturated at lower currents, only the airgap can control the magnetic flux reluctance. The maximum to minimum inductance ratio for the AFDRSRM is at 8.73, with the highest measured inductance being 21.1mH at 2A current and the lowest being 2.52mH.

Further, the static torque curves are depicted in Fig. 6(a) at different positions for the excitation currents of 0 to 10A. It is evident that the torque increases as the excitation current increases. The maximum and average values only for positive cycle are shown in Fig. 6(b).

B. Dynamic Analysis

JMAG FEA is used to simulate the dynamic behavior of the AFDRSRM. The machine is powered by an asymmetric H-bridge converter, and for this high-speed machine a typical angular position control technique was utilized. This 3-phase 6/4 arrangement uses a single pulse control method in which each phase activates at 0° unaligned and turnoff at 30°. Fig. 7(a) and 7(b) show the resultant current and torque dynamics at 7000 rpm, respectively. In addition, the phase current reaches the rated value of 4A while the average torque is 0.21 Nm.

Furthermore, the analysis extends to evaluating the impact of varying the axial length of the rotor poles from 1mm to 10mm, with the resulting effects on rotor positioning and torque illustrated in Fig. 8. As shown in Fig. 9(a), the average torque increases with pole length up to a certain point (5 mm), at which point it starts to decrease. As can be seen in Fig. 9(b), a 5mm pole length yields optimal power and torque densities.

To facilitate the mechanical assembly of all stator teeth into a single ring, a lip feature is added to the surface of each stator tooth. This lip projected outwards by 1mm and tapers down to 1mm on both sides. Fig. 10 illustrates the torque performance comparison between stators with and without the lip. Adding the lip causes a slight reduction of 7% in average torque compared to stators without the lip. However, the torque ripple increases significantly from 54.56% to 110.02%. Despite this increase in torque ripples, the modified design maintains a satisfactory average torque level, with further

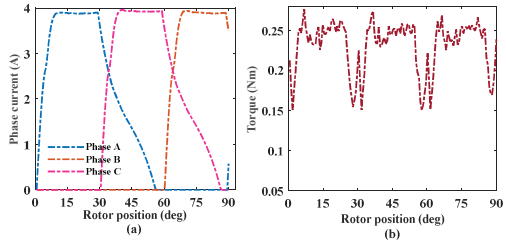


Fig. 7. Steady state operation of AFDRSRM at 7000rpm (a) Phase currents (b) Instantaneous torque

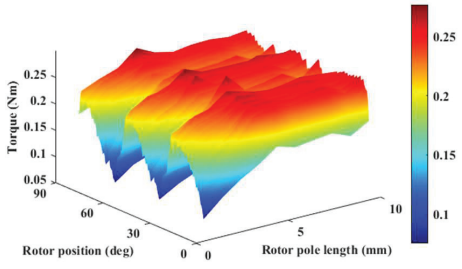


Fig. 8. Effect of different rotor pole lengths on average torque

Authorized licensed use limited to: Tallinn University of Technology. Downloaded on October 26,2026 at 09:07:12 UTC from IEEE Xplore. Restrictions apply.

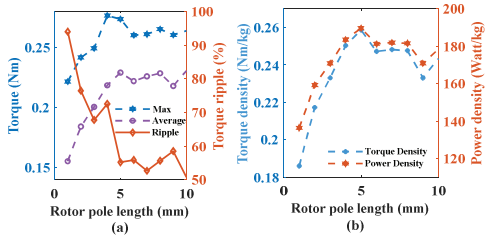


Fig. 9. Torque and density comparison (a) Torque and ripple performance of different pole length (b) Torque density and power density of AFDRSRM

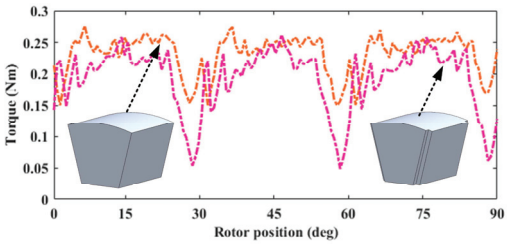


Fig. 10. Torque comparison with stator lip and without lip

TABLE II. COMPARISON OF PERFORMANCE PARAMETERS AT RATED CONDITION

Parameters	Analytical	FEM
Speed (rpm)	7000	
Rated peak current (A)	4.0338	
Average torque (Nm)	0.211	0.2067
Output power (watt)	155	151.51
Torque ripples (%)	-	54.56/110.02
Torque density (Nm/kg)	0.2386	0.2296
Power density (watt/kg)	174.93	168.34
Copper losses (watt)	12.26	12.26
Iron losses (watt)	99.11	99.11
Efficiency (%)	58.17	57.63

research to focus on reducing torque ripples. Additionally, Table II compares the performance parameters obtained from analytical calculations and FEA simulations.

IV. AM PROTOTYPE OF AFDRSRM

This section presents the manufacturing process of AFDRSRM using AM technique. Before printing, some design changes must be made in order to reduce core losses, as printing a solid piece would lead to significant core losses. To minimize eddy current losses in the design, the stator segments are constructed with parallel lamination, each layer being 0.6mm thick with incorporating a 0.2mm gap is introduced between each lamination as shown in Fig. 11. Two strategies were used to ensure the printing quality, low conductivity between the plates, and mechanical stability of the final parts.

- Strategically spaced distancers in the middle of the core to ensure even air-gap width throughout the core.
- Thin latticework on the sides of the core to consolidate the thin plates into a single mechanically stable core.

The lattice includes thick border elements to prevent warping and delamination of parts during the printing process. Fig. 12 illustrates the CAD model of the parallel laminated stator segment with the addition of the lattice structure on both sides of the stator tooth. Both the stator segments and rotors are manufactured using SLM techniques. The material used for the printer was silicon powder alloyed with 3wt% Fe-Si, with particle sizes ranging from 29 to 58 µm. The individual machine's parts were printed, which took 6h to print each rotor and all the stator segments were printed in 10h. Followed by a heat treatment at 1200°C, increasing at a rate of 5 degrees per minute for an hour. The cooling process begins uncontrolled and in the furnace, starting at 50 degrees per minute and gradually slowing down over time. Throughout this process, the vacuum level was maintained between 0.04 and 0.4 mbar. Fig. 13(a) and 13(b) depicts the AM printed stator tooth and the spacer on the stator tooth to hold the winding respectively.



Fig. 11. Parallel laminated stator without lattice

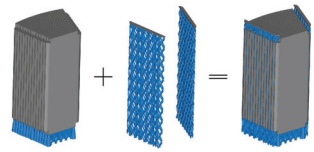


Fig. 12. Parallel laminated stator tooth with addition of lattice structure

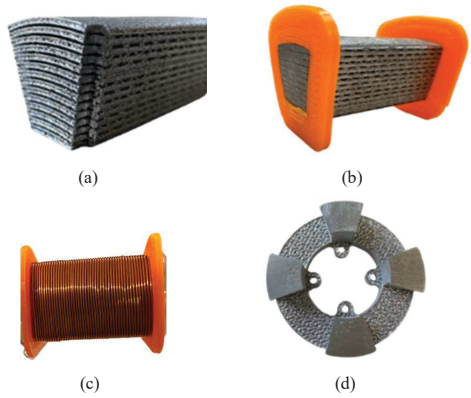


Fig. 13. AM AFDRSM parts (a) Stator tooth (b) Stator tooth with spacer (c) Stator winding (d) 4 pole rotor

The copper winding on single stator tooth and printed rotor are illustrated in Fig. 13(c) and 13(d) respectively. The complete assembly is shown in sectional view in Fig. 14, which gives the idea about the visual representation of how the entire machine will be assembled.

V. CONCLUSION

This paper outlines a design approach for an AFDRSRM, which involves to determining its parameters analytically and then validating these parameters through 3D FEA simulations. The results obtained from FEA were in good agreement with the analytical calculations. Further, a notable design feature is

Authorized licensed use limited to: Tallinn University of Technology. Downloaded on October 26,2026 at 09:07:12 UTC from IEEE Xplore. Restrictions apply.

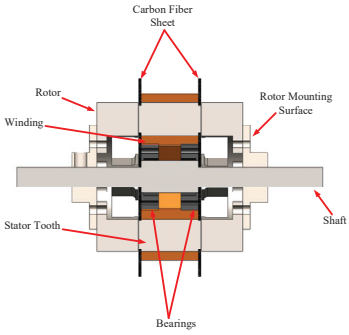


Fig. 14. Sectional view of the whole assembly of AFDRSRM

the inclusion of lip on stator tooth surface which aims to provide the mechanical assembly made possible to close all stator teeth together. Comparative analysis between the design with lip and without lip showed minimal variation in the average torque performance. However, the increase in the torque ripple for the design featuring the lip.

The paper also addresses the manufacturing challenges posed by complex axial machine geometries, which are difficult to produce using conventional manufacturing techniques. To overcome this problem, the proposed axial machine was fabricated using SLM utilizing a material composition of 3wt%Fe-Si. The design deliberately adopts parallel lamination to reduce the eddy current losses, incorporating a 0.2 mm gap between the laminations. In addition, a lattice structure was integrated on the core sides to join the thin plates into a cohesive and mechanically robust core, enhancing the structural integrity of the stator core.

The future work involves the assembling of the developed prototype and conducting AFDRSRM experimental testing. These tests aim to validate the prototype performance by comparing the experimental outcomes against both the analytical and FEM simulations. This future work will provide a detailed evaluation of the design efficacy and its potential for practical applications.

ACKNOWLEDGMENT

This work was supported by the Estonian Research Council grant (PRG-1827).

REFERENCES

[1] K. Kiyota, T. Kakishima, and A. Chiba, "Comparison of test result and design stage prediction of switched reluctance motor competitive with 60-kW rare-earth PM motor," *IEEE Transactions on Industrial Electronics*, vol. 61, no. 10, 2014, doi: 10.1109/TIE.2014.2304705.

[2] V. Valdivia, R. Todd, F. J. Bryan, A. Barrado, A. Lazaro, and A. J. Forsyth, "Behavioral modeling of a switched reluctance generator for aircraft power systems," *IEEE Transactions on Industrial Electronics*, vol. 61, no. 6, 2014, doi: 10.1109/TIE.2013.2276768.

[3] H. Chen and J. J. Gu, "Implementation of the three-phase switched reluctance machine system for motors and generators," *IEEE/ASME Transactions on Mechatronics*, vol. 15, no. 3, 2010, doi: 10.1109/TMECH.2009.2027901.

[4] A. Chiba, K. Kiyota, N. Hoshi, M. Takemoto, and S. Ogasawara, "Development of a rare-earth-free SR motor with high torque density for hybrid vehicles," *IEEE Transactions on Energy Conversion*, vol. 30, no. 1, 2015, doi: 10.1109/TEC.2014.2343962.

[5] B. Fahimi, A. Emadi, and R. B. Sepe, "A switched reluctance machine-based starter/alternator for more electric cars," *IEEE Transactions on Energy Conversion*, vol. 19, no. 1, 2004, doi: 10.1109/TEC.2003.822322.

[6] X. Zan and H. Chen, "Integrated design and control strategy study of switched reluctance starter/generator system," *Control and Intelligent Systems*, vol. 42, no. 2, 2014, doi: 10.2316/Journal.201.2014.2.201-2465.

[7] W. Uddin, T. Husain, Y. Sozer, and I. Husain, "Design Methodology of a Switched Reluctance Machine for Off-Road Vehicle Applications," *IEEE Trans Ind Appl*, vol. 52, no. 3, 2016, doi: 10.1109/TIA.2015.2514283.

[8] F. Yu *et al.*, "Design and Multiobjective Optimization of a Double-Stator Axial Flux SRM with Full-Pitch Winding Configuration," *IEEE Transactions on Transportation Electrification*, vol. 8, no. 4, 2022, doi: 10.1109/TTE.2022.3173938.

[9] R. Madhavan and B. G. Fernandes, "Performance improvement in the axial flux-segmented rotor-switched reluctance motor," *IEEE Transactions on Energy Conversion*, vol. 29, no. 3, 2014, doi: 10.1109/TEC.2014.2314657.

[10] W. Sun, Q. Li, L. Sun, L. Zhu, and L. Li, "Electromagnetic analysis on novel rotor-segmented axial-field srm based on dynamic magnetic equivalent circuit," *IEEE Trans Magn*, vol. 55, no. 6, 2019, doi: 10.1109/TMAG.2019.2901002.

[11] W. Sun, Q. Li, L. Sun, and X. Jiang, "Study on Magnetic Shielding for Performance Improvement of Axial-Field Dual-Rotor Segmented Switched Reluctance Machine," *CES Transactions on Electrical Machines and Systems*, vol. 5, no. 1, 2021, doi: 10.30941/CESTEMS.2021.00007.

[12] N. Taran, G. Heins, V. Rallabandi, D. Patterson, and D. M. Ionel, "Evaluating the Effects of Electric and Magnetic Loading on the Performance of Single- And Double-Rotor Axial-Flux PM Machines," in *IEEE Transactions on Industry Applications*, 2020. doi: 10.1109/TIA.2020.2983632.

[13] A. Selema, M. N. Ibrahim, H. Vansompel, and P. Sergeant, "Development of Yokeless Axial Flux Machine Using 3D-Printed Shape-Profiled Core," in *2022 International Conference on Electrical Machines, ICEM 2022*, 2022. doi: 10.1109/ICEM51905.2022.9910661.

[14] M. Garibaldi, "The Impact of Additive Manufacturing on the Development of Electrical Machines for MEA Applications : A Feasibility Study," *3rd International Conference More Electric Aircraft (MEA 2015)*, no. 1, 2015.

[15] F. N. U. Nishanth, A. D. Goodall, I. Todd, and E. L. Severson, "Characterization of an Axial Flux Machine With an Additively Manufactured Stator," *IEEE Transactions on Energy Conversion*, vol. 38, no. 4, 2023, doi: 10.1109/TEC.2023.3285539.

[16] H. Tiismus, A. Kallaste, T. Vaimann, A. Rassolkin, and A. Belahcen, "Additive Manufacturing of Prototype Axial Flux Switched Reluctance Electrical Machine," in *2021 28th International Workshop on Electric Drives: Improving Reliability of Electric Drives, IWED 2021 - Proceedings*, 2021. doi: 10.1109/IWED52055.2021.9376337.

[17] L. Gargalis *et al.*, "Additive manufacturing and testing of a soft magnetic rotor for a switched reluctance motor," *IEEE Access*, vol. 8, 2020, doi: 10.1109/ACCESS.2020.3037190.

[18] A. D. Goodall, F. N. U. Nishanth, E. L. Severson, and I. Todd, "Loss performance of an additively manufactured axial flux machine stator with an eddy-current limiting structure," *Mater Today Commun*, vol. 35, 2023, doi: 10.1016/j.mtcomm.2023.105978.

[19] A. Plotkowski *et al.*, "Influence of scan pattern and geometry on the microstructure and soft-magnetic performance of additively manufactured Fe-Si," *Addit Manuf*, vol. 29, Oct. 2019, doi: 10.1016/j.addma.2019.100781.

[20] H. Tiismus, A. Kallaste, M. U. Naseer, T. Vaimann, and A. Rassolkin, "Design and Performance of Laser Additively Manufactured Core Induction Motor," *IEEE Access*, vol. 10, 2022, doi: 10.1109/ACCESS.2022.3173317.

[21] S. Hussain, A. Kallaste, M. Usman Naseer, M. Sarap, H. Tiismus, and T. Vaimann, "Preliminary Design Analysis of an Axial Flux Yokeless Stator Switched Reluctance Machine."

Authorized licensed use limited to: Tallinn University of Technology. Downloaded on October 26,2026 at 09:07:12 UTC from IEEE Xplore. Restrictions apply.

Publication VII

S. Hussain, A. Kallaste, M. U. Naseer, H. Tiismus, M. Sarap, B. Asad, and T. Vaimann, "Design and Prototyping of Additively Manufactured Axial Flux Switched Reluctance Machine," *IEEE Transactions on Industry Applications*, vol. 62, no. 2, pp. 2587–2597, March–April 2026, doi: 10.1109/TIA.2025.3604357.

Design and Prototyping of Additively Manufactured Axial Flux Switched Reluctance Machine

Shahid Hussain, *Graduate Student Member, IEEE*, Ants Kallaste, *Senior Member, IEEE*, Muhammad Usman Naseer, Hans Tiismus, *Member, IEEE*, Martin Sarap, *Member, IEEE*, Bilal Asad, *Member, IEEE*, and Toomas Vaimann, *Senior Member, IEEE*

***Abstract*—This paper presents the development of an axial flux segmented stator dual rotor switched reluctance machine, specifically designed for high-speed propulsion applications. Due to the complex three-dimensional geometry of an axial flux machines, traditional production methods face substantial limitations in manufacturing accuracy and feasibility. However, advancements in additive manufacturing have addressed these challenges by enabling the production of intricate geometries with greater precision. The paper begins with the derivation of the output power equation for the proposed machine, followed by a detailed examination of key geometric parameters influencing performance. The design methodology is outlined from initial considerations to final performance targets, with a 3D finite element method analysis conducted to validate the calculated dimensions and assess performance. Furthermore, a physical prototype is fabricated using Selective Laser Melting, an additive manufacturing technique suited for producing complex structures with high precision. The prototype undergoes experimental testing, and the resulting performance data are compared with simulated results. The comparison between FEM simulations and experimental measurements indicates a close similarity between the experimental and simulated static and dynamic torque values.**

***Index Terms*—Axial flux switched reluctance machine, additive manufacturing, eddy currents, segmented stator.**

I. Introduction

THE rapid increase of electrification in the transportation sector, along with the available enabling technologies, creates possibilities for the integration of drones, flying cars and air taxi applications [1], [2]. This trend is reshaping traditional infrastructure requirements and reducing the need for extensive transportation networks and their associated maintenance. As drones become increasingly capable and efficient, they offer a viable alternative for transporting goods, delivering packages, and conducting surveillance operations, eliminating the need for extensive physical infrastructure such as roads or manned vehicles.

To drive these advanced aerial systems, Switched Reluctance Machines (SRM) are suitable for the application of drone propulsion system because it offers high speed, low weight and high power density which are the key requirement for such applications. The suitability of SRM as an option is also due to their simple and sturdy design, fault tolerance, and high reliability [3], [4], [5]. However, these machines suffer from limitations such as low torque density and significant torque ripples, which deter their widespread application [6], [7]. In the past few years, various innovative designs have been put forward to address these issues [7], [8], [9], [10], [11], [12], [13].

The existing literature acknowledges that axial flux SRM exhibits higher torque density and efficiency compared to radial counterparts due to their larger active air-gap surface area [14]. By using multiple air gaps, it is possible to significantly increase the utilization of the magnetic flux generated by the excitation coils, which will increase the torque density. To further improve the torque density, axial rotor segmented SRM has been introduced in which the author presented the double stator and segmented single rotor topology, and short pitch winding configuration is utilized which have the benefit of smaller end winding [15]. To make the magnetic flux shorter, full pitch winding configuration is adopted in which the magnetic flux path only traverses the two adjacent stator poles and segmental rotors [7]. However, the use of full pitch winding increases the end winding length, which also affects machine efficiency. Additionally, the segmented rotor construction can introduce mechanical challenges at higher speeds [16]. As the rotor segments move relative to each other, they can experience increased centrifugal forces, which can lead to higher stresses and potentially increase noise and vibration within the machine.

Another important aspect which enhances the performance of axial machines is to reduce the eddy current losses. For many years, electrical steel laminations have been utilized in electrical machines to minimize eddy current losses. However, these laminations restrict the manufacturing of axial flux SRM, particularly those which are asymmetrical in the axial direction. To address these limitations, Soft Magnetic Composites (SMCs)

Received 13 November 2024; revised 27 February 2025 and 16 May 2025; accepted 20 July 2025. Date of publication 1 September 2025; date of current version 10 February 2026. Paper 2024-EMC-1371.R2, presented at the 2023 IEEE 64th International Scientific Conference on Power and Electrical Engineering of Riga Technical University, Riga, Latvia, Oct. 09–11, and approved for publication in the IEEE TRANSACTIONS ON INDUSTRY APPLICATIONS by the Electric Machines Committee of the IEEE Industry Applications Society [DOI: 10.1109/RTUCON60080.2023.10413130]. This work was supported by Estonian Research Council under Grant PRG-1827. *(Corresponding author: Shahid Hussain.)*

The authors are with the Department of Electrical Power Engineering and Mechatronics, Tallinn University of Technology, 19086 Tallinn, Estonia (e-mail: shahid.hussain@taltech.ee; ants.kallaste@taltech.ee; muhammad.naseer@taltech.ee; hans.tissmus@taltech.ee; martin.sarap1@taltech.ee; bilal.asad@taltech.ee; toomas.vaimann@taltech.ee).

Color versions of one or more figures in this article are available at https://doi.org/10.1109/TIA.2025.3604357.

Digital Object Identifier 10.1109/TIA.2025.3604357

0093-9994 © 2025 IEEE. All rights reserved, including rights for text and data mining, and training of artificial intelligence and similar technologies. Personal use is permitted, but republication/redistribution requires IEEE permission. See https://www.ieee.org/publications/rights/index.html for more information.

Authorized licensed use limited to: Tallinn University of Technology. Downloaded on October 26,2026 at 09:07:14 UTC from IEEE Xplore. Restrictions apply.

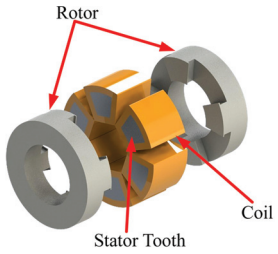


Fig. 1. Proposed axial flux dual rotor SRM.

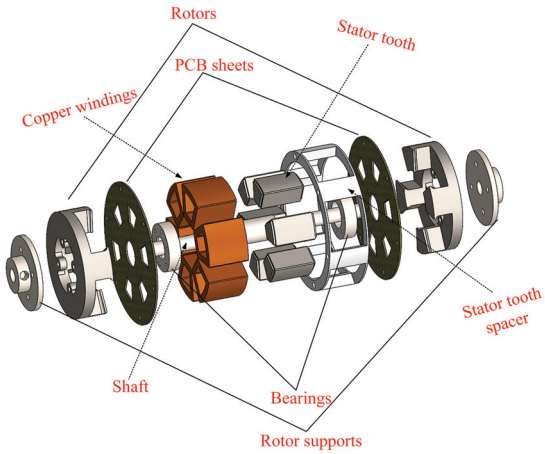


Fig. 2. Exploded view of AFDR-SRM.

have been employed in 3D magnetic circuits as they exhibit lower core losses, particularly at high frequencies.

Nonetheless, SMCs are constrained in terms of shape due to their uniaxial pressing operation. An alternative approach to overcome these limitations is the use of Additive Manufacturing (AM) or 3D printing techniques, which allow us to produce complex geometries while introducing the different lattice structure for the eddy current loss reduction. In [17], the author employed SLM to manufacture 3D printed axial flux machines with a 6/4 topology, consisting of two stators and one rotor. The entire rotor and stators were produced in 57 hours using this technique.

In [18], [19], an axial flux stator was manufactured through AM and compared the performance with the identical conventionally manufactured baseline machine. The results demonstrate that using Hilbert pattern can reduce the eddy current losses by approximately 50% compared with a solid structure. Although, the stacking factor of AM stator is lower than the baseline due to which it exhibits 18% lower magnetizing flux. Additionally, advancements in AM technology enable the production of structures with thinner features and improved stacking efficiency, enabling them to achieve comparable performance to laminated structures across a wider range of operating conditions.

Based on the existing literature, a new 6/4 Axial Flux Dual Rotor Switched Reluctance Machine (AFDR-SRM) is presented as shown in Fig. 1. The segmented stator enables higher utilization of the electrical loading, improve fault tolerant capability as each phase operates independently and meanwhile, solid rotors are well-suited for high speed applications. The following paper is organized as Section II comprehensively explains the design flow. The sizing equations and other geometrical parameters of the machine are calculated in Section III. In Section IV the Finite Element Method (FEM) is implemented on the basis of the calculated parameters in Section III. Section V discusses the prototype process of AM machine. Experimental setup and measured results are shown in Section VI. The conclusion and future work of this machine is explained in Section VII.

II. Design Flow of AFDR-SRM

For this study, the selection of 6/4 configuration of the SRM was due to simplicity of its structure and its inherent fault tolerant operating capability. The practical limitations and freedoms offered by the manufacturing process are also the important factors to be considered in the design process. Therefore, the main topological features of the said configuration and some important aspects from assembly point of view are discussed as follows. The three phase 6/4 SRM structure comprises a stator with six trapezoidal teeth and a dual rotor configuration with each rotor having four salient poles. Each stator tooth is equipped with concentrated winding where the pairs of diametrically opposite teeth have their windings connected in series, to constitute individual phases of the machine.

While the dual rotor SRM design is conceptually straightforward, the segmented nature of the stator teeth complicates mechanical assembly, as the stator is not a single structure. To address this, the stator tooth surfaces near the air gap are modified with a lip projected outward, as shown in the exploded view of Fig. 2. This lip enables all stator teeth to connect in a circular configuration, where they are held together on both sides with a PCB sheet. This not only helps to align the segments but also integrates the coil connections inside the PCB.

The design and analysis process itself consists of two major stages, the analytical design estimation, and the FEM based validation. The basic design and analysis flow is illustrated in Fig. 3. This process starts with specifying the design parameters in the form of fixed or free variables. The fixed variables primarily include desired machine output characteristics, such as rated voltage, output power, speed, and current density, which are held constant during the process. Additionally, to initiate the design process some variables are assigned values based on design constraints, specific design decisions, or empirical knowledge from established design practices. The value of these free variables is iteratively fine-tuned according to design constraints, through FEM simulation. The values of fixed variables and initial assumptions for the free variable are presented in Table I. Once these initial variables are set, the next step involves calculating the machine dimensions.

After analytical calculations, the design process undergoes into the static analysis. The design is validated through static

Authorized licensed use limited to: Tallinn University of Technology. Downloaded on October 26,2026 at 09:07:14 UTC from IEEE Xplore. Restrictions apply.

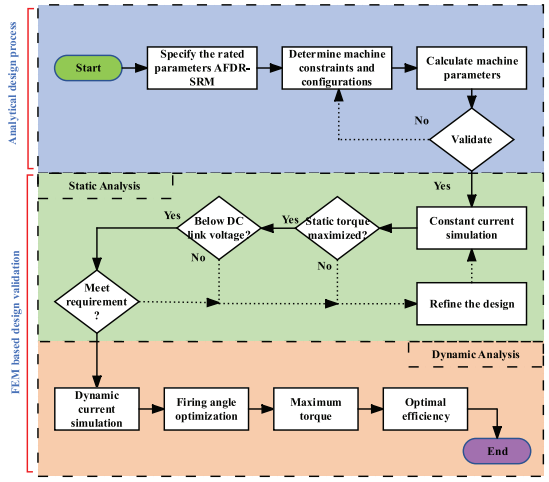


Fig. 3. Flow diagram of AFDR-SRM.

TABLE I
DESIGN REQUIREMENTS OF AFDR-SRM

Parameters	Symbol	Value
Rated voltage (V)	V	96
Assumed operating flux density in stator tooth (T)	B_{st}	1.5
Rated speed (rpm)	N_{rpm}	7000
Current density (A/mm^2)	J_{rms}	5
Output power (watt)	P_{out}	150

FEM analysis and once the static analysis phase is complete, the design proceeds to dynamic analysis. This phase includes dynamic current simulation, focusing on fine-tuning the machine's operational characteristics. The most optimal design from these simulations is chosen as the final configuration, ensuring that the AFDR-SRM meets its targeted performance criteria in terms of torque, speed, and efficiency. This systematic process optimizes the machine's design through iterative analysis and validation, delivering a final design that is both efficient and feasible from assembly point of view.

III. ANALYTICAL DESIGN PROCESS

The output equation for an axial flux SRM typically relates the machine's output torque or power to its key design parameters, such as the average diameter, speed, and magnetic and electric loadings. It is worth mentioning that the specific form of the output equation for an axial flux SRM can vary depending on the machine's configuration, control strategy, and the objectives of the design. Therefore, it is crucial to consider these factors while formulating the output equation to accurately represent the SRM performance characteristics. The general power equation for 6/4 axial SRM can be defined as [20]

$$P_{out} = \eta k_d V I m \tag{1}$$

where η is the efficiency, k_d represents the duty cycle, V and I are peak values of voltage and current respectively and m denotes the number of phases. The duty cycle can be expressed as

$$k_d = \frac{\theta_i \, m \, N_r}{360} \tag{2}$$

where θ_i is the conduction angle, and N_r is the number of rotor poles. The applied voltage can be determined in terms of inductance and current as

$$V = \frac{(L_a{}^s - L_u)\, i}{t} \tag{3}$$

where $L_a{}^s$ is the aligned saturated inductance, L_u is the unaligned inductance. The time it takes for the rotor to rotate from an unaligned position to an aligned position is denoted as t and can be expressed as

$$t = \frac{\beta_s}{\omega_m} \tag{4}$$

where β_s, ω_m are the stator pole arc and angular velocity in rad/sec respectively. Substituting (4) in (3) and the voltage Eq. becomes

$$V = \frac{\omega_m}{\beta_s} L_a{}^s i \left(1 - \frac{1}{\sigma_s \sigma_u}\right) \tag{5}$$

where σ_s, σ_u are the ratio of saturated aligned to unsaturated aligned inductance and ratio of unsaturated aligned and unaligned inductance. The flux linkages in the aligned position can be represented using either the flux and the number of turns, or the flux density and the dimensions of the machine.

$$L_a{}^s i = \varphi N_{ph} = B_g A_{sp} N_{ph} = \frac{1}{8} B_g \left(D_o{}^2 - D_i{}^2\right) \beta_s N_{ph} \tag{6}$$

where φ, N_{ph}, B_g and A_{sp} is the aligned flux, number of turns per phase, airgap flux density and stator pole area respectively. D_0, D_i are the outer and inner diameter of the machine. Moreover, the electric loading can be expressed as

$$A_s = \frac{2 N_{ph} i m}{\pi D_{avg}} \tag{7}$$

where D_{avg} is the average diameter of an axial machine. In the case of 6/4, only one phase conducts at a moment. Substituting (6) and (7) in (5).

$$V = \frac{\pi^2}{480} \frac{1}{im} B_g A_s D_{avg} \left(D_o{}^2 - D_i{}^2\right) \left(1 - \frac{1}{\sigma_s \sigma_u}\right) N_{rpm} \tag{8}$$

where N_{rpm} represents the rotor speed in revolution per minute. Putting the (8) in (1) to get the output power Eq.

$$P_{out} = \eta k_d k_1 k_2 B_g A_s D_{avg} \left(D_o{}^2 - D_i{}^2\right) N_r \tag{9}$$

where

$$k_1 = \frac{\pi^2}{480} \quad k_2 = \left(1 - \frac{1}{\sigma_s \sigma_u}\right) \tag{10}$$

The output torque Eq. can be derived from the above output power Eq. and can be expressed as

$$\tau = \frac{P_{out}}{\omega_m} \tag{11}$$

Authorized licensed use limited to: Tallinn University of Technology. Downloaded on October 26,2026 at 09:07:14 UTC from IEEE Xplore. Restrictions apply.

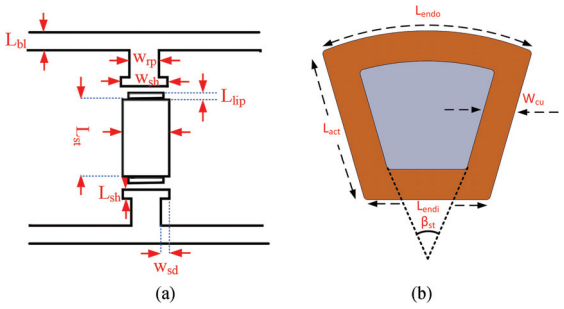


Fig. 4. Representation of geometrical parameters (a) Stator and rotor parameters (b) Coil parameters.

Substituting (9) in (11), the torque Eq. becomes

$$\tau = \eta k_d k_2 k_3 B_g A_s D_{avg} \left({D_o}^2 - {D_i}^2\right) \tag{12}$$

where

$$k_3 = \frac{\pi}{16} \tag{13}$$

The average torque of the machine depends on the inner and outer diameters of the stator once the electrical and magnetic loads have been set, and the maximum and minimum inductance ratios are specified. Based on [20], the maximum average torque can be achieved by maintaining an inner-to-outer diameter ratio of 0.577.

A. Geometrical Parameters

The geometrical parameters for the AFDR-SRM can be determined as follows. The geometrical parameters of the stator and rotor are illustrated in Fig. 4(a). The average width of the stator tooth can be expressed as [21]

$$w_{st} = \frac{B_g}{k_i B_{st}} \times \frac{\pi D_{avg}}{N_s} \tag{14}$$

where B_{st}, k_i are the magnetic flux density of the core material in the stator tooth and the stacking factor respectively, and N_s represent the number of stator teeth. Further, the width of copper around the stator tooth is illustrated in Fig. 4(b) and can be formulated as

$$w_{cu} = \frac{(\pi D_{avg}) - (N_s w_g) - (N_s w_{st})}{2N_s} \tag{15}$$

where w_g is the minimum possible gap between the coils and is assumed to be 1mm on the inner side of the coil. Setting up this threshold to a minimum possible gap between the coils at the inner diameter of the coil. Reducing this value will result in joining of the coils at the inner point. Moreover, the average width of the rotor pole, back iron length of the rotor, pole shoe width, pole shoe depth and length of pole shoe can be expressed as

$$\begin{cases} w_{rp} = \frac{B_g}{B_{st}} \times \frac{\pi D_{avg}}{N_r} \\ L_{bl} = \frac{B_g}{B_{bl}} \times \frac{\pi D_{avg}}{2N_r} \\ w_{sh} = \frac{\pi D_{avg}}{N_r} \times \frac{\beta_{sh}}{\tau_p} \\ w_d = \frac{w_{sh} - w_{st}}{2} \\ L_{sh} = \frac{B_g}{B_{sh}} \times w_d \end{cases} \tag{16}$$

where B_{bl} is the flux density in the rotor back iron, β_{sh}, τ_p are the arc of pole shoe and pole pitch of the rotor, respectively. w_d and L_{sh} are the depth of the pole shoe and length of the pole shoe, respectively. Moreover, the stator tooth length can be determined as

$$L_{st} = \frac{A_s \pi D_{avg}}{2 J_{rms} w_{cu} k_f N_s} \tag{17}$$

where J_{rms} is the current density and this value is selected based on the thermal consideration for air cooled machine [22]. k_f is the copper filling factor in the stator slot and the number of turns per phase can be calculated from (7) when the electric loading is fixed. For the phase resistance calculation, the mean length of wire can be calculated as

$$\begin{cases} L_{act} = \frac{D_o - D_i}{2} + w_{cu} \\ L_{endo} = \left(\frac{D_o + w_{cu}}{2}\right) \times (\beta_{st}) + w_{cu} \\ L_{endi} = \left(\frac{D_i - w_{cu}}{2}\right) \times (\beta_{st}) + w_{cu} \\ L_t = (2L_{act}) + L_{endo} + L_{endi} \end{cases} \tag{18}$$

where L_{act}, L_{endo}, L_{endi} are the active length, outer end winding length and inner end winding length, respectively. L_t is the total mean length for one complete turn. Then the calculation for the conductor area and wire diameter can be determined as follows

$$\begin{cases} A_{cond} = \frac{L_{st} w_{cu} k_f}{N_{tc}} \\ d_w = \sqrt{\frac{4A_{cond}}{\pi}} \end{cases} \tag{19}$$

where N_{tc} is the number of turns per coil and can be determined from the turns per phase. d_w is the wire diameter for selection of wire according to the wire gauge system, the value close to the data sheet will be selected. The resistance for the one complete turn can be

$$R = \frac{\rho_{cu} L_t}{A_{cond}} \tag{20}$$

where ρ_{cu} is the resistivity of copper and the phase resistance can simply be determined by multiplying the resistance of one turn to the number of turns per phase as $R_{ph} = R \times N_{ph}$. The geometrical parameters of the AFDR-SRM are presented in Table II. Furthermore, the copper loss calculation can be expressed as

$$P_c = 3{I_{rms}}^2 \times R_{ph} \tag{21}$$

where I_{rms} is the rms current. For the efficiency of AFDR-SRM, iron losses through empirical formula does not give accurate calculation due to the non-sinusoidal nature of magnetic excitation. For this reason, the iron losses are evaluated through FEM simulations. The weight of each part of AFDR-SRM can be

Authorized licensed use limited to: Tallinn University of Technology. Downloaded on October 26,2026 at 09:07:14 UTC from IEEE Xplore. Restrictions apply.

TABLE II
DESIGN AND ELECTRICAL PARAMETERS OF AFDR-SRM

Parameters	Symbol	Value
No. of stator/rotor poles	N_s/N_r	6/4
Number of turns per coil	N_{tc}	150
Electrical loading (A/mm)	A_s	28.485
Airgap length (single side)	l_g	0.25
Outer diameter (mm)	D_o	60
Inner diameter (mm)	D_i	33.6
Stator tooth width (mm)	w_{st}	13.1
Coil width (mm)	w_{cu}	3.7
Stator tooth height (mm)	h_{st}	13.2
Stator axial length (mm)	L_{st}	25.3
Pole shoe length (mm)	L_{sh}	0.6
Pole shoe depth (mm)	w_d	1.2
Rotor pole width (mm)	w_{rp}	19.6
Rotor back iron (mm)	L_{bi}	12.3
Phase resistance (Ω)	R_{ph}	0.7535

determined as

$$\begin{cases} W_{st} = d_i\, h_{st} w_{st} L_{st} N_s \\ W_{cu} = d_c\, L_t w_{cu} L_{st} k_f N_s \\ W_{sh} = d_i\, h_{st} w_{sh} L_{sh} N_r \\ W_{rp} = d_i\, h_{st} w_{rp} L_{rp} N_r \\ W_{bl} = d_i\, h_{st} \pi D_{avg} L_{bl} N_r \end{cases} \tag{22}$$

So, the whole weight of the machine can be determined as

$$W = W_{st} + W_{cu} + 2W_{sh} + 2W_{rp} + 2W_{bl} \tag{23}$$

where W_{st}, W_{cu} are the weight of the stator tooth and the weight of the copper, respectively. d_i and d_c are the densities of the iron and copper, respectively. W_{sh}, W_{rp} and W_{bl} are the weight of pole shoe, weight of the rotor pole and weight of the back iron, respectively. h_{st} is the height of the stator tooth and is same for the rotor pole height also, because the stator tooth height and rotor pole height are same. L_{rp} and L_{bl} are the rotor pole axial length and rotor back iron length, respectively. The torque density and power density can be calculated from the output torque and power equation with respect to the whole machine weight and can be expressed as

$$\begin{cases} P_d = \frac{P_{out}}{W} \\ T_d = \frac{T_{avg}}{W} \end{cases} \tag{24}$$

IV. FEM BASED DESIGN VALIDATION

To analyze the performance of the proposed machine design 3D FEM simulations are carried out using JMAG software.

A. Magnetic Flux Density

Fig. 5 shows the magnetic flux density distributions of the machine at the aligned and unaligned positions of the rotor when the excitation current of phase A is applied of 4 A. At the unaligned position, the magnetic flux density at the stator tooth is 0.28 T, while it achieves approximately 0.53 T and 0.17 T at the rotor pole shoe and at back iron respectively as shown in Fig. 5(a).

The magnetic flux density at the stator teeth is around 1.52 T in the aligned position shown in Fig. 5(b). The value increases to 1.65 T at the rotor pole shoe, which causes a red spot to appear on the edge of the pole shoe. This observation is noteworthy as the pole shoe was originally designed to accommodate a magnetic flux density of 1.6 T, and the FEA simulations closely approximate this designed value. These results prove that up to 4 A machine is operating close to the design values, except for the rotor pole shoe where the magnetic flux density is more extensive reaching about 1.65 T.

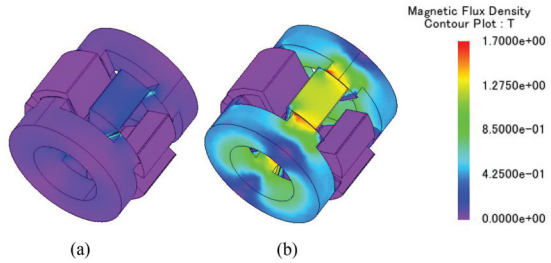


Fig. 5. Magnetic flux distribution (a) Unaligned position (b) Aligned position.

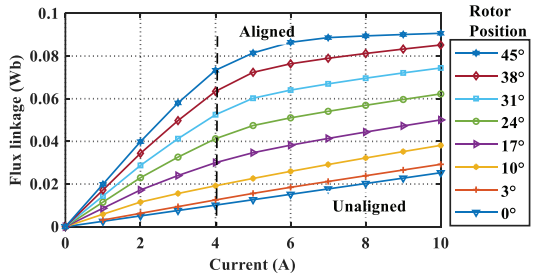


Fig. 6. Phase flux linkage at different current levels.

B. Static Simulation Results

The flux linkage characteristics of AFDR-SRM at unaligned to the aligned position at different current levels are studied in Fig. 6. It can be observed that the flux linkage at unaligned position is significantly low and at the aligned position it gets saturated at higher values of current. Moreover, Fig. 7(a) and (b) shows the static flux linkage and static torque of both designs a flat surface and with lip.

When comparing stator design with and without lip, a slight difference in torque and flux linkage characteristics is observed. Projected lips cause localized concentration of flux in the airgap but also cause localized saturation in the stator teeth facing the airgap. This localized magnetic saturation near the lip limits the total achievable flux linkage, yielding a slightly lower overall flux linkage compared to the flat surface design. Conversely, the flat stator tooth design allows for a more uniform flux distribution, which minimizes localized saturation and thereby achieves a higher total flux linkage. However, this design does not concentrate the magnetic flux as effectively at the airgap, resulting in a small reduction in torque.

Authorized licensed use limited to: Tallinn University of Technology. Downloaded on October 26,2026 at 09:07:14 UTC from IEEE Xplore. Restrictions apply.

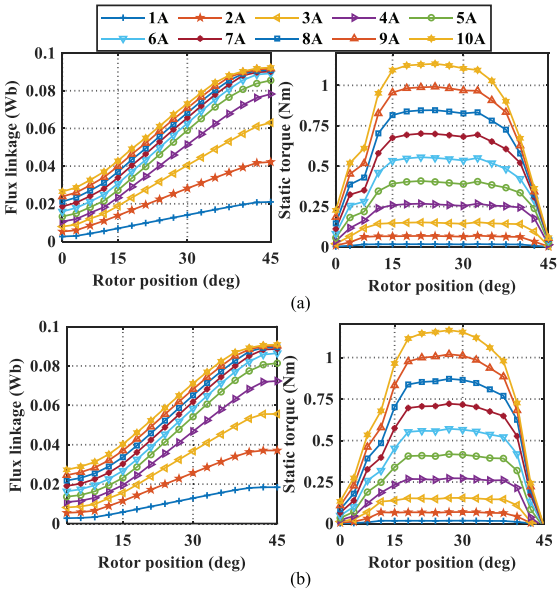


Fig. 7. Static flux linkage and static torque at different current levels (a) without lip on stator tooth (b) Lip on stator tooth.

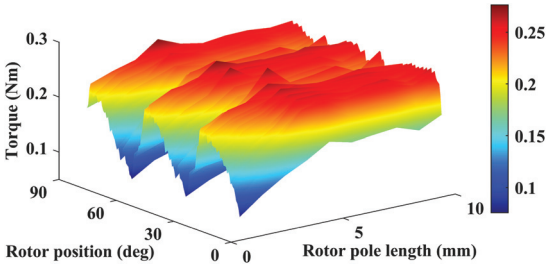


Fig. 8. Effect on average torque due to rotor pole length.

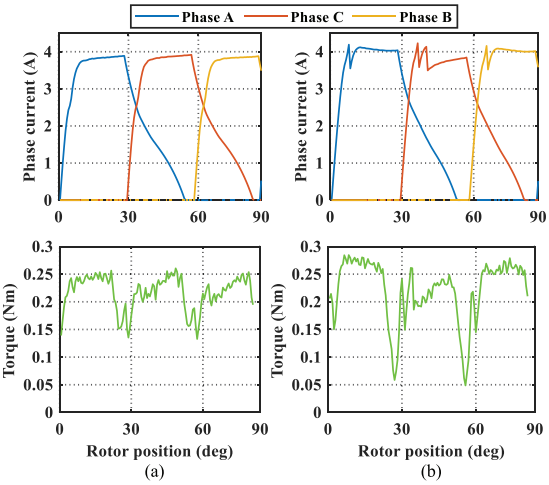


Fig. 9. Steady state current and torque waveform under SPC (a) without lip on stator tooth (b) Lip on stator tooth.

C. Dynamic Simulation Results

To further analyze the characteristics of the designed AFDR-SRM prototype, dynamic performance simulations are conducted. The phase switching is set to provide with the 30∘ conduction angle in the design value. The analysis explores the effects of changing the axial length of the rotor poles from 1mm to 10mm, with the corresponding impact on rotor positioning and torque is shown in Fig. 8. Fig. 9 presents the three-phase current and torque waveforms of the machine operating in Single Pulse Control (SPC) mode at a speed of 7000 rpm and a DC link voltage of 96 V.

In Fig. 9(a), a smoother current waveform is achieved by distributing flux more evenly across the tooth surface, reducing localized saturation. This uniform magnetic flux interaction results in a more stable torque profile with lower ripple than that produced by the lip stator tooth design. The current and torque waveform for lip-projected stator tooth, shown in Fig. 9(b), concentrates magnetic flux near the airgap, enhancing torque but also causing localized magnetic saturation, particularly during the initial phase of current buildup. This flux concentration and resultant saturation introduces ripples in the current waveform. The increased torque ripple in the lip-projected design is similarly due to this higher flux concentration at the airgap, creating fluctuations in magnetic force on the rotor as it passes the stator poles. Consequently, these fluctuations lead to torque pulsations or ripples, as the rotor experiences varying magnetic pull from the uneven flux distribution along the lip projection.

Moreover, the dynamic response of the SRM designs under Current Chopping Control (CCC) simulations were conducted at 1000 rpm on a constant load. At lower speed, the torque ripple is more pronounced in both SRM designs compared to the previous simulation at 7000 rpm. This increase in torque ripple at a lower speed is likely due to the extended conduction time for each phase at slower speeds, allowing flux variations to have a greater impact on the torque waveform as shown in Fig. 10(a) and (b) respectively.

The torque-speed and power characteristics of the proposed SRM machine are presented in Fig. 11. From 0 to the rated speed of 7000 rpm, the torque remains nearly constant, indicating the machine's ability to maintain consistent torque in the low-to-mid speed range. As the speed approaches the rated value, the machine's output power increases linearly due to the combination of constant torque and rising speed, reaching its peak at the rated speed. This optimal operating point is where the machine achieves maximum efficiency, as seen in Fig. 12.

Beyond the rated speed, the torque begins to decline, a typical behavior in SRMs. This decline is attributed to the increasing back EMF, which limits the effective current flowing through the windings. With reduced current, the torque output drops, leading to a decrease in power output. Additionally, higher speeds result in increased core (iron) losses due to eddy currents and hysteresis within the magnetic materials, as shown in Fig. 13.

Authorized licensed use limited to: Tallinn University of Technology. Downloaded on October 26,2026 at 09:07:14 UTC from IEEE Xplore. Restrictions apply.

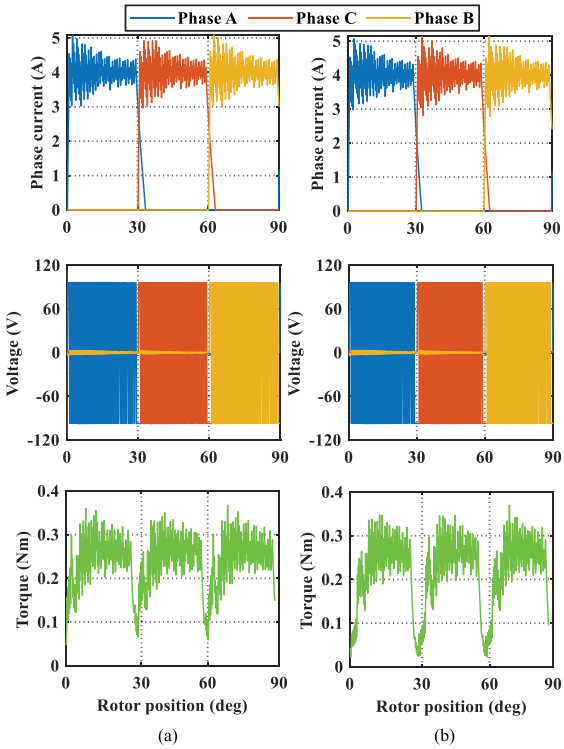


Fig. 10. Steady state current, voltage and torque waveform under CCC (a) without lip on stator tooth (b) Lip on stator tooth.

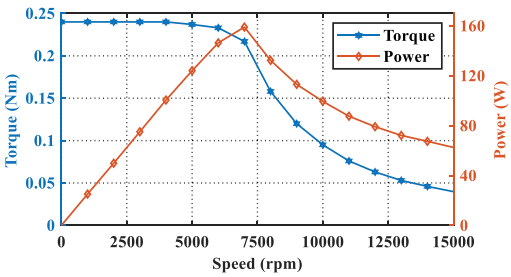


Fig. 11. Torque speed and power characteristics curve.

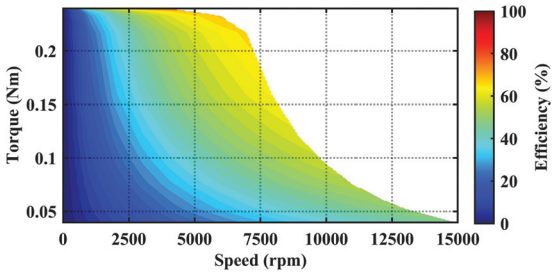


Fig. 12. Efficiency map of AFDR-SRM.

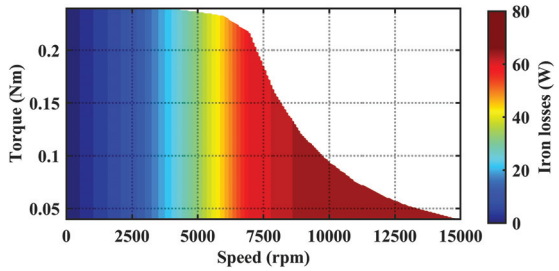


Fig. 13. Iron losses at different operating regions of AFDR-SRM.

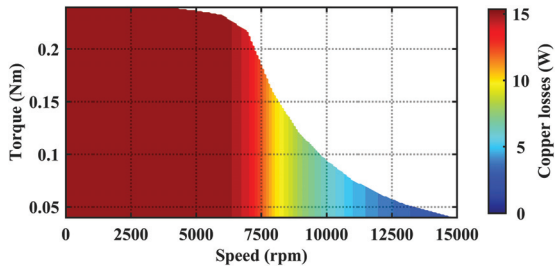


Fig. 14. Copper losses at different operating regions of AFDR-SRM.

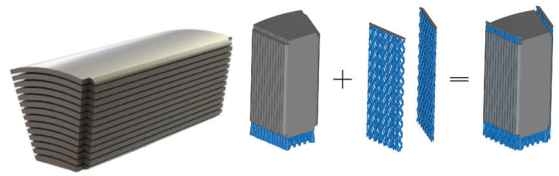


Fig. 15. Parallel laminated stator tooth with addition of lattice structure.

In Fig. 12, the efficiency map highlights the SRM's performance across various operating conditions. The results indicate that the machine operates with peak efficiency near the rated speed, where the power output is highest. In the constant torque region (up to the rated speed), iron losses remain relatively low due to limited eddy currents and magnetic hysteresis within the core.

However, as the speed exceeds the rated value, the iron losses increase significantly. This increase in iron losses at high speeds reduces the machine's efficiency, as more input power is lost as heat rather than being converted to useful torque and power. Fig. 14 presents the copper losses map which is high in the constant torque region due to the high current required to maintain steady torque. Copper losses are calculated using (20), which incorporates the resistivity of copper that varies with the machine's working temperature. Beyond the rated speed, the machine cannot achieve the reference current due to the increased back EMF, which leads to a significant reduction in current. As the current decreases, copper losses also decline, contrasting with the trend in iron losses. This behavior highlights the shift in loss mechanisms from copper losses in the constant torque region to iron losses at higher speeds.

Authorized licensed use limited to: Tallinn University of Technology. Downloaded on October 26,2026 at 09:07:14 UTC from IEEE Xplore. Restrictions apply.

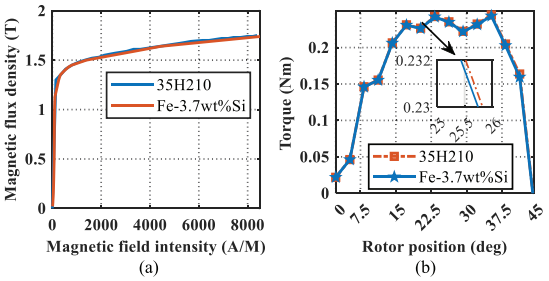


Fig. 16. Materials comparison (a) B-H curve of two different materials (b) Static torque comparison on different materials.

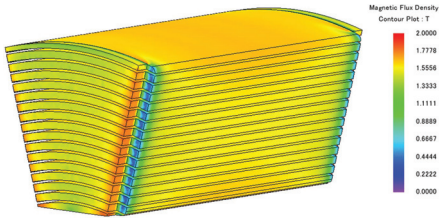


Fig. 17. Flux distribution in laminated stator tooth.

V. Design Fabrication of AM AFDR-SRM

This section presents the manufacturing process of the AFDR-SRM using AM techniques. To reduce the core losses in the prototype, certain design modifications were applied before printing, as a solid piece would lead to considerable eddy current losses. To address this, the stator segments were constructed using parallel laminations, with each layer being 0.6 mm thick and separated by a 0.2 mm gap, as presented in Fig. 15.

A. Fabrication Strategy

Two main strategies are employed to ensure high print quality, low conductivity between laminations, and mechanical stability in the final assembly:

- Strategically placed spacers within the core to maintain consistent air-gap width across the structure.
- Thin lattice structures along the sides of the core to combine the thin plates into a single, mechanically stable core.

To prevent warping and delamination during printing, the lattice includes thicker border elements. Fig. 15 displays the CAD model of the laminated stator segment with lattice structures on each side of the stator tooth. The FEM simulations are conducted on the laminated design, where the B-H curve of Fe-3.7wt% Si steel was experimentally measured from different toroid samples, by following standard magnetic characterization techniques as reported in [23]. Additionally, the B-H curve of 35H210 steel from the JMAG materials library and the experimentally obtained B-H curve of the Fe-3.7wt% Si material exhibit a strong similarity as shown in Fig. 16(a) . The complex

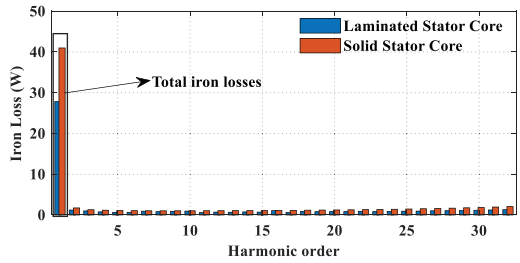


Fig. 18. Iron loss comparison of solid and parallel laminated stator core.

TABLE III
Summary of Printing Parameters

Parameter	Value
Layer thickness	50 µm
Hatch distance	120 µm
Laser Power	350 W
Scanning velocity	0.75 m/s
Volumetric energy density	83 J/mm³

geometry of the stator tooth (Fig. 15) required fine mesh settings for precise dynamic analysis.

Consequently, a static analysis for a single phase is performed, and the static torque results across different magnetic materials are shown in Fig. 16(b). It can be observed that the 35H210 and Fe-3.7wt% Si gives the same torque waveform when the constant current of 4A is applied. Fig. 17 shows the flux distribution within the laminated stator tooth, revealing a uniform flux distribution across each lamination layer. To evaluate the effectiveness of parallel lamination in minimizing iron losses in the stator core, a comparison of stator iron losses at the fundamental value is presented in Fig. 18. With parallel lamination, the iron losses in the stator core are reduced by 32.09% due to the restriction of eddy current circulation within the core.

B. Printing Process

Pre-alloyed, gas-atomized Fe-Si powder from Sandvik Group was utilized for manufacturing the machine cores through L-PBF, with its chemical composition confirmed using EDX and Spark AES [24]. The powder, comprising spherical particles ranging from 29-58 μm with a median diameter of 38 μm, was processed using an SLM Solutions GmbH Realizer SLM-280 printer equipped with a 350 W infrared laser. To mitigate density degradation in large-volume printing, the scan strategy was adjusted from a “stripe” to a “chessboard” pattern, enhancing part completion and uniformity, in alignment with prior research. Furthermore, the re-melting scan strategy was halted as it contributed to increased surface roughness and reduced powder flowability, leading to uneven part growth, with key printing parameters provided in Table III.

Each rotor took 6 hours to print, while the stator segments required 10 hours in total. Post-printing, the parts were heat-treated at 1200 °C, with a temperature rise of 5 °C per minute for one hour. Cooling was performed in the furnace at an initial

Authorized licensed use limited to: Tallinn University of Technology. Downloaded on October 26,2026 at 09:07:14 UTC from IEEE Xplore. Restrictions apply.

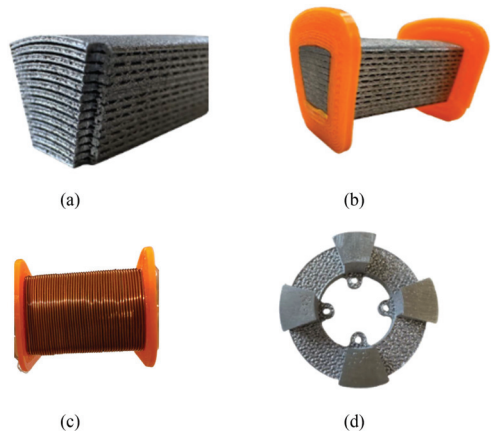


Fig. 19. AM AFDR-SRM parts (a) Stator tooth (b) Stator tooth with spacer (c) Stator winding (d) 4 pole rotor.

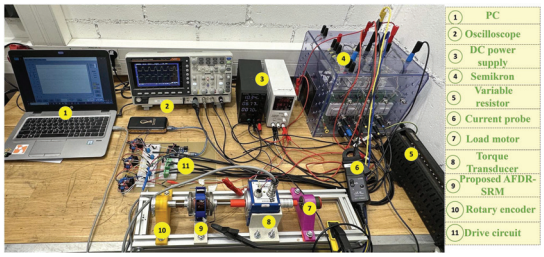


Fig. 20. Dynamic test setup of the proposed AFDR-SRM.

rate of 50 °C per minute, gradually decelerating. Throughout this process, vacuum levels were maintained between 0.04 and 0.4 mbar. Fig. 19(a) and (b) shows the AM-printed stator tooth and the spacer used to hold the winding, respectively, while Fig. 19(c) and (d) displays the copper winding on a single stator tooth and the printed rotor, respectively.

VI. Experimental Setup and Test Results

The objective of the experimental validation in this article is to confirm the effectiveness of the proposed machine manufactured through AM.

A. Test Setup

Fig. 20 shows the laboratory setup of the proposed machine. A dc motor is used as a load, and a rotary position encoder is mechanically coupled to the test machine to read the position of the rotor. An asymmetric three phase half bridge Semikron inverter is used to power the AFDR-SRM, in which the gate pulses for the IGBTs are generated based on the position of the rotor. An RWT421-DE-KG Sensor Technology torque transducer is used to extract the torque and speed waveforms.

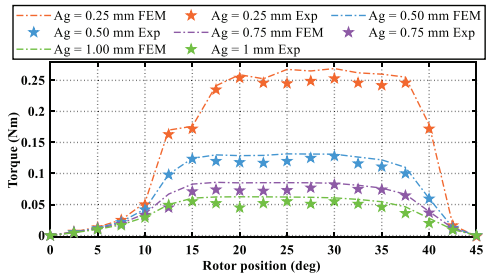


Fig. 21. Static torque comparison of FEM simulation and experimental.

B. Experimental Results

To validate the accuracy of the proposed AFDR-SRM, its static torque characteristics are experimentally measured and compare with FEM simulation results using Fe-3.7wt% Si as the core material. A servo motor is used to drive the prototype machine, rotating it to specific positions via a coaxial shaft coupling with an attached torque sensor. At each rotor position, the servo motor locks the proposed machine, and a constant current is applied to the winding, enabling the torque sensor to capture the static torque at that position.

Fig. 21 presents a comparison between the static torque profiles obtained from FEM simulations and experimental measurements across various rotor positions. Furthermore, a FEM-based sensitivity analysis was performed to assess the influence of varying air gap lengths, ranging from 0.25 mm to 1.00 mm, on static torque performance. The discrepancies observed between simulated and experimental results are mainly attributable to changes in the magnetic properties of the additively manufactured components following the post-printing process, as well as practical factors such as assembly misalignments and measurement uncertainties. Nonetheless, the experimental static torque waveform closely aligns with the trend of the simulated counterpart, thereby providing validation of the proposed machine static performance characteristics.

Additionally, a dynamic performance test was conducted in single pulse control mode. The AFDR-SRM is powered by a Semikron three-phase half-bridge inverter, with rotor position detected by an incremental encoder generating 1000 pulses per rotation. Fig. 22 shows the encoder pulses and the gate signals for the three phases, showing that when one phase deactivates, the next phase immediately activates. Fig. 23 displays the voltage and current waveforms with no load on the machine shaft. Due to the encoder limitation, the machine reaches a speed of 5200 rpm as shown in Fig. 24, when the applied voltage is 22 V and the machine draws 0.5 A current at no-load condition. The dynamic torque response of the machine was investigated using FEM and validated through experimental measurements, as shown in Fig. 25, presents the torque waveforms obtained under single-pulse control mode at the machine's rated speed of 7000 r/min. To simulate realistic full-load operating conditions, an external DC link voltage of 96 V was applied, causing the machine to draw a current of 4 A. The close correlation between the FEM and measured results confirms the accuracy of the FEM model in

Authorized licensed use limited to: Tallinn University of Technology. Downloaded on October 26,2026 at 09:07:14 UTC from IEEE Xplore. Restrictions apply.

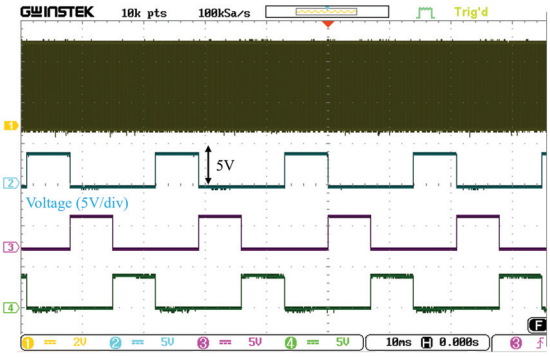


Fig. 22. Encoder pulses and switching signals for on/off phases.

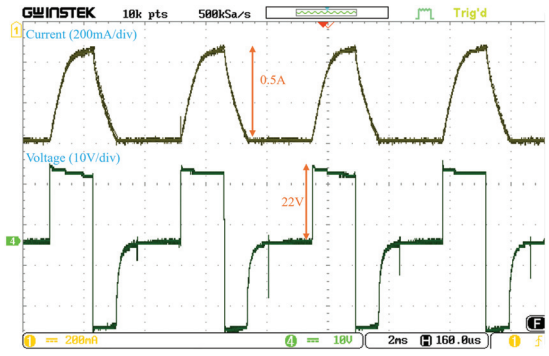


Fig. 23. Current and voltage waveform in SPC mode.

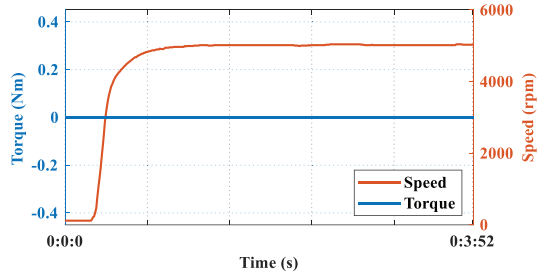


Fig. 24. Experimental speed of the proposed AFDR-SRM at no load.

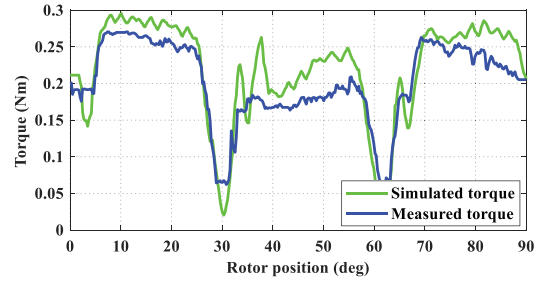


Fig. 25. Dynamic torque waveform at rated loaded condition.

representing the machine's performance under loaded operating conditions.

VII. Conclusion

This paper presented the design and development of an AFDR-SRM for high-speed propulsion applications. The study started the derivation of the output power equation, followed by calculations of other geometric parameters. The analytical results were validated through FEM simulations, demonstrating good agreement with the analytical calculations. Subsequently, a dynamic analysis based on the torque-speed curve across various operating points was performed to evaluate the machine efficiency. The analysis also investigated losses, quantifying both iron and copper losses in different regions of the machine.

A prototype was manufactured using SLM, an additive manufacturing technique that enabled precise fabrication of the complex machine geometry. The prototype was experimentally tested, and the results showed that the experimental static torque was approximately consistent with the simulated value, having minor deviations attributed to manufacturing variances. A comparison between the chosen JMAG library material and the 3D-printed material revealed that both exhibited similar static torque performance. The preliminary load torque waveform of the machine was validated through experimental testing, which demonstrated the consistency between the measured and simulated loaded torque waveforms. The future work involves detailed experimental testing under different dynamic conditions. In future studies, comprehensive experimental testing will be conducted, and topology optimization will be performed to enhance flux distribution and maximize the efficient utilization of the core volume.

References

[1] M. S. Islam, R. Mikail, and I. Husain, "Slotless lightweight motor for aerial applications," *IEEE Trans. Ind. Appl.*, vol. 55, no. 6, pp. 5789–5799, Nov./Dec. 2019, doi: 10.1109/TIA.2019.2935055.

[2] S. Hussain, A. Kallaste, M. U. Naseer, M. Sarap, H. Tiismus, and T. Vaimann, "Preliminary design analysis of an axial flux yokeless stator switched reluctance machine," in *Proc. IEEE 64th Int. Sci. Conf. Power Elect. Eng. Riga Tech. Univ.*, 2023, pp. 1–6, doi: 10.1109/RTUCON60080.2023.10413130.

[3] M. V. de Paula, T. A. d. S. Barros, H. S. Moreira, E. O. H. Catata, M. G. Villalva, and E. R. Filho, "A Dahlin cruise control design method for switched reluctance motors with minimum torque ripple point tracking applied in electric vehicles," *IEEE Trans. Transport. Electrific.*, vol. 7, no. 2, pp. 730–740, Jun. 2021, doi: 10.1109/TTE.2020.3019997.

[4] W. Cao, B. C. Mecrow, G. J. Atkinson, J. W. Bennett, and D. J. Atkinson, "Overview of electric motor technologies used for more electric aircraft (MEA)," *IEEE Trans. Ind. Electron.*, vol. 59, no. 9, pp. 3523–3531, Sep. 2012, doi: 10.1109/TIE.2011.2165453.

[5] W. Uddin, T. Husain, Y. Sozer, and I. Husain, "Design methodology of a switched reluctance machine for off-road vehicle applications," *IEEE Trans. Ind. Appl.*, vol. 52, no. 3, pp. 2138–2147, May/Jun. 2016, doi: 10.1109/TIA.2015.2514283.

[6] K. Kiyota and A. Chiba, "Design of switched reluctance motor competitive to 60-kW IPMSM in third-generation hybrid electric vehicle," *IEEE Trans. Ind. Appl.*, vol. 48, no. 6, pp. 2303–2309, Nov./Dec. 2012, doi: 10.1109/TIA.2012.2227091.

[7] F. Yu et al., "Design and multiobjective optimization of a double-stator axial flux SRM with full-pitch winding configuration," *IEEE Trans. Transport. Electrific.*, vol. 8, no. 4, pp. 4348–4364, Dec. 2022, doi: 10.1109/TTE.2022.3173938.

Authorized licensed use limited to: Tallinn University of Technology. Downloaded on October 26,2026 at 09:07:14 UTC from IEEE Xplore. Restrictions apply.

[8] G. Davarpanah and J. Faiz, "A novel structure of switched reluctance machine with higher mean torque and lower torque ripple," *IEEE Trans. Energy Convers.*, vol. 35, no. 4, pp. 1859–1867, Dec. 2020, doi: 10.1109/TEC.2020.2990914.

[9] S. E. M. Mohammadi, P. Chen, M. Moallem, B. Fahimi, and M. Kiani, "An alternate rotor geometry for switched reluctance machine with reduced torque ripple," *IEEE Trans. Energy Convers.*, vol. 38, no. 2, pp. 939–947, Jun. 2023, doi: 10.1109/TEC.2022.3229999.

[10] A. Ghaffarpour and M. Mirsalim, "Split-tooth double-rotor permanent magnet switched reluctance motor," *IEEE Trans. Transport. Electrific.*, vol. 8, no. 2, pp. 2400–2411, Jun. 2022, doi: 10.1109/TTE.2022.3147703.

[11] W. Yan, H. Chen, S. Liao, Y. Liu, and H. Cheng, "Design of a low-ripple double-modular-stator switched reluctance machine for electric vehicle applications," *IEEE Trans. Transport. Electrific.*, vol. 7, no. 3, pp. 1349–1358, Sep. 2021, doi: 10.1109/TTE.2021.3057133.

[12] W. Sun, Q. Li, L. Sun, and L. Li, "Development and investigation of novel axial-field dual-rotor segmented switched reluctance machine," *IEEE Trans. Transport. Electrific.*, vol. 7, no. 2, pp. 754–765, Jun. 2021, doi: 10.1109/TTE.2020.3033668.

[13] G. Wang et al., "Design, analysis, and comparison of a novel axial flux modular-double-stator hybrid excitation SRM," *IEEE Trans. Transport. Electrific.*, vol. 10, no. 3, pp. 6100–6114, Sep. 2024, doi: 10.1109/TTE.2023.3347742.

[14] H. Torkaman, A. Ghaheri, and A. Keyhani, "Axial flux switched reluctance machines: A comprehensive review of design and topologies," *IET Electric Power Appl.*, vol. 13, no. 3, pp. 310–321, 2019, doi: 10.1049/iet-epa.2018.5190.

[15] W. Sun, Q. Li, L. Sun, L. Zhu, and L. Li, "Electromagnetic analysis on novel rotor-segmented axial-field SRM based on dynamic magnetic equivalent circuit," *IEEE Trans. Magn.*, vol. 55, no. 6, Jun. 2019, Art. no. 8103105, doi: 10.1109/TMAG.2019.2901002.

[16] Z. Xu, T. Li, F. Zhang, Y. Zhang, D. H. Lee, and J. W. Ahn, "A review on segmented switched reluctance motors," Energies, vol. 15, no. 23, 2022, Art. no. 9212, doi: 10.3390/en15239212.

[17] H. Tiismus, A. Kallaste, T. Vaimann, A. Rassõlkin, and A. Belahcen, "Additive manufacturing of prototype axial flux switched reluctance electrical machine," in *Proc. 28th Int. Workshop Electric Drives, Improving Rel. Electric Drives*, 2021, pp. 1–4, doi: 10.1109/IWED52055.2021.9376337.

[18] A. D. Goodall, F. N. U. Nishanth, E. L. Severson, and I. Todd, "Loss performance of an additively manufactured axial flux machine stator with an eddy-current limiting structure," *Mater. Today Commun.*, vol. 35, 2023, Art. no. 105978, doi: 10.1016/j.mtcomm.2023.105978.

[19] N. Gadiyar, A. D. Goodall, I. Todd, and E. L. Severson, "Characterization of an axial flux machine with an additively manufactured stator," *IEEE Trans. Energy Convers.*, vol. 38, no. 4, pp. 2717–2729, Dec. 2023, doi: 10.1109/TEC.2023.3285539.

[20] J. Ma et al., "Optimal design of an axial-flux switched reluctance motor with grain-oriented electrical steel," *IEEE Trans. Ind. Appl.*, vol. 53, no. 6, pp. 5327–5337, Nov./Dec. 2017, doi: 10.1109/TIA.2017.2727438.

[21] S. Hussain, A. Kallaste, M. U. Naseer, H. Tiismus, and T. Vaimann, "Development of an axial flux SRM through additive manufacturing," in *Proc. 2024 Int. Conf. Elect. Machines*, 2024, pp. 1–6, doi: 10.1109/ICEM60801.2024.10700569.

[22] J. Pyrhönen, T. Jokinen, and V. Hrabovcová, *Des. of Rotating Elect. Machines*, Chichester, U.K.: Wiley, 2008, doi: 10.1002/9780470740095.

[23] H. Tiismus et al., "Laser additively manufactured magnetic core design and process for electrical machine applications," *Energies (Basel)*, vol. 15, no. 10, 2022, Art. no. 3665, doi: 10.3390/en15103665.

[24] H. Tiismus, A. Kallaste, M. U. Naseer, T. Vaimann, and A. Rassõlkin, "Design and performance of laser additively manufactured core induction motor," *IEEE Access*, vol. 10, pp. 50137–50152, 2022, doi: 10.1109/ACCESS.2022.3173317.

Authorized licensed use limited to: Tallinn University of Technology. Downloaded on October 26,2026 at 09:07:14 UTC from IEEE Xplore. Restrictions apply.

Curriculum Vitae

Personal data

Name:	Shahid Hussain
Date of birth:	16-03-1996
Place of birth:	Pakistan
Citizenship:	Pakistan

Contact data

E-mail:	shahid.hussain@taltech.ee shahidhissain@gmail.com

Education

2022–2026	PhD, Department of Electrical Power Engineering and Mechatronics, Tallinn University of Technology, Estonia
2020–2022	MSC, Department of Electrical and Computer Engineering, COMSATS University Islamabad, Abbottabad Campus, Pakistan
2015–2019	BSC, Department of Electrical and Computer Engineering, COMSATS University Islamabad, Abbottabad Campus, Pakistan

Language competence

English	Fluent
Estonian	Basic
Urdu	Native
Pashto	Native

Professional employment

2022-2026	Early-stage Researcher (1.00) Department of Electrical Power Engineering and Mechatronics, Tallinn University of Technology, Estonia

Projects

- PRG1827 “Additively Manufactured Electrical Machines” (01.01.2023-31.12.2027), Principal Investigator: Ants kallaste, Tallinn University of Technology, School of Engineering, Department of Electrical Power Engineering and Mechatronics. Financier: Estonian Research Council

Elulookirjeldus

Isikuandmed

Nimi:	Shahid Hussain
Sünniaeg:	16-03-1996
Sünnikoht:	Pakistan
Kodakondsus:	Pakistani

Kontaktandmed

E-post:	shahid.hussain@taltech.ee shahidhissain@gmail.com

Hariduskäik

2022–2026	PhD, Elektroenergeetika ja mehhatroonika instituut, Tallinna Tehnikaülikool, Eestonia
2020–2022	MSC, Elektri- ja arvutitehnika osakond, COMSATS Ülikool Islamabad, Abbottabad ülikoolilinnak, Pakistan
2015–2019	BSC, Elektri- ja arvutitehnika osakond, COMSATS Ülikool Islamabad, Abbottabad ülikoolilinnak, Pakistan

Keelteoskus

Inglise keel	kõrgtase
Eesti keel	algtase
Urdu keel	emakeel
Pashto keel	emakeel

Teenistuskäik

2022-2026	Nooremteadur (1.00) Elektroenergeetika ja mehhatroonika instituut, Tallinna Tehnikaülikool, Eestonia

Projektid

- PRG1827 “Kihtlisandustehnoloogial põhinevad elektrimasinad” (01.01.2023−31.12.2027); Vastutav täitja: Ants Kallaste, Tallinna Tehnikaülikool, Inseneriteaduskond, Elektroenergeetika ja mehhatroonika instituut; Finantseerija: Sihtasutus Eesti Teadusagentuur

ISSN 2585-6901
ISBN 978-9916-80-597-8